Eötvös Loránd University – Faculty of Science

Hevesy György PhD School of Chemistry

Analytical Chemistry, Materials Science, Electrochemistry, Colloidal and Environmental Chemistry Program

Conducting and non-conducting polymers in electrochemical systems – preparation, properties, and applications

Doctoral Dissertation

Krisztina J. Szekeres

Master of Science

Budapest, 2021

Supervisor: Győző G. Láng DSc, *professor*
Head of Doctoral School: Attila G. Császár DSc, *professor*
Head of Doctoral Program: Imre Salma DSc, *professor*
Research laboratory: ELTE Laboratory of Electrochemistry and Electroanalytical Chemistry
Head of Research Laboratory: György Inzelt DSc, *professor emeritus*

Conducting and non-conducting polymers in electrochemical systems – preparation, properties, and applications

Doctoral Dissertation

Prepared at Eötvös Loránd University (Department of Physical Chemistry, Institute of Chemistry, Laboratory of Electrochemistry and Electroanalytical Chemistry)
Budapest, 2017 – 2021.

Supervisor: Győző G. Láng DSc, *professor*

DOI: 10.15476/ELTE.2021.138

The research work was partly supported by the New National Excellence Program of the Ministry for Innovation and Technology from the source of the National Research; Development and Innovation Fund, by National Research, Development, and Innovation Office (NKFIH, grant nos. K129210 and FK135375). The work within project no. VEKOP-2.3.2- 16-2017-00013 and the ELTE Institutional Excellence Program (TKP2020-IKA-05) was partly financed by the European Union and the Hungarian Ministry of Human Capacities.

Table of Contents

Preface

Polymers – thousands of books and millions of scientific papers have been written about them, so one would think that there is nothing new to discover on this topic. I would like to show that there certainly is! In this thesis I present the main findings and results of my 4 year PhD research on preparation, properties, and applications of conducting and non-conducting polymers in electrochemical systems.

I joined to Professor Láng's research group (ELTE, Laboratory of Electrochemistry and Electroanalytical Chemistry) in 2014, as a second-year chemistry student at Eötvös Loránd University. During my bachelor's (2014–2015) and master's (2015–2017) research, I studied electrochemical and morphological properties of poly(3,4-ethylenedioxythiophene), so-called PEDOT conductive polymer. I investigated the effect of the composition and pH of the electrolyte solution on the polymer film and the structural changes suffered by the PEDOT film due to overoxidation. A work for Scientific Student Conference was also submitted from these studies. I studied the electrochemical behavior of PEDOT films deposited on different substrate materials: gold and glassy carbon. I prepared and investigated PEDOT layers with different thicknesses.

In 2017 I was admitted to the ELTE Hevesy György PhD School of Chemistry and I continued my research work in Professor Láng's group. In addition to PEDOT I investigated basic electrochemical properties of other conductive polymers such as poly(3,4-ethylenedioxypirrol) (PEDOP), polyaniline (PANI) and poly(o-phenylenediamine). I continued studies on alternative substrate materials for deposition of conductive polymer layers and I started to investigate carbon felt. For an industrial request, I studied the electrochemical behavior of bisphenol A (BPA) which led to unexpected results and prompted further investigations.

In 2020 I attained a Campus Mundi scholarship to spend a semester in the USA working in Professor Katz's research group at Clarkson University. I studied non-conductive polymer- and enzyme-modified magnetic nanoparticles.

During my PhD studies I was supported annually by New National Excellence Program (ÚNKP) of the Ministry for Innovation and Technology from the source of the National Research.

In this thesis, I describe the most important results of my PhD research. The publications on which the dissertation is based are papers with numbers [1–5] in the bibliography. A patent application, conference participations, and other publications, are: [6–19].

Acknowledgement

I would like to extend my gratitude to Prof. Dr. Győző G. Láng, who has always been patient and encouraging during my studies and research, and whose combined guidance and expertise in the field of electrochemistry have been essential to my development as a scientist. Professor Láng's unwavering commitment to his students and enthusiasm for research have kept me engaged in my research endeavors.

I am also very grateful to Professor Evgeny Katz from Clarkson University, who gave me the opportunity to work in his laboratory and gain unforgettable experiences. From his group I am really thankful to Paolo Bollella and Daniel Massana for their infinite kindness and support.

I also owe a great deal of gratitude to Dr. Mária Ujvári and Dr. Soma Vesztergom for their constant help and advices during various stages of this research work.

I would like to thank my colleagues and friends - with whom I learned or worked together at Eötvös Loránd University - for their help and support during my studies and research: Noémi Kovács, Balázs Broda, Dóra Zalka, Miklós Kuti, Éva Fekete, Ábel Zsubrits, and all of my friends from the Chemistry BSc. class 2012. I really appreciate their company and friendship.

This work would not have been possible without the support of our laboratory technicians Friderika Himics, Bea Marosvölgyi, and László Gajdos, and the always helpful and professional SEM operator, Gábor Varga.

And last but not least, I am very grateful to my family, who supported me during my university years and helped me reach my goals.

Budapest, September 2021.

Krisztina J. Szekeres

I. Introduction

Polymers are macromolecules of high relative molecular mass, the structure of which essentially comprises the multiple repetition of units derived, actually or conceptually, from molecules of low relative molecular mass [20]. Polymers are essential materials of modern industry and society. Until the ’70s, the scientific community (the common language maybe still) thought that polymers can be exclusively non-conductive materials. Alan J. Heeger, Alan G. MacDiarmid, and Hideki Shirakawa discovered, that the conductivity of polyacetylene can be increased more than 10^9 times by iodine vapor oxidation [21]. For the invention and development of conductive polymers they were awarded with Nobel prize in 2000 [22]. The invention of so-called conductive polymers was a real paradigm shift, however, their story had started much earlier. In 1862 Henry Letheby had already produced conductive and electrochromic (changes its color with the change of electrical potential) polyaniline with the anodic oxidation of aniline [23]. According to Electrochemical Dictionary [24], conducting polymers are “intrinsically electronically conducting polymers or “synthetic metals” that conduct electricity”.

The most interesting feature of the conductive polymers is the variability of their conductivity, that ranges from $<10^{-8}$ S·m^{-1} (like insulators) to $>10^{6}$ S·m^{-1} (like metals). It means, that these kind of materials can be reversibly switched between their insulating and conducting forms by oxidation and reduction.

Owning to this reversibility (reversible doping-dedoping) and the electrochromic property they can be utilized as (electro)chemical- and biosensors in electronic devices [25–27]. For example, polypyrrole is used in electronic noses [28].Conductive polymers are also used in field-effect transistors as a conductive coating [29], and for the formation of electromagnetic radiation-absorbing coatings for military stealth aircrafts [30]. A group of the conductive polymers capable of electroluminescence, so they can be used in light-emitting devices [31], another group is used in smart windows because of their electrochromic behavior [32]. CPs are also promising materials in neural probes and brain computer interfaces [33–36]. These were only a few interesting examples from the endless list of usage of the conducting polymers.

The most important one from the point of view of the present thesis is that conductive polymers are promising materials in energy storage [37–43] due to their high charge density, mechanical flexibility, conformability, versatility, ease in fabrication into composites, and low cost compared to expensive metal oxides. Nanostructured conductive polymers can be used as active electrode materials in lithium ion batteries and in supercapacitors [44,45]. However, these materials often suffer from cycling stability problems because of the swelling and shrinking during the charging/discharging processes. This problem can be solved by composite formation, therefore, composites containing conductive polymers are used for example in solid-state flexible supercapacitors [46]. On the other hand, this swelling-shrinking behavior can be utilized in artificial muscles [47]. The field of biomimetic electrochemistry also uses nanostructured polypyrrole films as electrically controllable drug release systems [48].

I.1. Categories of conductive polymers

A conductive polymer can be *electro-conducting* or *proton (ion)-conducting*, which depends on the mode of charge propagation. This behavior is in connection with the chemical structure of the polymer. Based on the electron transport's mode, **electro-conducting** polymers can be also classified into two further groups [49].

I.1.1. Electronically conductive polymers (intrinsically conductive polymers – ICPs)

The motion of delocalized electrons occurs through conjugated systems. However, the so-called electron hopping, that is electron exchange reaction between polymer chains, also plays a role in the formation of conduction. This conduction mechanism can be assumed in the case of the most commonly used conductive polymers, as polyaniline and its derivatives, poly(diphenylamine), poly(o-phenylenediamine), poly(o-aminophenol), polyluminol, polypyrrole and its derivatives, polycarbazoles, polythiophene and its derivatives, polyazines, polyfluorene, etc.

I.1.2. Redox polymers

These kinds of polymers have oxidizable and reducible redox sites. When the segmental motions allow it the electrons between close redox sites are transported by electron hopping. Several subclasses of redox polymers can be distinguished:

> 1) Polymers that contain covalently attached organic or organometallic redox centers. The functional groups are either built into the polymer chain or as pendant groups. For example: poly(tetracyanoquinodimethane), poly(viologens), poly(tetrathiafulvalene), quinone polymers, poly(vinylferrocene).
>
> 2) Ion-exchange polymeric systems with redox active ions connected to the polymer chains by electrostatic binding. For example: Nafion, Poly(Styrene Sulfonate), Poly(4-Vinylpyridine).

A simple distinction between the intrinsically conducting and redox polymers is that in dry state the intrinsically conducting polymers are conducting while redox polymers have high electrical resistance [50,51]. This is simply due to the fact that redox polymers and ionically conducting polymers need a liquid (water or other solvent) which acts as a plasticizer and makes the chain and segmental motions possible. It is also known that for intrinsically conducting polymers with high conjugation lengths nearly ideal capacitive behavior and “rectangular-shaped” cyclic voltammograms can be observed in a rather broad potential range [52]. The shapes of these curves are quite different from the shapes of cyclic voltammograms recorded for redox polymer modified electrodes where peaks (one or more minima and maxima) related to redox processes can be observed (see **Figure 1.**, where cyclic voltammograms recorded at PEDOT and PTCNQ modified electrodes [53] are shown).

With the combination of different materials, there is an endless opportunity for inventing electronically conductive polymers, with brand new behaviors.

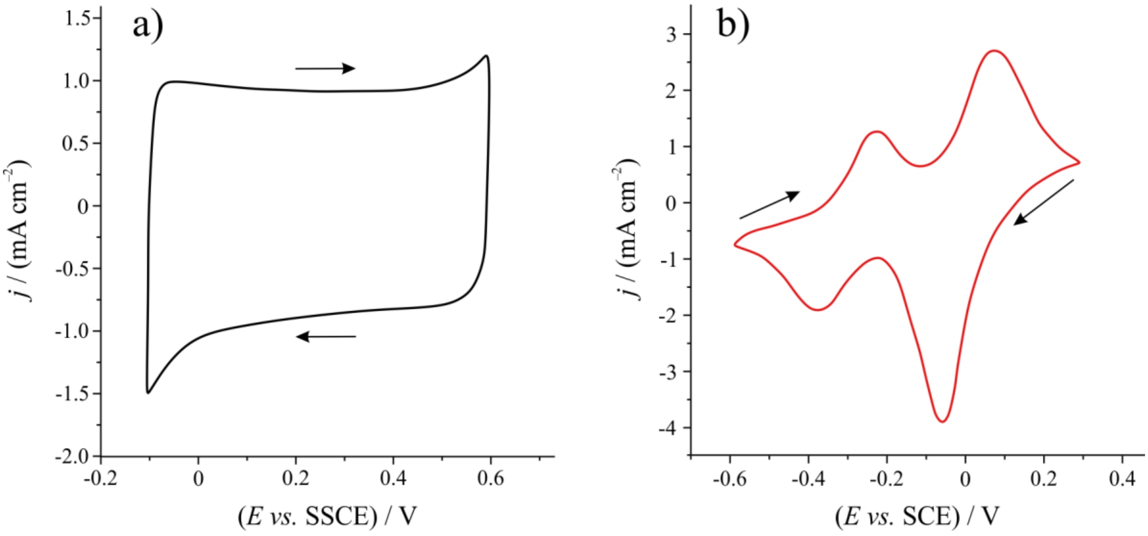

Figure 1. Cyclic voltammograms of **a)** a Au|Poly(3,4-ethylenedioxythiophene) electrode in contact with 0.1 mol·dm^{-3} aqueous solution of H_2SO_4, scan rate $v = 50$ mV·s^{-1}, $E = -0.1 – 0.6$ V *vs*. SSCE and **b)** a Pt|poly(tetracyanoquinodimethane) electrode in contact with 10 mol·dm^{-3} aqueous solution of LiCl, scan rate $v = 4$ mV·s^{-1}, $E = -0.6 – 0.3$ V *vs*. SCE.

I.1.3. Copolymers

Copolymers are usually prepared by the electropolymerization of the mixture of two or more different monomers, or rarely the monomers can also be electropolymerized separately. Since the electropolymerization of a monomer mixture is not a well-controlled process, the structures of the copolymers are not well-defined in many cases. The molar ratio of the monomers defines the properties of a copolymer, which can be regulated by different experimental conditions such as scan rate or pH. Usually, the electrochemical response of a copolymer shows the characteristics of all polymers it was prepared from. However, in many cases the electrochemical and other behaviors of a copolymer is completely different.

I.1.4. Composite materials

This is not a well-defined class, since different systems can be classified here, for example, systems where conductive polymers are deposited onto inorganic materials as carbon or metal oxides. Systems, where the monomer is polymerized in the presence of polymeric counterions, are also common. Important to note, that between the builder components, there is a special interaction, so the composite materials are more than just a simple mixture of its components.

I.2. Producing of a conductive polymer layer

There are many ways to create a surface layer of a conductive polymer. Based on the bond formed between the layer and the surface, the producing methods can be separated into two main groups:

a) Chemical reaction (also chemisorption) is used when larger amounts of polymer are needed for further measurements or applications. These processes are hardly controllable, so rarely used for producing polymer film electrodes.

b) Physical adsorption can be used either by the direct application of the polymer onto the surface (spin-coating, electrolysis) or by the precipitation of the polymer layer directly on the surface (electrochemical polymerization). The morphology and conductivity of the polymer is controllable by the parameters of the electrochemical polymerization (potential, current density, monomer concentration, pH, time, temperature, etc.) [54–60]. For this reason, usually this method is preferable when the polymeric product is intended for use as a polymer film electrode, thin-layer sensor, or in microtechnology.

The three main cases of electrochemical polymerization are galvanostatic, potentiostatic, and potentiodynamic methods [61–63]. In galvanostatic method, the current between the working electrode and the counter electrode is held constant and the potential difference between the working electrode and the reference electrode is followed in time. In the case of potentiostatic polymerization, the electrode potential is held on a specific value, and the amount of charge used for the process is calculable from the current-time curves. With the static methods, overoxidation can be avoided, the polymer layer will be porous, and its porosity can be increased by increasing the current or the voltage. In potentiodynamic polymerization (cyclic voltammetry), the potential of the working electrode is cyclically varied according to a suitably selected control triangle signal, while the current flowing through the cell is measured. In this case the synthesis is less constrained by monomer diffusion and the formation of the polymer layer takes place layer by layer (one layer is formed in each potential cycle). Hence, this method leads to a homogeneous and smooth layer with a high intrinsic conductivity. The amount of deposited polymer depends on the sweep rate. With a higher scan rate the residence time of the electrode in the potential range of the deposition in a cycle is less, so the quantity of the polymer deposited in a sweep decreases. A higher anodic potential limit during the deposition can cause the oxidation of the deposited polymer layer. In this case the regular globular structure possibly changes, and the morphology becomes rod-like and fibrous.

According to the general experience, after polymerization, the deposited layer should be allowed to relax in a suitable solvent for a couple of hours or better overnight. During this relaxation period a well-conducting structure is formed by desolvation [64], and the unattached oligomers leave the surface.

Substrate material quality and its surface roughness are important factors during the preparation of a conductive polymer modified electrode. In laboratory practice well-defined and reproducible surface is the most important in choosing a substrate. However, in the industry low price, ready availability, and robustness are also essential. Onto a higher surface area larger quantity of polymer can be deposited and the layer possibly will have higher porosity and therefore higher capacitance [65]. The surface of precious metals (gold or platinum) is well-defined, and their electrochemical behaviors are well-known, but due to the high price, these are not considered in industry.

Glassy carbon is also an often used substrate of conductive polymer modified electrodes. This material has a very low porosity, but on a polished surface microscopic pitting can be observed [66]. It is not easy to obtain well-defined and reproducible surfaces. The electrochemical properties of glassy carbon electrodes are strongly dependent on the pretreatment of the surface. The electrodes have to be abraded with emery paper of increasing fineness followed by fine polish.

Other carbon contained materials as carbon cloth, carbon paper, graphite rod are also widely used substrates in conductive polymer modified electrodes, especially in microbial fuel cells (MFC) [67–69]. The textile structure facilitates different applications, where rigidity causes difficulties. The advantages of these materials are also low cost, easy availability, chemical stability, and good electrical conductivity. However, their surface is not well-defined, there are several gaps and crevices which decreases the reproducibility.

I.3. Materials investigated in the present work

I.3.1. PEDOT

Poly(3,4-ethylenedioxythiophene) (PEDOT) [70] belongs to the family of conducting polymers with high electronic conductivity, good chemical stability, controllable optoelectronic and redox properties. The alkylenedioxy substitution pattern serves to enhance the electrochemical, optical, and electrochromic properties of the polythiophene backbone. PEDOT is therefore an often-used conductive polymer in sensors. It can be found in TNT sensors [71], hydrogen chloride and ammonia vapor detectors [72], NO_2 sensors [73], neural probes [74], uric acid and dopamine sensors [75,76], and a bunch of other medical biosensors [77]. Connecting electronics directly to human tissues in the body ("cyborg technology") is a huge challenge. Traditional optoelectronic and microelectronic materials, such as semiconductors, gold, iridium, or stainless steel may cause scarring when implanted. For applications in living tissue, electrical signals need to be transmitted between the implant and the tissue to operate properly, but scars cause interruptions. According to recent results PEDOT dramatically improved the performance of medical implants with lowering their impedance by two to three orders of magnitude [78,79].

In these devices PEDOT is often in the so called "overoxidized" state (or turns to this state during operation). In studies performed to investigate the electrochemistry of PEDOT in more detail by using cyclic voltammetry (CV) it has been found that when the positive potential limit of the CV is extended into the region in which the "overoxidation" of the polymer film takes place, an oxidation peak (without a corresponding reduction peak) appears [12,13,15,52,80–83]. According to experimental results, the mechano-electrochemical properties of conductive polymers may change significantly during oxidation or reduction processes [84–86]. The same is true for PEDOT layers in polymer modified electrodes. Note that a polymer in different overoxidation states may have beneficial properties as well, among them increased porosity and higher affinity for adsorption of different substances [12,87]. Unfortunately, overoxidation is very often accompanied by delamination at the film/substrate interface making the unit unusable. The fracture generally starts with growth of a flaw on the film surface and continues with channel cracking in the film [13,81].

To solve this problem, we need to find a solution that could keep the electrochemical properties - especially conductivity - of the PEDOT polymer practically intact while changing the mechanical properties of the layer in order to make it more resistant against the effects of overoxidation.

Electropolymerization of PEDOT (**Figure 2.**) in aqueous solutions results typical cauliflower-like structure (**Figure 3.**). The monomer 3,4-ethylenedioxythiophene (EDOT) is poorly soluble in aqueous solutions, therefore a low concentration ($\sim10^{-2} - 10^{3}\ \mathrm{mol\cdot dm^{-3}}$) is needed to guarantee homogeneous media. Under these conditions polymerization of EDOT occurs above 0.70 V *vs*. SSCE [88]. Nevertheless, potential should be kept under 1.0 – 1.1 V *vs*. SSCE to avoid overoxidation. The material and surface quality of the substrate determined the homogeneity of the deposited PEDOT layer, since scratches on the surface help in starting the growth of polymer nuclei [63].

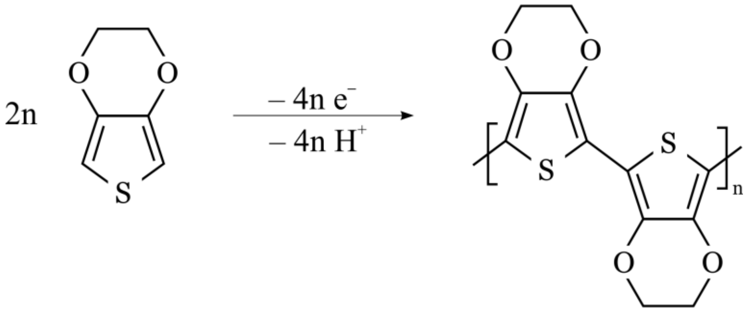

Figure 2. Polymerization of the monomer 3,4-ethylenedioxythiophene (EDOT)

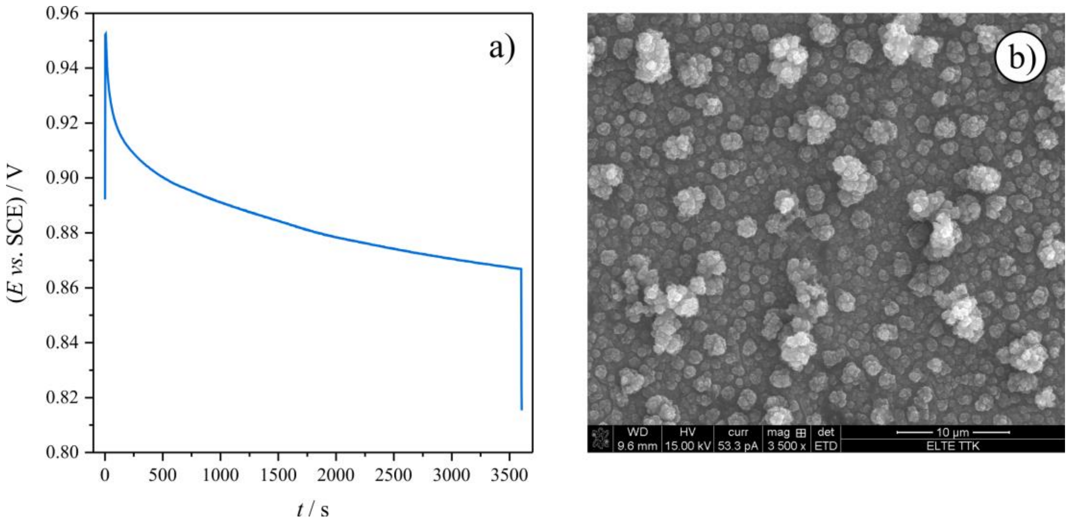

Figure 3. a) Potential data recorded during the deposition of a PEDOT layer. **b)** A typical SEM image of a PEDOT layer. Deposition conditions: 0.01 mol·dm^{-3} EDOT / 0.1 mol·dm^{-3} Na_2SO_4 (aq.) solution onto gold substrate (A = 0.196 cm^2) under galvanostatic conditions (j = 0.2 mA·cm^{-2}, t = 3600 s).

I.3.2. PEDOP

Poly(3,4-ethylenedioxypyrrole) (PEDOP) belongs to the family of conducting polymers with high electronic conductivity, controllable optoelectronic and redox properties. Its structure is very similar to PEDOT, instead of the sulfur atom it contains a nitrogen atom (**Figure 4.**). The alkylenedioxy substitution pattern serves to enhance the electrochemical, optical, and electrochromic properties of the polypyrrole backbone in a manner that is analogous to that observed for PEDOT. PEDOP has a fairly negative oxidation potential (half wave potential ($E_{1/2}$) of about −0.3 *vs.* SCE), therefore this polymer is one of the most easily oxidizable conducting polymers. In addition, PEDOP shows outstanding redox stability upon potential cycling [89]. The advantageous properties of PEDOP allow it to be used in a variety of applications including solar cells, smart windows, color sensors, biosensors, or other biological systems [90–94]. Nevertheless, the scientific literature published on PEDOP [95–98], with special regard to its electrochemical behavior is much less compared to that of other conducting polymers [99]. Dimerization of the monomer EDOP, similarly to pyrrole [100] can be spontaneously occurred by light, room temperature, or oxygen, therefore the monomer solution should be kept at −20 °C, under Ar atmosphere and dark, and it needs to be distilled before electropolymerization is attempted.

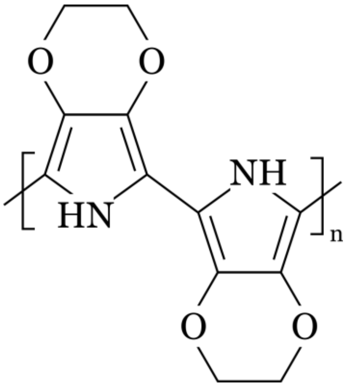

Figure 4. Structure of poly(3,4-ethylenedioxypyrrole) (PEDOP)

I.3.3. BPA

Bisphenol A (BPA, 4,4'-(propane-2,2-diyl)diphenol or 2,2-bis(4-hydroxyphenyl)propane, CAS 0000080-05-7, molar mass: M_{BPA} = 228.29 g/mol, **Figure 5.**) is a synthetic organic compound with two unsaturated phenolic rings. It is widely used in plastic industry as a monomer to produce epoxy resins, polycarbonate plastics, and flame retardants. Phenolic compounds are toxic to humans, animals and plants and despite its widespread use, many reports claim that BPA can leach out from plastic products such as food packaging materials and act as an endocrine disrupting chemical (EDC) [101–104]. The European food Safety Authority (EFSA) published its comprehensive re-evaluation of BPA exposure and toxicity, in January 2015 when it reduced the TDI (Tolerable Daily Intake) for BPA from 50 to 4 μg/kg bw/day [105]. On the basis of evidence published in the literature it has been asserted that there is an association between exposure to EDCs and risk of alterations in human health [106]. Recently, the European Chemicals Agency concluded that BPA should be listed as a substance of very high concern due to its properties as an endocrine disruptor [107], and an EFSA working group started evaluating recent toxicological data on BPA in 2018 [108,109].

The determination and the possibility of removal of phenolic type compounds from the environment has been extensively studied due to their widespread presence in the atmosphere and in industrial waste waters [110–115]. Chromatographic methods like gas chromatography (GC), liquid chromatography (LC), and gas chromatography-mass spectrometry (GC–MS) can achieve highly sensitive and precise detection of BPA

[114,115]. Each chromatographic technique has its own merits to be used for analysis in different applications. However, these methods can only be used in laboratory environments, require expensive instruments, time-consuming sample pretreatment processes, and highly trained technical personnel. Thus, these methods are unsuitable for rapid on-site detection.

Conversely, electrochemical methods of detection offer a potentially simpler, more rapid, and cost-effective alternative to traditional analytical methods [116,117]. In fact, electrochemical methods are preferred since there is no need for extensive separation. To oxidize and remove organic pollutants, electrochemistry has long been studied for wastewater treatment. However, direct oxidation kinetics are usually slow and often accompanied by gradual fouling of the electrode [116], e.g. it is well known that the electrochemical oxidation of phenolic compounds causes the inactivation of graphite or noble metal electrodes, via the deposition of electropolymerized films which are formed when phenoxy radical attacks an unreacted substrate [118–121].

A number of innovative attempts have been made to improve the BPA-sensing performance of electrochemical sensors (electrodes). For instance, electrodes modified with porous carbon materials, carbon nanotubes, graphene, graphite or gold nanoparticles, aptamer-functionalized nanoporous gold films, metallophthalocyanine complexes, and a series of other materials to increase the surface area of the electrodes have been considered [117,122–129]. From reviewing the relevant literature, it can be seen that gold has been widely used (frequently in the form of clusters or nanoparticles) in modified electrodes and sensors for the detection of phenolic-type compounds including BPA [130]. Nevertheless, it is sometimes assumed that metallic gold is electrocatalytically less active towards the oxidation of BPA. On the other hand, it is known that in alkaline media, gold electrodes are often more active than platinum and palladium electrodes in the oxidation of carbon monoxide and some small organic molecules [131].

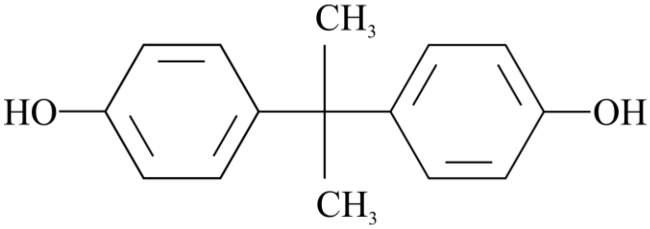

Figure 5. Structure of bisphenol A (BPA)

I.4. Objectives of the thesis

The main objectives during my 4 year PhD research were the following: assembly and application of combined electrochemical measuring system enabling new types of measurements. Development of electrochemical measurement methods and procedures for the monitoring of the degradation of conductive polymers and electron-conducting phases in modified electrodes. A better understanding of the mechanism of degradation processes in modified electrodes and electrode components. Obtaining new information on practically important electrochemical processes.

The above described PEDOT and BPA are frequently used compounds in the industry. There are tens of thousands of scientific publications about these materials (separately). However, the basic electrochemical and morphological properties of a thin layer PEDOT deposited on a suitable substrate, or electrochemical detection/analysis of BPA in aqueous solutions have left many unanswered questions and lots of room for research on several topics. For further use answering these questions is important. Conductive and non-conductive polymers can be used to solve various problems since both of them have their advantages. With the combination of these materials several interesting properties can be investigated and the newly gained knowledge can be applied in industry as well. At first glance, PEDOP is very similar to PEDOT, but its basic electrochemical and morphological properties are incompletely discussed in the literature.

In this thesis, I summarize the answers I have found to many raised questions and I show an interesting application of non-conducting polymers. During my work, I got some unexpected and really interesting results which maybe will help someone in the future to reach important practical goals.

II. Investigation methods

In this section investigation methods used during my research are introduced. I describe the main theoretical background of each technique but avoid excessive immersion in details. There are equations and figures, which are referenced in later sections of this work. Investigation conditions are significantly different in each chapter, therefore, this section is not followed by a general “experimental” part, but specific experimental conditions will be described in each chapter separately.

II.1. Cyclic voltammetry (CV)

Cyclic voltammetry is the most commonly used potentiodynamic method, which is suitable for rapid, routine studies of electrochemically active components. The technique is based on the measurement of the current response of an electrode to a linearly increasing and decreasing potential cycle (**Figure 6. a)**). The potential is scanned back and forth between two potential limits while the current that circulates through the circuit is recorded [132,133]. The scan rate (v / mV·s^{-1}) of the measurement shows that during the experiment, at what rate the potential changes:

$$v = \frac{\mathrm{d}E}{\mathrm{d}t} \qquad \text{Eq. 1}$$

The graph of the current (or current density, where the surface area of the electrode is well-defined) as a function of potential is called a cyclic voltammogram (**Figure 6. b), c)**). In the case of conducting polymers, cyclic voltammetric measurements give information about the oxidation potential of the monomer and the growth of the polymer film. Furthermore, the redox properties and kinetic parameters of the polymer can be determined.

In the case of a simple electrochemical process:

$$\mathrm{Ox} + ne^{-} \rightleftharpoons \mathrm{Red} \qquad \text{Eq. 2}$$

where $n = 1$, controlled by the rate of mass transport (that is usually means only diffusion, since migration is eliminated by the usage of high concentration supporting electrolyte, and convection is reduced by the absence of stirring or vibration) a peak pair can be observed on the cyclic voltammogram (**Figure 6. b)**). The explanation of this characteristic shape is the following: from the start potential (E_{start}) to the switch potential (E_{swich}) the anodic process takes place, so the reduced form (Red) is oxidized to Ox and depleted near the electrode surface. As the concentration of Red on the surface decreases, the concentration gradient increases, so does the current (from E_{start} to $E_{\mathrm{p,a}}$). After the anodic peak potential ($E_{\mathrm{p,a}}$) the concentration of Red slowly reaches zero, the thickness of the diffusion layer increases, and the current decreases because of the decrease of the concentration gradient. At E_{swich} the scan direction is reversed and the process described above goes backwards (cathodic process). In a reversible (or Nernstian) system Nernst equation describes the equilibrium and the peak-to-peak separation at 25°C is $\Delta E_{\mathrm{p}} = 59$ mV. In this case the value of the peak current (I_{p}) is given by the Randles-Ševčík equation:

$$I_{\mathrm{p}} = 0.4463 \cdot nFAc_{\mathrm{i}}^{*}\sqrt{\frac{nFvD_{\mathrm{i}}}{RT}} \qquad \text{Eq. 3}$$

where n is the number of the electrons involved in the reaction, F is Faraday's constant, A is the surface of the electrode, c_{i}^{*} is the bulk concentration of the species, v is the scan rate, D_{i} is the diffusion coefficient, R and T are the universal gas constant and the temperature. It is obvious from Eq. 3 that in Nernstian systems the peak current is proportional to the root of the scan rate. The peak potentials are independent of the scan rate.

In the case of quasi-reversible systems, Nernst law is not satisfied on the electrode surface, Erdey-Grúz–Volmer–Buttler equation describes the rate of the electrochemical reaction as a function of the electrode potential:

$$j = j_0\left(\exp\left[\frac{\alpha nF\eta}{RT}\right] - \exp\left[-\frac{(1-\alpha)nF\eta}{RT}\right]\right) \qquad \text{Eq. 4}$$

where j is the current density, j_0 is the exchange current density, α is the charge transfer coefficient, n is the number of the electrons involved in the reaction, F is Faraday's constant, η is the overvoltage ($\eta = E - E_{\mathrm{eq}}$), R and T are the universal gas constant and the temperature. The peak separation in these kind of systems depends on the rate constant of the reaction.

In the case of irreversible processes, electron transfer at the electrode surface is slow compared to mass transport and the peak potentials depend on the scan rate.

In the case of an ideal capacitor, it is expected to get a typical rectangular voltammogram shape (**Figure 6. c)**). The capacitive current follows a linear relationship with the scan rate [134,135]:

$$I = vC_{\mathrm{d}}\left(1 - \exp\left(-\frac{t}{R_{\mathrm{s}}C_{\mathrm{d}}}\right)\right) \qquad \text{Eq. 5}$$

where I is the current, v is the scan rate, C_{d} is the double layer capacitance, R_{s} is the solution resistance, t is the time and $\tau = R_{\mathrm{s}}C_{\mathrm{d}}$ is the so-called time constant. From Eq. 5 it is obvious that the shape of the voltammogram is more like a rectangle if the system has a smaller time constant.

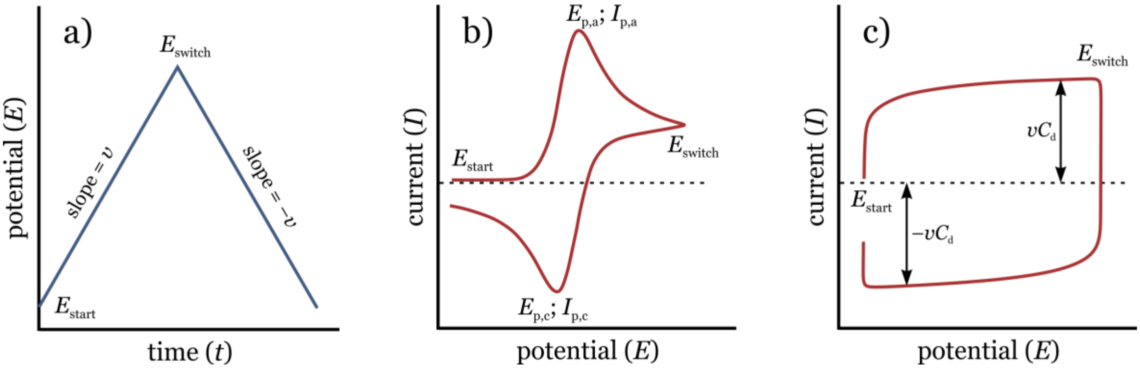

Figure 6. a) The triangle-shape potential program of cyclic voltammogram; **b)** Typical cyclic voltammogram of a redox system; **c)** Typical cyclic voltammogram of a capacitor.

II.2. Electrochemical impedance spectroscopy (EIS)

Electrochemical impedance spectroscopy (EIS) is a widely used, powerful, non-invasive technique for the study of electrochemical systems and the determination of their kinetic and transport parameters. Impedance measurements are performed by applying a sinusoidal voltage perturbation signal with a sufficiently small amplitude superimposed on the DC voltage level, for a range of frequencies, and the output current response signal is measured. The output signal responds to the input signal with the same frequency and a phase shift (**Figure 7.**). The output signal is measured in the frequency domain and therefore contains both real and imaginary components. Impedance is defined as the ratio of the change in potential ΔV to the change in current ΔI [136],

$$Z = \frac{|\Delta V|}{|\Delta I|} e^{i\varphi} = \mathrm{Re}Z + i\ \mathrm{Im}Z \tag*{Eq. 6}$$

where φ is the phase difference between potential and current, $i = \sqrt{-1}$ is the imaginary number, ReZ and ImZ are the real and the imaginary components of the impedance, respectively. The IUPAC convention is that the real part of the impedance is given by Z' and the imaginary part is given by Z''. In this thesis, the latter forms will be used for actual measured values, and ReZ, ImZ forms will be used in equations and on explanatory figures.

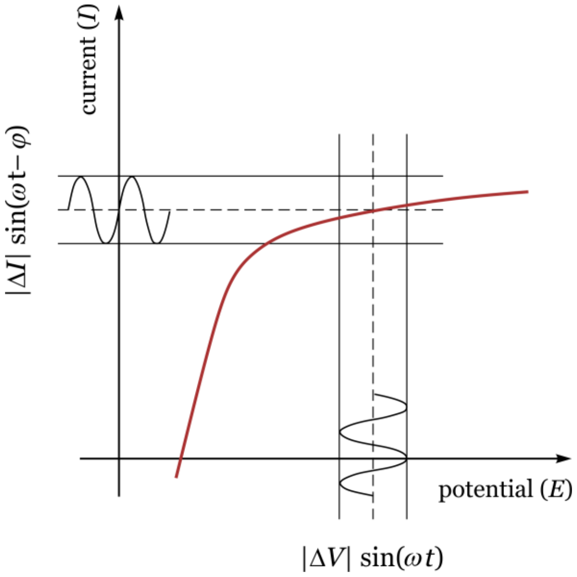

Figure 7. Sinusoidal perturbation of an electrochemical system at steady state, where ΔV and ΔI represent the potential and current oscillating at the same frequency ω. The phase difference between input and output signal is φ.

If the potential and current are in phase, the impedance is a real number and is actually a resistance:

$$Z_{\mathrm{resistor}} = R \qquad \text{Eq. 7}$$

When there is a 90° phase shift between the current and potential, the impedance is a pure imaginary number, which relates to capacitance (Eq. 8) or inductance (Eq. 9):

$$Z_{\mathrm{capacitor}} = \frac{1}{i\omega C} \qquad \text{Eq. 8}$$

or

$$Z_{\mathrm{inductor}} = i\omega L \qquad \text{Eq. 9}$$

where $\omega = 2\pi f$ is the angular frequency.

In an electrochemical system, the measured impedance is usually a complex quantity (i.e. its numerical value is a complex number), which means that these systems can be described by a combination of resistors, capacitors, and inductors with the creation of so-called equivalent circuits. The conducting polymer modified electrodes are systems with mixed kinetic and diffusion control. Randles–Ershler equivalent circuit can be used to describe these kinds of systems (**Figure 8.** insert).

Impedance data are often represented in a complex plane, which is also known as the Nyquist plot or Argand diagram. **Figure 8.** shows a typical Nyquist plot corresponding to a system in which the electrode process is a charge transfer coupled with mass transport (semi-limited diffusion). There are cases, when at small impedances (high frequencies) inductivity (L) from wires causes non-negligible error, so the imaginary part of the impedance needs to be corrected:

$$-\mathrm{Im}Z \approx -(\mathrm{Im}Z)_{\mathrm{meas}} + L2\pi f \qquad \text{Eq. 10}$$

where $(\mathrm{Im}Z)_{\mathrm{meas}}$ is the measured ImZ.

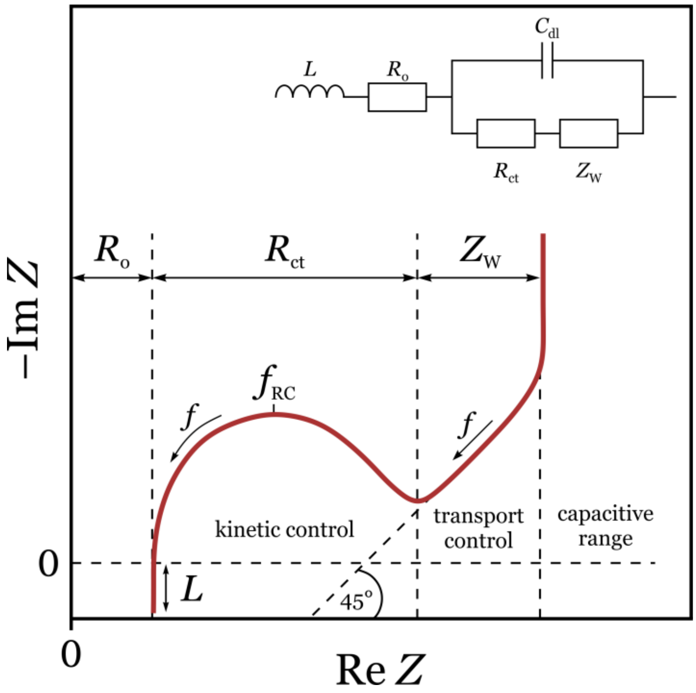

Figure 8. Representation of the impedance of an electrode in the complex plane (Nyquist plot) when the electrode process is a charge transfer coupled with mass transport [49]. Insert: the corresponding Randles–Ershler equivalent circuit. R_{ct} is the charge transfer resistance, Z_W is the Warburg-impedance, C_{dl} is the double layer capacitance, R_o is the Ohmic resistance of the electrolyte solution, L is the inductance, and f_{RC} is the characteristic frequency.

In high frequency regions of **Figure 8.** a small diameter semicircle can be observed. The characteristic frequency or time constant for the system

$$f_{\mathrm{RC}} = \frac{1}{2\pi R_{\mathrm{ct}} C_{\mathrm{dl}}} \qquad \text{Eq. 11}$$

can be obtained from the peak of this arc at which the negative value of imaginary part of the impedance is maximum. The medium-frequency range is dominated by a 45° section, which refers to transport processes inside the film. The low-frequency part indicates capacitive behavior. Next to a bunch of useful features, a disadvantage is that the Nyquist plot hides the frequency dependence, hence it is advantageous to label some points with their corresponding frequency.

Bode plot is used to show impedance as a function with respect to frequency. This plotting type shows magnitude of the impedance (Eq. 12), and phase angle (Eq. 19) as a function of frequency usually in logarithmic scale. **Figure 9.** shows the relationships between complex impedance, magnitude, and phase angle.

$$|Z| = \sqrt{(\mathrm{Re}Z)^2 + (\mathrm{Im}Z)^2} \qquad \text{Eq. 12}$$

$$\varphi = \tan^{-1}\frac{\mathrm{Im}Z}{\mathrm{Re}Z} = \cos^{-1}\frac{\mathrm{Re}Z}{|Z|} \qquad \text{Eq. 13}$$

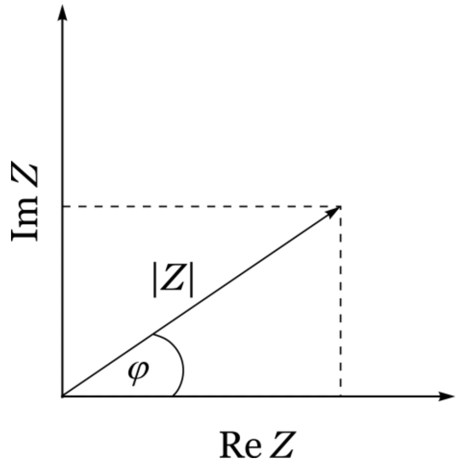

Figure 9. Phasor diagram showing relationships among complex impedance, magnitude (|Z|), and phase angle (φ).

In this thesis some more types of transformed plots are used. Admittance plot: the imaginary part of the admittance (ImY) as a function of the real part of the admittance (ReY).

$$\mathrm{Re}Y = \frac{\mathrm{Re}Z}{|Z|^2}; \mathrm{Im}Y = \frac{-\mathrm{Im}Z}{|Z|^2} \qquad \text{Eq. 14}$$

Valuable information can be gained from pseudocapacitance plotted as a function of frequency in logarithmic scale (log(Im$Y \cdot \omega^{-1}$) *vs.* (log f) plots).

II.2.1. Nonstationarity

In electrochemical practice the impedance is measured as a function of frequency. If the “potentiostatic” method is used, a small sinusoidal voltage is superimposed upon the DC polarization potential, and the current is measured. This is perhaps the most popular technique for electrochemical testing in which the AC stimulus level is usually about

5−10 mV. In the “galvanostatic” case a sinusoidal current is superimposed on the DC polarization current and the voltage response is recorded. Under appropriate conditions, that is, at properly selected cell geometry, working and auxiliary electrodes and so on, the impedance response will be related to the properties of the working electrode and the uncompensated (ohmic) resistance between the working and the reference electrodes. Assuming ideal single-sine perturbation, the excitation signal is time-invariant and deterministic. When this method is employed the system under test is sequentially excited by applying small sinusoidal waves of voltage or current within a given frequency range (e. g. from some mHz to some MHz). However, when data recording occurs at low frequencies, a complete measurement sequence can take at least several minutes. From this point of view, it should be taken into account that many electrochemical systems (including biological, reacting, and corroding systems) are intrinsically non-stationary and are affected by time-dependent phenomena [137]. This may be a serious problem since according to the traditional interpretation, impedance is not defined as a time-dependent quantity and, therefore, there should not exist an impedance out of stationary conditions. This means that if the requirement of stationarity (stability) during the measurement of “impedance” is not fulfilled, the measured data points are not “impedances”, the obtained sets of frequency dependent data points are not “impedance spectra” and their use in any analysis based on traditional impedance models is very questionable. Ignoring this issue may lead to serious problems and confusion, or even to misinterpretation of the experimental data.

II.2.1.a. Selected methods for the determination of instantaneous impedance spectra in *non-stationary systems*

II.2.1.a.1. The Gaussian window

Darowicki et al. [138–141] developed a method to determinate instantaneous impedance spectra by the connection of the pseudo-white noise [142], and the short-time Fourier transformation (STFT) methods [143,144]. By this coupling, the impedance spectra can be determined as the function of time. The perturbation signal was a package of n sinusoidal voltage signals with the same amplitude but different frequencies. The response of the investigated signal was a package of elementary current components of the same frequency composition. However, phase angels depend on the properties and characteristics of the investigated process. The Fourier transformations of the elementary current signal do not reflect changes in the investigated system in time. In contrast, STFT transformation, which differs from the regular Fourier transform by a term called the Gaussian window, reflects the frequency composition of the perturbation package and the amplitude changes in time, allows determination of the frequency spectrum changes as the function of time. Basically, during the STFT transform a signal portion was cut out by the window with a Gaussian peak shape, and then a regular Fourier transformation was performed. The procedure was carried out in the whole time range, in which the analyzed signal has been recorded. By carrying out a local Fourier transformation for each localized time range determined by the value σ(t) (where σ^2(t) is the variance of the Gaussian peak in the domain of time), instantaneous power density spectra were obtained. In the case of the stationary signal, there was no time dependence of the obtained power density spectra. When the signal was non-stationary, the dependence of the spectral power density on time becomes evident. By using the method of pseudo-white noise analyzed by the STFT method time–frequency impedance/admittance spectra can be obtained. The frequency resolution and time selectivity of the total time–frequency analysis of impedance/admittance spectra depends on the choice of size of the Gaussian window. However, a drawback of the method is that it is not possible to register the impedance spectra in a wide range of frequencies. See **Figure 10.**

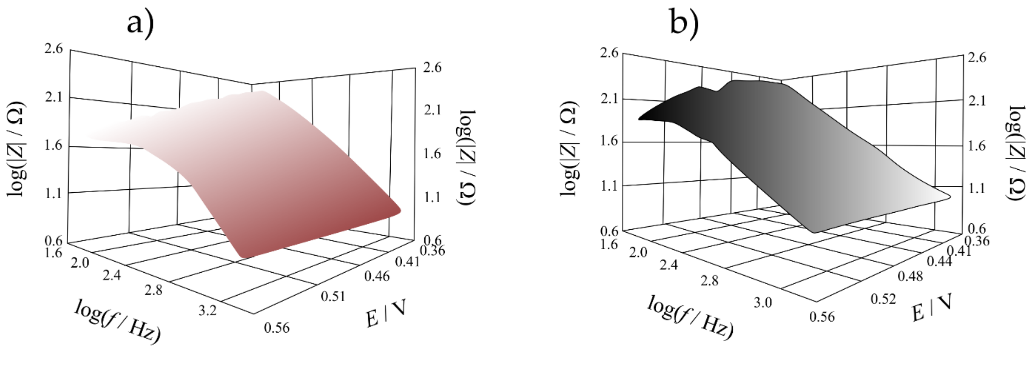

Figure 10. Three-dimensional spectra determined on the basis of **a)** peak value changes of each frequency peak in the function of polarization and **b)** of static impedance measurements of the investigated model electrical system. The figures were adapted with permission from Ref. [139]. Copyright (2000) Elsevier. License number: 5024961417529.

II.2.1.a.2. Odd random phase multisine with a random harmonic grid

Hubin et al. [145–150] described a measurement method for electrochemical impedance spectroscopy, using specially designed broadband excitation signals. A procedure was proposed to quantify and correct for the time-evolution by means of the calculation of an instantaneous impedance. A multisine composed by odd harmonics of abase frequency, removing every third frequency was employed. The impedance, the level of the disturbing noise, the non-linear distortions, and the non-stationary behavior were measured simultaneously. Using the odd random phase multisine excitation signal (ORP-EIS), they were able to correct the effect of the time-evolution of the system on the impedance spectra. By the acquisition of consecutive data sets, the variation of the impedance with time was reconstructed. However, they needed to assume a particular shape of the time variation of the impedance. The final results were modeled using equivalent circuits.

II.2.1.a.3. Dynamic multi-frequency analysis

Battistel et al. [151,152] introduced the dynamic multi-frequency analysis (DMFA) and compared it with a set of consecutive stationary impedance spectra on the ground of a simulated system consisting of a redox couple in solution in contact with a platinum electrode. The mathematical formulation of the conciliation of time dependence into the concept of impedance was presented. A new fitting algorithm with the usage of standard equivalent circuits and an algorithm [153] for handling the time variation of the fitting parameters were proposed and tested. During the fitting procedure, the Randles circuit: $R_s + C_h / (R_{ct} + W)$, (where R_s is the resistance of the electrolyte, C_h is the differential interface capacitance, R_{ct} is the charge transfer resistance) was used. C_h was larger in the case of the dynamic impedance and shows a lower variation. The voltage profile of the cyclic voltammetry had a small influence on the value of the double layer capacitance both in stationary and dynamic conditions. The Warburg element (σ) had a minimum in correspondence of $E_{1/2}$ which is influenced by the ratio of the diffusion coefficients of the redox couple, while the minimum of the charge transfer resistance was determined also by the symmetry factor of the reaction. R_{ct} and σ did not overlap either between stationary and dynamic impedance nor between cathodic and anodic scan. See **Figure 11**.

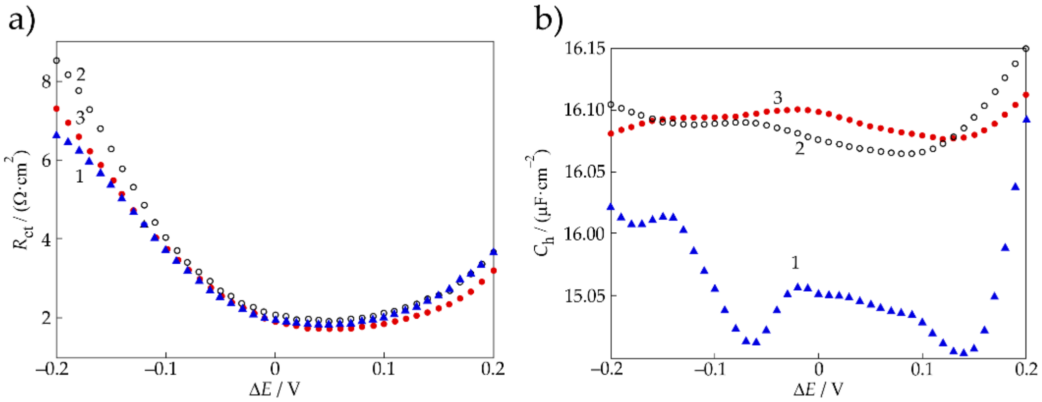

Figure 11. Comparison of **a)** charge transfer resistance (R_{ct}) and **b)** double layer capacitance (C_h) derived from the fitting of the static impedance (1) and for the dynamic impedance (cathodic scan (2) and anodic scan (3)). The figures were adapted from [151]. Copyright (2016) Wiley-VCH. License number: 5024981429616.

II.2.1.a.4. Potentiodynamic electrochemical impedance spectroscopy

Ragoisha et al. [154] used the so-called potentiodynamic electrochemical impedance spectroscopy (PDEIS) to investigate the irreversible lead underpotential deposition (upd) on tellurium. The idea of PDEIS bases on the extension of electrochemical impedance spectroscopy (EIS) to use it under non-stationary conditions, similar to cyclic voltammetry (CV). With the usage of potentiodynamic electrochemical impedance spectroscopy 3D picture can be got that characterizes not only the dc current but the potential dependence of the impedance spectra as well. In order to measure a PDEIS spectra of non-stationary systems virtual instruments operating in the real-time mode are needed. It is important to note, that in this case, the frequency range is necessarily narrower compared to the commonly used non-dynamic EIS.

II.2.1.a.5. Dynamic electrochemical impedance spectroscopy

Sacci and Harrington [155–157] developed software and hardware for dynamic electrochemical impedance spectroscopy (dEIS), which is a similar method to short-time Fourier Transform (STFT). The system on top of a potential sweep applies a continuous computer-generated small-amplitude multisine waveform. The hardware is compatible with any analog potentiostat since the digitalization of the current and voltage sings takes place in a USB controlled instrument. Advantage of this method, that the impedance spectra can be measured incessantly around a cyclic voltammogram, ergo it is suitable for non-stationary conditions. In addition, when dc and ac signals are generated from separate sources, one can get more freedom in the types of dEIS experiments.

Before the fast-Fourier transform of the measured signals (current and potential), a baseline correction needs to be taken. The impedances can be got by the quotient of the complex transformed potential and current. Dummy cell was used to test the dEIS method, which is usable both steady-state EIS, chronoamperometric EIS, and potential sweep EIS experiments.

II.2.1.a.6. Rotating Fourier transform

One of the kernels of electrochemical impedance spectroscopy is the Fourier Transform (FT). However, its usage under nonstationary conditions is not recommended, because methodical errors are produced. To solve this problem, Stoynov [158–160] developed a new mathematical transform, the so-called Rotating Fourier Transform (RFT), and also showed its first experimental application. This method keeps the basic properties of the original Fourier Transform, it filtrates orthogonally the linear term, and to the higher terms of the noise Taylor spectrum it is suboptimal.

The form of the new transform is

$$X(i\omega,\psi,N)=\frac{1}{2\pi n_1}\int_{\psi}^{\psi+2\pi n_1} w\,\mathrm{d}\varphi \qquad \text{Eq. 15}$$

where

$$w=\frac{1}{nT}\int_{t_\mathrm{i}}^{t_\mathrm{i}+nT} x(t)\mathrm{e}^{-i\omega t}\mathrm{d}t \qquad \text{Eq. 16}$$

where $x(t)$ is the input signal. As it can be seen in Eq. 15 and Eq. 16, the classical integration of the Fourier Transform is spread over an integer number of periods and it rotates *n* times, in this reason the suggested name of the transform is “Rotating”.

Eq. 15 can be generalized further and Multiple Rotating Transform (MRT) is defined:

$$x^{\nu}(i\omega) = \left\{(2\pi)^{\nu}\prod_{i}^{\nu} n_i\right\}^{-1} \times \int_{\psi}^{\psi+2\pi n_{\nu}} \dots \int_{\psi_1}^{\psi_1+2\pi n_1} w\,\mathrm{d}\varphi \dots \mathrm{d}\psi_{\nu-1} \qquad \text{Eq. 17}$$

where the order v is orthogonal to all n terms ($n = v$) of the aperiodic noise Taylor spectrum.

Both of the new methods (RFT and MRFT) keep the property of the original Fourier Transform with respect to periodic signals.

It is important to note, that simple back transforms are unable to restore the filtrated initial constant value and its time-derivatives, for that other mathematical tools should be used. The robustness of the RFT was also tested: the variations of the initial phase of a single frequency record was produced impedance results with $\Delta < 0.25°$ phase differences.

The author recommends some electrochemical fields, where RFT method can be used: corrosion, passivation, AC polarography, or measurement of the battery impedance during its operation, but it can be also useful in physics, geophysics, and material science.

II.2.1.a.7. Fast time-resolved EIS

Popkirov developed a two-cells measurement method for fast EIS measurements, that can be used under non-stationary conditions [161]. The relaxation component of the response signal is subtracted in real-time. This experimental method uses two identical electrochemical cells (the second one is a reference cell) to eliminate relaxation currents from the response current due to changes in the DC bias voltage.

As the schematic diagram of the measurement set-up (**Figure 12.**) shows, in order to set equal DC conditions for both cells, DC bias voltage ($U_{\mathrm{bias}}^{=}$) is applied to the input terminals of both potentiostats. To avoid phase and amplitude distortions the second potentiostat needs better frequency response, that is the reason for the usage of the perturbation AC voltage ($U_{\mathrm{pert}}^{\sim}$) in this case. To get a voltage proportional to the response current ($I^{\sim}_{\mathrm{resp}}$) the IC #3 differential amplifier was used. In this way, the relaxation currents can be eliminated from the response current, if both cells are identical.

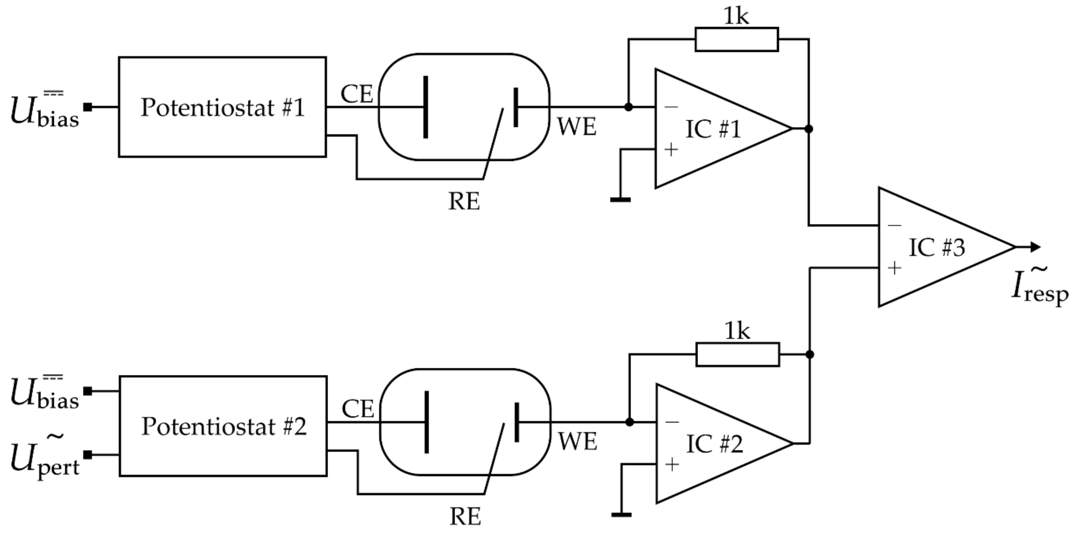

Figure 12. Electronic circuit diagram of the “two-cells experimental technique for fast EIS” measurements set-up. The figure was adapted with permission from Ref. [161] Copyright (1996) Elsevier. License number: 5024970467228.

II.2.1.a.8. Method of determining instantaneous impedance diagrams for non-stationary systems based on a four-dimensional approach

Stationarity usually refers to a system that exhibits stationary behavior through time. Non-stationarity then refers to something that is changing over time. This means that nonstationary behavior of a system clearly violates the stability criterion for transfer functions. However, it is possible to show that under some suitable conditions time dependence can be conciliated into the concept of impedance. Perhaps the most straightforward (approximative) method is that proposed by Stoynov (and developed further by other authors) for determining (or reconstruction) instantaneous impedance diagrams for non-stationary systems based on a four-dimensional approach [160,162–165]. The “instantaneous impedance” is defined as an instantaneous projection of the non-stationary state of the system into the frequency domain.

This post-experimental analytical procedure (the “4-dimensional analysis”) provides for correction of the systematic errors, arising during the measurements of time-evolving impedance, i. e. when the consecutive impedance measurements are performed at different system states, but each of the data points obtained at a given frequency can be accepted as "valid" impedances in the classical sense. The method is, in principle, based on the assumption that only insignificant changes in the system occur during the time required for measurement of a single data point, and the measured "impedance spectra" (and not the single data points) are corrupted by errors caused by the system evolution during the experiment [15,82,83,163,164,166,167]. In other words, the errors due to non-stationarity are reflected by the structure of the data and not by the individual data values.

The basis of the four-dimensional analysis method is the assumption that the state space and the parameter space (i. e., the space of possible parameter values that define a particular mathematical model) are continuous. On the other hand, no assumptions concerning the quality or structure of the system under investigation are needed for the application of the method. The application of the method requires the subsequent recording of "impedance" data sets at the same set of frequencies (**Figure 13. a)**). A data point recorded at a particular test frequency should additionally contain the time information of the measurement (these so-called "timestamps" can be the starting or ending times of the measurements of the individual impedance values, arithmetic or other suitably selected averages, etc.). Thus, the experimental data form a set of 4-dimensional arrays, containing the timestamp, frequency, and the real and imaginary components of the impedance (**Figure 13. b)**, **c)**). For every measured frequency two one dimensional functions of "iso-frequency dependencies" (e. g., for the real and for the imaginary components) are constructed. On the basis of the continuity of the evolution, interpolation (and/or extrapolation) is performed (e. g., by using smoothing or interpolating cubic spline or other interpolation functions) resulting in instantaneous projections of the full impedance-time space and "reconstructed" instantaneous impedances related to a selected instant of time (i. e., the beginning of each frequency scan) (**Figure 13. d)**). Thus, a set of impedance diagrams is obtained, containing instantaneous impedances corresponding to the same time moments. Each of these impedance diagrams can be regarded as stationary, free of nonsteady-state errors.

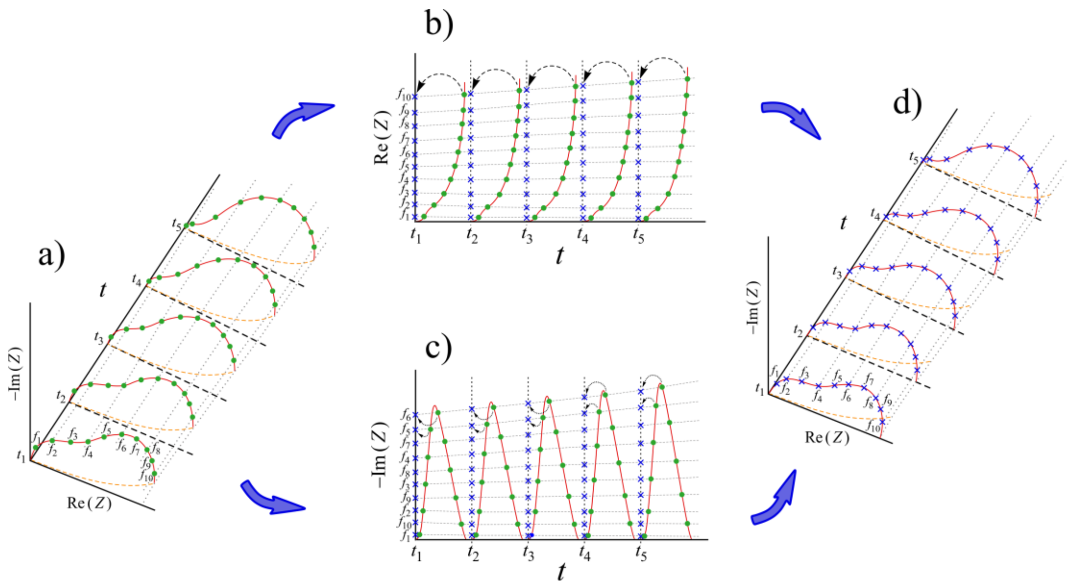

Figure 13. The schematic principle of the four-dimensional analysis (FDA) method. **a)** Time evolution of the impedance in Re(Z), −Im(Z) and time (t) coordinates (3D representation). ●: measured data points (impedances) corresponding to the frequencies f_j (in the figure: j = 1...10), t_i: starting time of the i-th frequency scan (in the figure: i = 1...5). **b)** Iso-frequency dependencies and calculation of the instantaneous (corrected) Re(Z) values (×) by interpolation of the measured Re(Z) data (2D representation). **c)** Iso-frequency dependencies and calculation of the instantaneous (corrected) −Im(Z) values (×) by interpolation of the measured Im(Z) data (2D representation). **d)** The “reconstructed” instantaneous impedances related to the beginning of each frequency scan (3D representation). ×: corrected data points (impedances) corresponding to the frequencies f_j.

One may conclude from the above considerations that that the four-dimensional analysis method is most effective in the correction of impedance data measured at low frequencies. Whereas this conclusion may be correct, it has recently been shown that the 4-dimensional analysis method is an effectual tool for handling non-stationary data sets recorded at higher frequencies as well [15,82].

In these studies, the method was successfully applied for the determination of some characteristic impedance parameters of overoxidized gold | poly(3,4-ethylenedioxytiophene) (PEDOT) | sulfuric acid (aq) electrodes. For instance, the charge transfer resistance corresponding to different time moments, including the time instant just after the overoxidation of the polymer film, could be determined, proving that the 4-dimensional analysis method can not only be used for the correction of the actually measured impedance data, but it opens up the possibility of the estimation of the impedance spectra outside the time interval of the measurements. According to the results the so called “low frequency capacitance” or “redox capacitance” of the polymer film is almost time independent. This means that the changes of the impedance spectra with time are solely due to time evolution of the charge transfer resistance and the double layer capacitance at the gold substrate/polymer interface. Consequently, in these cases the high and medium frequency regions of the impedance spectra are stronger affected by the time evolution than the values measured at low frequencies. (It should be noted here that apparently there are no generally accepted standard frequency ranges in electrochemical impedance spectroscopy (EIS). To assist with the interpretation of the EIS data, usually three frequency ranges are identified. These include a “high” frequency range from about 1 kHz up to 1–10 MHz, an “intermediate” (or “medium”) frequency range from 1 kHz to 1 Hz (or 0.1 Hz), and a “low” frequency range with frequencies below 1 Hz (or 0.1 Hz). However, the selection (or definition) of the potential ranges may depend on the properties of the system under investigation and the boundaries may be blurred.)

However, non-stationary behavior of the system is not the only issue one faces when attempting to evaluate impedance data obtained for conducting polymer modified electrodes. The nonuniform film thickness causes further complications. The problem of thickness distribution of polymer films in modified electrodes has been addressed in several papers [53,168–171], only few studies have focused on the development of "complete" impedance models which allow the simultaneous estimation of impedance parameters by fitting experimental data in wide frequency ranges.

II.3. Electrochemical quartz crystal microbalance (EQCM)

The EQCM technique is based on piezoelectricity. If properly cut crystal (so-called AT-cut) is exposed to an AC current, the crystal starts to oscillate at its resonant frequency and a standing shear wave is generated. This resonant frequency depends on the thickness of the crystal. Therefore, when mass is deposited on its surface, so the thickness increases, the frequency of oscillation decreases from the initial value. Sauerbrey's equation describes the relationship between the frequency change (Δf) and the mass change (Δm):

$$\Delta f = -\frac{2f_0^2}{\sqrt{\rho_\mathrm{q}\mu_\mathrm{q}}} \cdot \frac{\Delta m}{A} = -C_f \cdot \frac{\Delta m}{A} \qquad \text{Eq. 18}$$

where f_0 is the nominal resonant frequency of the crystal, $\rho_q = 2.648$ g·cm^{-3} and $\mu_q = 2.947 \cdot 10^{11}$ g·cm^{-1}·s^{-2} are the density and the shear modulus of the quartz crystal respectively, and A is the piezoelectrically active area. C_f is the integral sensitivity of the quartz crystal (**Table 1**) [49].

Table 1. Integral sensitivity values (C_f) of quartz crystals with a different nominal resonant frequency (f_0).

f_0 / MHz	C_f / Hz cm^2 µg^{-1}
5	56.6
6	81.5
10	226.4

With the combination of the Faraday law and the Sauerbrey equation (Eq. 18) the molar mass (M) of the deposited material can be calculated:

$$M = \frac{\Delta f}{\Delta Q} \cdot \frac{nFA}{C_f} \qquad \text{Eq. 19}$$

where Q is the charge, n is the charge number, F is Farday's constant. Follows from Eq. 19 that the C_f of the crystal can be calibrated with the deposition of a material of known molar mass.

II.4. UV-VIS spectroelectrometry

UV-VIS spectrometry combined with electrochemical techniques are often used investigating methods. Structural changes of conductive polymers caused by potential/current/charge change can be followed by them. Optically transparent electrodes (OTEs) are needed for these methods, which are usually indium–tin oxide (ITO) or a very thin (less than 100 nm) layer of gold or platinum on a glass or quartz substrate. To connect the electrodes inside the spectrometer cuvette with the potentiostat is not trivial since between the light source and the detector completely dark environment is needed.

II.5. Scanning electron microscopy (SEM)

A scanning electron microscope is an electro-optical device that scans the surface of an object with a thin electron beam in high vacuum to form various “products”: secondary electrons, back scattered electrons, and X-ray photons generated from the sample. Signals produced from the interaction of the electron beam and the object are detected by suitable detectors. This makes it possible to visualize the surface properties of the sample and to determine other properties of the test substance (e.g. chemical composition). As the energies of the emerging products are different, they provide information from different depths.

The *secondary electrons* have the lowest energy (3–5 eV) and they are produced by being knocked out of the surface by inelastic collisions with the beam electrons. Because of the low energy they provide only surface information (approx. 1 nm ultimate resolution).

The energy of the *backscattered electron* (BSE) can be as high as 10–30 keV, so they carry information about the deeper layers of the sample. These electrons are experiencing large angle (or multiple) elastic scattering. In this case, the resolution is approx. 2–4 nm. Their yield depends on the atomic number of the sample.

The energy of *X-ray photon*s is characteristic of the atoms they originate from, thus they can be used for elemental analysis. The analysis can be point or surface analysis (elemental mapping). With proper calibration, the EDX (Energy-Dispersive X-ray Spectroscopy) spectrum allows not only qualitative but also quantitative analysis.

Focused Ion Beam (FIB) with maximum energy of 30 keV can be a second beam of an electron microscope. Unlike the electron beam, the FIB is inherently destructive for the specimen. The surface of the sample can be sputtered by the ion beam (e.g. Ga ion beam), and thus the sample surface can be manipulated by high efficiency with this method. In the case of conductive polymer films, a layer of one-micrometer thick platinum is applied to the surface prior to cutting with the intention to protect and preserve the sample and to avoid Ga contamination. FIB can be used for several function: manufacturing sample of cross section, thin TEM lamella or nanolithography etc.

II.6. Bending beam (BB) technique

The bending beam technique [172–174] can be effectively used in electrochemical experiments, because the changes of the surface stress (Δg) for a thin metal film on one side of an insulator (e.g. glass) strip (or a metal plate, one side of which is coated with an insulator layer) in contact with an electrolyte solution can be estimated from the changes of the radius of curvature of the strip. If the electrode potential changes, electrochemical processes resulting in the change of g can take place exclusively on the metal side of the sample. The change in g induces a bending moment and the strip bends. In case of a thin conductive (e.g. metal or conducting polymer) film on a plate if the thickness of the film (t_f) is sufficiently smaller than the thickness at of the substrate (t_s), the change of g can be obtained by an expression based on a generalized form of Stoney's equation:

$$\Delta g \; = \; k_{\mathrm{i}} \, \Delta \left(R^{-1} \right) \qquad \text{Eq. 20}$$

where Δg is the change of the surface stress, R is the radius of curvature of the plate. The value of k_i depends on the design of the electrode, and in most case

$$k_{\mathrm{i}} = \frac{E_s t_s^2}{6(1 - \nu_s)} \qquad \text{Eq. 21}$$

where E_s is the Young's modulus, υ_s is the Poisson's ratio.

The derivation of Eq. 20 and Eq. 21 imply the assumption that $\Delta g = t_f \cdot \Delta g_f$, where Δg_f is the change of the film stress. According to Eq. 20, for the calculation of Δg the changes of the reciprocal radius $\Delta(R^{-1})$ of curvature of the plate must be known.

The values of $\Delta(R^{-1}) = \Delta g \cdot k_i$ can be calculated, if the changes of the deflection angle of a laser beam mirrored by the metal layer on the plate are measured using an appropriate experimental setup as shown in **Figure 14**, or the deflection of the plate is determined directly, e.g. with a scanning tunneling microscope.

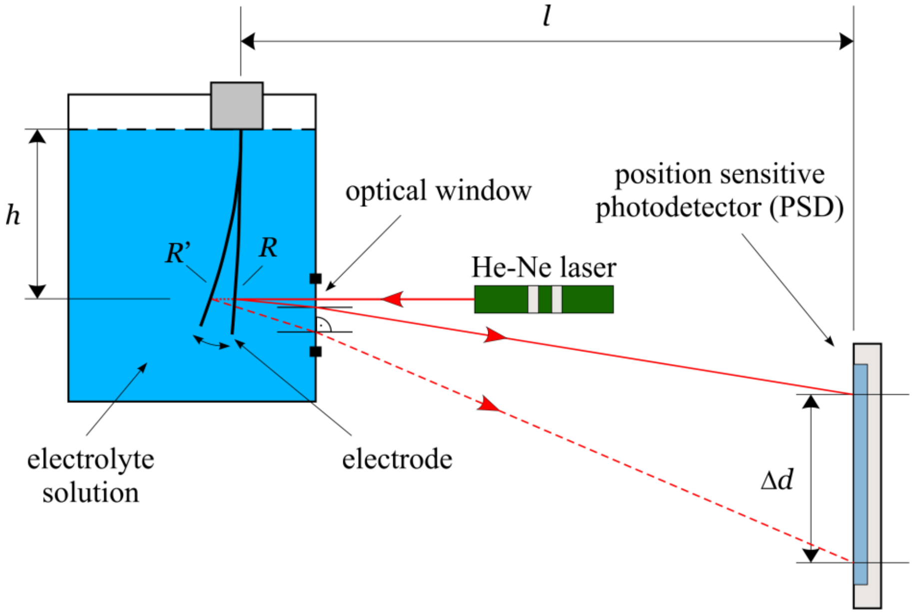

Figure 14. Scheme of a bending beam setup. Δ*d* is the displacement of the light spot on the position sensitive detector if the radius of curvature changes from *R* to *R*'. *l* and *h* are the distance between the electrode and the photodetector, and the distance between the solution level and the reflection point, respectively [173].

II.7. Fluorescent confocal microscopy

A fluorescent microscope consists of magnifying lenses, a dichromic mirror, and filters. The first filter selects the light which will excite the fluorophores contained in the sample. This light illuminates a large portion of the sample. When the fluorophores in the sample are illuminated with the proper wavelength they emit fluorescent light of another wavelength. The dichroic mirror and the second filter select only this fluorescent light emitted by the sample. Therefore, the microscope detects the image of only the fluorescent part of the sample. In this case, all parts of the sample are excited simultaneously, and the resulting fluorescence is detected by the microscope's photodetector or camera including a large unfocused background part.

The confocal microscope is a special type of fluorescent microscope, the difference is that two pinhole apertures are positioned at confocal positions. The light beam is focused by the first pinhole on only a small part of the sample. If fluorophores are present there, they emit light which is then filtered by the dichromic mirror and the filter. The second pinhole positioned in the focal plane selects only the light coming from the target point of the sample, so the objective collects only this light. The surface of the sample can be scanned by moving either the sample or the light beam. This allows the reconstruction of a 2D image at a given height. By a vertical move the sample can be scanned at different heights. A 3D image of the sample can be reconstructed using proper software.

II.8. Dynamic light scattering (DLS)

Dynamic light scattering is a useful, rapid, and non-invasive tool to determine the size and size distribution of small particles or polymers in suspension or solution. The technique is based on measuring the Brownian motion of particles in dispersion and using this information to determine their hydrodynamic size. Particles are illuminated with a laser and the light is scattered by the particles on its way. In dispersion, the measured intensity signal of scattered light is fluctuating because particles move continuously. The fluctuations are caused by the interference of light scattered by each individual particle. The intensity changes over time as particles continue to diffuse. The speed of these intensity fluctuations depends on diffusion rate of the particles. Smaller particles cause a more rapid fluctuation in scattered light than bigger particles. To measure the size of the particles temporal fluctuations are analyzed by means of the intensity or photon auto-correlation function. In the case of larger particles the diffusion is slower, so the correlation coefficient decreases more slowly. In the case of smaller particles, rapid diffusion causes rapid correlation coefficient decrease. Stokes – Einstein equation is used to obtain the size information:

$$d_{\mathrm{H}} = \frac{kT}{3\pi\eta D} \qquad \text{Eq. 22}$$

where d_{H} is the hydrodynamic diameter, k and T are the Boltzmann’s constant and the temperature, respectively. D is the diffusion coefficient and η is the solvent viscosity.

III. Investigation of the electrochemical properties of PEDOP films electrodeposited from aqueous solutions

In this chapter, results of electrochemical experiments on gold | poly(3,4-ethylenedioxypyrrole) modified electrodes are presented. The poly(3,4-ethylenedioxypyrrole) (PEDOP) films on gold substrate were prepared by electropolymerization of ethylenedioxypyrrole monomer (EDOP) under potentiodynamic conditions in aqueous sodium sulfate solutions. The aim of this work was twofold: i) to characterize the gold | PEDOP electrodes in aqueous sulfuric acid solutions (this system is assumed to be suitable for specific practical applications) ii) to compare the results with those of other studies that investigated similar systems (e.g. polypyrrole films [175]). However, the experimental results obtained for the modified electrodes in contact with sulfuric acid solutions significantly deviated from those expected based on studies with similar system types. According to the results, two distinct types of polymer films were formed depending on the storage history of the monomer solutions. By using “fresh”, “distilled”, and “home-made” monomer solutions polymer films with nearly ideal capacitive behavior were obtained and almost rectangular-shaped cyclic voltammograms could be observed in a rather broad potential range. Impedance spectra revealed that the charge transfer resistance between the substrate and the film was low. According to the SEM images the polymer layer on the gold substrate was relatively smooth with some small and short cracks. In contrast, working with “stale” monomer solution that was not properly stored, the shapes of the cyclic voltammograms recorded at the Au | PEDOP | 0.1 mol·dm^{-3} sulfuric acid (aq.) electrode exhibited two peaks, a reduction peak at about −0.2 V *vs.* SSCE and an oxidation peak close to 0.2 V *vs.* SSCE, and the charge transfer resistances were considerably higher than those estimated for the electrode prepared using “fresh” / “distilled” / “home-made” monomer solutions. SEM images showed that the surface of the polymer film was extremely rough, with several wrinkles, creases and large cracks. This behavior was quite unexpected, because the two types of samples were prepared in the same way.

III.1. Experimental

III.1.1. Instruments

A Metrohm Autolab PGSTAT 302N potentiostat (controlled by the Autolab Nova software) and a Zahner IM6 electrochemical workstation (controlled by the Thales software package) was used in all electrochemical experiments.

A Quanta™ 3D FEG high-resolution dual beam scanning electron microscopy (SEM/FIB) instrument was used for SEM analysis.

A Perkin Elmer Lambda 2S double beam UV/VIS spectrophotometer was used for the spectrophotometric analysis.

Dionex Ultima 3000 UHPLC system directly coupled to a Thermo Scientific Q Exactive Focus, Bremen, Germany mass spectrometer was used for recording MS spectra.

III.1.2. Solutions

Cyclic voltammetry and impedance measurements were carried out in 0.1 mol·dm^{-3} H_2SO_4 (analytical grade, Merck) aqueous solutions. According to ref.[176] the aqueous medium facilitates EDOP polymerization. For this reason the polymerization was performed in aqueous solutions as well: 0.01 mol·dm^{-3} EDOP (Sigma-Aldrich) / 0.1 mol·dm^{-3} Na_2SO_4 (Fluka) aqueous solution. All these solutions were prepared using ultra-pure water (specific resistance 18.3 MΩ·cm^{-1}). The solutions were purged with oxygen-free argon (Linde 5.0) before use, and an inert gas blanket was maintained throughout the experiments.

III.1.3. Electrodeposition of poly(3,4-ethylenedioxypyrrole)

Several batches of the EDOP monomer solution was purchased from Sigma-Aldrich (2 % (*w*/*v*) in THF). Before the preparation of the aqueous solutions the organic solvent (THF) was removed by rotary vacuum evaporator. The evaporation was made in Ar atmosphere (Messer 4.6) on maximum 1 mbar without heating.

A portion of the EDOP monomer was used for the preparation of the PEDOP layers immediately after the material was received from Sigma-Aldrich, i.e. the aqueous solution used for the polymerization process contained 0.01 mol·dm^{-3} “fresh” EDOP / 0.1 mol·dm^{-3} Na_2SO_4 (“solution #1”).

“Solution #2” was prepared using the EDOP monomer in THF solution six months after its arrival. The EDOP solution was kept in the refrigerator at about 4 °C until use instead of the prescribed −20 °C. After the vacuum evaporation a 0.01 mol·dm^{-3} “stale” 3,4-ethylenedioxypyrrole / 0.1 mol·dm^{-3} Na_2SO_4 solution was made.

Cyclic voltammograms recorded during the electropolymerization of PEDOT films from solution #1 and solution #2 are shown in **Figure 15.** After electrodeposition of the films, the PEDOP coated gold plates were rinsed with deionized water to remove monomer molecules.

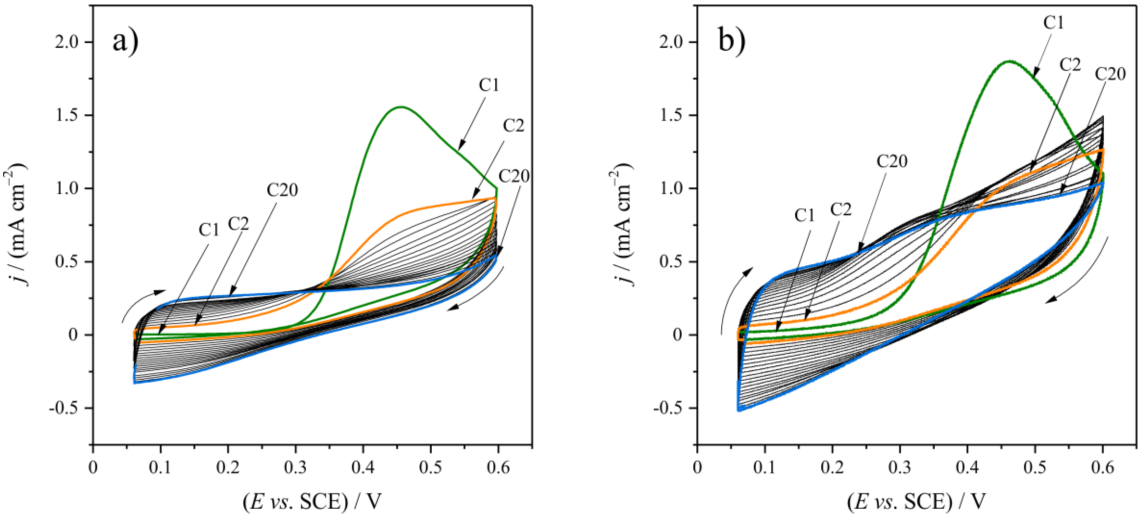

Figure 15. Potentiodynamic electropolymerization of PEDOP film on Au plates (geometric surface area A = 0.2 cm^2) from 0.01 mol·dm^{-3} EDOP / 0.1 mol·dm^{-3} Na_2SO_4 aqueous solution. v = 10 mV·s^{-1}; E = 60 – 600 mV *vs*. SCE. The number of cycles was 20.
a) Solution #1. **b)** Solution #2.

Another case the “fresh” monomer after the vacuum evaporation (Ar atmosphere, 400 mbar, 50 °C) was vacuum distillated in a Hickman flask (Ar atmosphere, 2 mbar and

75 °C oil-bath) and a 0.01 mol·dm^{-3} “distilled” 3,4-ethylenedioxypyrrole / 0.1 mol·dm^{-3} Na_2SO_4 (“solution #3”) was used for the polymerization process.

A “home-made” monomer solution was used for the preparation of the “solution #4”. The 3,4-ethylenedioxypyrrole was prepared by Kristóf Hegedüs [177] who used the slightly modified method published by Murashima et.al. [178]. During this method 2,5-dicarboxyalkyl-3,4-dialkoxypyrrole was decarboxylated in one step (**Figure 16.**) under hot and inert atmosphere in hot ethylene glycol and potassium hydroxide solution at 180 °C. The product 3,4-ethylenedioxypyrrole was isolated by extractive workup using dichloromethane, followed by vacuum-distillation of the crude product. The white-yellowish crystalline product was stored under argon atmosphere, in a freezer, light-tight environment. In a 250 ml argon flushed flask 10.4 g (150 mmol) 95 % pure KOH was weighted and dissolved in 100 ml of water free ethylene glycol. The flask was heated on an oil bath to 180 °C inner temperature and 14.75 g of 3,4-ethylenedioxypyrrole-2,5-dicarboxylic acid was added portion wise while keeping the flask under a gentle argon flow. The reaction mixture was kept at same temperature for further 3 hours while the color changed from yellow to black. The contents of the flask was cooled to room temperature, diluted with 300 ml of water, extracted 3x300 ml of dichloromethane. The combined organic extracts were washed twice with brine (200 ml), dried over anhydrous sodium sulfate, filtered through a plug of silica and concentrated to dryness under reduced pressure. The crude product (black oil) was purified by short path vacuum distillation. The main fraction distilled between 150-180 °C at 80 mTorr vacuum and yielded 3,1 g 25 mmol, 76 % of the title product.

^{1}H NMR: (250 MHz, $CDCl_3$) δ 4,194 s (4H), 6,199 s (2H)
^{13}C NMR: (62,9 MHz, $CDCl_3$) δ 65,791, 98,538, 132,68

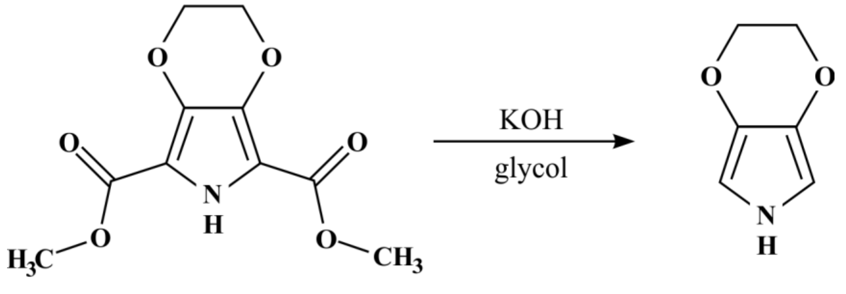

Figure 16. Last step of preparation of “home-made” EDOT monomer by Kristóf Hegedüs [177].

The Au | poly(3,4-ethylenedioxypyrrole) (Au | PEDOP) films for electrochemical experiments were prepared by electropolymerization from the different monomer solutions (solution #1, #2, #3, #4) under potentiodynamic conditions. The depositions were carried out in a standard three electrode cell in which the Au (A = 0.196 cm^2) plate in contact with the solution served as the working electrode (WE). A gold ring (a circular Au wire) immersed in the same solution served as the counter electrode (CE), and a KCl-saturated calomel electrode (SCE) was used as the reference electrode (RE). The PEDOP films were formed on gold plates (scan rate: 10 mV·s^{-1}, 20 polymerization cycles) in the range of 0.06 – 0.60 V *vs*. SCE. The resulting modified electrodes will be referred to as electrode #1, #2, #3, #4 depending on the number of the monomer solution was used during the preparation.

For the UV/VIS spectrometry optically transparent gold electrodes (Metrohm, AUTR10) were used. These electrodes are specially designed for spectroelectrochemical applications and the three electrodes can found on a transparent plastic substrate. The material of the working electrode is an optically transparent gold layer (A = 0.11 cm^2), the material of the counter electrode is carbon, and the built-in reference electrode is made from silver. The PEDOP films were formed on transparent gold layers from solution #2 and solution #3 (scan rate: 10 mV·s^{-1}, Q = 1.065 mC) in the range of 0.06 – 0.60 V *vs*. SCE.

After electrodeposition of the films, the PEDOP coated gold plates were rinsed with deionized water to remove monomer molecules.

III.1.4. Cyclic voltammetry and impedance measurements

In the conventional three-electrode cell configuration the PEDOP-modified gold substrate in contact with 0.1 mol·dm^{-3} H_2SO_4 solution was used as the working electrode (WE), and a high surface area cylindrical gold-foil (immersed in the same solution) was arranged cylindrically around the working electrode to maintain a uniform electric field and served as counter electrode (CE). A NaCl-saturated calomel electrode (SSCE) through a Luggin-capillary was used as the reference electrode (RE). Cyclic voltammetric curves were recorded in the potential range of –0.5 V to 0.5 V *vs*. SSCE at different sweep rates (e.g. 100; 50; 20 and 10 $mV \cdot s^{-1}$).

Impedance measurements were performed at 67 discrete frequencies in the frequency range of 50 kHz – 7.5 mHz at an amplitude of 5 mV rms.

III.1.5. UV/VIS spectrophotometry

During the spectrometric measurements an optically transparent gold electrode in ultra-pure water was used as a blank sample. Optically transparent gold electrodes covered by different types of PEDOP-layers in connected with 0.1 $mol \cdot dm^{-3}$ H_2SO_4 solution were measured. 1x1 cm plastic cuvettes were used for the observations. During the measurements the potential of the PEDOP-layer was controlled by a Metrohm Autolab PGSTAT 302N potentiostat. Spectra were recorded between $\lambda = 1100–350$ nm on different potentials (−0.2, 0, 0.2 V *vs*. SSCE).

III.1.6. LC-MS measurements

The 0.01 $mol \cdot dm^{-3}$ EDOP / 0.1 $mol \cdot dm^{-3}$ Na_2SO_4 aqueous solutions were analyzed by liquid chromatography–mass spectrometry (LC-MS). In order to the salt does not interfere with the determination, the sodium sulfate buffer was separated from the components by chromatographic separation. Samples were diluted 100 times, centrifuged and 50 µl was injected. The HPLC separations were performed on a Dionex Ultima 3000 UHPLC system using a Phenomenex Kinetex C8 (100 Å, 1.7 µm, 100 x 2.1 mm) UPLC column which was directly coupled to a high resolution and high mass accuracy mass spectrometer (Thermo Scientific Q Exactive Focus, Bremen, Germany) with electrospray ionization in positive ion mode. The flow rate was 400 µl / min. „A": 0.1 % HCOOH in water and „B": 0.1 % HCOOH / 80 % acetonitrile in water (*V*/*V*) were used as eluents. The gradient elution was 0 min: 5 % B, 2 min: 5 % B, 15 min: 100 % B. Mass spectra were recorded in $m/z = 50–1200$ range.

In all cases, the monomer compound appears as the major peak, and the dimer compound can be also observed. Larger oligomers were not detected on the chromatograms, because they may precipitate under the conditions used.

III.2. Results and discussion

III.2.1. Cyclic voltammetry

Cyclic voltammetric curves recorded at a gold | PEDOP | 0.1 $\mathrm{mol \cdot dm^{-3}}$ sulfuric acid (aq.) electrode prepared from the four types of monomer solutions (#1: fresh, #2: stale, #3: distilled, #4: home-made) at sweep rate of $v = 50\ \mathrm{mV \cdot s^{-1}}$ ($E = -0.5 – 0.5$ V *vs*. SSCE) are presented in **Figure 17.** It is well seen, that with the exception of electrode #2, the curves are very similar. In the presented potential interval the electrodes #1, #3, #4 are remarkably stable, retaining their properties even after several consecutive cyclic voltammetric scans. A nearly ideal capacitive behavior and almost rectangular-shaped cyclic voltammograms could be observed in this potential range. This is not too surprising (although we could not find similar results in previous work), when one considers that under identical conditions gold | PEDOT | sulfuric acid (aq.) electrodes.

In contrary, the shapes of the cyclic voltammograms recorded at the gold | PEDOP | 0.1 $\mathrm{mol \cdot dm^{-3}}$ sulfuric acid (aq.) electrode prepared from solution #2 differs considerably from the shapes of the CVs described previously. It is already a surprising result that an electro-conducting polymer can be produced from a "stale" monomer solution. Additionally, the cyclic voltammetric curve has two peaks, a reduction peak at about −0.2 V *vs*. SSCE and an oxidation peak close to 0.2 V *vs*. SSCE (electrode #2, see **Figure 17.** curve 2). This behavior usually can be observed for redox polymers, although PEDOP is considered as an intrinsically conductive polymer (see **Figure 1**) This feature could be used e.g. in the design of sensors.

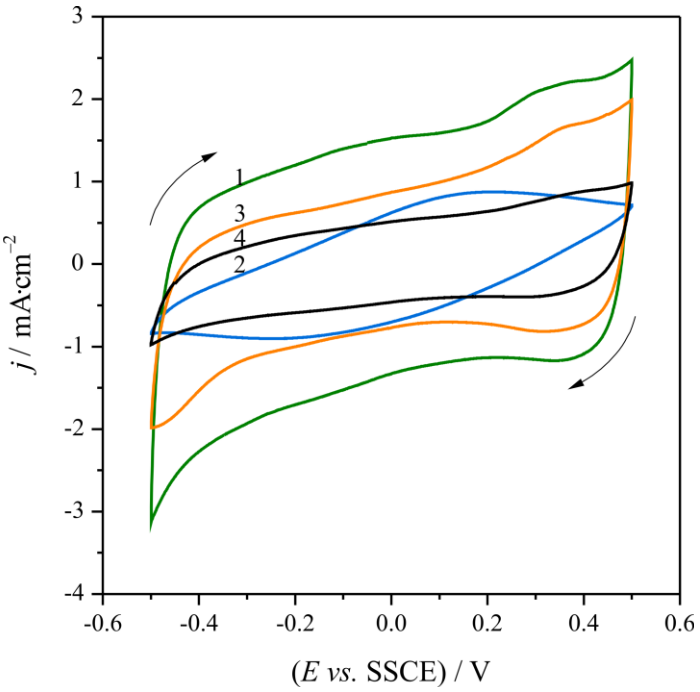

Figure 17. Cyclic voltammograms of the Au | PEDOP electrodes (1: electrode #1 2: electrode #2 3: electrode #3 4: electrode #4) recorded in 0.1 mol·dm^{-3} aqueous H_2SO_4 solutions at v = 50 mV·s^{-1} scan rate. E = −0.5 – 0.5 mV *vs*. SSCE. The 3rd scans are showed.

In **Figure 18.** cyclic voltammograms of the Au | PEDOP electrode #1 (**a**) and electrode #2 (**b**) recorded in 0.1 mol·dm^{-3} aqueous H_2SO_4 solutions at different scan rates: (1) v = 100 (1); 50 (2); 20 (3); 10 mV·s^{-1} (4) are shown (E = −0.5 – 0.5 mV *vs*. SSCE). While electrode #1 shows capacitive behavior (**Figure 18. a)**), the redox peak pair of electrode #2 is well observed at all of the used scan rates (**Figure 18. b)**). This behavior was quite unexpected, because the different samples were prepared in the same way and only the storage histories of the two commercial monomer solutions were different.

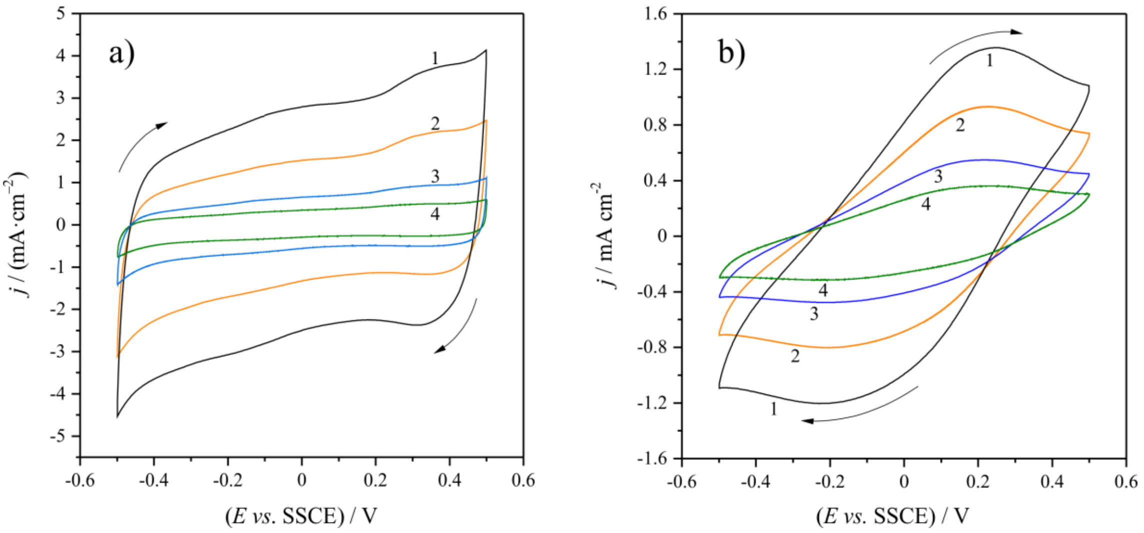

Figure 18. Cyclic voltammograms of the Au | PEDOP electrodes (**a)** electrode #1 **b)** electrode #2) recorded in 0.1 mol·dm^{-3} aqueous H_2SO_4 solutions at different scan rates: (1) v = 100 (1); 50 (2); 20 (3); 10 mV·s^{-1} (4) . $E = -0.5 – 0.5$ mV *vs*. SSCE. The 3rd scans are showed.

III.2.2. Impedance measurements and scanning electron microscopy

In **Figure 19.** and **Figure 20.** impedance spectra of Au | PEDOP | 0.1 mol·dm^{-3} sulfuric acid electrodes recorded at three different electrode potentials (−0.3 V, 0 V and 0.5 V *vs*. SSCE) are shown. The impedance spectra of electrode #1 revealed that the charge transfer resistance between the substrate and the film was quite low (the diameter of the high frequency semicircle in the complex plane impedance plot varied between 5 and 20 Ω, depending on the electrode potential, see **Figure 19. a)**). According to the SEM images (**Figure 21. a), b)**) the polymer layer on the gold substrate was relatively smooth with some small and short cracks.

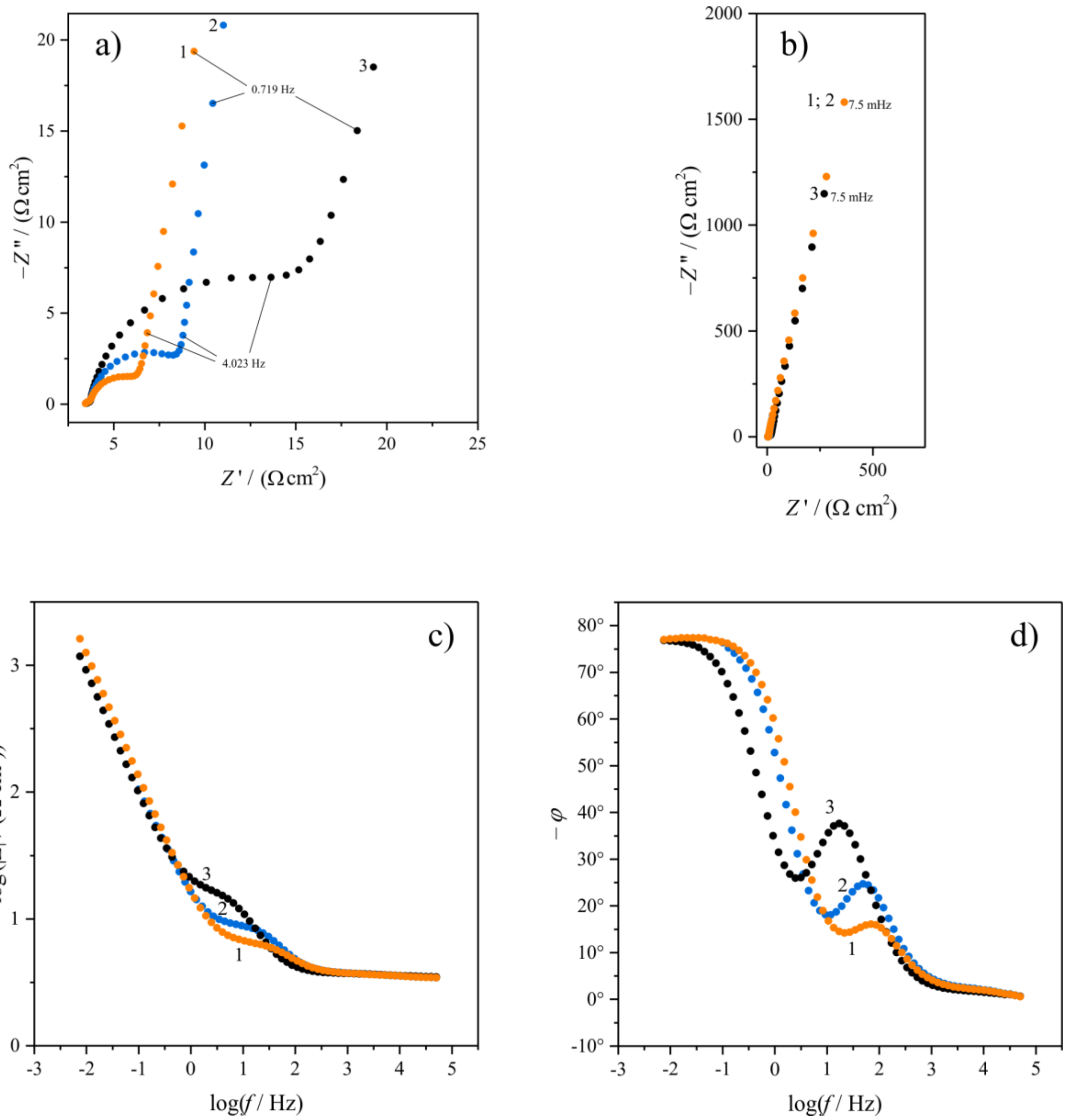

Figure 19. Impedance spectra of the Au | PEDOP electrode #1 in contact with 0.1 mol·dm^{-3} H_2SO_4 aqueous solution at potentials: (1) $E = -0.3$ V; (2) $E = 0.0$ V and (3) $E = 0.5$ V *vs.* SSCE. Small numbers refer to values of the frequency. **a)**, **b)** Complex plane plot; **c)**, **d)** Bode plots.

On the other hand, at the corresponding electrode potentials the charge transfer resistances in the case of electrode #2 appear to be considerably higher than those estimated for electrode #1. According to **Figure 20. a)** the diameter of the high-frequency arc in the complex plane impedance diagram varies between 70 and 700 Ω, since as it can be seen in the SEM images shown in **Figure 21. c), d)** the surface of the polymer film contacting with the electrolyte solution is extremely rough and rugged, with several wrinkles, creases and large cracks, but some filament-like structures can also be observed.

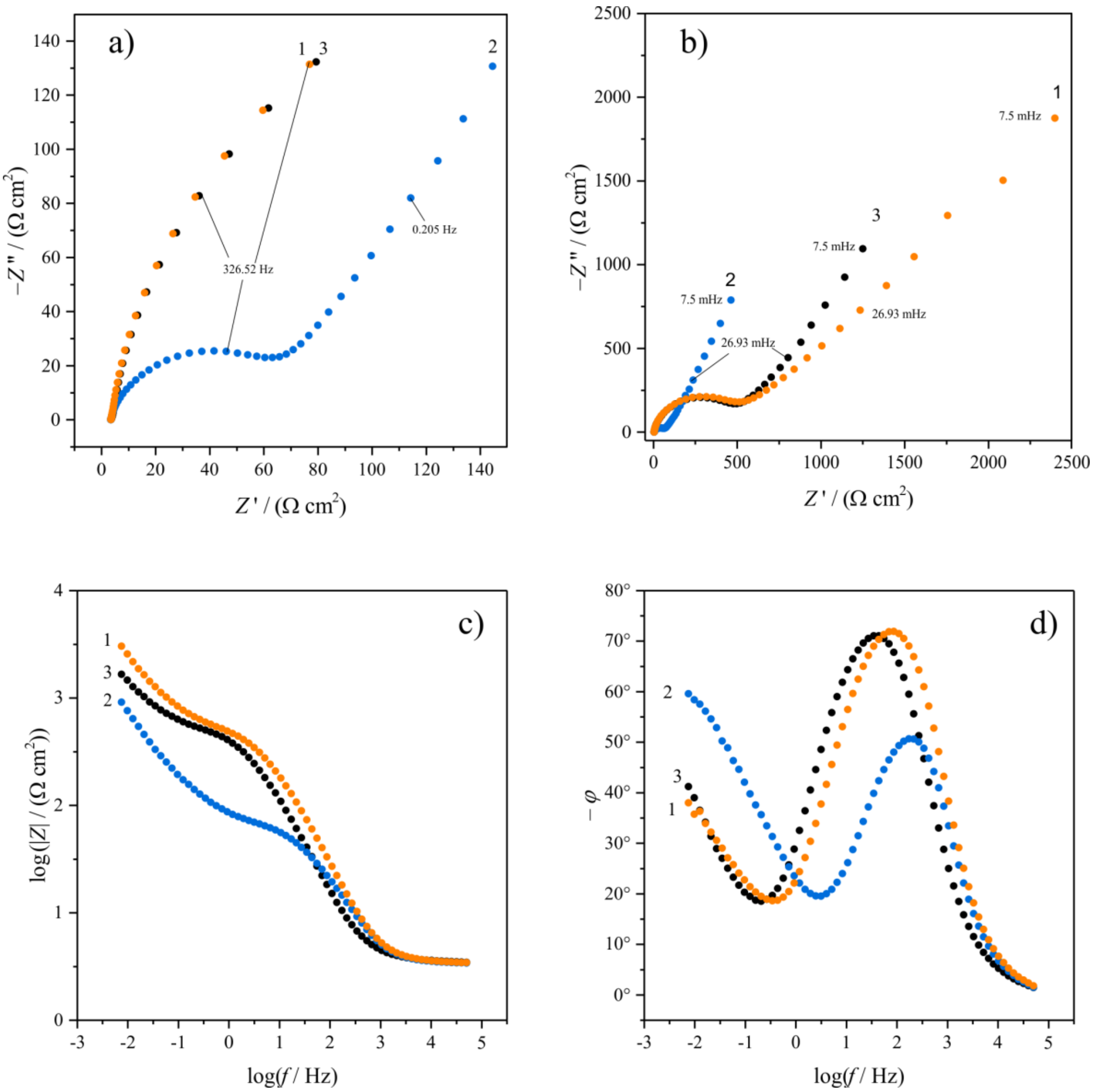

Figure 20. Impedance spectra of the Au | PEDOP electrode #2 in contact with 0.1 mol·dm^{-3} H_2SO_4 aqueous solution at potentials: (1) $E = -0.3$ V; (2) $E = 0.0$ V and (3) $E = 0.5$ V *vs.* SSCE. Small numbers refer to values of the frequency. **a)**, **b)** Complex plane plot; **c)**, **d)** Bode plots.

What can be the reason of this behavior?

The answer does not seem to be simple. Since electrode #1 and electrode #2 were prepared under identical conditions the observed significant differences in morphology and electrochemical behavior can only be attributed to differences in the properties of the monomer solutions. Therefore, the solutions used for film deposition was investigated with high-performance liquid chromatography-mass spectrometry (HPLC–MS). In case of solution #1 no other peaks than those originating from the solvent and the EDOP monomer could be observed in the chromatograms. On the other hand, according to HPLC-MS analyses solution #2 contained considerable amounts of dimers and oligomers in addition to the monomer and solvent molecules.

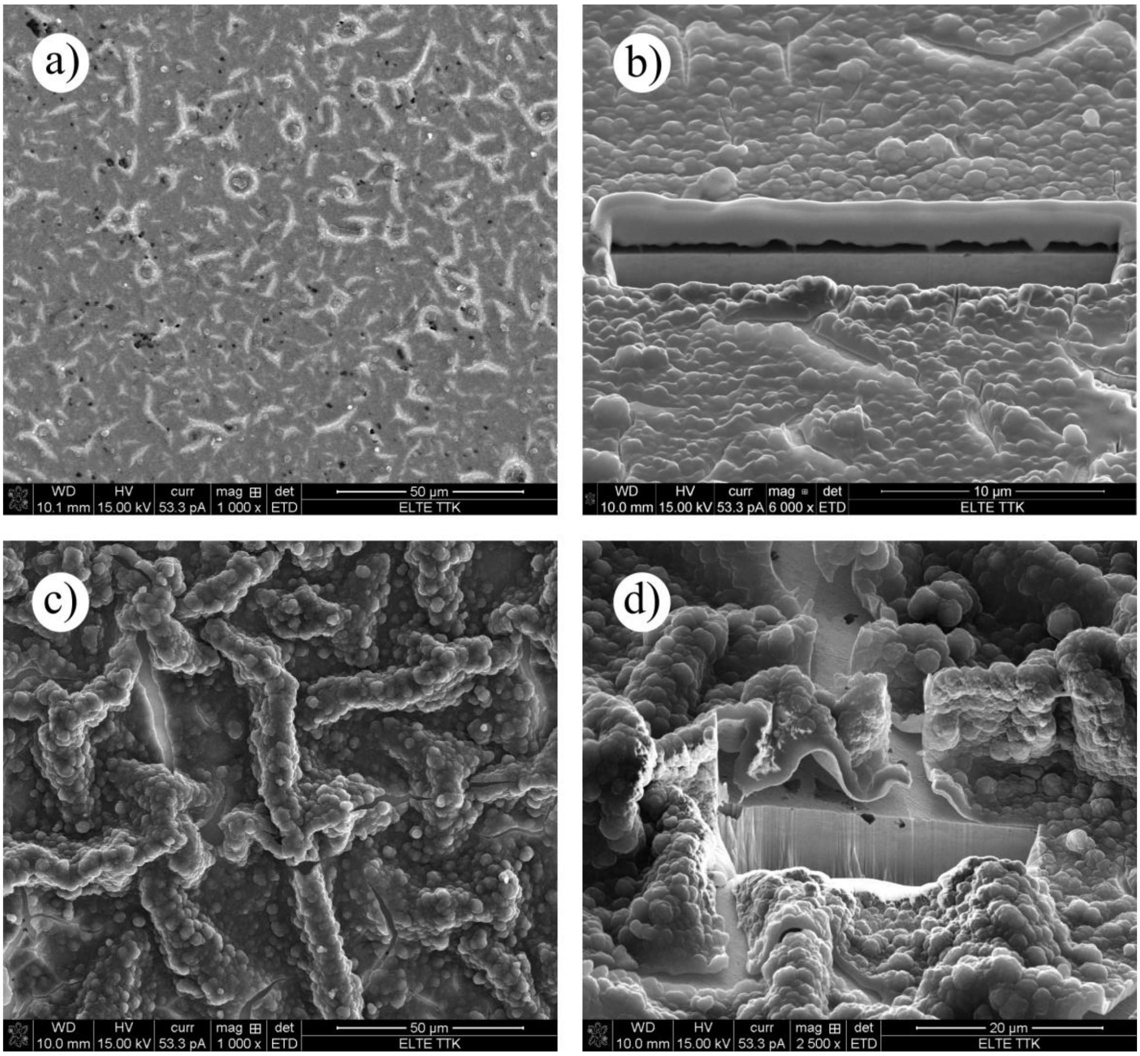

Figure 21. Secondary electron SEM images of electrode #1: **a)**, **b)** and electrode #2: **c)**, **d)**. Image of a cross section made by FIB-milling: **b)**, **d)**. The length of the horizontal white bar below the images corresponds to 50 μm (**a)**, **c)**), 10 μm (**b)**) and 20 μm (**d)**).

The dimers and oligomers were formed most probably by spontaneous dimerization and polymerization during the improper storage of the monomer solution. The presence of dimers and oligomers in the solution may strongly influence the polymerization mechanism. In the case of electrode #1 long conjugated systems were able to form (**Figure 22. a)**), while in the case of electrode #2 probably there are defects in the conjugated system of the polymer chain (**Figure 22. b)**).

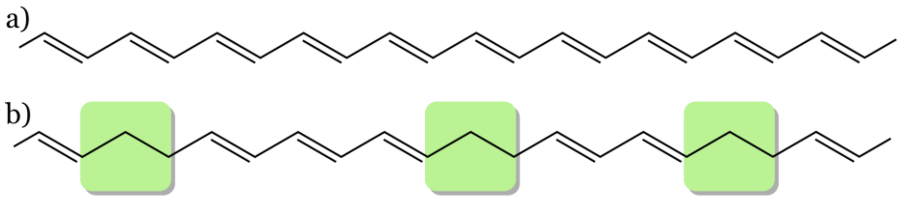

Figure 22. Demonstration of long conjugated system of electrode #1 (**a)**) and defects in conjugated system of electrode #2 (**b)**).

III.2.3. UV/VIS spectrophotometry

UV/VIS spectrophotometric measurements confirm the results described above. In the case of the PEDOP layer deposited from the “fresh” monomer solution (solution #1), the absorbance values on a wide wavelength range were higher on different potentials than in the case of the PEDOP layer deposited from the “stale” monomer solution (solution #2) (**Figure 23.**). It means that electrodeposition from solution #1 results in a much more compact, contiguous film with a strong connection to the substrate gold without bigger cracks. While using solution #2, poorly connected, full with creases and large cracks polymer layer can be deposited.

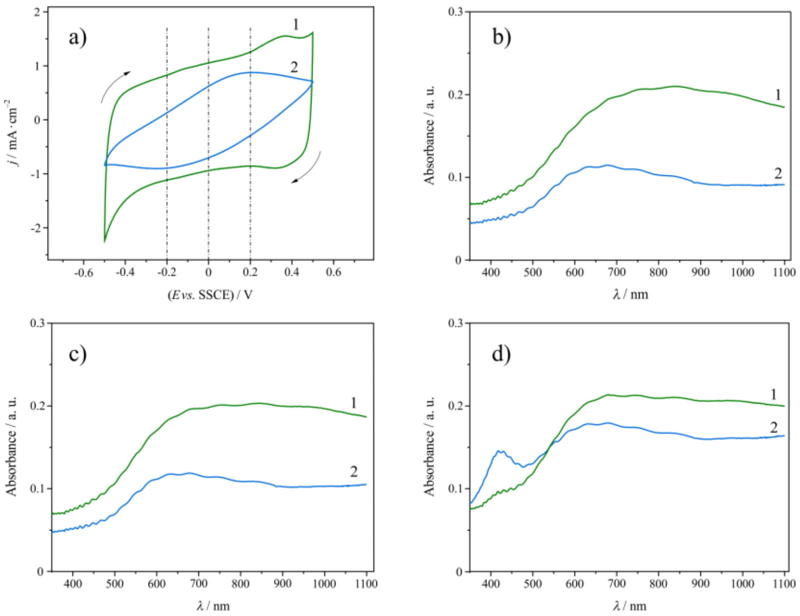

Figure 23. Cyclic voltammogram (**a)**) and UV/VIS spectra (**b)**, **c)**, **d)**) of Au | PEDOP | 0.1 mol·dm^{-3} H_2SO_4 “transparent” electrodes. The PEDOP layers were deposited from monomer solution #1 (“fresh”) and solution #2 (“stale”). The wavelength range of the UV/VIS spectra is $\lambda = 350 – 1100$ nm, the potential during the measurements was held on 0.2 V (**b)**), 0 V (**c)**) and −0.2 V (**d)**) *vs*. SSCE.

It is known that despite some differences in interpretation of literature results on the electropolymerization of monomers and oligomers, there seems to be a general consensus that long conjugated oligomers are poorly (if at all) electropolymerizable because of the increased stabilization of their extended cation radicals, which prevents further coupling toward the formation of polymers [49,179–181]. Nevertheless, it has been shown e.g. in [181] that “extending oligothiophene length beyond certain limit apparently brings them to an “island of reactivity” toward electropolymerization”. On the other hand, the conjugation length of the polymer chains, which is a primary indicator of conductivity, may also be influenced by oligomerization. It is known that rather short conjugation lengths are usually sufficient for reasonable conductivity [182]. Intuitively, conjugation should be important in two respects. First, carrier generation upon oxidation or reduction should be facilitated with high conjugation lengths since the resulting radical cation or anion will be more highly delocalized. Second, higher conjugation lengths ought to facilitate intermolecular charge transport by providing more frequent π-π overlap between adjacent backbones. Nevertheless, it is clear from these results, that the conjugation length is longer in the case of the PEDOP film prepared from “fresh” monomer solution.

III.3. <u>Concluding remarks</u>

The above results indicate that the conjugation length of the polymer chains increases if the time interval between the preparation of the monomer and the electropolymerization experiment is shorter. A surprising result, that a “stale”, not properly stored monomer solution is still suitable for production of polymer films. Additionally, the deposited polymer films mimicking the behaviors of redox polymers. The further characterization and analysis of polymer modified electrodes presented here could be of value in the design and preparation of such electrochemically responsive systems for a range of applications requiring a high degree of stability and tunability, including their use as polymer matrix in supercapacitors or in composite materials. It is expected that the polymers with unusual properties (i.e., the transition between the properties of conductive and redox polymers) can be effectively used in sensing applications

IV. Investigation of the electrochemical and morphological properties of PEDOT modified electrodes using carbon felts as substrate material

In laboratory practice usually gold or platinum is used as substrate material of conductive polymers. Electrochemical properties of these metals are well known, their surface can be polished easily and reproducibly. Because of their lower prices, graphite and glassy carbon are also often used substrate materials. However, from the industrial point of view, none of the above-mentioned materials are porous and flexible enough. High porosity allows bigger capacity increase by polymer deposition, and flexibility gives an opportunity for wide usage. Carbon felt (or carbon fiber, or carbon cloth) is a promising candidate for industrial usage. However, there are only a few founds in the literature about the electrochemical behavior of pure carbon felt (CF) [183–185]. This material is already applied in microbial fuel cells (MFCs) or in redox flow batteries as anode or cathode material both in pure or conductive polymer modified form [67,186–188]. PEDOT coated CFs are really popular, since PEDOT is a stable and user-friendly polymer. PEDOT modification increases the availability of redox active sites and the electrical capacity of the carbon felt. These modified electrodes are usually produced by chemical polymerization [69,189,190]. Nevertheless, it seems that electrochemical polymerization results in a more homogeneous polymer layer on the filaments of carbon paper and carbon cloth [187].

In this section the electrochemical behaviors of pure carbon felts and PEDOT coated CFs in different pH aqueous solutions are shown. Scanning electron microscopy (SEM) was used for the study of the structure/morphology of the polymer coating on the filaments of carbon felt.

IV.1. Experimental

IV.1.1. Instruments

Zahner IM6 electrochemical workstation (controlled by the Thales software package) was used in all electrochemical experiments.

A Quanta™ 3D FEG high-resolution dual beam scanning electron microscopy instrument was used for SEM analysis.

Jenway 3520 pH meter with Jenway 924005 combination pH electrode was used for pH measurements.

IV.1.2. Reagents

3,4-Ethylenedioxythiophene (EDOT) was purchased from Aldrich and Aldrich-Chemie. All chemical reagents were used as received without further purification. All solutions were prepared with ultrapure water (Milli-Q®, specific resistance: 18.2 $M\Omega\cdot cm^{-1}$). Reagent grade sulfuric acid (Merck), sodium sulfate decahydrate (VWR), perchloric acid (Merck), sodium perchlorate (Sigma-Aldrich) were used for the preparation of 0.1 M H_2SO_4 (pH = 1.33), 0.1 M Na_2SO_4 (pH = 4.85), 0.2 M $HClO_4$ (pH = 1.02), 0.2 M $NaClO_4$ (pH = 4.97) solutions.

Zoltek PXFT 145 $g\cdot cm^{-2}$ carbon felt pieces (0.1×1.0×1.8 cm, A = 4.16 cm^2) were used during the experiments in pure or PEDOT modified forms. The upper part of the carbon felt was pushed firmly to an L-shaped bent iron rod by two pieces of rectangular plastic to make electrical contact (see **Figure 24.**). Since in the literature there are no clear descriptions on electric contact of carbon felts during electrochemical examinations, this is a unique solution. At first sight, the solution showed in **Figure 24.** carries the risk of developing a potential gradient. Full side contacting with gold smoke foil was tried to avoid potential gradient, but this solution needed a careful sample preparation, and in bigger scale because of the price of the gold foil this solution would not be suitable for industrial usage. Additionally, in this composition there was a direct contact between the electrolyte solution and the gold foil, and during electrochemical experiments, the sign of the carbon felt was suppressed by the gold. Finally, experiments showed, that the assumed potential gradient does not cause significant effect, and there are no remarkable differences between full side contact or only upper part contact of the carbon felt.

All electrochemical measurements were carried out at ambient temperature (22.0 ± 0.5) °C.

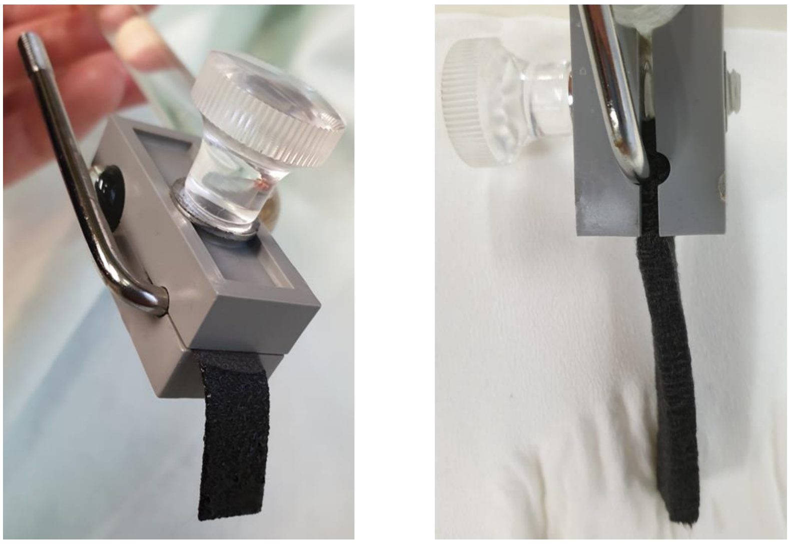

Figure 24. The electrical contact of the carbon felts during the electrochemical experiments.

IV.1.3. Electrodeposition of poly(3,4-ethylenedioxythiophene)

Electrodeposition of the PEDOT layer was carried out in a common three electrode cell in which the working electrode was a piece of carbon fiber ($A = 4.16$ cm^2) in contact with freshly prepared 0.01 mol·dm^{-3} EDOT / 0.1 mol·dm^{-3} Na_2SO_4 solution, the counter electrode was a ring-shaped Pt wire immersed into the same solution, and a KCl-saturated calomel electrode (SCE) was used as reference electrode. During the galvanostatic deposition $j = 0.2$ mA·cm^{-2} current density was used. The deposition time was $t = 3600$ s or $t = 10800$ s. After the deposition, the polymer layer was left for one-day relaxation in ultrapure water.

IV.1.4. Cyclic voltammetry and impedance measurements

In the conventional three-electrode cell configuration the pure or PEDOT-modified carbon felt substrate in contact with the current electrolyte solution was used as the working electrode (WE), and a high surface area cylindrical gold-foil (immersed in the same solution) was arranged cylindrically around the working electrode to maintain a uniform electric field and served as counter electrode (CE). A NaCl-saturated calomel electrode (SSCE) through a Luggin-capillary was used as the reference electrode (RE).

Cyclic voltammetric curves were recorded in the potential range of $E = (-0.1 – 0.6)$ V *vs*. SSCE (narrow range), or $E = (-0.3 – 1.0)$ V *vs*. SSCE (wide range) at different sweep rates (100 and 50 $\mathrm{mV \cdot s^{-1}}$).

Impedance measurements were performed at 67 discrete frequencies in the frequency range of 50 kHz – 7.5 mHz at an amplitude of 5 mV rms, $E = 0.4$ V *vs*. SSCE.

IV.2. Results and discussion

In **Figure 25.** cyclic voltammograms of the pure carbon felt recorded in different electrolyte solutions with different pHs are shown. As expected, the potential window in the neutral pH solutions (**Figure 25.** curve 3 (—) and curve 4 (—)) is shifted towards the negative voltages. The beginning of the hydrogen evolution can be observed in the voltammograms recorded on the wide potential range ($E = (-0.3 – 1.0)$ V *vs.* SSCE) and in acidic pH solutions (**Figure 25. b)** curve 1 (—) and curve 2 (—)). Except for this, carbon felt did not show a significant difference in the examined solutions.

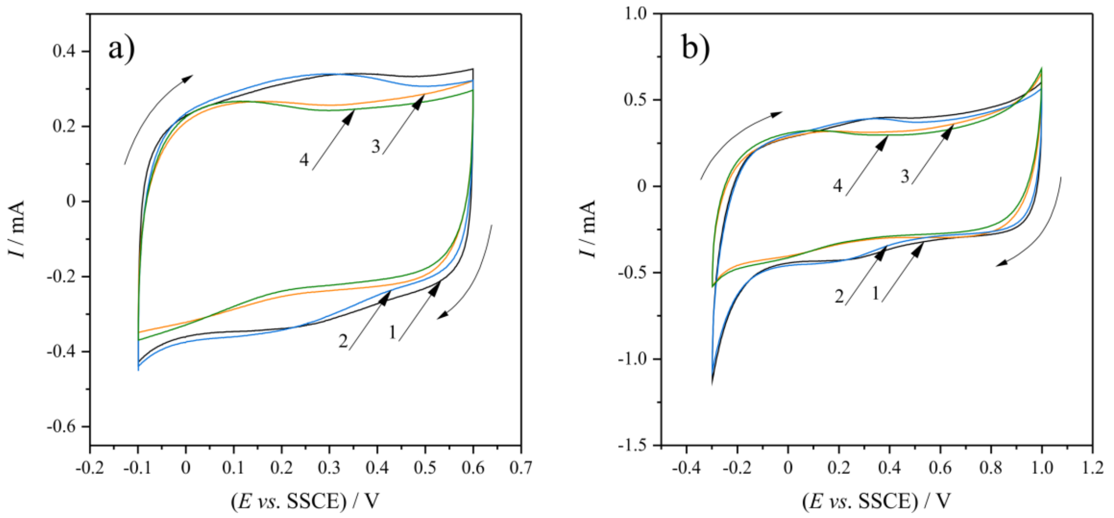

Figure 25. Cyclic voltammograms of pure carbon felt recorded in aqueous 0.2 mol·dm^{-3} $HClO_4$ (curve 1 (—)), 0.1 mol·dm^{-3} H_2SO_4 (curve 2 (—)), 0.2 mol·dm^{-3} $NaClO_4$ (curve 3 (—)), 0.1 mol·dm^{-3} Na_2SO_4 (curve 4 (—)) solutions at a sweep rate of $v = 100$ mV·s^{-1} in the potential range of **a)** $E = -0.1$ V – 0.6 V *vs*. SSCE and **b)** $E = -0.3$ V – 1.0 V *vs*. SSCE. 2nd scans are shown.

A similar result is observed in the electrochemical impedance spectra (**Figure 26.**). The ohmic resistance (R_o) of the solution is growing with the pH value (**Figure 26. a)**), and the small-frequency capacitance of the CF is a little bit higher in the acidic solutions (**Figure 26. b)** 1, 2).

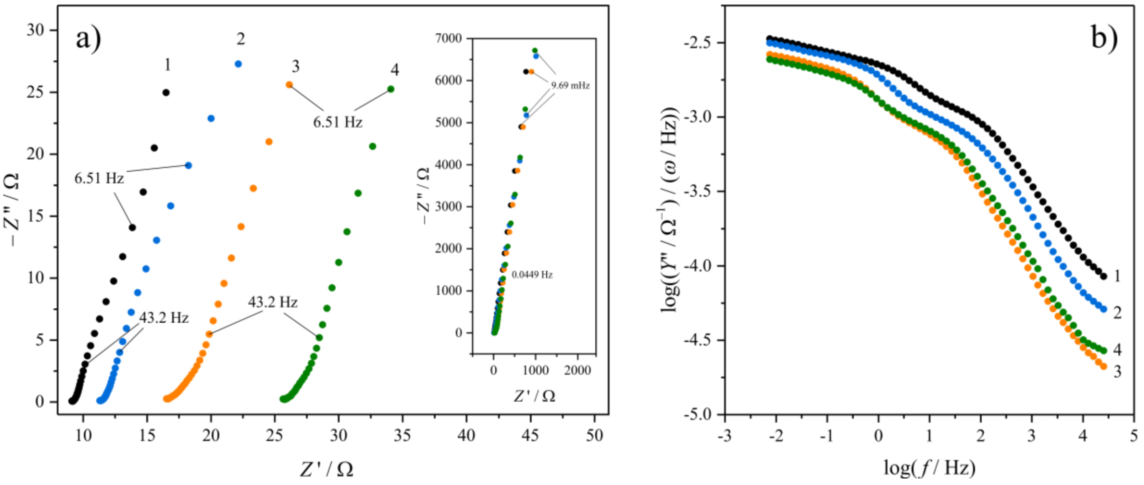

Figure 26. Electrochemical impedance spectra of pure carbon felt recorded in aqueous (1) 0.2 mol·dm^{-3} $HClO_4$ (●), (2) 0.1 mol·dm^{-3} H_2SO_4 (●), (3) 0.2 mol·dm^{-3} $NaClO_4$ (●), (4) 0.1 mol·dm^{-3} Na_2SO_4 (●) solutions at the electrode potential of $E = 0.4$ V *vs*. SSCE, in the frequency range of 50 kHz – 7.5 mHz. The amplitude of the perturbing signal was 5 mV. **a)** Complex plane impedance plots, the high frequency regions are shown in the insert (small numbers in the plots refer to frequency values). **b)** The "parallel" capacitances as a function of frequency.

PEDOT was deposited onto carbon felt. The thickness of the deposited conductive polymer was set by the deposition time (longer deposition results in a thicker polymer layer). Liu et al. [187] used 10 min long galvanostatic polymerization (j = 200 μA·cm^{-2}), which resulted in a homogeneous, but thin PEDOT layer on carbon paper and carbon cloth. In the hope of higher capacity growth, in the present work I used 1 h and 3 h long deposition with the same monomer concentration and current density as in ref.[187]. The success of these long deposition times was not trivial, since there was a risk that the thicker polymer layer could become more easily detached from the filaments of the carbon felt. Cyclic voltammetric results (see **Figure 27.**) show a significant increase in the capacitive current as a result of the polymer layer deposition. The rate of this increase is higher in the case of the thicker PEDOT layer, and an almond-shaped CV can be observed in **Figure 27. b)** curve 2. That shape indicates a high capacitance value.

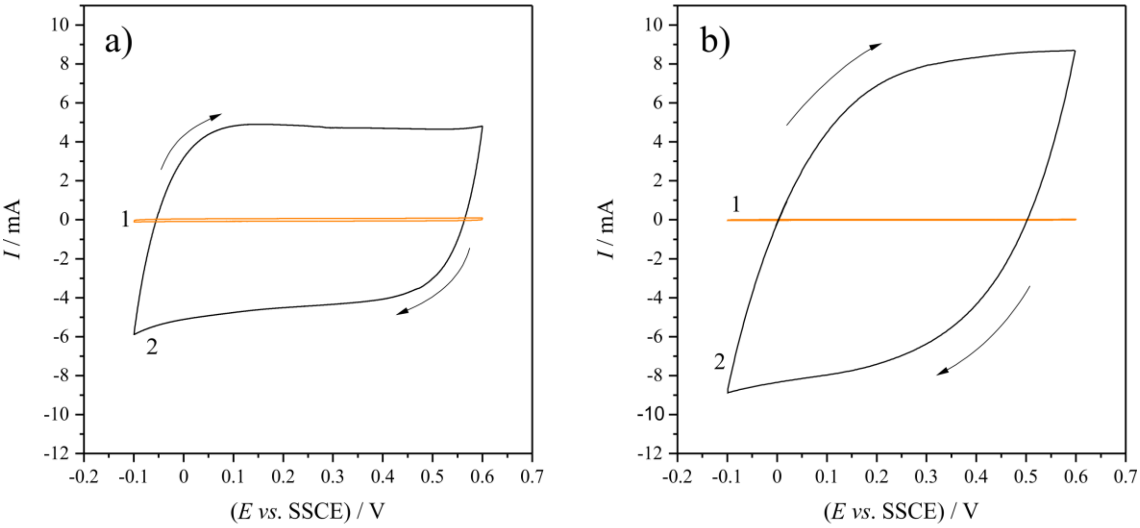

Figure 27. Cyclic voltammograms of pure carbon felt (curves 1 (—)) and CF | PEDOT (curves 2 (—)) recorded in 0.1 mol·dm^{-3} H_2SO_4 (aq.) solution at a sweep rate of v = 50 mV·s^{-1} in the potential range of E = −0.1 V – 0.6 V *vs*. SSCE. The deposition time of the polymer layer was **a)** t = 3600 s and **b)** t = 10800 s. 2nd scans are shown.

By plotting the capacitance values calculated from the impedance spectra ($C = Y'' \cdot \omega^{-1}$), the rate of the capacitance increase can be quantified. It is clearly seen in **Figure 28**, that in the case of the thick PEDOT layer, the increase of the capacitance is nearly 3 orders of magnitude compared to the empty carbon tissue.

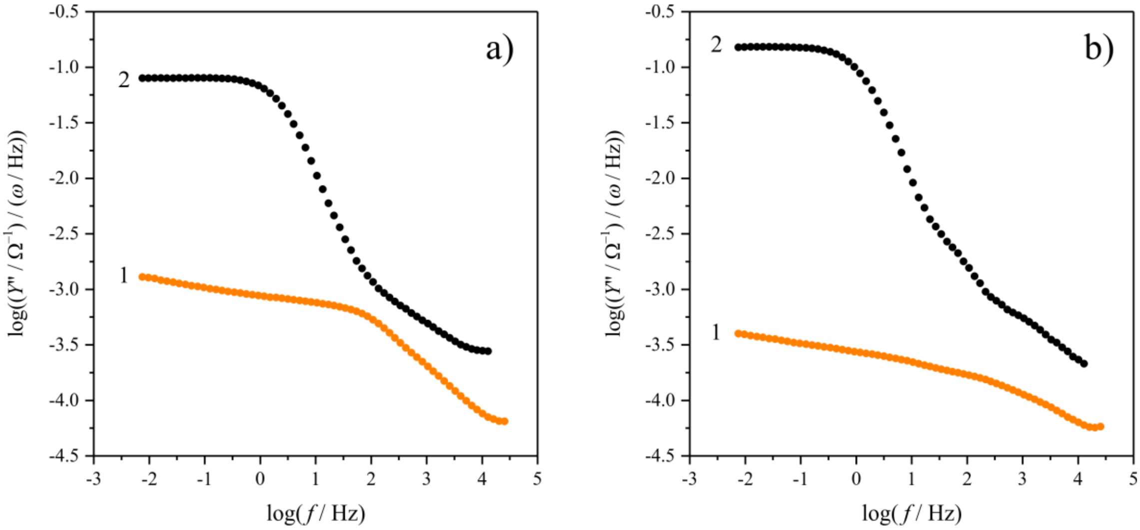

Figure 28. Electrochemical impedance spectra (the "parallel" capacitances) of (1) pure carbon felt (●) and (2) CF | PEDOT (●) in 0.1 mol·dm^{-3} H_2SO_4 (aq.) solution at the electrode potential of E = 0.4 V *vs*. SSCE, in the frequency range of 50 kHz – 7.5 mHz. The amplitude of the perturbing signal was 5 mV. The deposition time of the polymer layer was **a)** t = 3600 s and **b)** t = 10800 s.

Scanning electron micrographs (**Figure 29.**) confirm that a longer deposition time results in a thicker film. The cauliflower-like structure characteristic of PEDOT is clearly visible at higher magnifications (**Figure 29. c), d)**).

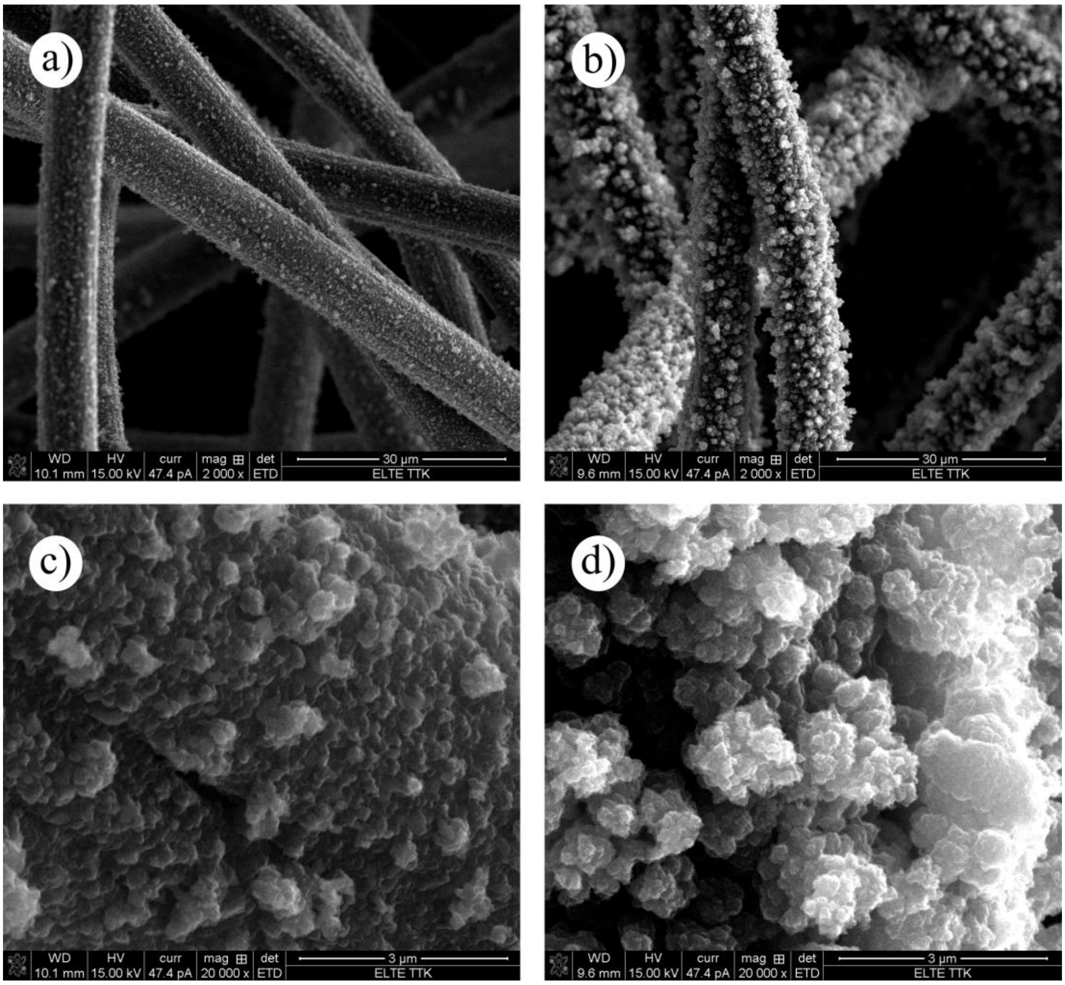

Figure 29. Secondary electron SEM images of the PEDOT-covered carbon felts. The deposition time of the polymer layer was **a), b)** t = 3600 s and **c), d)** t = 10800 s. The length of the horizontal white bar corresponds to **a), b)** 30 μm and **c), d)** 3 μm.

IV.3. Concluding remarks

The results above show that in the case of carbon felt significant increase of capacitance can be reached by PEDOT deposition. Galvanostatic deposition is a proper way to create CF | PEDOT modified electrodes for industrial usage. The thickness of the polymer layer can be tuned by the deposition time, and the sample preparation is not a complicated procedure with several steps.

V. Some observations on the electrochemical reactions of BPA on polycrystalline gold

As it was mentioned in Section I.3.3, there is an interesting and less researched behavior of bisphenol A (BPA): sometimes it can be assumed that metallic gold is electrocatalytically less active towards the oxidation of BPA. Based on the this observation, it is evident that the understanding the electrochemical properties of BPA is critical for the design and successful application of electrochemical BPA sensors. In this chapter, some new results are presented concerning the electrochemical reactions of BPA at a gold electrode during the cycling of the electrode potential, while an adherent thin polymer layer was formed on the electrode. The film buildup process, i.e. the electropolymerization of BPA on gold, was followed in-situ with an electrochemical quartz crystal microbalance (EQCM) and ex-situ by electrochemical impedance spectroscopy (EIS). Scanning electron microscopy with a focused Ga ion beam (SEM–FIB) was used for the study of the structure/morphology of the polymer coating.

V.1. Experimental

All electrochemical measurements were carried out in air-conditioned rooms at (20.0 ± 0.5) °C. The solutions were purged with oxygen-free argon (Linde 5.0) before use, and an inert gas blanket was maintained throughout the experiments.

V.1.1. Instrumentation

A Metrohm Autolab PGSTAT 302N potentiostat (controlled by the Autolab Nova software) was used in cyclic voltammetric and quartz crystal microbalance measurements. A Zahner IM6 electrochemical workstation (controlled by the Thales software package) was used in cyclic voltammetric and impedance measurements. A

Quanta™ 3D FEG high-resolution dual beam scanning electron microscopy (SEM/FIB) with silicon drift X-ray detector (EDX) instrument was used for SEM and elemental analysis. The properties of the ion beam used for milling process was 30 kV high voltage and 3 nA beam current.

V.1.2. Solutions

- Blank solutions:

a) 0.01 mol·dm^{-3} $HClO_4$ aq. (Merck), pH = 1.96.
b) 0.1 mol·dm^{-3} $NaClO_4$ aq. (Merck), pH = 7.63.
c) 0.1 mol·dm^{-3} $Na_2HPO_4 \cdot 2\ H_2O$ aq. (Molar Chemical), pH = 9.18 was titrated with 0.1 mol·dm^{-3} NaOH aq. (Molar Chemical), pH = 12.74) until its pH has been set to 11.99.
d) 0.1 mol·dm^{-3} NaOH aq. (Molar Chemical), pH = 12.70.

- Solutions containing BPA:

100 ppm ($4.4\cdot10^{-4}$ mol·dm^{-3}) Bisphenol A (Aldrich) was dissolved in the blank solutions. In the case of neutral and acidic pH-s ultrasonic mixer was needed to solve the BPA. The dissolved 100 ppm BPA did not change the pHs of the blank solutions.

V.1.3. Voltammetric experiments

The voltammetric experiments were carried out in common three-electrode cell in which a gold plate (surface area $A = 0.196$ cm^2) in contact with one of the BPA contained solutions served as working electrode, a gold ring (a circular Au wire) immersed in the same solution served as counter electrode and a NaCl-saturated calomel electrode (SSCE) was used as reference electrode. The potential range was different in the different solutions (**Table 2.**). The curves were recorded at 20 mV·s^{-1} sweep rate.

Table 2. Experimental conditions during the separate voltammetric experiments.

pH	potential range
1.96	−0.4 V to 1.0 V *vs*. SSCE
7.63	−1.2 V to 1.2 V *vs*. SSCE

V.1.4. Impedance measurements

Impedance measurements were carried out in a common three-electrode cell in which a gold plate or a gold plate with polymer coating (the geometrical surface area in both cases: $A = 0.196\ \mathrm{cm}^2$) in contact with the electrolyte solution served as working electrode, a gold ring (a circular Au wire) immersed in the same solution served as counter electrode and NaCl-saturated calomel electrode (SSCE) was used as the reference electrode. The measurements were performed in the frequency range of 11.4 kHz – 0.10 Hz (amplitude of the perturbing signal: 5 mV. The electrode potential was different in the different solutions (**Table 3.**).

Table 3. Experimental conditions during the impedance measurements.

pH	electrode potential
7.63	0.3 V, 0.5 V *vs*. SSCE
12.70	0.1 V *vs*. SSCE

V.1.5. Simultaneous cyclic voltammetric and quartz crystal microbalance experiments

Cyclic voltammetric (CV) and electrochemical quartz crystal microbalance (EQCM) experiments were performed in an Autolab EQCM cell (Metrohm) in which a Au/TiO_2 quartz crystal (Metrohm, polished quartz crystal, nominal resonant frequency $f_0 = 6$ MHz, integral sensitivity $C_\mathrm{f} = 81.5\ \mathrm{Hz\ cm^2\ \mu g^{-1}}$, surface area $A = 0.36\ \mathrm{cm}^2$) in contact with the electrolyte solution served as working electrode, a gold wire immersed in the same solution served as counter electrode. A Ag(s) | AgCl(s) | aq. KCl (sat’d) sol. gel electrode was used as reference. The cyclic voltammograms were recorded in different potential ranges and at different sweep rates in the different electrolyte solutions (**Table 4.**).

During the measurements the frequency change (Δf) of the quartz crystal was measured with respect to a control situation, i.e. Δf was set to 0 Hz with the "Reset EQCM ΔFrequency" command before all measurements. The driving force of the quartz crystal was minimized by adjusting the trimmer on the EQCM oscillator.

Table 4. Experimental conditions during the cyclic voltammetric and quartz crystal microbalance experiments.

pH	potential range*	sweep rate
7.63	−1.16 V to 0.95 *vs.* Ag|AgCl, KCl (3M)	20 $mV\cdot s^{-1}$
11.99	−1.36 V to 1.14 V *vs.* Ag|AgCl, KCl (3M)	100 $mV\cdot s^{-1}$

*$\Delta E_r = E_r$ [SSCE: (Hg(l) | Hg_2Cl_2(s) | sat'd aq. NaCl sol.)] −
E_r [Ag(s) | AgCl(s) | 3M aq. KCl sol.] ≈ 26 mV (25 °C) [191].

V.1.6. pH measurements

The pH measurements were carried out with a glass electrode connected with an OP 211/1 digital pH meter.

V.2. Results and discussion

V.2.1. Voltammetric results

Figure 30. shows the results of the EQCM experiments, with cyclic voltammograms recorded at a thin Au layer (deposited on the surface of a 6 MHz quartz crystal) in contact with a 0.1 $mol\cdot dm^{-3}$ $NaClO_4$ solution, pH = 7.63 (**Figure 30.** curve **A**) and with a 0.1 $mol\cdot dm^{-3}$ $NaClO_4$ / 100 ppm BPA (aq.) solution (**Figure 30.** curve **B**). For the latter case, the corresponding changes in the EQCM frequency are also given

(**Figure 30.** curve **C**). The potential sweep was initiated at 0 mV *vs.* Ag | AgCl, KCl (3 M) and scanned in the positive direction at a scan rate of 20 mV·s^{-1}.

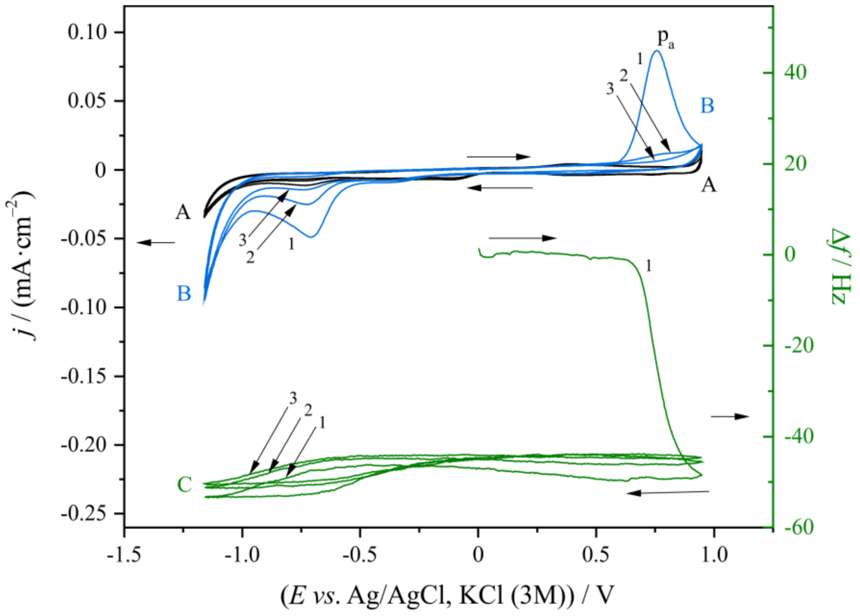

Figure 30. Cyclic voltammograms (**A**, **B**) and the corresponding changes in the EQCM frequency (**C**) recorded at a Au / TiO$_2$ quartz crystal in contact with (**A**) 0.1 mol·dm^{-3} NaClO$_4$ aq., pH = 7.63; (**B**, **C**) 100 ppm bisphenol A / 0.1 mol·dm^{-3} NaClO$_4$ aqueous solutions. Sweep rate: v = 20 mV·s^{-1}, E = −1.16 V – 0.95 V *vs.* Ag|AgCl, KCl (3M). (Δ*f*: frequency change of the quartz oscillator, *E*: electrode potential, *j*: current density, surface area *A* = 0.36 cm^2).
E(p$_a$) = 0.76 V *vs.* Ag | AgCl, KCl (3 M).

As it can be seen in **Figure 30**, in the closely neutral 0.1 mol·dm^{-3} NaClO$_4$ solution there is an abrupt decrease of the frequency at potentials more positive than about 0.7 V in the positive-going scan of the 1st CV (**C**, curve 1 in **Figure 30.**) together with an increase of the current flowing through the electrode, i.e. a current peak (p$_a$) appears at about *E* = 0.76 V *vs.* Ag | AgCl, KCl (3 M) (**B**, curve 1 in **Figure 30.**). A decrease in frequency corresponds to an increased mass on the surface of the gold-coated quartz crystal, i.e. the creation of a surface film. In the 2nd positive-going potential scan (**B**, curve 2 in **Figure 30.**) only a poorly resolved current peak or plateau could be observed in the potential range of 0.6 – 0.9 V *vs.* Ag | AgCl, KCl (3 M). This peak disappeared during the third scan (**Figure 30. B**, curve 3) and the shape of the CV remained practically unchanged during the subsequent potential scans. After the first CV, the simultaneously recorded Δ*f* *vs.* *E* curves show a periodic change in the EQCM frequency, however, the average frequency remains practically unchanged over time (**Figure 30. C**, curves 2, 3). It may be worth to note, that a negative current peak can be observed on the reverse (negative-going) scan of the first (and 2nd) potential cycle (at about $E = -0.77$ V *vs*. Ag | AgCl, KCl (3 M)).

According to **Figure 30.** (**C**, curve 1), and Eq. 18 the total frequency change during the mass-increasing process is $\Delta f = -49.0$ Hz, and the mass change is about $\Delta m = 216$ ng. The charge consumed during the process (Δq) can be calculated from the corresponding CV (**Figure 30. B**, curve 1) through integration under the curve (after correction for the double-layer charging current) followed by dividing by the sweep rate (v), i.e. by integrating the current versus time data over the relevant potential range, yielding a value of $\Delta q = 2.76 \cdot 10^{-4}$ C. Based on the above values, the effective molar mass corresponding to $F = 96485$ C·mol^{-1} charge is $M_{\mathrm{eff}} = 75.5$ g·mol^{-1}.

Cyclic voltammetric experiments with a gold plate (surface area $A = 0.196$ cm^2) in contact with 0.1 mol·dm^{-3} aqueous $NaClO_4$ solution containing 100 ppm bisphenol provided similar results (**Figure 31. B**). In these experiments the positive potential limit of the cyclic voltammogram was increased to 1.2 V *vs*. SSCE (which corresponds to 1.226 V *vs*. Ag | AgCl, KCl (3 M)). The first cyclic voltammogram (**B**, curve 1 in **Figure 31.**) is characterized by the occurrence of an anodic peak (p_a) at 0.72 V *vs*. SSCE on the positive-going scan of the first potential cycle, which corresponds to the formation of the polymer film, and a negative current peak on the negative-going scan (at about −0.75 V *v*s. SSCE). The current density of the anodic p_a peak is somewhat smaller in the this case, than in the EQCM measurements. The explanation of this phenomenon can be found in the difference of the roughness factor of the two kinds of gold electrodes. The surface of the Au / TiO_2 quartz crystal is much smoother, than the gold plate's which was used during the separated voltammetric experiments. The latter peak may be attributed to the reduction of certain oxidation products of BPA. The cyclic voltammograms of the bare and the polymer coated gold plate in the supporting electrolyte are also presented (curves **A** and **C** in **Figure 31,** respectively).

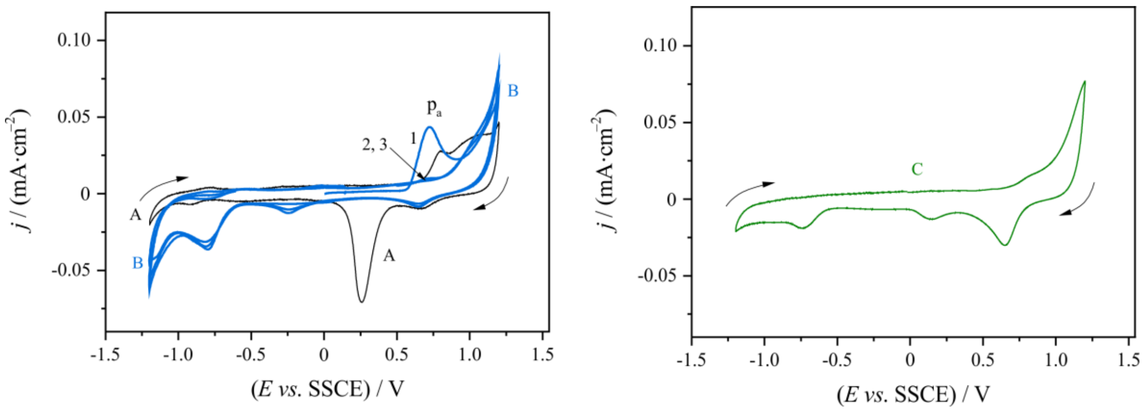

Figure 31. Cyclic voltammograms recorded at a gold plate in contact with 0.1 mol·dm^{-3} NaClO$_4$ solution (**A**) and with 100 ppm bisphenol A / 0.1 mol·dm^{-3} NaClO$_4$ solution (**B**), (pH = 7.63); Cyclic voltammogram recorded at a gold plate completely covered by the polymer layer in contact with 0.1 mol·dm^{-3} NaClO$_4$ solution (**C**). Potential sweep rate: v = 20 mV·s^{-1}, E = −1.2 V – 1.2 V *vs.* SSCE. (E: electrode potential, j: current density, surface area A = 0.196 cm^2). E(p$_a$) = 0.72 V *vs.* SSCE.

The results in acidic environment (**Figure 32.**) are similar to the above observations in the neutral solution. In 100 ppm BPA / 0.01 mol·dm^{-3} HClO$_4$ solution, pH = 1.96 the first cyclic voltammogram (**B**, curve 1 in **Figure 32.**) is also characterized by the occurrence of an anodic peak (p$_a$) at 0.80 V *vs.* SSCE on the positive-going scan of the first potential cycle. As expected, this value is more positive than in the neutral solution, so this peak is also corresponds to the formation of the polymer film. However, in this case, there is no negative current peak on the negative-going scan.

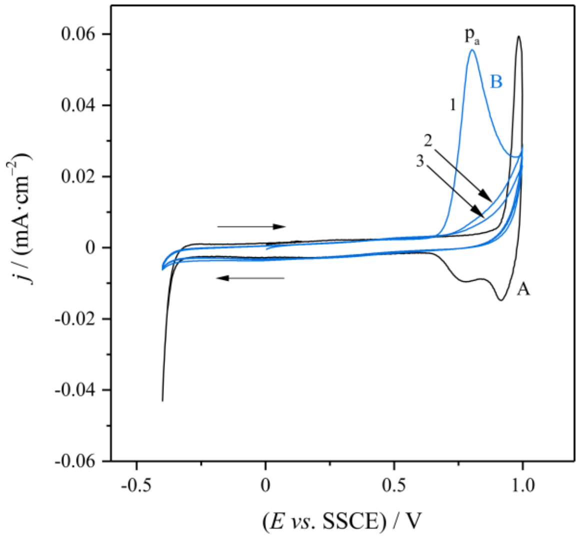

Figure 32. Cyclic voltammograms recorded at a gold plate in contact with 0.01 mol·dm^{-3} HClO$_4$ solution, pH = 1.96 (**A**) and with 100 ppm bisphenol A / 0.01 mol·dm^{-3} HClO$_4$ (**B**). Potential sweep rate: v = 20 mV·s^{-1}, E = −0.4 V – 1.0 V *vs.* SSCE (E: electrode potential, j: current density, surface area A = 0.196 cm^2). E(p$_a$) = 0.80 V *vs.* SSCE.

In the light of the present results it is interesting to note that according to [125] no oxidation peak of BPA could be observed in the CV recorded for Au in pH = 12 phosphate buffer. This finding seems to be correct according to the EQCM + CV experiments measured in 0.1 mol·dm^{-3} $Na_2HPO_4 \cdot 2\,H_2O$ solution (pH = 9.18) titrated with 0.1 mol·dm^{-3} NaOH aq. (pH = 12.74) until its pH has been set to 11.99. In curve **A Figure 33.** cannot be observed a well-defined p_a, which corresponds to the formation of a BPA polymer film. However, during the first cycle, a significant frequency decrease can be observed (curve **B Figure 33.)**, which indicates a mass increase on the electrode surface. The total frequency change during the mass-increasing process is $\Delta f = -45.9$ Hz, and the mass change is about $\Delta m = 202.75$ ng (Eq. 18).

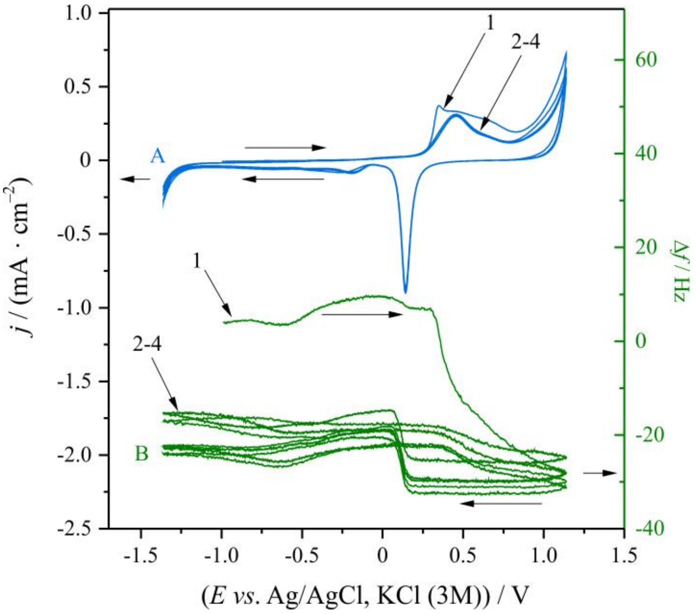

Figure 33. Cyclic voltammogram (**A**) and the corresponding changes in the EQCM frequency (**B**) recorded at a Au / TiO_2 quartz crystal in contact with Na_2HPO_4 / NaOH / 100 ppm BPA, pH=11.99. Sweep rate: $v = 100$ mV·s^{-1}, $E = -1.36$ V – 1.14 V *vs.* Ag|AgCl, KCl (3M) (Δf: frequency change of the quartz oscillator, E: electrode potential, j: current density, surface area $A = 0.36$ cm^2).

V.2.2. Impedance measurements

As it can be seen in **Figure 34**, the (frequency dependent) capacitances of the Au | pBPA | 0.1 mol·dm^{-3} $NaClO_4$ electrode (the pBPA layer was deposited from 100 ppm BPA / 0.1 mol·dm^{-3} $NaClO_4$ aq., pH = 7.63 solution) are somewhat lower than those of the Au | 0.1 mol·dm^{-3} $NaClO_4$ electrode, suggesting that the polymer is electrochemically inactive at the applied potentials [49,192,193]. In addition, the frequency dependence of the capacitance is stronger in case of the polymer modified electrode, especially at E = 0.3 V *vs.* SSCE. In accordance with the above all complex plane admittance plots have the shape of a “depressed semicircle,” but the arches are much flatter in the case of the Au | pBPA | 0.1 mol·dm^{-3} $NaClO_4$ electrode. Similar results were obtained in acidic environment.

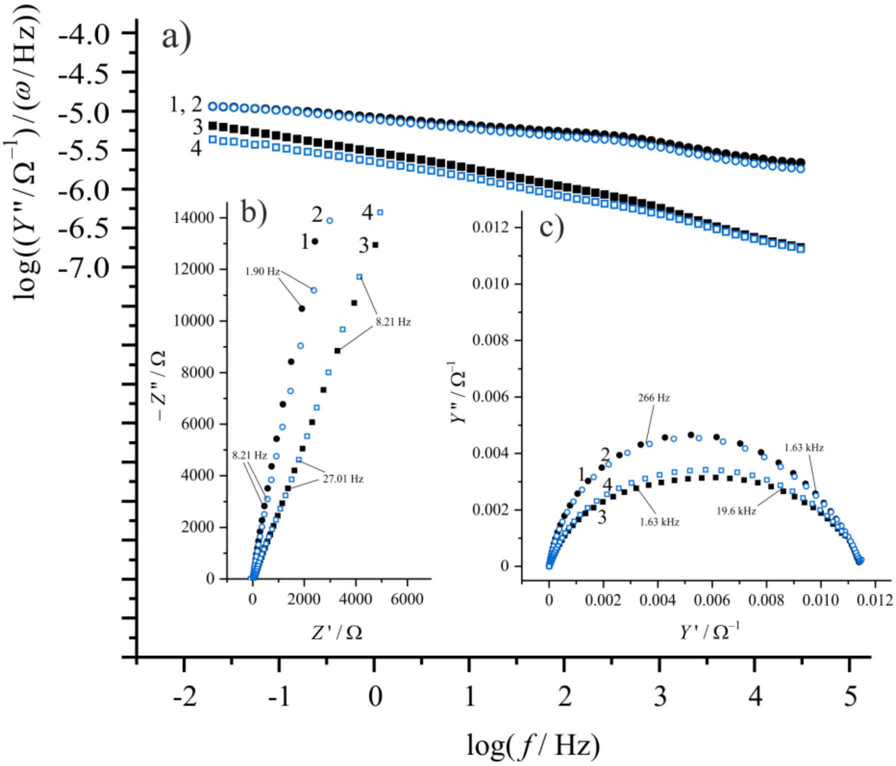

Figure 34. a) The “parallel” capacitances as a function of frequency, **b)** complex impedance and **c)** admittance plane plots for a bare gold plate in contact with 0.1 mol·dm^{-3} $NaClO_4$ aq., pH = 7.63 (**1, 2**) and the same gold plate completely covered by poly-bisphenol A layer (deposited from 100 ppm BPA / 0.1 mol·dm^{-3} $NaClO_4$ aq., pH = 7.63) solution in contact with the same electrolyte solution (**3, 4**) at potentials: E = 0.3 V *vs.* SSCE (**1, 3**); E = 0.5 V *vs.* SSCE (**2, 4**). Selected frequencies of the perturbing signal are also indicated in the complex plane plots (small numbers). Surface area A = 0.196 cm^2.

In contrast, the (frequency dependent) capacitances of the Au | pBPA | 0.1 mol·dm^{-3} NaOH electrode (the pBPA layer was deposited from 100 ppm BPA / 0.1 mol·dm^{-3} NaOH aq., pH = 12.70 solution) are similar values to those of the Au | 0.1 mol·dm^{-3} NaOH electrode: **Figure 35. a)**. It seems, that in basic environment the poly(BPA) coated gold (the polymer layer was deposited from basic solution) behaves just like pure gold.

Important to note, that during the above describes experiments, the pH of the solution in which the pBPA deposition was took place and the pH of the solution in which the deposited polymer layer was characterized were the same. It is an interesting question that how poly(BPA) layer deposited from a basic solution behaves in an acidic solution, or vice versa, how a poly(BPA) layer deposited from an acidic environment behaves in a basic electrolyte solution. An empirical observation is that BPA significantly easier can be dissolved in a basic solution than in a neutral or acidic solution. Maybe this also contributes to the above described properties. However, this is an open point for now and for proper explanation, more experiments are needed.

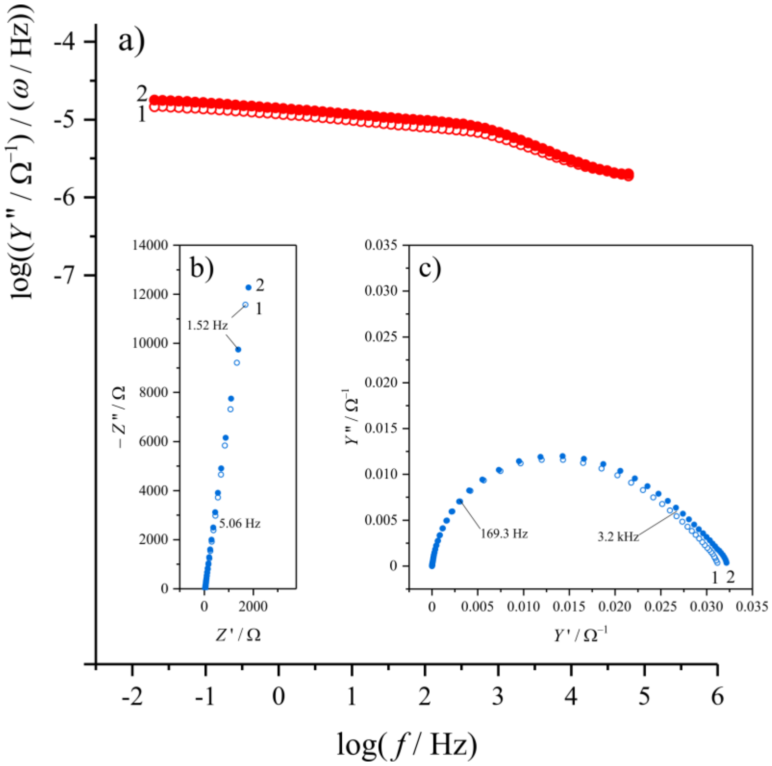

Figure 35. a) The "parallel" capacitances as a function of frequency, **b)** complex impedance, and **c)** admittance plane plots for a bare gold plate in contact with 0.1 mol·dm^{-3} NaOH aq., pH = 12.70 (**1**) and the same gold plate completely covered by poly-bisphenol A layer (deposited from 100 ppm BPA / 0.1 mol·dm^{-3} NaOH aq., pH = 12.70 solution) in contact with the same electrolyte solution (**2**) at potentials: E = 0.1 V *vs*. SSCE. Selected frequencies of the perturbing signal are also indicated in the complex plane plots (small numbers). Surface area A = 0.196 cm^2.

V.2.3. SEM micrographs of the polymer layers

The SEM images of the polymer film formed on gold from a neutral electrolyte solution are presented in **Figure 36.** One can see in the images that the surface of the sample is relatively smooth, apart from some small holes and cracks (see **Figure 36. a)**). The backscattered electron (BSE) micrographs (i.e. the electrons were backscattered from the gold layer, **Figure 36. a)** indicates that the polymer coating is very thin. The structure of the Pt/polymer/Au interface region has also been investigated by focused ion beam (FIB) cross section imaging. The Ga ion cutting (incision) was performed perpendicular to the sample surface. The SEM micrographs taken from the cross-section of the Pt/polymer/Au "sandwich" reveals the highly porous structure of the polymer layer (**Figure 36. c)** and **d)**). SEM micrographs of poly(BPA) layers deposited from acidic or basic solution do not show any significant differences from those are shown in **Figure 36.**

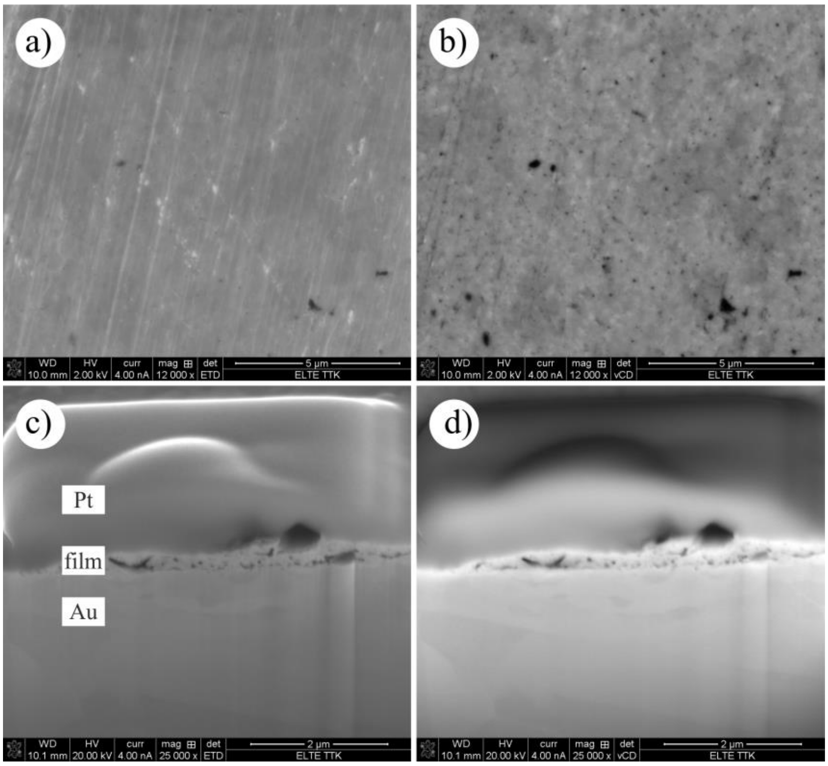

Figure 36. SEM images of a gold plate covered by the poly(BPA) layer formed from neutral solution. **a)** Secondary electron SEM image and **b)** the corresponding backscattered SEM images taken from the same area. The length of the horizontal white bar below the images corresponds to 5 µm. Secondary electron SEM image of a cross section made by FIB-milling **c)**, and the corresponding backscattered SEM image **d)** taken from the same area.

V.2.4. The polymerization mechanism of BPA

The number of mechanistic studies dealing with the electropolymerization of bisphenol A is rather limited, and, to our knowledge, a thorough kinetic/mechanistic study of the polymerization reactivity of BPA on gold has not been published yet. On the other hand, the oxidative degradation of phenols including BPA in general was relatively widely studied [112,118–122,194–198], and this may provide an insight into the oxidation or electropolymerization mechanism of BPA on gold as well. Nevertheless, the main features of the electropolymerization mechanism of BPA should be very similar to that of the electropolymerization mechanism of substituted phenols.

In **Figure 37.** three different (rather speculative) schemes (all taken from [121,125,197,199]) are presented. Let the parameter x_e be the fraction of the charge that each monomer unit shares during the oxidation / polymerization process, e.g. $x_e = 2$ if 2 electrons per monomer are needed to form the oligomer or polymer. According to the scheme for the electrooxidation of BPA (scheme **a)** in **Figure 37.**), $x_e = 1$ for the dimerization process. Consequently, $x_e = 1$ for the “whole” process if the mechanism of the polymerization process follows essentially the same pathway. Scheme **b)** in **Figure 37.** is quite oversimplified and obviously does not reflect the complexity of the polymerization process. In this case polymerization is taking place by formation of C–C bonds between benzene rings and the oxidation of the 4-hydroxyphenyl rings, i.e. $x_e = 2$.

In electrochemical oxidation of phenolic compounds, including BPA several aromatic intermediates have been identified, including hydroxylated BPA and phenol derivatives such as hydroquinone and benzoquinone [112,121,195]. The accumulation of hydroxylated phenol derivatives can result in polymer formation. However, according to [121] the aromatic polymerization on different anode materials may be a reversible reaction. Nevertheless, if the degradation of the monomer also occurs in parallel with the polymerization process, it can significantly affect (in fact, increase) the (apparent) value of the x_e parameter.

In the experiments reported in this chapter, the estimated value of x_e (using the EQCM and voltammetric data) is about 3. This may suggest that polymerization and degradation of the BPA monomer may occur simultaneously during its electrochemical oxidation.

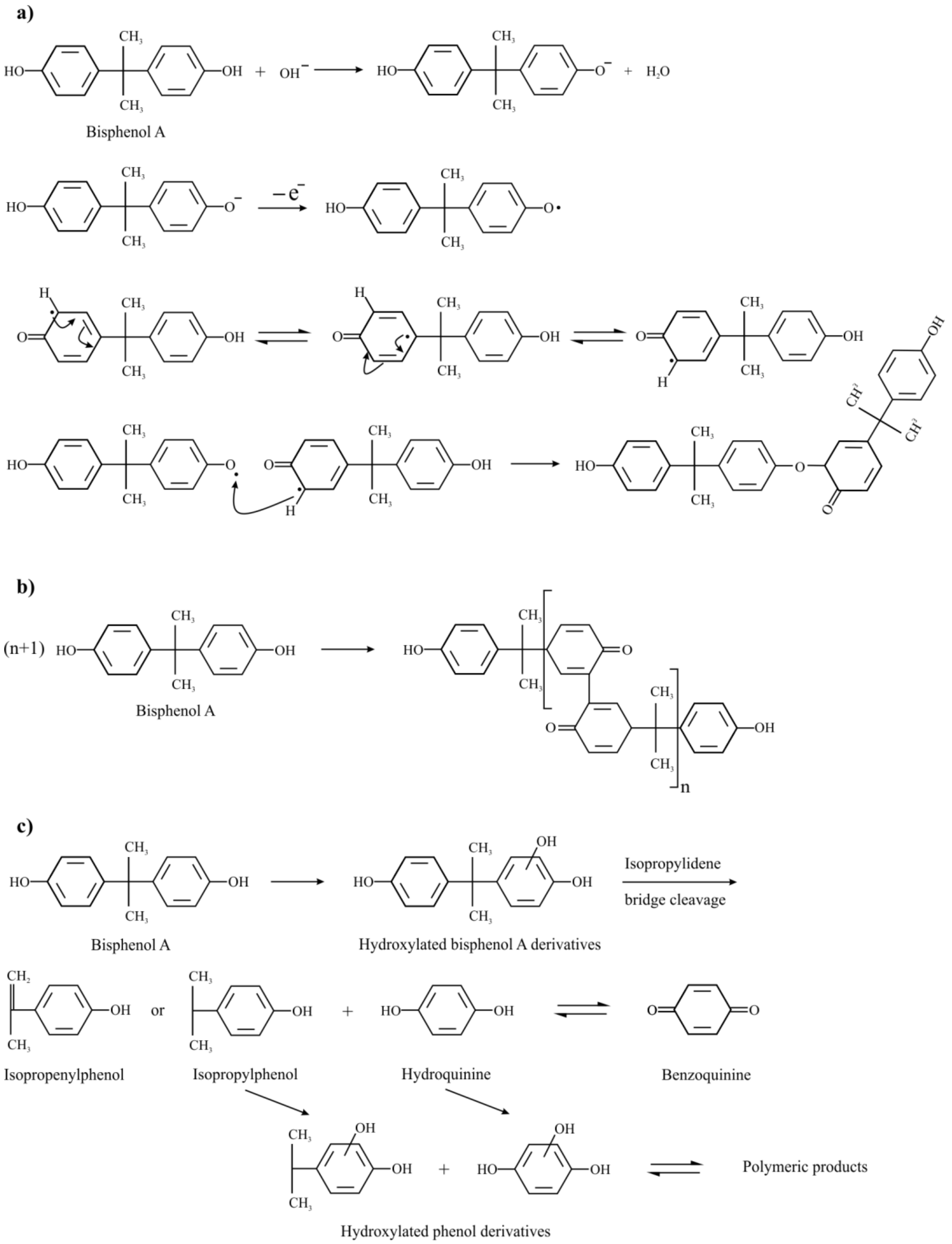

Figure 37. Suggested polymerization mechanisms, adapted from **a)** [125], **b)** [197,199], **c)** [121].

V.3. Concluding remarks

According to the literature the electrochemical oxidation of phenolic compounds including bisphenol A often causes the inactivation of different electrodes, via the deposition of electropolymerized films. In this project, a similar behavior was observed in the gold | 0.1 mol·dm^{-3} sodium perchlorate / 100 ppm BPA system, calling into question the earlier assumption that there is no oxidation peak for BPA on bare Au. In-situ measurements were made by using an Electrochemical Quartz Crystal Microbalance (EQCM) coupled with cyclic voltammetry to monitor the surface changes. The experimental results reviewed above support the mechanistic picture, according to which during the cycling of the electrode potential a strongly adherent thin polymer layer is forming on the electrode surface. Impedance measurements suggest that the polymer is practically electrochemically inactive at the applied potentials. According to the SEM images the surface of the polymer layer is quite smooth, apart from some small holes and cracks. The results of the present chapter imply that polymerization and degradation of the BPA monomer may occur simultaneously, and the coating decreases the electrocatalytic activity of the electrode. Nevertheless, further research is needed to conclusively clarify these points and to elucidate the mechanism of the polymerization process.

VI. Analysis of poly(bisphenol A) supported PEDOT layers deposited on gold

This section describes the preparation and electrochemical characterization of poly(bisphenol A) (pBPA) supported poly(3,4-ethylenedioxythiophene) (PEDOT) modified gold electrodes before and after overoxidation. As we saw in Chapter V, during the cycling of the electrode potential an adherent, flexible and poorly conducting poly(bisphenol A) film was formed on the gold surface. On the other hand, the redox activity exhibited by a pBPA film coated on a PEDOT-modified glassy carbon electrode has been proposed to determine the concentration of BPA in aqueous solutions. However, the removal of the pBPA film from electrode substrates presented difficulty for subsequent measurements [130,200]. Based on these findings, the idea arose that the mechanical properties of a PEDOT layer and its resistance against the consequences of overoxidation could be improved by the electrochemical deposition of pBPA on its surface and in its pores, i.e. by the combination of the two polymers. It was showed in Chapter V that pure pBPA has low electrochemical conductivity and poor electrochemical activity, therefore, it was expected that its presence would not affect considerably the electrochemical properties of the PEDOT layer, even after its overoxidation.

Similarly to overoxidized PEDOT modified gold electrodes [15,82], time evolution of the electrochemical properties of the poly(BPA)/PEDOT films could be observed after overoxidation. The four-dimensional (4D) analysis method (i.e., a post-experimental mathematical/analytical procedure to overcome the problems caused by non-stationarity) and complex nonlinear least-squares (CNLS) fitting has been used for the estimation of the impedance parameters corresponding to different time instants after overoxidation of the [poly(BPA)/PEDOT] film.

The deviations of the impedance responses from the purely capacitive behavior predicted at low frequencies by the theoretical models could be well explained solely by the assumption of uneven film thickness. It has been found that the impedance model, which takes into

account the film thickness distribution gives a good description of the impedance data, both before and after overoxidation.

According to the results, after the electrochemical deposition of poly(BPA) on the PEDOT layer the resulting [poly(BPA)/PEDOT] modified electrode becomes more resistant against the negative effects of overoxidation.

VI.1. Experimental

VI.1.1. Apparatus

A Zahner IM6 electrochemical workstation (controlled by the Thales software package) was used in all electrochemical measurements. The impedance measurements were performed using single sine excitation at 57 discrete frequencies ('frequency by frequency' mode) in the frequency range of 96.1 mHz – 50 kHz by applying an AC amplitude of 5 mV rms.

A He–Ne laser (Melles Griot 05-LHP-151, 1 mW, operating at a wavelength of 632.8 nm) was used during the stress change (bending beam) measurements. The displacement of the reflected beam (Δd) was measured with a position-sensitive photodetector (PSD, Hamamatsu S1300). This device was attached to a signal processing unit (Hamamatsu C4757) that can provide analog output signals proportional to the coordinates of the incident light spot. The position-sensitive detector, the laser and the electrochemical cell were assembled on an optical bench in order to avoid vibrations. All measurements were carried out at 25.0 ˚C.

A Quanta™ 3D FEG high-resolution dual beam scanning electron microscopy (SEM/FIB) with silicon drift X-ray detector (EDX) instrument was used for SEM and elemental analysis.

VI.1.2. Reagents

3,4-Ethylenedioxythiophene (EDOT) and Bisphenol A (BPA) were purchased from Aldrich and Aldrich-Chemie, respectively. All chemical reagents were used as received without further purification. All solutions were prepared with ultrapure water (Milli-Q®, specific resistance: 18.2 MΩ·cm^{-1}). Reagent grade sulfuric acid (Merck) and sodium sulfate decahydrate (VWR) were used for the preparation of 0.01 mol·dm^{-3} EDOT / 0.1 mol·dm^{-3} Na_2SO_4 (aq.) and 100 ppm BPA / 0.5 mol·dm^{-3} H_2SO_4 (aq.) solutions. The polymer films were formed on gold discs (Metal-Art 0.9999, projected area, $A = 0.196$ cm^2). Before electrodeposition, the gold surface was polished by 1 μm diamond suspension (Struers DP). The roughness factor of the gold electrodes (calculated from the charge associated with the oxide formation on the gold surface) was $f_r \approx 2$. All electrochemical measurements were carried out at ambient temperature (22.0 ± 0.5) °C. The solutions were purged with oxygen-free argon (Linde 5.0) before use, and an inert gas blanket was maintained throughout the experiments.

VI.1.3. Preparation and electrochemical characterization of PEDOT- and poly(BPA)/PEDOT-modified gold electrodes

Step 1 – deposition of the PEDOT layer

Electrodeposition of PEDOT layer was carried out in a common three electrode cell in which the working electrode was a gold disc ($A = 0.196$ cm^2) in contact with freshly prepared 0.01 mol·dm^{-3} EDOT / 0.1 mol·dm^{-3} Na_2SO_4 solution, the counter electrode was a ring-shaped Pt wire immersed into the same solution, and a KCl-saturated calomel electrode (SCE) was used as reference electrode. During the galvanostatic deposition $j = 0.2$ mA·cm^{-2} current density was used. 2-2 PEDOT modified gold electrodes was prepared under identical conditions, except for the deposition time. In the case of samples S1 and S2 the deposition time was shorter ($t = 1800$ s), while for samples L1 and L2 the deposition time was longer ($t = 3600$ s).

After the deposition, the polymer layer was left for one-day relaxation in ultrapure (“Milli-Q®”) water.

Step 2 – investigation of the PEDOT-modified electrodes

Investigation of PEDOT layers was carried out in common three electrode cell in which the working electrode was a gold plate (A = 0.196 cm^2) with the deposited PEDOT layer in contact with 0.5 $mol\cdot dm^{-3}$ H_2SO_4 solution, the counter electrode was a ring-shaped Pt plate immersed into the same solution. A NaCl-saturated calomel electrode (SSCE) was used as reference electrode.

The potential range during the cyclic voltammetric measurements was E = (−0.1 – 0.8) V *vs.* SSCE (samples S1, S2) or E = (−0.4 – 1.0) V *vs.* SSCE (samples L1, L2), the scan rate was v = 50 $mV\cdot s^{-1}$ or v = 100 $mV\cdot s^{-1}$.

Impedance measurements were performed on sample S1 in 0.1 $mol\cdot dm^{-3}$ H_2SO_4 solution in the frequency range of 50 kHz – 96.1 mHz (amplitude of the perturbing signal: 5 mV rms, electrode potential E = 0.4 V *vs.* SSCE). A high surface area gold-foil (immersed in the 0.1 $mol\cdot dm^{-3}$ H_2SO_4 solution) was arranged cylindrically around the working electrode to maintain a uniform electric field (counter electrode). The reference electrode was a saturated sodium calomel electrode (SSCE). The linearity of the system has been checked by comparing the impedance spectra obtained with different amplitudes (ranging from 1 mV to 5 mV rms)

Step 3 – deposition of poly(BPA)

Electrodeposition of poly(BPA) was carried out in common three electrode cell in which the working electrode was a gold plate (A = 0.196 cm^2) with deposited PEDOT layer in contact with a 100 ppm BPA / 0.5 $mol\cdot dm^{-3}$ H_2SO_4 solution, the counter electrode was a Pt wire immersed into the same solution, and SSCE was used as reference electrode. The potentiodynamic electrodeposition was performed in the potential window of E = (−0.1 V – 1.0) V *vs.* SSCE (sample S1) or E = (−0.4 V – 1.0) V *vs.* SSCE (sample L1), the scan rate was v = 100 $mV\cdot s^{-1}$, the number of cycles was 10.

After the deposition, the poly(BPA) supported PEDOT layer was left for one-day relaxation in ultrapure water.

Step 4 – investigation of the poly(BPA)/PEDOT-modified electrodes

Investigation of poly(BPA)/PEDOT layer was carried out in common three electrode cell in which the working electrode was a gold plate (samples S1 and L1, $A = 0.196\ \mathrm{cm^2}$) with the deposited poly(BPA)/PEDOT layer in contact with 0.1 mol·dm^{-3} H_2SO_4 solution, the counter electrode was a ring-shaped Pt plate immersed in the same solution, and the reference electrode was SSCE.

The potential range during the cyclic voltammetric measurements was $E = (-0.1 – 0.8)$ V *vs*. SSCE (sample S1) or $E = (-0.4 – 1.0)$ V *vs.* SSCE (sample L1), the scan rate was $v = 50\ \mathrm{mV \cdot s^{-1}}$ or $v = 100\ \mathrm{mV \cdot s^{-1}}$.

Electrochemical impedance measurements were performed on sample S1 in 0.1 mol·dm^{-3} H_2SO_4 solution in the frequency range of 50 kHz – 96.1 mHz (amplitude of the perturbing signal: 5 mV rms, electrode potential $E = 0.4$ V or 0.2 V *vs.* SSCE). The cell geometry was the same as that described in **Step 2**. Linearity of the impedance response was analyzed as previously described (**Step 2**) using different AC perturbation amplitudes.

Step 5 – overoxidation of the PEDOT and poly(BPA)/PEDOT layers

The overoxidation of the PEDOT and the poly(BPA)/PEDOT layers was carried out in a common three electrode cell in which the working electrode was the PEDOT+poly(BPA) modified gold electrode (sample S1 and L1) or the PEDOT modified gold electrode (samples S2 and L2), the reference electrode was SSCE, and the counter electrode was a ring-shaped Pt plate. Electrolyte solution: 0.1 mol·dm^{-3} H_2SO_4(aq.).

The potential range of the potentiodynamic/cyclic voltammetric (over)oxidation was $E = (0.4 – 1.5)$ V *vs.* SSCE (sample S1 and S2) or $E = (-0.4 – 1.5)$ V *vs.* SSCE (sample L1 and L2) the scan rate was $v = 50\ \mathrm{mV \cdot s^{-1}}$, number of cycles: 3.

Step 6 – Electrochemical impedance study of the poly(BPA)/PEDOT layer after overoxidation

Investigation of the overoxidized poly(BPA)/PEDOT layer was carried out in common three electrode cell in which the working electrode was a gold plate (sample S1, $A = 0.196\ \mathrm{cm^2}$) with the overoxidized poly(BPA)/PEDOT layer on it in contact with 0.1 mol·dm^{-3} H_2SO_4 solution, the counter electrode was a ring-shaped Pt plate in the same solution, and the reference electrode was SSCE. Electrochemical impedance measurements were performed right after the overoxidation in 0.1 mol·dm^{-3} H_2SO_4 solution in the frequency range of 50 kHz – 96.1 mHz (amplitude of the perturbing signal: 5 mV rms, electrode potential E = 0.4 V *vs.* SSCE). The cell geometry was the same as described previously. 16 subsequent sets of impedance data were recorded continuously to monitor changes in the polymer film. The start times of the recording of the successive impedance data sequences ("timestamps") were as follows: #1: 0 s, #2: 341.569 s, #3: 683.452 s, #4: 1025.516 s, #5: 1371.936 s, #6: 1718.288 s, #7: 2064.538 s, #8: 2411.373 s, #9: 2754.216 s, #10: 3101.185 s, #11: 3448.118 s, #12: 3795.114 s, #13: 4142.181 s, #14: 4488.584 s, #15: 4839.730 s, #16: 5190.759 s.

Finally, cyclic voltammograms were recorded after the impedance measurements in the potential range of $E = -0.4 – 1.0$ V *vs.* SSCE at scan a rate of v = 100 mV·s^{-1}.

VI.1.4. Stress change (bending beam) measurements

Cantilever probes for the measurement of surface stress changes were made by evaporating 150 nm thick gold layer on a very thin layer of titanium evaporated on one side of a glass plate (supplier: Matsunami Glass Ind., Ltd., Japan, total length: l_s = 60.0 mm, width: w_s = 5.0 mm, thickness: t_s = 100 μm, $E_s = 7.09\cdot10^{10}$ Nm^{-2}, υ_s = 0.230) after careful cleaning of the surface of the substrate. The PEDOT and PEDOT+poly(BPA) films were formed by electrodeposition on the metal layers of the bending beam probes. Taking into account the above data and the estimated average thickness of the polymer films ($t_f \approx 0.25$ μm), the calculated value of k_i is about $0.71\cdot10^9$ N·m^{-1}.

VI.2. Results and discussion

VI.2.1. The morphology of the electrochemically deposited PEDOT and poly(BPA)/PEDOT layers

The morphology of the PEDOT layer deposited at a current density of $j = 0.2\ \mathrm{mA{\cdot}cm^{-2}}$ for 1800 s was studied by analyzing the scanning electron micrograph shown in **Figure 38**. “Dark pixels” (corresponding to the polymer layer) from the SEM micrograph were extracted (**Figure 38. b)**) and the thickness values were determined by a column-by-column pixel counting and a subsequent scaling based on the image resolution.

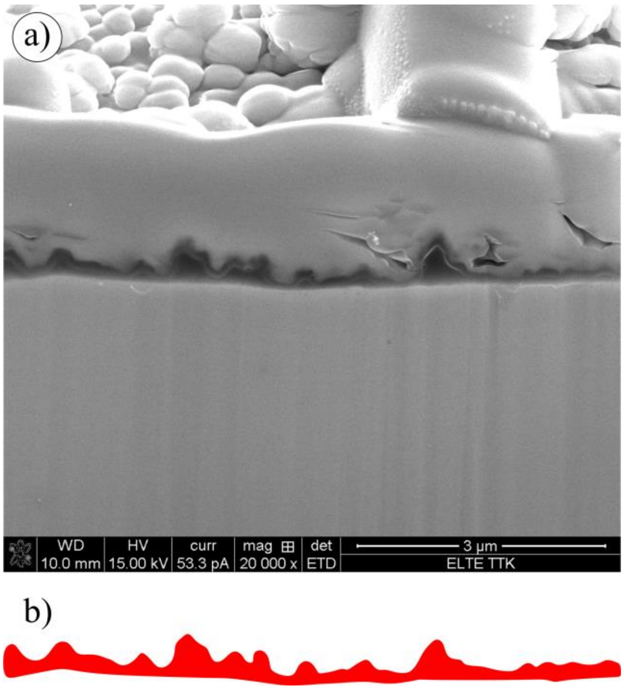

Figure 38. a) Focused ion beam (FIB) cross section image of PEDOT film deposited on gold. Deposition time: 1800 s. The length of the horizontal white bar corresponds to 3 µm. **b)** “Dark pixels” corresponding to the polymer layer extracted from the SEM micrograph.

For the image presented in **Figure 38.** the calculated thicknesses were made subject to a kernel density estimation algorithm [201] that allowed determination of the $p(d)$ probability density function of the d thicknesses in the form of

$$p(d) = \frac{1}{nh}\sum_{\mathrm{i}=1}^{n} K\left(\frac{d-d_{\mathrm{i}}}{h}\right) \qquad \text{Eq. 23}$$

where n is the number of samples in a dataset and h is the window width. For the density estimation a Gaussian kernel defined as

$$K(u) = \frac{1}{\sqrt{2\pi}} \exp\left[-\frac{1}{2}u^2\right] \qquad \text{Eq. 24}$$

was used.

The distribution function in **Figure 39. a)** implies that 4 characteristic thicknesses can be distinguished in the thickness distribution. Based on this observation, it was expected that the thickness distribution function of the polymer film can be roughly approximated with the distribution of 4 distinct thicknesses, assuming that the surface of the electrode can be divided into 4, not necessarily contiguous segments, each of which is covered with uniform layers (**Figure 39. b)**).

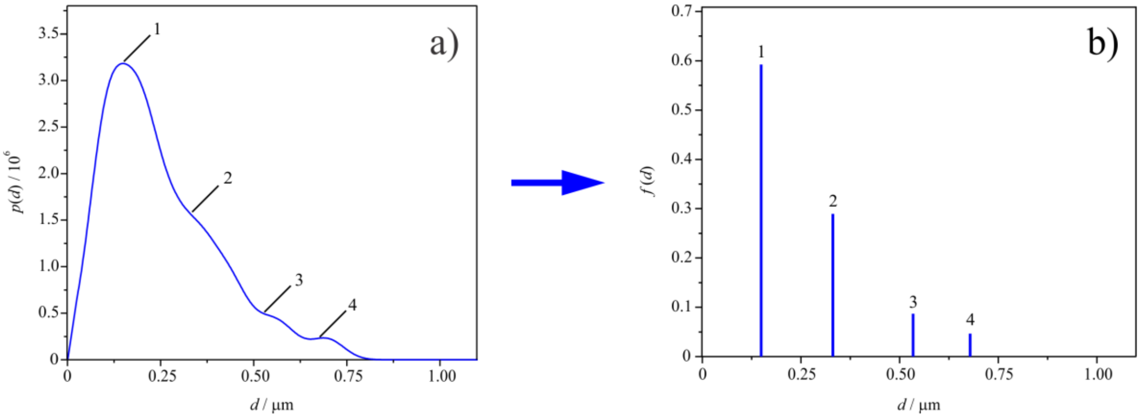

Figure 39. a) Estimated function for the thickness distribution of a PEDOT layer deposited on gold (d is the thickness, $p(d)$ is the probability density function of d. **b)** The 4 characteristic thicknesses. $f(d)$ is the relative frequency of thickness d in the thickness distribution.

In other words, the probability density function of a continuous variable has been replaced by a histogram or a discrete valued probability mass function. In **Figure 39. b)** $f(d)$ is the relative frequency of thickness d in the thickness distribution, which corresponds to the surface portion or relative area:

$$x_\mathrm{i} = \frac{A_\mathrm{i}}{A} \qquad \text{Eq. 25}$$

covered by a film of thickness L_i. (In Eq. 25 A_i is the area of the electrode covered by the film of thickness L_i, and A is the total area of the electrode.)

In **Figure 40.** the SEM micrograph of the poly(BPA)-covered Au | PEDOT electrode is presented. In the SEM image of the overoxidized poly(BPA)/PEDOT (**Figure 40. b)**) in addition to the cauliflower-like structure cracks or crevices formed during overoxidation [13,81] are clearly visible.

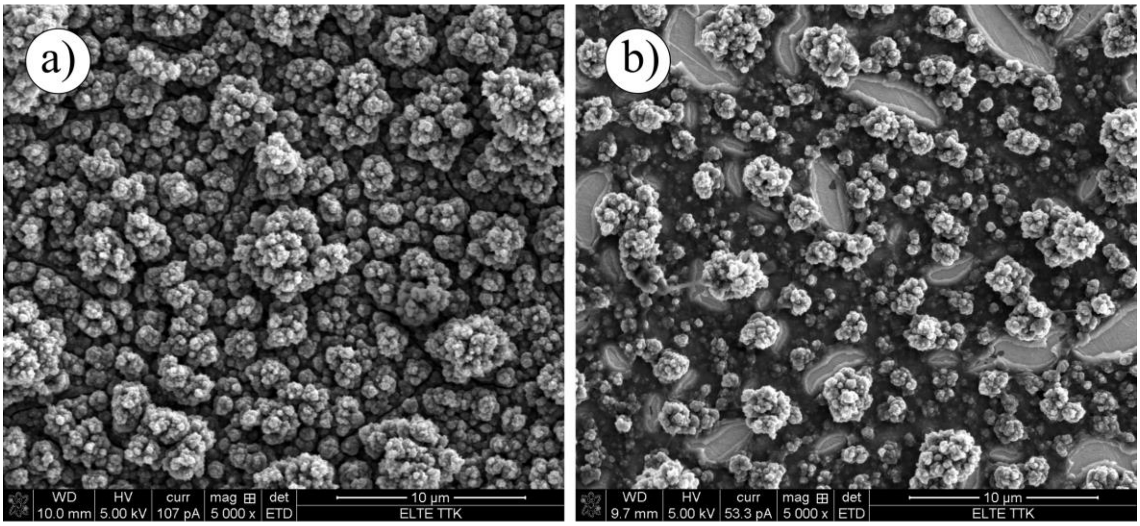

Figure 40. a) SEM image of the poly(BPA)-covered Au | PEDOT system. **b)** SEM image of the overoxidized poly(BPA)/PEDOT layer on gold. The length of the horizontal white bar corresponds to 10 μm.

In **Figure 41.** focused ion beam (FIB) cross section images taken on the overoxidized poly(BPA)/PEDOT layer (sample S1) are shown. The following procedure was applied: first, a Pt layer was deposited onto the area of the planned hole to protect and preserve the polymer layer and to avoid Ga contamination (**Figure 41. a)**). The big “cauliflower” like structure with the long filament (what is probably poly(BPA)) in the foreground of **Figure 41. a)** was cut with the Ga ion beam. During the cut, the filament broke away but a piece of it was left behind (**Figure 41. b)**). After that, focused ion beam (FIB) cutting was performed (in the region covered by Pt) to obtain cross sections of the film. The cross-section of the polymer layer can be seen in the SEM image shown in **Figure 41. c)**. As a result, it can be concluded that the thickness distribution of the PEDOT layer is quite similar to that shown in **Figure 38**.

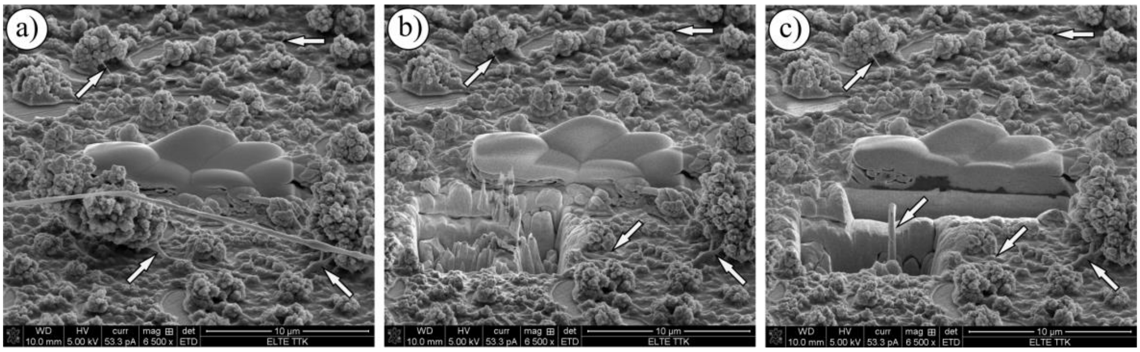

Figure 41. Focused ion beam (FIB) cross section images **a)** before, **b)** during and **c)** after the cutting process of the overoxidized PEDOT/poly(BPA) layer. The white arrows point to the filaments that presumably belong to the poly(BPA) layer. The deposited platinum layer can be seen in the center of the images.

VI.2.2. Results of cyclic voltammetry and electro-chemo-mechanical experiments

In **Figure 42. a)** and **b)** the cyclic voltammograms recorded during the deposition of poly(BPA) on the PEDOT layer (preparation **step 3**, sample S1) and during the overoxidation of the poly(BPA)/PEDOT film (preparation **step 5**, sample S1) are shown.

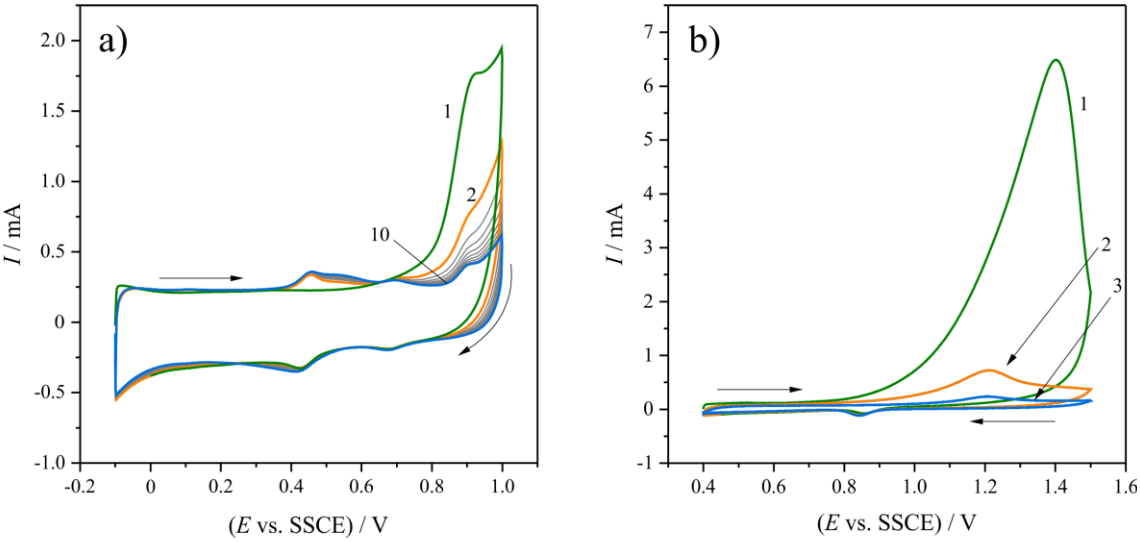

Figure 42. Cyclic voltammograms of sample S1 (surface area of the gold substrate: $A = 0.196\ \mathrm{cm}^2$, PEDOT layer deposited from 0.01 mol·dm^{-3} EDOT / 0.1 mol·dm^{-3} Na_2SO_4 solution, deposition time: $t = 1800$ s, current density: $j = 0.2$ mA·cm^{-2}) recorded **a)** during the deposition of poly(BPA) on the PEDOT layer (in 100ppm BPA / 0.5 mol·dm^{-3} aqueous H_2SO_4 solution, scan rate: $v = 100$ mV·s^{-1}, potential range: $E = -0.1$ V – 1.0 V *vs.* SSCE, 10 cycles) and **b)** during overoxidation of the poly(BPA)/PEDOT film in 0.1 mol·dm^{-3} aqueous H_2SO_4 solution ($v = 50$ mV·s^{-1}, $E = 0.4$ V – 1.5 V *vs.* SSCE, 3 cycles).

Cyclic voltammograms of sample S1 recorded at a sweep rate of $v = 100$ mV s^{-1} in 0.5 mol·dm^{-3} H_2SO_4 solution in the potential range of $E = (-0.1 - 0.8)$ V *vs.* SSCE after preparation (**step 2**), after the deposition of poly(BPA) (**step 4**), and after overoxidation (recorded after the impedance measurements), respectively, are compared in **Figure 43**.

There are some differences between the CVs for Au | PEDOT | 0.5 mol·dm^{-3} H_2SO_4 (aq.) and for Au | PEDOT/poly(BPA) | 0.5 mol·dm^{-3} H_2SO_4 (aq.) electrodes (curves 1 and 2 in **Figure 43.**). Although the currents (redox capacities) are practically equal in the potential range of $E = (-0.1 - 0.1)$ V *vs.* SSCE, a slight decrease of the current was observed after the deposition of poly(BPA) probably due to a possible (mild) overoxidation of the PEDOT layer. On the other hand, in the voltammogram of the Au | PEDOT / poly(BPA) | 0.5 mol·dm^{-3} H_2SO_4 (aq.) electrode a clear oxidation/reduction peak pair can be observed at about 0.50 V (positive-going potential scan) and 0.33 V (negative-going potential scan), respectively (curve 2 in **Figure 43.**). This redox peak pair practically disappears during overoxidation of the poly(BPA)/PEDOT film (see curve 3 in **Figure 43.**).

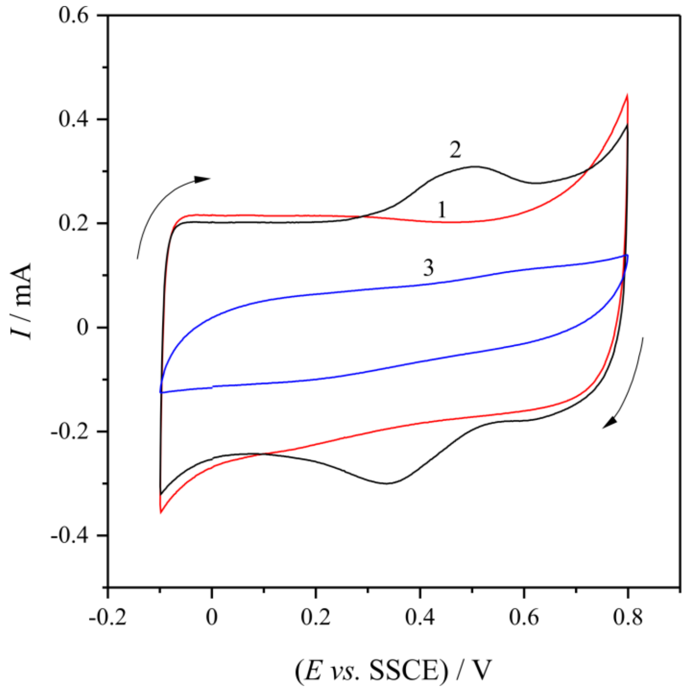

Figure 43. Cyclic voltammograms of sample S1 recorded in $c = 0.1$ mol·dm^{-3} aqueous H_2SO_4 solution at a sweep rate of $v = 100$ mV·s^{-1} in the potential range of $E = (-0.1 - 0.8)$ V *vs.* SSCE: (1) after the preparation of the PEDOT layer, (2) after the deposition of the poly(BPA) layer, (3) after the overoxidation of the PEDOT + PBPA layer and recording the impedance data (16 successive data sets). 2nd scans are shown.

In case of sample L1 ($A = 0.196\ \mathrm{cm}^2$, PEDOT layer deposition from $0.01\ \mathrm{mol{\cdot}dm^{-3}}$ EDOT / $0.1\ \mathrm{mol{\cdot}dm^{-3}}$ Na_2SO_4 solution, longer deposition time: $t = 3600\ \mathrm{s}$, current density: $j = 0.2\ \mathrm{mA{\cdot}cm^{-2}}$), the oxidation/reduction peak pair in the voltammogram of the Au | PEDOT/poly(BPA) | $0.5\ \mathrm{mol{\cdot}dm^{-3}}$ H_2SO_4 (aq.) electrode appears at about 0.5 V and 0.4 V *vs*. SSCE, respectively. However, the redox peak pair does not disappear completely during the overoxidation process, but the potential maximum of the reduction peak shifts in the negative direction to about 0.34 V *vs*. SSCE (see curves 2 and 3 in **Figure 44. a)**).

As it can be seen in **Figure 43.** and **Figure 44. a)**, after overoxidation of the poly(BPA)/PEDOT layer the redox capacities of the modified electrodes (i.e., the currents in the cyclic voltammograms) are always considerably smaller than those of the freshly prepared films. This observation is also true for the electrodes containing layers of "pure" PEDOT. Cyclic voltammograms of sample L2 recorded after deposition of the PEDOT film (**step 1**) and after overoxidation of the polymer (using cyclic voltammetry: 3 potential cycles in the potential range up to 1.5 V *vs*. SSCE) are presented in **Figure 44. b)**. By comparing **Figure 44. b)** curve 2 and **Figure 44. a)** curve 3 it can be clearly seen that at the same level of overoxidation the CV currents (i.e., the absolute values of the positive and negative currents) measured for the overoxidized PEDOT modified electrode are considerably lower than those measured in the case of overoxidized poly(BPA)/PEDOT.

One plausible reason for this can be identified by a simple visual inspection of the PEDOT and poly(BPA)/PEDOT layers after intensive overoxidation. The photographs in **Figure 45.** were taken after dipping samples L1 and L2 into ultrapure water multiple times. It can be well seen that a significant part of the overoxidized PEDOT layer has been detached from the gold substrate, while the overoxidized poly(BPA)/PEDOT layer has remained more or less intact.

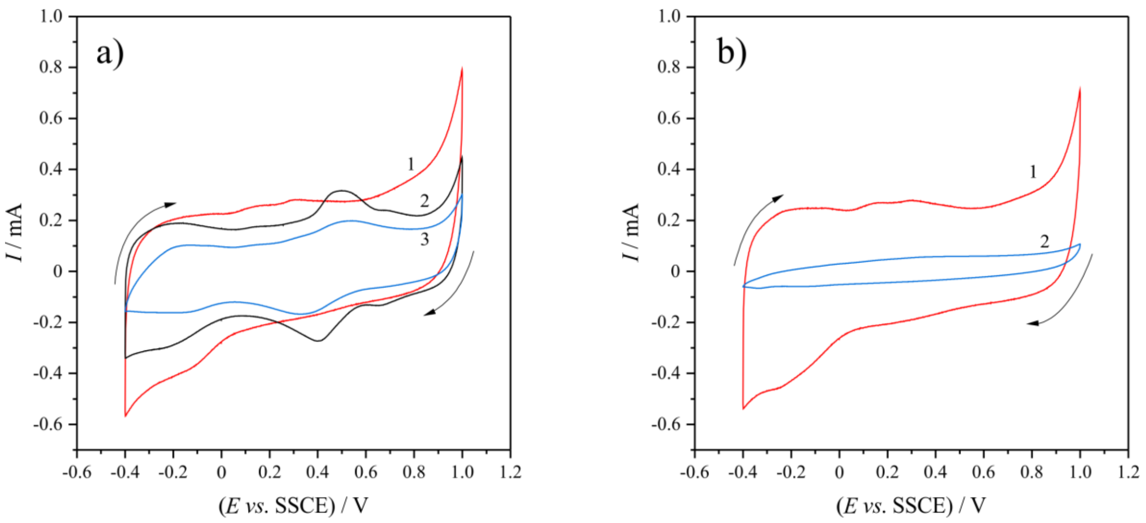

Figure 44. Cyclic voltammograms recorded in 0.5 mol·dm^{-3} aqueous H_2SO_4 solution at v = 50 mV·s^{-1} scan rate in the potential range of E = (−0.4 – 1.0) V *vs.* SSCE. **a)** sample L1 (1) after the preparation of the PEDOT layer, (2) after the deposition of the poly(BPA) layer, (3) after the overoxidation of the PEDOT + poly(BPA) layer. **b)** sample L2 (1) after the preparation of the PEDOT layer, (2) after the overoxidation of the PEDOT layer. (Preparation conditions of the samples: surface area of the gold substrate: A = 0.196 cm^2, PEDOT layer deposited from 0.01 mol·dm^{-3} EDOT / 0.1 mol·dm^{-3} Na_2SO_4 solution, deposition time: t = 3600 s, current density: j = 0.2 mA·cm^{-2}. Conditions of overoxidation: v = 50 mV·s^{-1}, E = 0.4 V – 1.5 V *vs.* SSCE, 3 cycles). 2nd scans are shown.

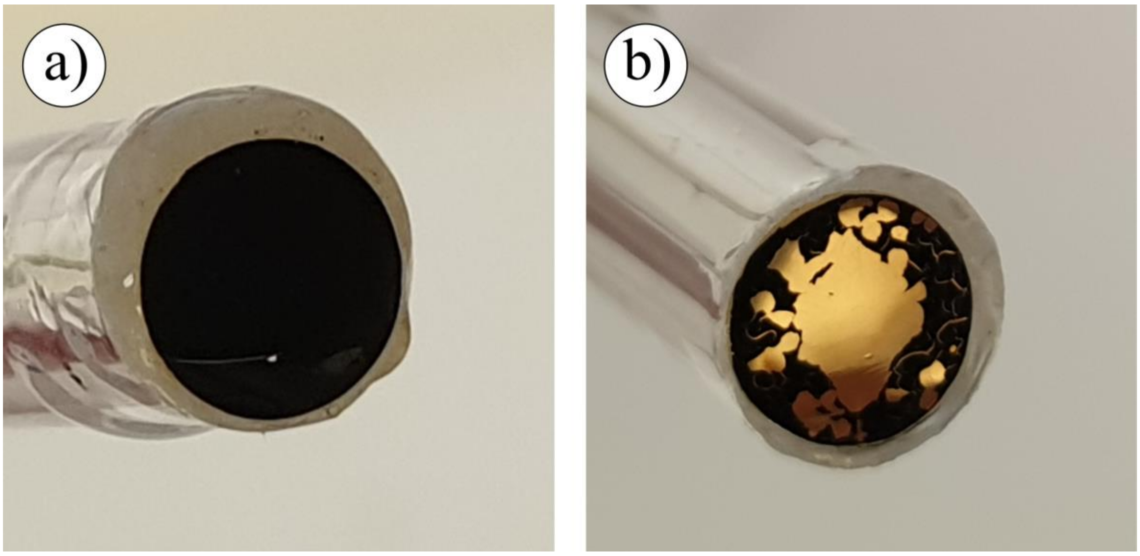

Figure 45. Photographs (taken with a Samsung Galaxy S9 phone) of **a)** the PEDOT + poly(BPA) layer (sample L1) and **b)** the "pure" PEDOT layer (sample L2) after (strong) overoxidation.

In order to justify the above observations, changes in the mechanical properties of the polymer layers due to overoxidation was investigated with bending beam technique. Cantilever electrodes covered by PEDOT/poly(BPA) and PEDOT films corresponding to those of samples S1 and S2 were used. The results of the stress change measurements in the potential range from (−0.1 – 0.8) V *vs.* SSCE show that in case of the Au | PEDOT/poly(BPA) | 0.1 mol·dm^{-3} H_2SO_4 electrode the difference between the minimum and maximum values of the change in the film stress ($\Delta\Delta g_f$) is about 3.2 MPa, while for the Au | PEDOT | 0.1 mol·dm^{-3} H_2SO_4 electrode the corresponding value is about 4.3 MPa. The observed difference can be at least partly attributed to the mild overoxidation of the PEDOT film during the deposition of poly(BPA). Both voltdeflectograms (the change of the curvature of the strip, $\Delta(R^{-1})$, with respect to the electrode potential, E) show pronounced hysteresis implying that stress changes in the polymer films may significantly contribute to the changes in R^{-1} (see **Figure 46. b)**, curves 1 and 2). The cyclic voltammogram recorded for the Au | PEDOT/poly(BPA) | 0.1 mol·dm^{-3} H_2SO_4 electrode after overoxidation (**Figure 46. a)**, curve 3) is similar to the CV of the Au | PEDOT | 0.1 mol·dm^{-3} H_2SO_4 electrode (**Figure 46. a)**, curve 4) in shape, but the charging currents are somewhat smaller in the latter case.

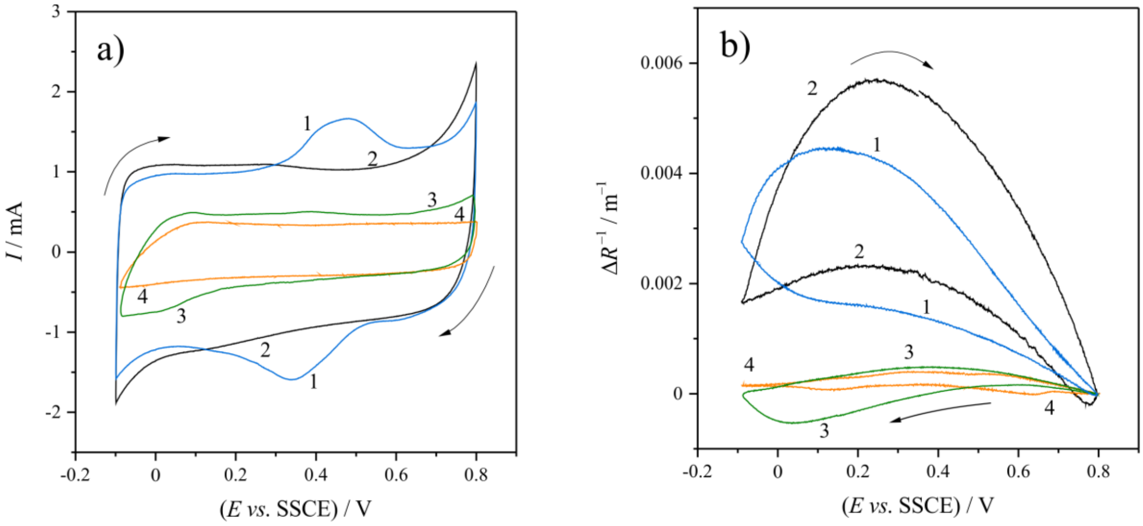

Figure 46. a) The cyclic voltammograms recorded simultaneously during the bending beam measurements (v = 50 mV·s^{-1}, E = (−0.1 – 0.8) V *vs.* SSCE). **b)** Changes of the reciprocal radius of curvature ($\Delta(R^{-1})$) with respect to the electrode potential (E) (“voltdeflectograms”) of Au | PEDOT/poly(BPA) | 0.1 mol·dm^{-3} H_2SO_4 (curves 1 and 3) and Au | PEDOT | 0.1 mol·dm^{-3} H_2SO_4 (curves 2 and 4) electrodes before (curves 1 and 2) and after overoxidation (curves 3 and 4). The $\Delta(R^{-1})$ values at E = 0.8 V *vs.* SSCE are arbitrarily set to 0 m^{-1}. (A = 2 cm^2, potential range of the potentiodynamic overoxidation: E = (−0.2 – 1.5) V *vs.* SSCE, v = 50 mV·s^{-1}, number of cycles: 3).

On the other hand, as it can be well seen in **Figure 46. b)** that the shapes of the $\Delta(R^{-1})$ *vs*. E curves change considerably as a result of overoxidation. After the application of 3 potential cycles up to 1.5 V *vs*. SSCE, in case of the Au | PEDOT/poly(BPA) | 0.1 mol·dm^{-3} H_2SO_4 electrode the difference between the minimum and maximum values of $\Delta(R^{-1})$ is about 0.0015 m^{-1} (**Figure 46. b)**, curve 3). This corresponds to $\Delta\Delta g_f \approx 1.1$ MPa, indicating some remaining electro-chemo-mechanical activity of the residual polymer layer. In contrary to this, in case of the Au | PEDOT | 0.1 mol·dm^{-3} H_2SO_4 electrode the difference is less than 0.0006 m^{-1} (curve 4 in **Figure 46. b)**) corresponding only to about 0.4 MPa. These results are in line with the (qualitative) finding that the poly(BPA) supported PEDOT film is mechanically more resistant to the effects of overoxidation than the “pure” PEDOT film.

It should be mentioned here, that the original bending beam theory treats the thin layer on the substrate as a uniform material. It is well known, however, that polymer films have complex internal structure. Although in some polymer/metal systems the polymer film completely blocks the metal surface, but this is not always the case. For example, if pores are present in the film, the electrolyte solution may contact the underlying metal layer at the bottom of the pores, and the change in the surface stress of the metal/solution interface with electrode potential occurs simultaneously with the change of the film stress. Both processes can result in a change in the radius of curvature (R) of the strip. The contributions from surface and bulk cannot be separated in the general case, and the exact values of the film stress changes remain uncertain. (Therefore, only the “voltdeflectograms”, i.e. the $\Delta(R^{-1})$ *vs*. E plots are shown in **Figure 46. b)**). Nevertheless, the results of the bending beam experiments can be used quite effectively to compare the electro-chemo-mechanical properties of similar systems.

VI.2.3. Impedance measurements

VI.2.3.a. Impedance of the modified electrodes before overoxidation

In **Figure 47.** results of impedance measurements in different representations are plotted (complex plane impedance plots, Bode plots, capacitance $C_p = (Y''/\omega)$ *vs*. log(frequency) plots, and complex plane admittance plots). The impedance spectra shown in **Figure 47.**

were recorded for the Au | PEDOT | 0.1 mol·dm^{-3} H_2SO_4 (aq.) and Au | PEDOT / poly(BPA) | 0.1 mol·dm^{-3} H_2SO_4 (aq.) electrodes (sample S1), i.e. before and after the deposition of poly(BPA), respectively, in the frequency range of 50 kHz – 96.1 mHz, at the electrode potential *E* = 0.4 V *vs.* SSCE. The excitation signal was 5 mV (rms).

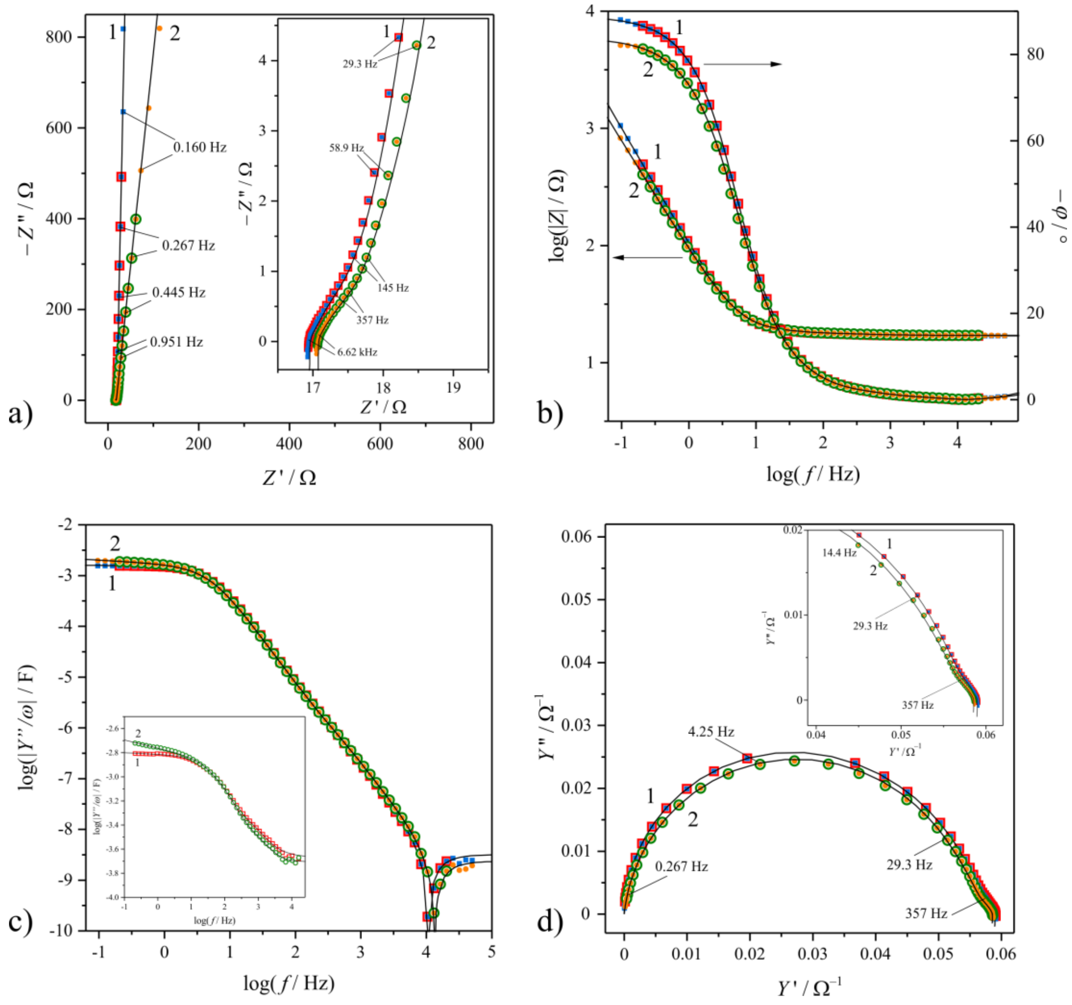

Figure 47. The results of the impedance measurements on the Au | PEDOT | 0.1 mol·dm^{-3} H_2SO_4 (aq.) (1) and Au | PEDOT / poly(BPA) | 0.1 mol·dm^{-3} H_2SO_4 (aq.) (2) electrodes in different representations (sample S1 before and after the deposition of poly(BPA)): **a)** Complex plane impedance plots, the high frequency regions are shown in the insert, small numbers in the plots refer to frequency values; **b)** Bode plots; **c)** Logarithm of the absolute value of the “parallel capacitance” of the electrode as a function of the logarithm of the frequency. The same data corrected by the estimated ohmic resistance (R_o) are shown in the insert, small numbers in the plots refer to frequency values; **d)** Complex admittance plane, the high frequency regions are shown in the insert. The impedances data were measured at the electrode potential of *E* = 0.4 V *vs*. SSCE, in the frequency range of 50 kHz – 96.1 mHz. The amplitude of the perturbing signal was 5 mV. The data points are indicated by “full” symbols, (1): ■ and (2): ●. The solid curves were calculated (simulated) by using the “best-fit” parameters given in **Table 5**. The impedance data in the 20.4 kHz – 207 mHz frequency range were fitted. The data points used in the CNLS fitting process are indicated by “empty” symbols, (1): □ and (2): ○.

As it can be seen in **Figure 47.** curve 1, the impedance response of the Au | PEDOT | 0.1 mol·dm^{-3} H_2SO_4 (aq.) electrode at medium and low frequencies is similar to that of a pure capacitor (near −90° phase angle). On the other hand, the Au | PEDOT / poly(BPA) | 0.1 mol·dm^{-3} H_2SO_4 (aq.) electrode shows at low frequencies a pattern characteristic for a constant phase element (CPE) with an exponent different from unity (**Figure 47.** curve 2). The impedance *vs*. angular frequency function of a CPE is given as

$$Z(\omega) = (\mathrm{i}\omega T)^{-\theta} = \frac{1}{T^{*}}(\mathrm{i}\omega)^{-\theta} \qquad \text{Eq. 26}$$

where $\theta \leq 1$, but in the above discussed case θ is usually close to 1. This behavior can be attributed e.g. to the presence of the poly(BPA) layer on the PEDOT film and/or to the mild overoxidation of the PEDOT film during the electrochemical deposition of poly(BPA). At higher frequencies an arc can be identified in both cases (see **Figure 47. a)**, insert).

VI.2.3.b. *Results of the parameter estimation for the modified electrodes before overoxidation*

Impedances measured in the frequency range of 20.4 kHz to 207 mHz were fitted using the Marquardt least squares algorithm [202–204]. Statistically, the fitting results were not satisfactory in all respects. While well-defined mean values of the parameter estimates ("best-fit" parameters) were could be obtained, several parameters are strongly correlated, and the method did not yield reliable confidence intervals for them. (The mean values of the parameter estimates for both the Au | PEDOT | 0.1 mol·dm^{-3} H_2SO_4 (aq.) and Au | PEDOT / poly(BPA) | 0.1 mol·dm^{-3} H_2SO_4 (aq.) electrodes are listed in **Table 5.**) On the other hand, despite the uncertainties of the parameter estimation, the visual inspection of the fitted curves and the original data presented in **Figure 47.** suggests that the model fits the observed data quite well. The curves calculated by using the best-fit parameters (represented by the solid lines in **Figure 47.**) fit the measured data reasonably well even outside the frequency range used for parameter estimation (from 50 kHz down to 96.1 mHz), asserting that the parameter estimation is robust in this regard. In addition, the values of all fitting parameters appear physically reasonable. (This points up the fallacy of evaluating the ‘goodness’ of a result in terms of statistical significance alone.)

In addition, the investigation of the deviation between the measured and the best fit simulated curves can provide information in respect of the nature (systematic or random) of the fitting errors. In the case of unweighted data, a “good” fit the deviations show a normal (Gaussian-like) distribution. In the case of weighted data, one can usually be satisfied if the deviations do not show a systematic trend. This can best be determined by plotting the real and imaginary components of the deviations against each other (“scatter plot”). Based on the visual inspection of the plots in **Figure 48.** we may arrive at the conclusion, that the results of the parameter estimation procedures are acceptable in both cases, although in **Figure 48. b)** some faint trend can be identified in the diagrams.

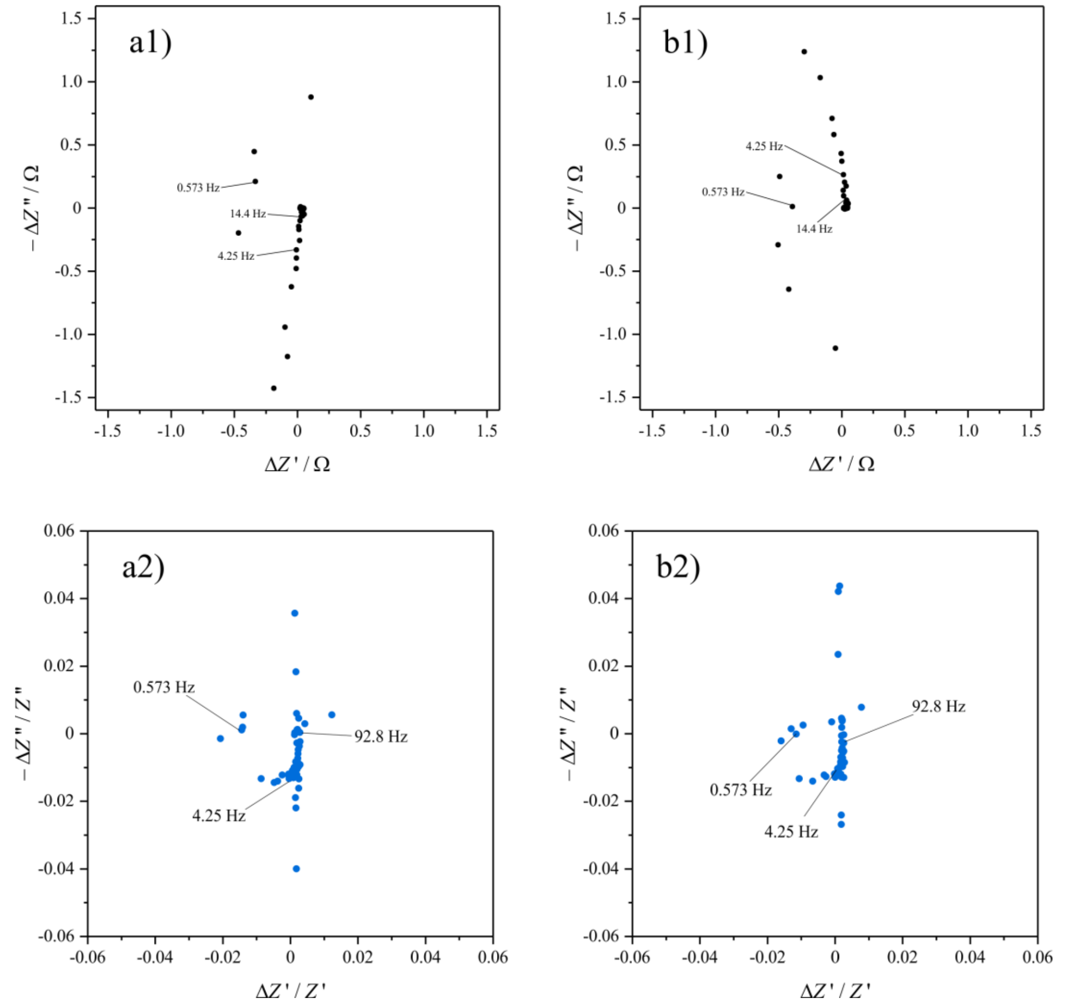

Figure 48. Absolute (**a1** and **b1**) and relative (**a2** and **b2**) deviations of the measured and the best fit data in the complex plane. (The measured and fitted data for sample S1 are presented in **Figure 47.**). **a1)** and **a2)** Au | PEDOT | 0.1 mol·dm^{-3} H_2SO_4 (aq.) electrode, **b1)** and **b2)** Au | PEDOT / poly(BPA) | 0.1 mol·dm^{-3} H_2SO_4 (aq.) electrode, respectively.

Table 5. Results of CNLS fitting of impedance data obtained for the Au | PEDOT | 0.1 mol·dm^{-3} H_2SO_4 (aq.) and Au | PEDOT / poly(BPA) | 0.1 mol·dm^{-3} H_2SO_4 (aq.) electrodes (sample S1) before overoxidation (estimated mean values and standard errors). The electrochemical impedance measurements were performed in the frequency range of 20.4 kHz to 207 mHz, amplitude of the perturbing signal: 5 mV rms, electrode potential $E = 0.4$ V *vs.* SSCE. L: inductance, R_o: uncompensated ohmic resistance (solution resistance), R_{ct}: the charge transfer resistance at the metal/polymer interface, B and b: parameters of the constant phase element (B can be regarded as the approximate value of the capacitance of the double layer region, P_1: parameter of the finite-length transport impedance, F_i: parameters corresponding to $L_i/(D^*)^{1/2}$ (L_i: layer thickness of region i, D^*: effective diffusion coefficient of the moving species), x_i: the fraction of the total electrode area covered by a polymer layer of thickness L_i.

	Au | PEDOT | 0.1 mol·dm^{-3} H_2SO_4 (aq.)		Au | PEDOT / poly(BPA) | 0.1 mol·dm^{-3} H_2SO_4 (aq.)	
degrees of freedom	37		37	
weighted sum of squares (Q)	$1.54020\cdot10^{-1}$		$1.36674\cdot10^{-1}$	
weighted standard error	$4.16271\cdot10^{-3}$		$3.69388\cdot10^{-3}$	
parameter	estimated value	standard error	estimated value	standard error
L / H	$9.567990\cdot10^{-7}$	$1.291090\cdot10^{-7}$	$8.521437\cdot10^{-7}$	$1.267654\cdot10^{-7}$
R_o / Ω	16.94284	$5.440365\cdot10^{-2}$	17.05140	$4.819549\cdot10^{-2}$
R_{ct} / Ω	$2.391469\cdot10^{-2}$	$(1.912878)^*$	$4.566461\cdot10^{-2}$	$(2.661143\cdot10^{-1})^*$
B / F·$\Omega^{1-1/b}$	$1.920205\cdot10^{-4}$	$(6.659594\cdot10^{-4})^*$	$1.691200\cdot10^{-4}$	$7.108548\cdot10^{-5}$
b	$9.366462\cdot10^{-1}$	$1.337212\cdot10^{-1}$	$8.217659\cdot10^{-1}$	$2.475208\cdot10^{-2}$
P_1 / Ω·s^{-1}	55.10507	7.604196	62.90910	9.372214
F_1 / s$^{1/2}$	$2.677074\cdot10^{-1}$	$1.697638\cdot10^{-1}$	$2.368964\cdot10^{-1}$	$9.222801\cdot10^{-2}$
F_2 / s$^{1/2}$	$1.421732\cdot10^{-1}$	$6.807794\cdot10^{-2}$	$5.695281\cdot10^{-2}$	$1.301238\cdot10^{-2}$
F_3 / s$^{1/2}$	$2.522524\cdot10^{-2}$	$(6.807794\cdot10^{-2})^*$	$2.437433\cdot10^{-2}$	$(3.847408\cdot10^{-2})^*$
F_4 / s$^{1/2}$	$6.231921\cdot10^{-2}$	$3.888597\cdot10^{-2}$	$1.299026\cdot10^{-1}$	$5.542458\cdot10^{-2}$
x_1	$1.980080\cdot10^{-2}$	$(4.479857\cdot10^{-2})^*$	$4.618395\cdot10^{-2}$	$(7.718645\cdot10^{-2})^*$
x_2	$1.533732\cdot10^{-1}$	$6.719340\cdot10^{-2}$	$6.748237\cdot10^{-1}$	$1.413855\cdot10^{-1}$
x_3	$2.677470\cdot10^{-1}$	$1.450069\cdot10^{-1}$	$1.026513\cdot10^{-1}$	$(1.867130\cdot10^{-1})^*$
$1-x_1-x_2-x_3$	$5.59079\cdot10^{-1}$	-	$1.7634105\cdot10^{-1}$	-

*: poorly determined

VI.2.3.c. Impedance of the Au | PEDOT / poly(BPA) | 0.1 mol·dm^{-3} H_2SO_4 (aq.) electrode after overoxidation

As described in the experimental section, subsequent impedance measurements were performed on the strongly overoxidized Au | PEDOT / poly(BPA) | 0.1 mol·dm^{-3} H_2SO_4 (aq.) electrode at the electrode potential of $E = 0.4$ V *vs*. SSCE in the a frequency range of 50 kHz – 96.1 mHz (see **step 6** in section VI.1.3). The impedance measurements started immediately after the last overoxidation cycle, and this time instant was chosen as the starting time of the impedance measurements (“timestamp”: $t = 0$ s). 16 successive impedance spectra were recorded. The recording time of a “single” spectrum was about 342 s. The complex plane diagrams in **Figure 49.** are similar to those reported for other polymer modified electrodes, including electrodes with overoxidized PEDOT films [13,15,82,83,192,193]. The impedance data show a capacitive arc in the high-frequency region and a capacitive domain at low frequencies. Only a narrow Warburg-like region (if any) can be observed between the high-frequency arc and the low frequency sloped line.

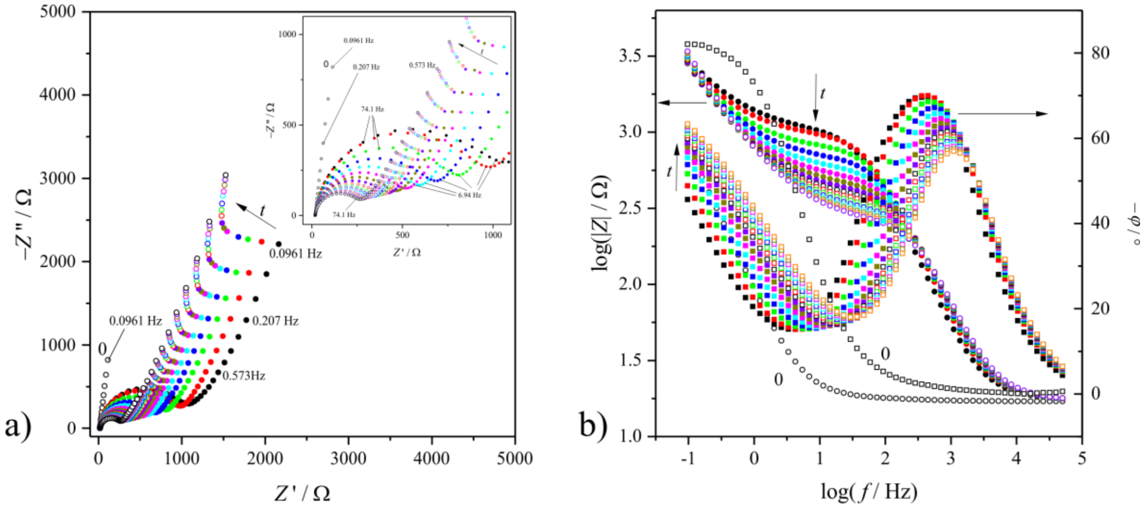

Figure 49. Impedance data sets recorded before (0) and subsequently after overoxidation (*t*) on the Au | PEDOT / poly(BPA) | 0.1 mol·dm^{-3} H_2SO_4 (aq.) at electrode potential $E = 0.4$ V *vs.* SSCE, and in the frequency range $f = 50$ kHz – 96.1 mHz. The start times of the recording of the successive impedance data sequences (“timestamps”) were as follows: #1: 0 s, #2: 341.569 s, #3: 683.452 s, #4: 1025.516 s, #5: 1371.936 s, #6: 1718.288 s, #7: 2064.538 s, #8: 2411.373 s, #9: 2754.216 s, #10: 3101.185 s, #11: 3448.118 s, #12: 3795.114 s, #13: 4142.181 s, #14: 4488.584 s, #15: 4839.730 s, #16: 5190.759 s. **a)** Complex impedance plane plots. The high frequency regions are shown in the insert. Small numbers in the plots refer to frequency values; **b)** Bode plots.

As it can be seen in **Figure 49**, the impedance data sets recorded successively after overoxidation of the poly(BPA) / PEDOT change continuously with time, it is evident that the system is in a transient state. In principle, in such cases corrections are necessary to obtain true impedance spectra suitable for parameter estimation based on model impedance functions. As discussed in Appendix A, the calculation of the "instantaneous impedances" was carried out using the real and imaginary parts of the impedances measured at identical frequencies („isofrequential components"). The diagrams in **Figure 50.** show selected sets of experimental data points measured during the frequency sweeps, each of which started at a given time t_i (see also **step 6** in section VI.1.3), together with the corresponding calculated impedance spectra. According to **Figure 50.** the differences between the measured and corrected/calculated impedance values are quite small at high frequencies but are more significant in the low-frequency range.

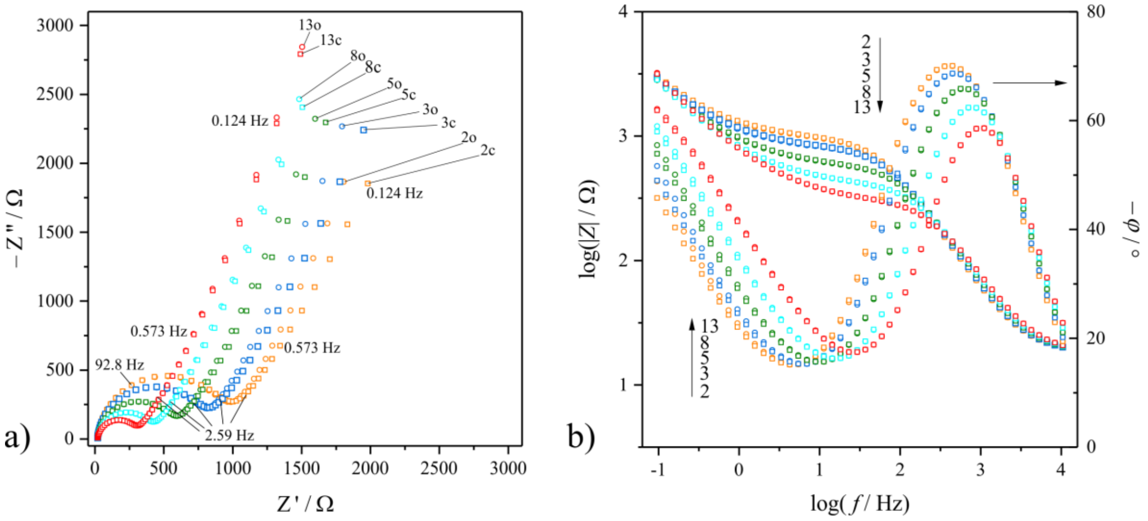

Figure 50. Comparison of directly measured ("original") impedance data sets (○: 2o, 3o, 5o, 8o, 13o) and calculated ("instantaneous") impedance spectra (□: 2c, 3c, 5c, 8c, 13c) recorded for the Au | PEDOT / poly(BPA) | 0.1 mol·dm^{-3} H_2SO_4 (aq.) electrode (sample S1) at the electrode potential E = 0.4 V *vs.* SSCE in the frequency range of f = 50 kHz – 96.1 mHz after the overoxidation of the film. **a)** Complex impedance plane plot. Small numbers in the plots refer to frequency values; **b)** Bode plots.

To investigate the implications of the FDA corrections on the values of the estimated parameters, parameter estimations were carried out using both the uncorrected and corrected impedance data sets. The impedance data measured in the frequency range from f = 96.1 mHz to f = 10.378 kHz were used for parameter estimation. The "direct" application of equation A(14) in a parameter estimation procedure encounters problems due to the high number of correlated variables. Nevertheless, equation A(14) can be simplified by omitting the iωL term, since it is expected that $L < 10^{-6}$ H (see **Table 5.**), and the contribution of the parasitic inductances to the total impedance is less than 0.07 Ω.

Models with many free parameters (like equation A(14)) can often have significant parameter degeneracies, making the correlation matrix obtained from the parameter estimation procedure a valuable tool for evaluating the specific model parameterization. Absolute values of correlation coefficients close to unity indicate significant degeneracies ($|c_{jk}| = 1$ can be interpreted as perfect synchrony) which can prevent the minimization algorithm from efficiently and accurately converging [205]. From the correlation matrices it can be concluded that there are strong correlations between the parameters $x_1 – x_3$ and $F_1 – F_4$. Therefore, knowing that in equation A(14) the parameters $x_1 – x_4$ represent the fractions of the total electrode area covered with layers of different thicknesses, we tried to estimate the empirical distribution of the x_i values (this clearly differs from that before overoxidation). Several attempts were made to find the best combination, the only (arbitrary) assumption was that the distribution is independent of time. The lowest values of the objective functions were attained by using the following values: $x_1 = x_3 = 0.25$, $x_2 = 0.30$. These results match quite well with those estimated by visual inspection of the SEM images taken on dry samples.

After the above simplifications (and by neglecting the contribution of the cracks and other uncovered segments of the substrate to the overall electrode impedance) the model function used for fitting can be written as:

$$Z(\omega) = R_\mathrm{o} + \frac{1}{(\mathrm{i}\omega B)^b + \sum_{\mathrm{i}=1}^{4} \hat{x}_\mathrm{i} \frac{1}{R_\mathrm{ct} + \frac{P_1}{s} coth[F_\mathrm{i} s]}} \qquad \text{Eq. 27}$$

where the $\hat{x}_\mathrm{i}$-s are fixed, and the adjustable parameters are: R_o, R_ct, B, b, P_1, F_1, F_2, F_3, and F_4. The results of the fitting (including mean values of the estimated parameters, standard deviations, and confidence intervals at the 95% confidence level) are summarized in **Table B1** in Appendix B. As it can be seen from **Table B1**, despite the still high number of the parameters, most of them could be determined with good statistics, and reasonable estimated mean values have been obtained for all of them. And this is, somewhat surprisingly, true for all data sets, including the directly measured impedances and the impedance spectra calculated by using the 4-dimensional analysis method [5,15,82,160,163,164]. In addition, as it can be seen in **Figure 51.** and **Figure 52**, the curves (impedance spectra) simulated by using the mean values of the estimated parameters closely fit the measured data, and this holds for both the complex plane impedance plots and the transformed data representations (Bode plots, complex plane admittance plot, C_p *vs*. log *f* plot).

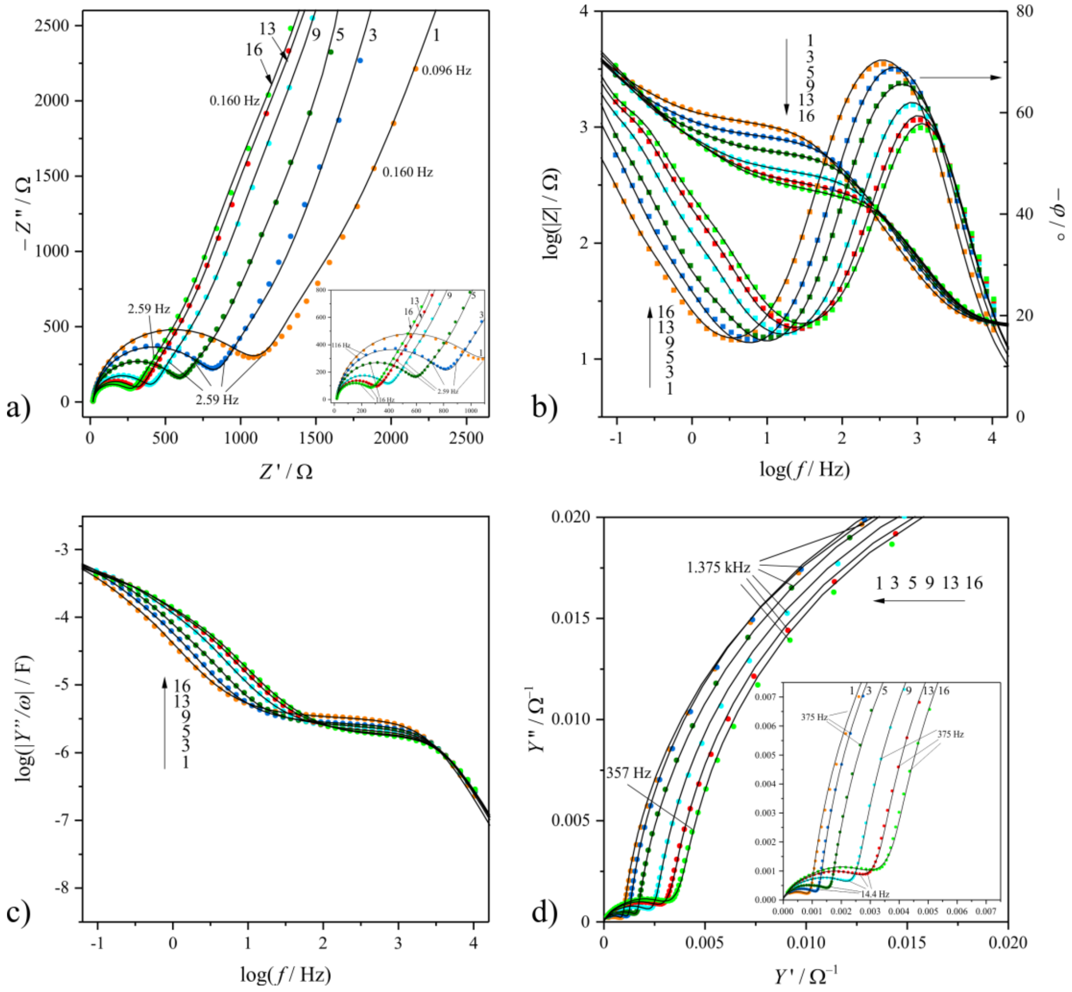

Figure 51. Selected directly measured ("original") impedance data sets (#1, #3, #5, #9, #13, #16) and the corresponding fitted curves (continuous lines) calculated using the best fit parameters (**Table B1. b)**). The experimental impedance data points are denoted by dots (●) (or squares (■) in the case of the phase angles in the Bode plot) of different colors. The impedance data sets were recorded for the Au | PEDOT / poly(BPA) | 0.1 mol·dm^{-3} H_2SO_4 (aq.) electrode (sample S1) successively after overoxidation in the frequency range of $f = 50$ kHz – 96.1 mHz at $E = 0.4$ V *vs*. SSCE. **a)** Complex plane impedance plots. The high frequency regions are shown in the insert, small numbers in the plots refer to frequency values; **b)** Bode plots; **c)** Logarithm of the "parallel capacitance" of the electrode as a function of the logarithm of the frequency; **d)** Complex admittance plane plots. The high frequency regions are shown in the insert, small numbers in the plots refer to frequency values.

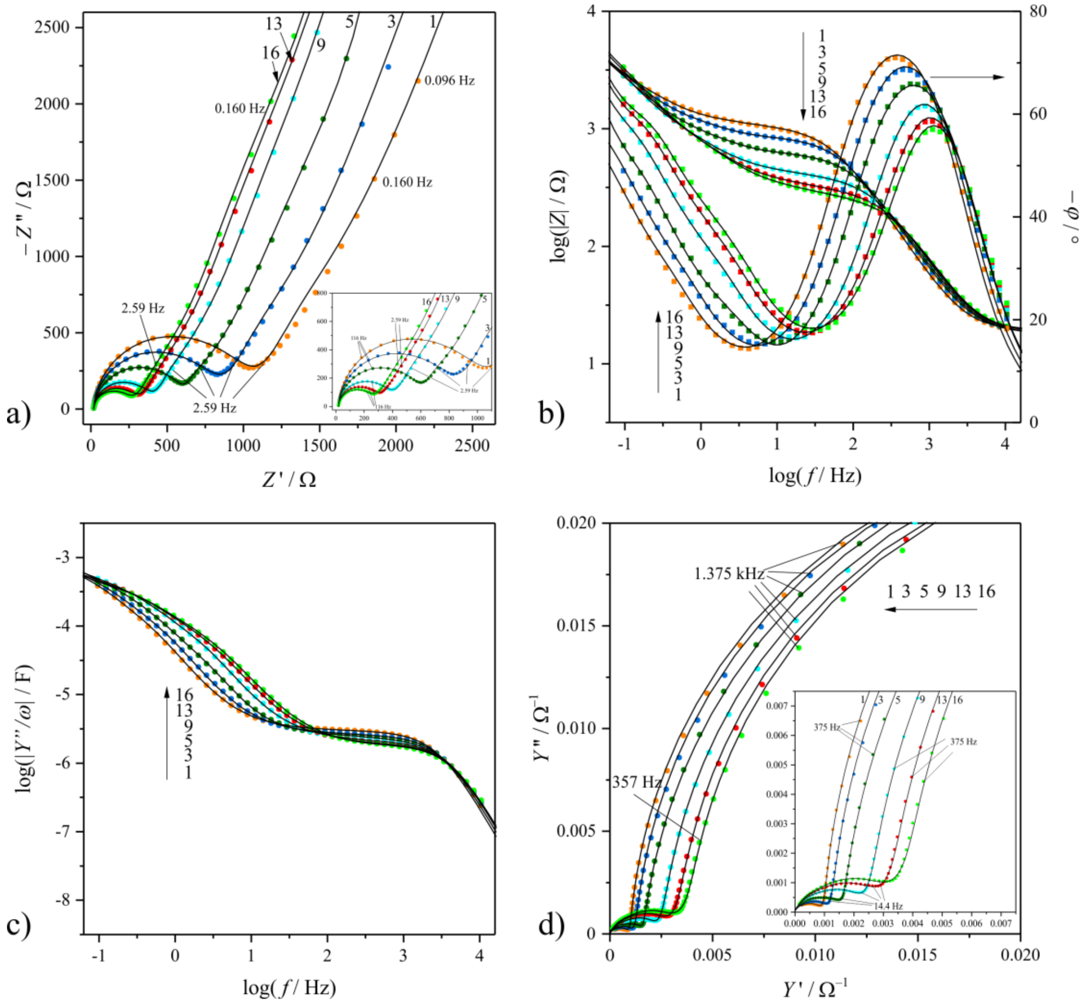

Figure 52. Instantaneous impedance spectra calculated from the directly measured data sets presented in **Figure 51.** (#1, #3, #5, #9, #13, #16) and the corresponding fitted curves (continuous lines) calculated using the best fit parameters (**Table B1. c)**). The experimental impedance data points are denoted by dots (●) (or squares (■) in the case of the phase angles in the Bode plot) of different colors. **a)** Complex plane impedance plots. The high frequency regions are shown in the insert, small numbers in the plots refer to frequency values; **b)** Bode plots; **c)** Logarithm of the “parallel capacitance” of the electrode as a function of the logarithm of the frequency; **d)** Complex admittance plane plots. The high frequency regions are shown in the insert, small numbers in the plots refer to frequency values.

Figure 53. shows the weighted sum of squares (i.e., the optimized values of the objective function denoted by Q) as a function of time. According to the results the optimum values of the objective functions obtained for the instantaneous impedance spectra and for the sets of measured impedance data differ quite markedly until about 1100 s after the end of the overoxidation process. From the statistical point of view, in this time interval the fit is better in case of the calculated (instantaneous) impedance spectra. After this period, the differences are no longer significant.

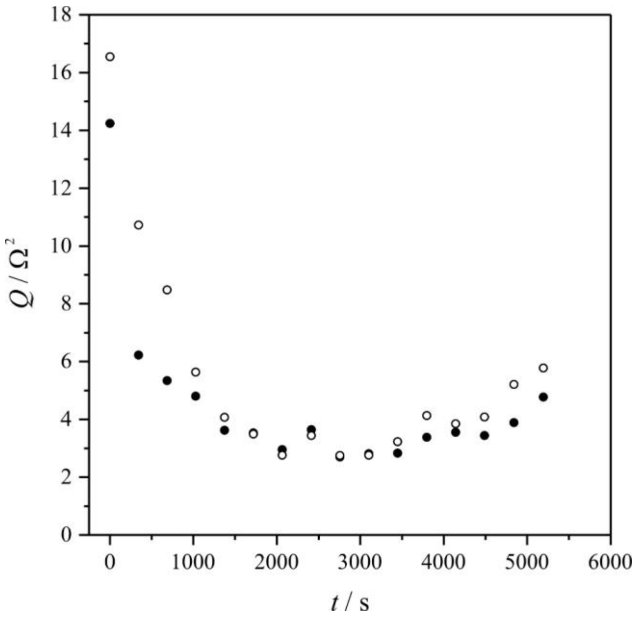

Figure 53. The optimized values of the objective functions (weighted sum of squares, Q) resulting from the parameter estimation procedures as a function of time (see **Table B1**). The Q values belonging to the directly measured ("original") impedance data sets recorded for the Au | PEDOT / poly(BPA) | 0.1 mol·dm^{-3} H_2SO_4 (aq.) electrode are denoted by (**○**), the Q values belonging to the instantaneous impedance spectra obtained using the 4-dimensional analysis method are denoted by (●).

Estimated (best fit) parameter values and uncertainties determined for the sequentially recorded impedance data sets (both for the experimentally obtained data and for the instantaneous impedance spectra) are presented in **Figure 54.** and **Table B1**. When comparing the corresponding fitting results for the corrected and uncorrected impedance data it can be seen that the estimates of the parameters R_o, R_{ct}, B, and b differ only slightly in the two cases (see **Figure 54. a)** and **b)**). This is also true for the other parameters, if $t > 2000$ s (**Figure 54. c)** and **d)**). The observed behavior can be well explained by the time evolution of the system, considering, that the values of the parameters R_o, R_{ct}, B, and b are mainly determined by the impedances measured at medium and high frequencies. As the system changes slowly enough, the values recorded at these frequencies are closer to the "true" impedance values corresponding to the stationary state, i.e., to the instantaneous impedance spectra, simply because the time required to determine the impedance data points is sufficiently short. Since the rate of change continuously slows down as time progresses, the differences between the measured and calculated ("instantaneous") impedance values become more and more negligible over time.

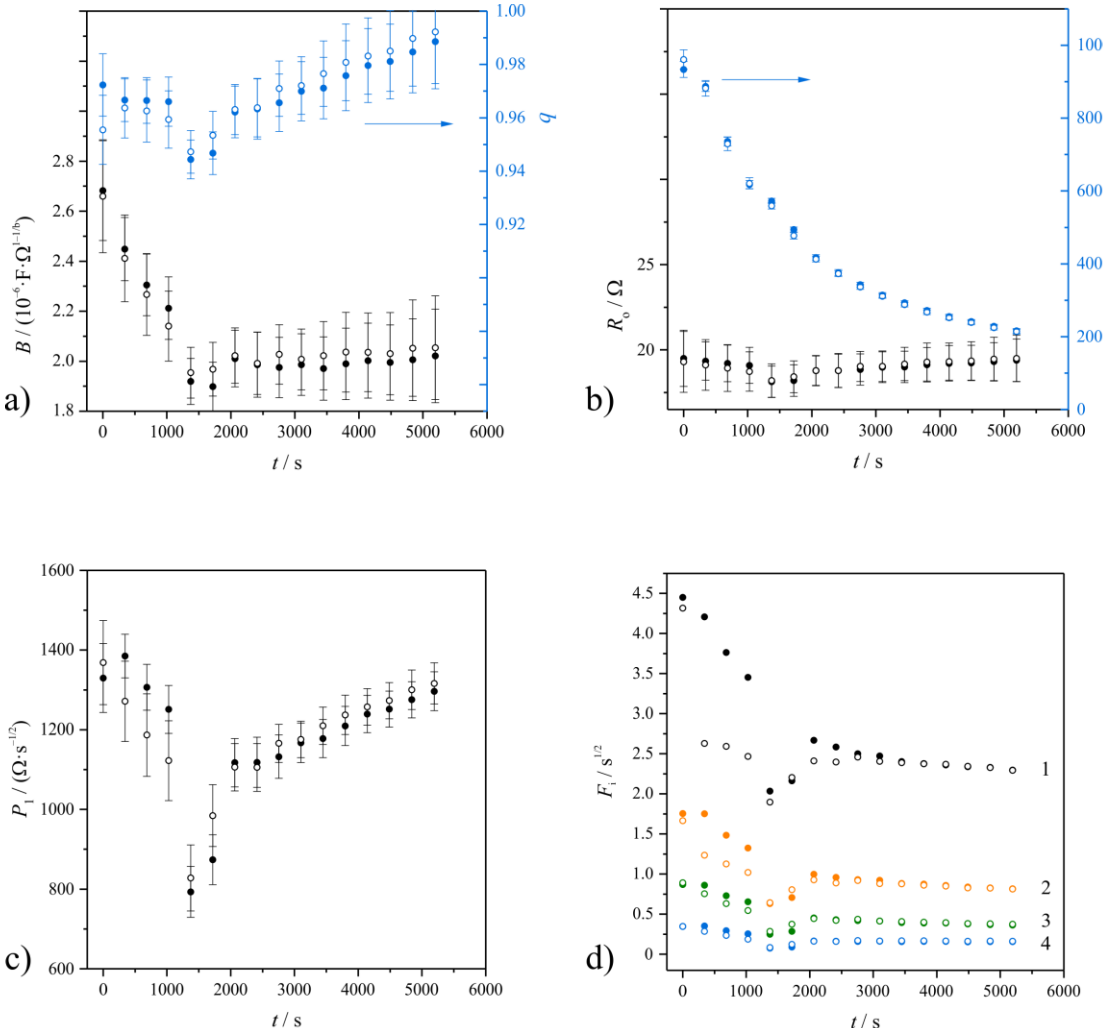

Figure 54. The estimated (best fit) parameter values as a function of time (t). **a)** the B parameter values of the CPE in Eq. 27 and the corresponding CPE exponents. Since the CPE exponents (b) are close to unity, B can be regarded as the approximate value of the capacitance of the double layer region at the gold/polymer film interface; **b)** The ohmic resistance (R_o) and charge transfer resistance (R_{ct}); **c)** The parameter of the finite-length transport impedance P_1; **d)** The F parameters (F_1, F_2, F_3, and F_4). The parameter values resulting from the fitting of the directly measured (“original”) impedance data sets recorded for the Au | PEDOT / poly(BPA) | 0.1 mol·dm^{-3} H_2SO_4 (aq.) electrode are denoted by (**○**), the values obtained from the fitting of the instantaneous impedance spectra are denoted by (●). The vertical segments (bars) in **a)**, **b)** and **c)** indicate the confidence intervals at 95% confidence levels. The confidence intervals for the F parameters are given in **Table B1. a)** and **b)**.

By analyzing the time evolution of the parameters in detail (see **Figure 54. a)-d)**), it can be seen that, as expected, the uncompensated ohmic resistance (R_o) remains practically constant during the experiment. The charge transfer resistance (R_{ct}) corresponding to the time instant just after overoxidation of the film is about 900 Ω. Starting from this value, R_{ct} decreases continuously with experiment time to a terminal value of about 200 Ω. Since the value of the CPE exponent (b) varies between 0.94 and 0.99, the B parameter of the

CPE can be regarded as the approximate value of the capacitance of the double layer region at the gold / polymer film interface, which initially decreases with time, and then approaches a limiting value. It should be stressed here that B represents not only the capacitance of the double layer at the substrate / film interface itself but also the capacitance associated with the polymer chains close to the interface [206,207]. As it can be seen from the above results, the direction, dynamics, and nature of the time evolution of R_{ct} and B are consistent with the mechanistic picture suggested in refs. [15,83], according to which during overoxidation a significant fraction of the polymer chains become detached from the substrate surface, while at electrode potentials more negative than those at which overoxidation takes place the readsorption of the polymer chains (polymer chain ends) becomes possible. This can also be formulated as follows: the “effective” coverage of the substrate by the polymer decreases during overoxidation, and the coverage starts to increase again when the potential is held in an appropriate potential range. Obviously, the first process leads to an increase, and the second to a decrease of the charge transfer resistance. The other parameters, namely P_1, F_1, F_2, F_3, and F_4, depend mainly on the characteristics of the “bulk” of the polymer layer, especially on its morphology and transport properties. However, the time evolution of the best fit parameter estimates is shown in **Figure 54. c)** and **d)**, contrary to what was expected on the basis of the above simple delamination/readsorption model [15,82,83], these parameters do not change monotonically over time, and sudden changes in the parameter values is observed at $t = 1371$ s. This suggests that something happened around this time inside the polymer layer, most likely structural changes of the polymer chains or formation of cracks due to the evolution of internal stress. In contrast, it is highly unlikely that the (sudden) decrease of the parameter values is caused by an increase in the value of the effective diffusion coefficient (D^*). (Formally, the observed changes in the values of the P_1 and F_i parameters could also be explained by the increase of D^* since they are inversely proportional to the square route of D^*.) Instead, the observed behavior may somehow be related to changes in the conjugation length of the PEDOT backbone.

VI.3. **Concluding remarks**

One of the most important results of the work described in this chapter is that the electrochemical deposition of poly(BPA) on the PEDOT layer in a PEDOT modified gold electrode results in an improved stability of the system against the adverse effects of overoxidation. It is well known that overoxidation of polymer films in polymer modified electrodes is very often accompanied by delamination at the film/substrate interface making the unit unusable. For instance, the observed results indicate a significant improvement of the mechanical stability of the polymer structures, resulting in a more adherent layer and reduced degradation. Another important feature is that both polymers can be deposited electrochemically. The above findings suggest that poly(BPA)-like polymers can be effectively used to enhance the electrochemical/mechanical properties of conductive polymer fibers, microwires and bundles as well, and therefore the combination of poly(BPA) and PEDOT (or more generally the combination of electrochemically deposited conducting and non-conducting polymers) offer some potential e.g. for biomedical applications.

VII. Magneto-controlled enzyme activity with locally produced pH changes

In this chapter, an example of practical application of non-conducting polymers is shown. Magnetic nanoparticles (MNPs), namely silica core-shell iron oxide particles with grafted PAA-b-PPEGMA copolymer were modified with different enzymes and the enzyme activity was controlled by locally produced pH changes.

Adaptivity and regulation based on sophisticated multi-level regulatory mechanisms is the major feature of biological living systems [208–210]. Mimicking this feature, obviously at a much simpler level, is a desirable goal in many artificial systems [211] in biotechnological and biomedical applications. Particularly, switching and tuning of enzyme activity, targeting selected enzymes participating in different biocatalytic reactions, is important for regulation and optimization of biocatalytic networks for in vitro applications [212,213]. Direct transfer of biological regulatory mechanisms to artificial systems is impractical or even impossible due to the complexity of biological mechanisms, thus, novel approaches and artificial mechanisms should be considered. Various methods for dynamic and reversible regulation of enzyme biocatalytic activity by different chemical and physical external stimuli have been studied recently [214], including use of natural allosteric [215] or artificial chimeric enzymes with fused affinity units [216–218], incorporation of photoisomerizable chromophores into protein backbones [219,220], use of nanoparticles resulting in a thermal effect on the enzyme activity originating from absorbing light or electromagnetic irradiation [221], etc. Another approach based on incorporation of enzymes into signal-controlled polymeric matrices with porosity, permeability, electrical charge variability controlled by external stimuli, for example, pH or temperature changes, have been studied extensively [222–224]. While some of the methods used for regulation of the enzyme activity require direct physical contact, e.g., immobilization of enzymes at various interfaces or electrodes, and other techniques depend on optical transparency of the medium, the use of magnetic field as a stimulus controlling the enzyme activity is particularly attracting due to its effect at a distance, thus allowing the regulatory function under conditions when the direct contact is not possible and light irradiation is problematic, for example, in a biological tissue for medical applications. Association of enzymes with magnetic nanoparticles allows their translocation [225] and aggregation [226] stimulated by an external magnetic field. This has been already used for magneto-stimulated reactions between enzymes and substrates bound to magnetic nanoparticles [227] and for reversible switching between bulk-diffusion and substrate-tunneling mechanisms of enzymatic reactions affecting their rates [226]. For many enzymes their catalytic functions are pH-dependent [228], thus allowing their regulation by local pH change produced electrochemically at electrode surfaces [229] affecting the activity of enzymes immobilized at the interface [230]. While this method reported recently is very powerful, it requires the use of electrodes wired to electronics, thus limiting its application to biotechnological systems where electrodes are allowed, for example, in some implantable [231] or wearable [232] bioelectronic devices. In many biomedical applications the presence of electrodes is not possible and a different approach is needed.

VII.1. Experimental

VII.1.1. Chemicals and reagents

Amyloglucosidase from *Aspergillus niger* (AMG; EC 3.2.1.3), urease from *Canavalia ensiformis*, Jack bean, (Ur; EC 3.5.1.5), esterase from *porcine liver* (Est; EC 3.1.1.1), glucose oxidase from *Aspergillus niger* (GOx; EC 1.1.3.4), peroxidase from horseradish (HRP; EC 1.11.1.7), D(+)-maltose monohydrate, urea, ethyl acetate, 2,2'-azino-*bis*(3-ethylbenzthiazoline-6-sulphonic acid) (ABTS), 1-ethyl-3-(3-dimethylaminopropyl)carbodiimide (EDC), *N*-hydroxysuccinimide (NHS), 2-(*N*-morpholino)ethanesulfonic acid (MES-buffer), 4-(2-hydroxyethyl)-1-piperazineethanesulfonic acid (HEPES-buffer), and other standard organic and inorganic chemicals, reactants and materials were purchased from MilliporeSigma (formerly Sigma Aldrich). Chemicals listed above were used as supplied without further purification. All experiments were carried out in ultrapure water (18.2 MΩ·cm; Barnstead NANOpure Diamond).

The magnetic nanoparticles (MNPs) in this work include an iron oxide superparamagnetic core (approximately 28 nanometer diameter) encased in a silica oxide shell (approximately 30 nanometer layer thickness) and then modified with a grafted polymeric brush of a block copolymer composed of poly(acrylic acid) and poly(ethylene glycol) methyl ether acrylate (PAA-*b*-PPEGMA) (approximately 108 nanometer layer thickness). Preparation and full characterization of surface modified magnetic nanoparticles (MNPs) were reported in [227].

VII.1.2. Characterization of surface modified magnetic nanoparticles (MNPs)

Malvern Zetasizer Nano instrument was used for dynamic light scattering (DLS) and zeta-potential measurements. MNPs were easily dispersed in water and formed stable colloidal status with an average size of 300 nm and zeta potential (ζ) = −30 mV at pH = 7.4, characterized by dynamic light scattering (DLS).

Preventing aggregation of the magnetic nanoparticles in the absence of a magnetic field was an extremely important issue in this project. The polymer brush bound to the solid core is ended with polyacrylic acid, which provides negative charges at the polymer shell. The negatively charged nanoparticles are electrostatically repulsed from each other, thus preventing their aggregation in the absence of the external magnetic field. Importantly, when the particles are magnetized in the presence of the magnetic field, the magnetic attraction overcomes the electrostatic repulsion, thus resulting in the nanoparticles aggregation. The repulsion (electrostatic) and attraction (magnetic) forces should be optimized to prevent the nanoparticle aggregation in the absence of the magnetic field and allow their aggregation in the presence of the magnetic field. This optimization was performed experimentally.

VII.1.3. Covalent functionalization of the MNPs with enzymes (AMG, Ur, Est)

A suspension of the MNPs (1 mg/mL) in MES-buffer (50 $\mathrm{mmol \cdot dm^{-3}}$, pH = 7.4) was reacted with 20 $\mathrm{mmol \cdot dm^{-3}}$ EDC and 50 $\mathrm{mmol \cdot dm^{-3}}$ NHS for 25 min at ambient temperature (24 ± 2 °C). Then, the MNPs were collected by sedimentation with a magnet and the previous reaction solution was replaced with a MES-buffer (50 mmol·dm^{-3}, pH = 7.4) containing an enzyme (note that different enzymes were used in preparation of different kinds of the modified MNPs): AMG (2 kU/mL) or urease (1 kU/mL) or esterase (1 kU/mL). The reacting suspension was placed in a shaker for overnight at room temperature. After that, the enzyme functionalized MNPs were collected by sedimentation with a magnet, then rinsed three times and re-suspended in 1 mL HEPES-buffer (50 mmol·dm^{-3}, pH = 7). The enzyme assay performed before and after the enzyme immobilization demonstrated small decrease of the enzyme activity after the immobilization (ca. 80 % retained activity of the immobilized enzymes). Since the assay of the immobilized enzymes was only possible as the rough estimation, one can conclude that the enzyme activity was almost unaffected by the immobilization procedure. The activity of the enzymes per single magnetic nanoparticle was estimated as: ca. $1.8 \cdot 10^{-15}$ U (AMG), ca. $1.7 \cdot 10^{-15}$ U (urease), ca. $1.0 \cdot 10^{-15}$ (esterase). The total amounts of the immobilized enzymes included in the reacting system was approximately 15 mU/mL (AMG), 11 mU/mL (urease) or 18 mU/mL (esterase); optimized experimentally.

VII.1.4. Activation and inhibition of AMG bound to the MNPs with urease-functionalized MNPs

The reaction was performed in 1 mL 20 mmol·dm^{-3} maltose solution in a HEPES-buffer, pH = 6.0, using three different buffer concentrations: 1 mmol·dm^{-3}, 50 mmol·dm^{-3} and 1000 mmol·dm^{-3}. The solution also included 2.5 mmol·dm^{-3} urea, ca. 0.08 mg AMG-functionalized MNPs and ca. 0.08 mg urease-functionalized MNPs. The reaction was performed in the absence or presence of a magnet (OFF or ON magnetic field state, respectively). Two magnets (NdFeB, grade N42, plating/coating: Ni-Cu-Ni, dimensions: 1.27 cm × 0.635 cm × 0.318 cm, B842 from K&J Magnetics, Inc.) were placed below the reaction tube to create a nearly uniform (homogeneous) magnetic field in the liquid system with the intensity of 0.4 T measured at the bottom of the reaction tube. The magnetic field was measured with Bell-5180 Gauss/Tesla meter (OECO LLC, Milwaukie, OR, US) with a detachable axial probe that was placed in the immediate proximity of the reaction tube. In the OFF state (absence of the magnet) the MNPs were dispersed in the solution by vigorous mixing. In this state the AMG catalytic activity was high at the bulk pH = 6.0, thus, the reaction resulted in the formation of glucose upon

AMG-catalyzed hydrolysis of maltose. In the ON state (presence of the magnet) the MNPs were aggregated and local pH increased up to ca. pH = 9 inhibiting the AMG catalytic activity. The local pH value was roughly estimated near the aggregated MNPs using pH-sensitive paper-indicator (GE Whatman 10360005, Sigma Aldrich). For this measurements aliquot samples were collected near the magnetic cluster and then applied on the pH-indicator paper. The analysis of the AMG activity was performed in aliquots taken from the main reacting solution containing the enzymemodified magnetic nanoparticles. The aliquots were analyzed in a separate solution. The glucose formation was analyzed using standard assay solution composed of GOx (300 U/mL), HRP (300 U/mL) and ABTS (25 mmol·dm^{-3}) in HEPES-buffer (10 mmol·dm^{-3}, pH = 7.0). The kinetics of ABTS oxidation was measured at λ = 420 nm using VARIAN CARY Eclipse UV-visible spectrophotometer and used to characterize indirectly the AMG activity. The ON-OFF magnetic field states were repeated several times to analyze reversible dynamic switch of the AMG activity. The minor absorbance increase (related to a minor AMG activity) in the presence of the magnetic field (**Figure 59.**) originated from the incomplete (but still significant) inhibition of the AMG enzyme. It is not always possible to achieve the complete switch off the enzyme activity - some minor activity might be still present. The present project was not aimed at the total (complete) inhibition of the enzyme, but rather at the demonstration that the enzyme activity can be significantly changed due to local pH changes triggered by the magnetic signal. It should be noted that many different chemical inhibitors for various enzymes do not completely switch off the enzyme activity. Partial inhibition of enzymes is a common situation. In this specific case the complete inhibition might be achieved upon bigger pH changes (reaching more basic pH values). However, this extreme pH change may result in the irreversible loss of the enzyme activity, which will not allow reversible inhibition/activation of the biocatalytic reaction. It should be noted, that if the pH-changing enzymatic reaction runs long enough, it can overcome the buffer capacitance, thus resulting in the bulk pH changes. In this case the effect of the pH change on the AMG activity will be irreversible. In order to prevent this unwanted bulk pH change the concentration of the substrate (urea for urease or ester for esterase) should be limited. This concentration should be below the limit set by the buffer capacitance, thus the optimized substrate concentration depends on the buffer concentration. During this project, the substrate concentration and the time of the reaction were optimized experimentally. It should be noted that the decrease of the activity of urease and esterase could limit the pH changes generated by them. Eventually, this might be even better for our system preventing formation of extreme pH values, which can lead to the AMG irreversible inactivation. We didn't study the pH dependence of the urease and esterase activity – this was outside the scope of this preliminary project. However, the literature suggests [233,234] that their pH dependence in the studied range of pH values is not high and may be neglected. In a control experiment magnetic nanoparticles functionalized with AMG were used in the absence of the magnetic nanoparticles modified with esterase or urease. The aggregation and dispersion of the AMG-particles in the presence or absence of the magnetic field did not change the AMG activity (**Figure 55.**).

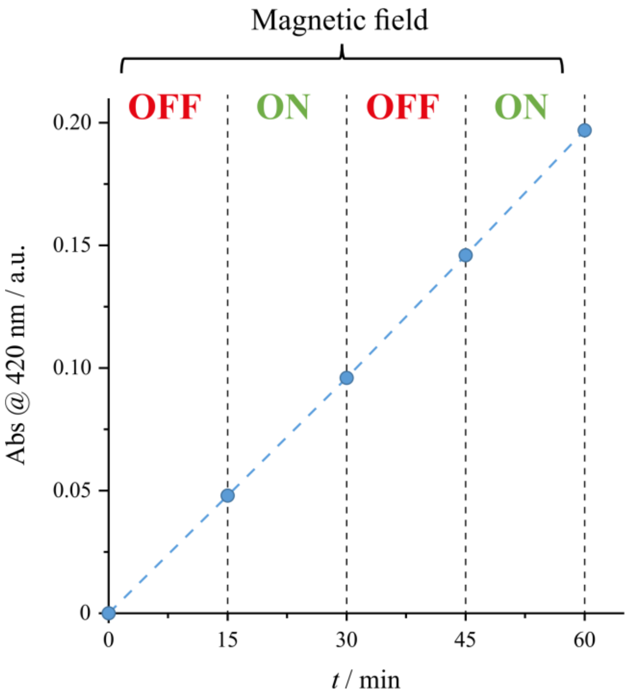

Figure 55. Absorbance changes corresponding to the AMG activity in the absence (OFF) and presence (ON) of the external magnetic field applied on the suspension of the AMG-functionalized magnetic nanoparticles. In this control experiments the magnetic nanoparticles functionalized with esterase or urease were not added to the system.

VII.1.5. Activation and inhibition of AMG bound to the MNPs with esterase-functionalized MNPs

The reaction was performed in the same way as described above for the urease-functionalized MNPs with the following difference: the bulk pH value of the reacting solution was 9.0; the esterase-functionalized MNPs (ca. 0.08 mg) were used in combination with the AMG-modified MNPs (ca. 0.24 mg); the reaction solution included ethyl acetate (0.25 mmol·dm^{-3}) instead of urea.

VII.1.6. Characterization of MNPs aggregation by optical microscopy and fluorescent confocal microscopy

Optical microscope (Nikon) was used to visualize aggregation of the MNPs in the presence of a magnetic field and the formation of pH gradient around the aggregated MNPs. The formation of the pH gradient was investigated with a confocal microscope (Leica Confocal Microscope LM6, Leica Microsystems, Buffalo Grove, IL, USA) in presence of 3,4’-dihydroxy-3’,5’-*bis*-(dimethylaminomethyl)flavone (FAM345) [235], the dye with pH-dependent fluorescence [236].

VII.2. Results and discussion

In order to realize dynamic control of the enzyme activity, two kinds of enzyme-modified magnetic nanoparticles (MNPs) were used. (MNPs means here the iron oxide (Fe_3O_4) superparamagnetic core (ca. 28 nm diameter) encased in a SiO_2-shell (ca. 30 nm layer) and then modified with a grafted polymeric brush of a block-copolymer PAA-*b*-PEGMA composed of poly(acrylic acid) (PAA) and poly(ethylene glycol) methyl ether acrylate (PEGMA) (ca. 108 nm layer) [227]. The polymer brush served as an organic support for the enzyme immobilization and also prevented nanoparticle aggregation in the absence of magnetic field. The MNPs were aggregated or dispersed in the presence or absence of the external magnetic field, respectively, **Figure 56**.

One kind of MNPs was covalently modified with amyloglucosidase (AMG; EC 3.2.1.3). This enzyme was selected as a convenient model with the biocatalytic activity controlled by a pH value [230,237]. Indeed, the biocatalytic activity of AMG decreases dramatically with the pH increase, **Figure 57. c)**. The second kind of MNPs was modified either with urease (Ur; EC 3.5.1.5) or with esterase (Est; EC 3.1.1.1) because these enzymes catalyze reactions resulting in an increase or decrease of the pH value, respectively. It should be noted that Ur and Est have been already used to control pH values in solutions [238] or at interfaces [239] for various bioelectronic applications with signal-switchable features.

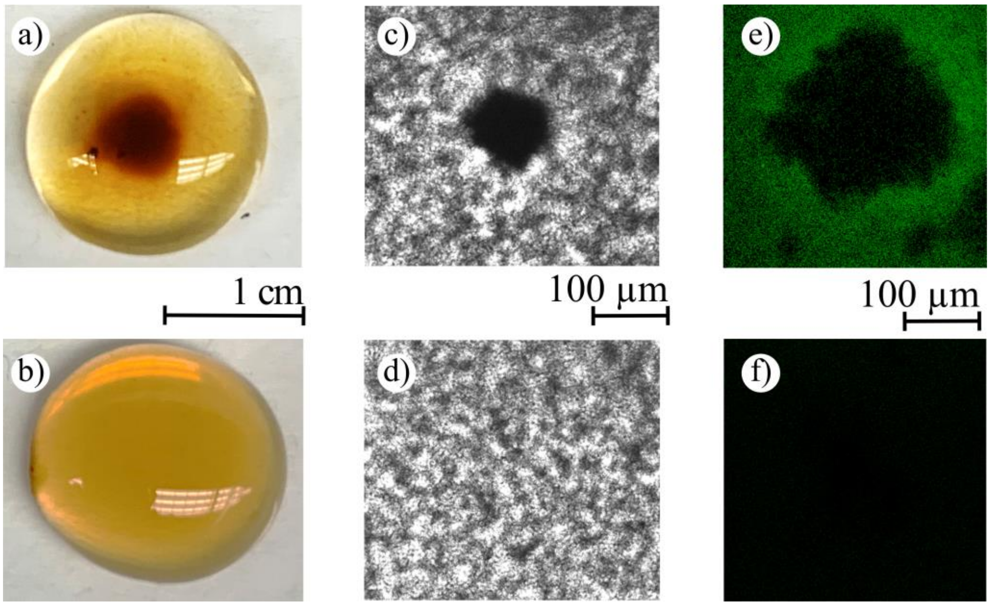

Figure 56. (**a)**, **b)**) Photos showing aggregated (**a)**) and dispersed (**b)**) states of the urease-functionalized MNPs in the presence and absence of the magnetic field, respectively. The MNPs were in an aqueous droplet (50 mmol·dm^{-3} HEPES-buffer, pH = 6.0) containing 20 mmol·dm^{-3} urea and 1 µmol·dm^{-3} FAM345 (the dye with pH-dependent fluorescence). (**c)**, **d)**) The same system visualized with an optical microscope at the microscale. Image **c)** shows the aggregated microcluster composed of the aggregated MNPs in the presence of the magnetic field. Image **d)** corresponds to the dispersed state of the MNPs in the absence of the magnetic field. (**e)**, **f)**) Images obtained with a confocal microscope. Image **e)** shows green fluorescence of the FAM345 dye characteristic of basic pH produced biocatalytically by aggregated MNPs in the presence of the magnetic field. Image **f)** does not show any green fluorescence in the dispersed state of the MNPs in the absence of the magnetic field, corresponding to the initial bulk pH = 6.0.

Application of an external magnetic field resulted in magnetization of the MNPs and their aggregation, **Figure 56. a), c)**, while they are dispersed in the absence of the magnetic field, **Figure 56. b), d)**. Local pH change produced by enzyme reactions with aggregated MNPs was visualized using a dye with pH-dependent fluorescence, **Figure 56. e), f)**. **Figure 57.** and **Figure 58.** explain the concept of the magneto-controlled enzyme activity. When an external magnetic field is not applied and the MNPs are dispersed the biocatalytic activity of AMG is controlled by a bulk solution pH value.

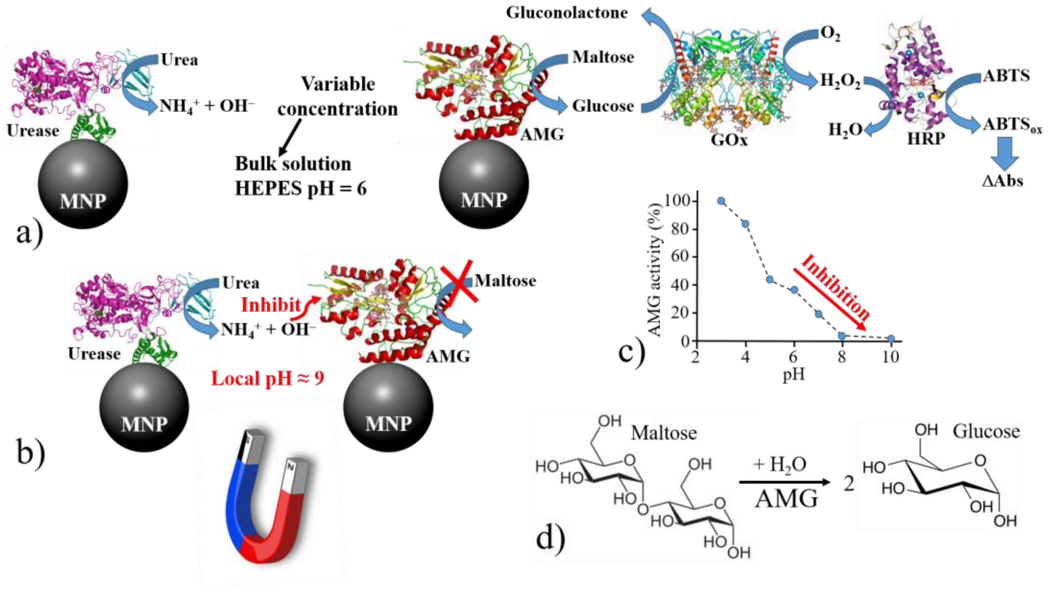

Figure 57. Scheme for the switchable catalytic activity of AMG controlled by the pH value: (**a)**) in the absence and (**b)**) in the presence of the magnetic field. The local pH change in the aggregated state of the MNPs was produced by the reaction catalyzed by urease immobilized at the MNPs. The AMG activity assay was performed with soluble GOx and HRP. (**c)**) The pH dependence of the AMG activity measured for the soluble enzyme. (**d)**) Maltose hydrolysis resulting in glucose production catalyzed by AMG.

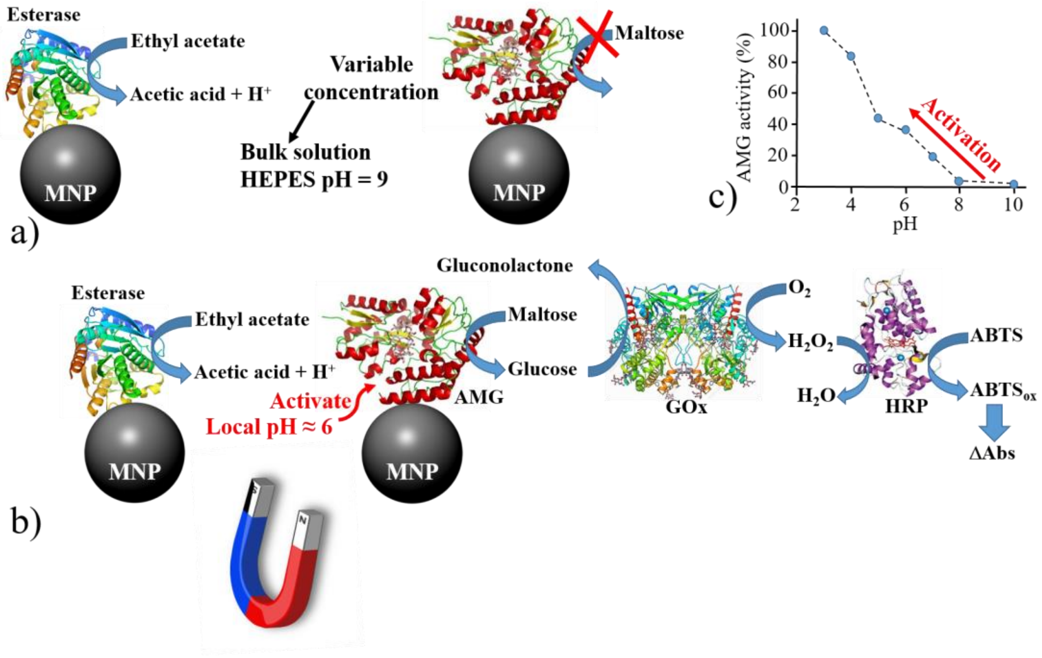

Figure 58. Scheme for the switchable catalytic activity of AMG controlled by the pH value: (**a)**) in the absence and (**b)**) in the presence of the magnetic field. The local pH change in the aggregated state of MNPs was produced by the reaction catalyzed by esterase immobilized at the MNPs. The AMG activity assay was performed with soluble GOx and HRP. (**c)**) The pH dependence of the AMG activity measured for the soluble enzyme.

The reactions catalyzed by Ur or Est (**Figure 57. a)** and **Figure 58. a)**) do not result in the bulk pH change, if the buffer capacity is sufficient for keeping pH unchanged (the effect of the buffer concentration will be discussed later). When the experiment is performed at nearly neutral pH (HEPES-buffer, pH = 6.0) the AMG enzyme is catalytically active (**Figure 57. c)**) to hydrolyze maltose yielding glucose as the product (**Figure 57.d)**). A biocatalytic cascade performed in the solution involving glucose oxidation catalyzed by soluble glucose oxidase (GOx) and color-producing reaction catalyzed by horseradish peroxidase (HRP) allowed the assay of the AMG activity, **Figure 57. a)**. Application of an external magnetic field (**Figure 57. b)**) results in aggregation of the MNPs and local pH increase because the pH change produced locally by the Ur-functionalized MNPs is not anymore compensated by the bulk buffer solution. This results in inhibition of the AMG catalytic activity assayed with GOx-HRP system. A similar effect, but in the opposite direction, can be achieved with Est-modified MNPs when the process is performed in a basic solution (HEPES-buffer, pH = 9.0), **Figure 58. a)**, **b)**. Indeed, the AMG biocatalytic activity is inhibited at the basic bulk pH when the MNPs are dispersed in the solution in the absence of the magnetic field, **Figure 58. a)**. Application of the magnetic field results in aggregation of the MNPs and then local pH decreases, thus activating AMG bound to the MNPs (**Figure 58. b)**), as expected from the pH dependence of the AMG activity, **Figure 58. c)**. The AMG assay performed with the GOx-HRP reactions demonstrated the enzyme activity increase stimulated by the magnetic field, **Figure 58. b)**. **Figure 59. a)** shows the switching effect of the magnetic field on the AMG catalytic activity when the Ur-MNPs are used to control the local pH value. As expected from the mechanism of the process (**Figure 57. a), b)**), AMG is catalytically active in the absence of the magnetic field (OFF state), but it is inhibited in the presence of the magnetic field (ON state) when the local pH is increased due to the Ur-catalyzed reaction, **Figure 59. a)**. The opposite effect of the magnetic field was observed (**Figure 59. b)**) when the local pH was decreased due to the Est-catalyzed reaction when the MNPs are aggregated in the presence of the magnetic field. The observed magneto-switchable AMG activity (**Figure 59.**) corresponds to the proposed mechanism of the processes (**Figure 57.** and **Figure 58.**).

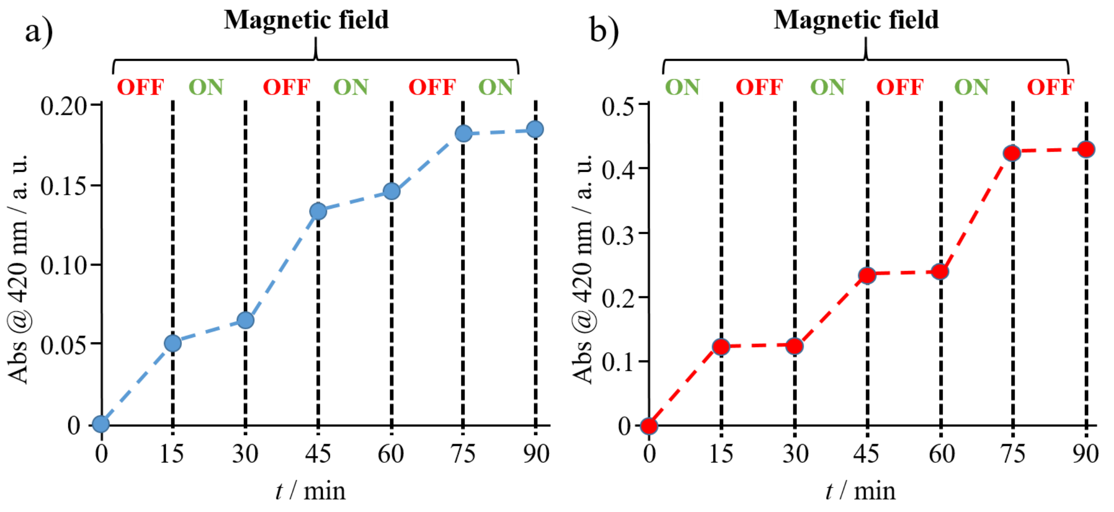

Figure 59. Reversible dynamic changes of the AMG activity by applying and removing a magnetic field using urease (**a)**) or esterase (**b)**) bound to the MNPs for producing local pH changes. The HEPES-buffer concentration was 50 mmol·dm^{-3}. The bulk pH was 6.0 (**a)**) or 9.0 (**b)**).

Simple qualitative reasoning suggests that the buffer concentration should be optimized. Indeed, if the buffer concentration is too high, it will not allow local pH changes around aggregated MNPs. On the other hand, if it is too small, the pH change will proceed to affect the bulk pH value, thus, preventing the system relaxation to the initial pH value when the magnetic field is released and the nanoparticles are dispersed. **Figure 60. a)**, **b)**, **c)** show the effect of buffer concentration on the system with the MNPs functionalized with urease.

Low buffer concentration (HEPES-buffer, 1 mmol·dm^{-3}, bulk pH = 6.0) allows local pH increase within the aggregated MNPs in the presence of the magnetic field (state ON), thus, inhibiting the AMG catalytic activity, **Figure 60. a)**. However, this buffer concentration does not maintain the original bulk pH value, which is changing to ca. pH = 9, thus, keeping the low enzyme activity after removing the magnetic field (state OFF) and dispersing the MNPs. The experimentally optimized buffer concentration (HEPES-buffer, 50 mmol·dm^{-3}, bulk pH = 6.0) allows the local pH increase and inhibition of the AMG activity when the MNPs are aggregated in the presence of the magnetic field (state ON), **Figure 60. b)**.

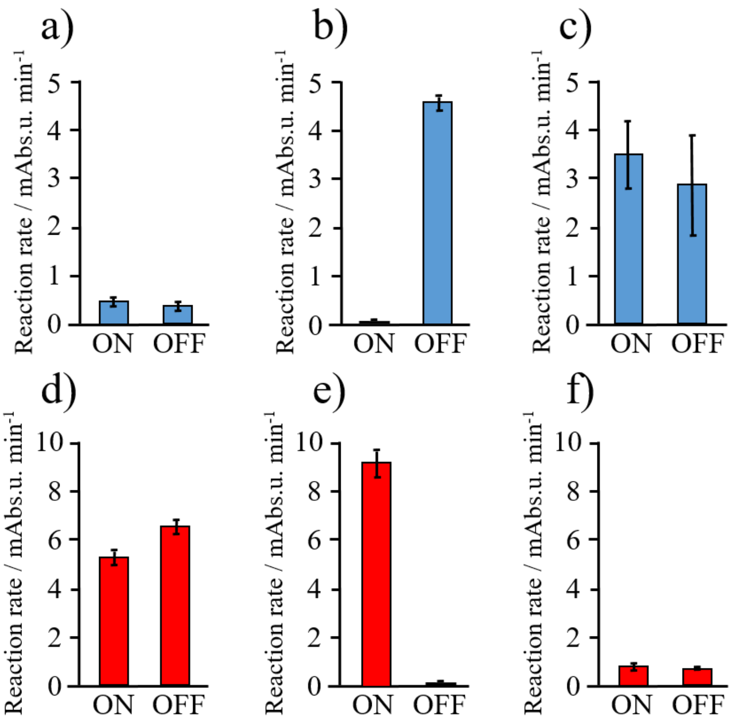

Figure 60. Effect of the buffer concentration on the switchable magneto-controlled AMG activity using MNPs functionalized with urease (**a)** – **c)**) or with esterase (**d)** – **f)**). The initial bulk pH was 6.0 (**a)** – **c)**) or 9.0 (**d)** – **f)**). The HEPES-buffer concentration was 1 mmol·dm^{-3} (**a)**, **d)**), 50 mmol·dm^{-3} (**d)**, **e)**) and 1 mol·dm^{-3} (**c)**, **f)**). Note the opposite effect of the buffer concentration on the AMG activity shown in parts **a)** – **c)** and in parts **d)** – **f)**. The results correspond to three repeated experiments.

This buffer concentration was sufficient to protect the bulk solution from the pH change, thus, removing the magnetic field (state OFF) and dispersing the nanoparticles reactivated AMG, which returned to its normal activity typical for pH = 6. The high buffer concentration (HEPES-buffer, 1 mol·dm^{-3}, bulk pH = 6.0) did not allow any pH change, even in the aggregated MNPs, thus supporting the high catalytic activity of AMG regardless of the presence or absence of the magnetic field (states ON/OFF), **Figure 60. c)**. **Figure 60. d), e), f)** show the buffer concentration effect on the system with the MNPs functionalized with esterase, where the effect of the magnetic field was opposite. Low buffer concentration (HEPES-buffer, 1 mmol·dm^{-3}, bulk pH = 9.0) allows local pH decrease and AMG activation when the magnetic field was applied but did not allow enzyme relaxation to the inhibited state when the magnetic field was removed and the MNPs were re-dispersed, because of the bulk pH change to ca. pH = 6, **Figure 60. d)**. Experimentally optimized buffer concentration (HEPES-buffer, 50 mmol·dm^{-3}, bulk pH = 9.0) allowed local pH decrease and AMG activation, Figure 5E. Importantly, the bulk pH was preserved at its original high value, thus, AMG was returned to its inhibited state upon removing the magnetic field and re-dispersing the nanoparticles. Finally, the high buffer concentration (HEPES-buffer, 1 mol·dm^{-3}, bulk pH = 9.0) did not allow any pH changes, thus maintaining the AMG inhibited state regardless of the presence or absence of the magnetic field, **Figure 60. f)**. It should be noted that the switchable performance of the system in the presence of 50 mmol·dm^{-3} buffer is particularly important for possible future biomedical applications where the buffer capacity is approximately at the same level.

VII.3. Concluding remarks

In conclusion, the catalytic activity of AMG, used as a model enzyme, was controlled by the external magnetic field leading to the aggregation or dispersion of the MNPs serving as transporters of the immobilized enzyme. Other enzymes, urease and esterase, produced pH changes affecting the AMG activity. Optimization of the buffer concentration allowed the process-control only upon local pH changes without affecting the bulk pH values. Depending on the initial bulk pH value (pH = 9.0 or pH = 6.0 in the present experiments) and direction of the local pH change (acidification with Est or increase of basicity with Ur) the AMG activity was switched from the inhibited state to the active state or changed in the opposite direction. While the above presented project was only aimed at the proof of the concept, future extension of the study can be directed to regulation of multi-enzyme/multi-step biocatalytic cascades where some enzymes can operate in a solute state being insensitive to the magnetic field, while other enzymes bound to the transporting MNPs will be affected by the magnetic field. Switching or even tuning activity of selected enzymes would allow controlling kinetics of complex biocatalytic process and their directions. It is particularly important that the magnetic control can be performed at a distance from the reacting species, thus, allowing regulation in biological systems for possible medical applications.

Summary

Polymers are essential materials of modern industry and society, thousands of scientific books and papers dealing with them in different aspects. Both conductive and non-conductive polymers can be used to solve various problems since both of them have their advantages. However, the topic of preparation, properties and application of conducting and non-conducting polymers have left many unanswered questions and lots of room for research on several topics. In this thesis I described my 4 years PhD research work. I investigated the basic electrochemical and morphological properties of a thin layer poly(3,4-ethylenedioxythiophene) (PEDOT) deposited on carbon felt, which proved to be a suitable substrate material. I also investigated the electrochemical and morphological properties of a thin layer poly(3,4-ethylenedioxypyrrole) (PEDOP) which is a conductive polymer structurally very similar to PEDOT. During the electrochemical detection and analysis of bisphenol A (BPA) in aqueous solutions, I observed an unexpected property of this material, which encouraged me to try to combine PEDOT with BPA. I used non-conducting polymers to modify magnetic nanoparticles (MNP) and via this modification, it was possible to functionalize the nanoparticles with enzymes to observe magneto-controlled enzyme activity.

During my research work I used several investigation techniques. Cyclic voltammetry (CV), electrochemical impedance spectroscopy (EIS), electrochemical quartz crystal microbalance (EQCM), and bending beam (BB) technique were used for the study of electrochemical behavior of the different systems. From microscopic methods scanning electron microscopy (SEM), and fluorescent confocal microscopy were used. UV-VIS spectrometry combined with electrochemical techniques and dynamic light scattering (DLS) were also used.

I summarize the results described in the dissertation in points in the thesis book attached to the dissertation.

Összefoglaló

A polimerek a modern ipar és társadalom nélkülözhetetlen anyagai, több ezer tudományos könyv és cikk foglalkozik a témával különböző szempontokat alapul véve. Sajátos előnyeiket kihasználva mind a vezető-, mind a nem vezető polimerek használhatóak különféle problémák megoldására. A vezető- és nem vezető polimerek előállítása, tulajdonságaik vizsgálata, valamint alkalmazási lehetőségeik azonban még számos kiaknázatlan területet tartogat a kutatók számára. Jelen dolgozatban 4 éves PhD kutatómunkám eredményeit foglaltam össze. Vizsgáltam szénszövetre (amely megfelelő hordozó-alapanyagnak bizonyult) leválasztott poli(3,4-etiléndioxitiofén) (PEDOT) vékonyréteg alapvető elektrokémiai- és morfológiai tulajdonságait. Vizsgáltam továbbá a PEDOP-ra szerkezetileg igen hasonló poli(3,4-etiléndioxipirrol) (PEDOP) vékonyréteg elektrokémiai- és morfológiai tulajdonságait. A biszfenol A (BPA) vizes közegben való elektrokémiai kimutatását és vizsgálatát célzó kísérletek során ezen anyag egy nem várt tulajdonságát figyeltem meg, mely a PEDOT és a BPA kombinálására ösztönzött. Nem vezető polimereket használtam mágneses nanorészecskék felületi módosítására, mely módosítás révén lehetővé vált a nanorészecskék enzimekkel történő funkcionalizálása, majd a mágnes által vezérelt enzimaktivitás megfigyelése.

Kutatási munkám során különféle vizsgálati módszereket alkalmaztam. A különféle elektrokémiai rendszerek tanulmányozása során ciklikus voltammetriát (CV), elektrokémiai impedancia spektroszkópiát (EIS), elektrokémiai kvarckristályos mikromérleget (EQCM) és bending beam" (BB) módszert használtam. A mikroszkópos vizsgálati módszerek közül pásztázó elektronmikroszkópot és fluoreszcens konfokális mikroszkópot használtam. UV-VIS spektrofotométert és dinamikus fényszórás (DLS) méréseket is végeztem.

A tézisben közölt eredményeket pontokba szedve is összefoglalom a disszertációhoz mellékelt tézisfüzetben.

Appendix A

A.1. Impedance modeling and the calculation of instantaneous impedances

A.1.1. Impedance modeling

In [240] a theoretical impedance function for polymer modified electrodes involving coupled diffusion-migration charge transport mechanism with three charge carriers has been derived, which is one of the most general models available in the literature, for which attempts were made to provide a theoretical basis.

In the so called "**brush model**" [206] it was assumed, that if the cross-sections of the bundles formed by several polymer chains are great enough, their impedance can be described by the equations corresponding to the homogeneous model, or can be well approximated by the expressions derived for the double-channel transmission line model. In many cases the mathematical forms of the impedance functions derived for the "homogeneous" and "heterogeneous" models are equivalent, and can be given as [207]:

$$Z_{\mathrm{p}}(\omega) = R_0 + \frac{P_{11}}{s}\coth[Fs] + \frac{P_{12}}{s}\tanh[Fs] \qquad \text{A(1)}$$

where $s = (\mathrm{i}\omega)^{1/2}$, (i stands for the imaginary unit, ω is the angular frequency) and the parameters R_0, P_{11}, P_{12} and F are frequency-independent and real. By introducing the thickness of the film L_f, in the simplest cases equation A(1) can be rewritten as [206,207,240]

$$Z_{\mathrm{p}}(\omega) = R_0 + \frac{P_{11}}{s}\coth\left[\frac{L_{\mathrm{f}}s}{2\sqrt{D^*}}\right] + \frac{P_{12}}{s}\tanh\left[\frac{L_{\mathrm{f}}s}{2\sqrt{D^*}}\right] \qquad \text{A(2)}$$

with a frequency–independent D^*, representing the effective diffusion coefficient of the moving species. It is worth to note here that the different “homogeneous” models have in common that the P_{i} parameters are inversely proportional to the square route of D^*. On the other hand, most of the models described in the literature predict a so called “Randles circuit behavior” at high frequencies, a Warburg section at intermediate frequencies, and a purely capacitive behavior at low frequencies. Nevertheless, such an “ideal” behavior can seldom be observed in “real” systems. The deviations of the impedance responses from those predicted by the theories have been explained by considering different effects such as interactions between redox sites, ionic relaxation processes, distribution of diffusion coefficients, migration, film swelling, slow reaction with solution species, nonuniform film thickness, inhomogeneous oxidation/reduction processes, experimental artefacts etc. [15,53,192,241].

It is well known that PEDOT is a good conductor because of its conducting mechanism, and its relation to the doping process [242,243]. These features facilitate modeling, since it can be assumed that simpler *models derived for* one moving species can be relevant for the description of the impedance response of the system. Such simplified models have been developed and used in several past publications, e.g., in [53,244–248] as well as in more recent works [249,250]. In accordance with the above studies the expression for the “Faradaic” impedance, when there is only one diffusing species (or in case of electron hopping control or ion movement control) is:

$$Z_{\mathrm{p}}(\omega) = R_{\mathrm{ct}} + \frac{P_1}{s}\coth\left[\frac{L_{\mathrm{f}}s}{\sqrt{D^*}}\right] = R_{\mathrm{ct}} + Z_{\mathrm{W}} \qquad \text{A(3)}$$

This differs from the impedance of the “classical” Randles equivalent circuit through the presence of the term $\coth\left[\frac{L_{\mathrm{f}}s}{\sqrt{D^*}}\right]$. In equation A(3) the frequency independent resistive element, R_{ct}, which can be identified as the charge transfer resistance at the metal / polymer interface, is in series with a frequency-dependent impedance element Z_{W} (sometimes called finite-length transport impedance, or finite-length Warburg impedance). P_1 and L_{f} are frequency independent and real.

A respective equivalent circuit analog for a polymer modified electrode is shown in **Figure 8.** insert. It contains two non-faradaic elements, R_o and Z_W, an uncompensated, frequency independent ohmic resistance (solution resistance) and a capacitive element (double layer capacitance), respectively.

Thus, the overall impedance function of the system is

$$\begin{aligned} Z(\omega) = \mathrm{Re}\big(Z(\omega)\big) + \mathrm{i}\,\mathrm{Im}\big(Z(\omega)\big) &= R_o + \frac{1}{1/Z_{\mathrm{p}}\,(\omega) + 1/Z_{\mathrm{dl}}\,(\omega)} \\ &= R_o + \frac{1}{Y_{\mathrm{p}}(\omega) + Y_{\mathrm{dl}}(\omega)} \end{aligned} \qquad \text{A(4)}$$

where $\mathrm{Re}(Z(\omega))$ and $\mathrm{Im}(Z(\omega))$ are the real and imaginary parts of the impedance, $Y_{\mathrm{p}}(\omega)$ and $Y_{\mathrm{dl}}(\omega)$ are the admittances corresponding to $Z_{\mathrm{p}}(\omega)$ and $Z_{\mathrm{dl}}(\omega)$, respectively. In the ideal system Eq. 8 is true.

It should be stressed here that equation A(3) has been derived for the case of uniform film thickness. However, it is well known that uneven layer thickness is a peculiarity of PEDOT-modified electrodes [12,13,81]. In the SEM images of PEDOT films deposited on gold (**Figure 3. b)**) well-separated globules (or hierarchical cauliflower-like structures) can be seen on the top of the polymer layer. These structures are highly reproducible and well connected. This means that any quantitative, or even semi-quantitative information about the morphology of the electrodeposited polymer film can be very helpful in modeling the impedance of the electrodes.

A.1.2. Impedance of the modified electrodes if the thickness of the polymer film is non-uniform

If the thickness of the polymer film is much greater than the thickness of the double layer region at the polymer film/metal interface, it can be assumed that the double layer capacitance and the charge transfer resistance are independent on the thickness and/or the thickness distribution of the polymer layer. This means, that only the thickness dependence of Z_{p} should be considered in the model.

Without loss of generality, we can assume that the surface of the electrode can be divided into *n*, not necessarily contiguous segments, each of which is covered by uniform layers of thickness L_i. This means that a discrete-valued distribution (i.e., an empirical frequency distribution) of thickness is used instead of a continuous-valued distribution.

In this case, an approximate impedance function of the system can be expressed as

$$\begin{aligned} Z(\omega) &= R_o + \frac{1}{\frac{1}{Z_{dl}(\omega)} + \sum_{i=1}^{n} \frac{1}{Z_{p,i}(\omega)}} \\ &= R_o + \frac{1}{Y_{dl}(\omega) + \sum_{i=1}^{n} Y_{p,i}(\omega)} \\ &= R_o + \frac{1}{Y_{dl}(\omega) + \sum_{i=1}^{n} x_i \frac{1}{R_{ct} + Z_{W,i}(\omega)}} \end{aligned} \qquad \text{A(5)}$$

where x_i is the fraction of the total electrode area covered by a polymer layer of thickness L_i, $Y_{p,i}$ and $Z_{W,i}$ are the faradaic admittance and the finite-length transport impedance, respectively, both corresponding to a uniform layer of thickness L_i. Obviously, $\sum_{i=1}^{n} x_i = 1$.

The equivalent circuit corresponding to equation A(5) is shown in **Fig.A1 a)**.

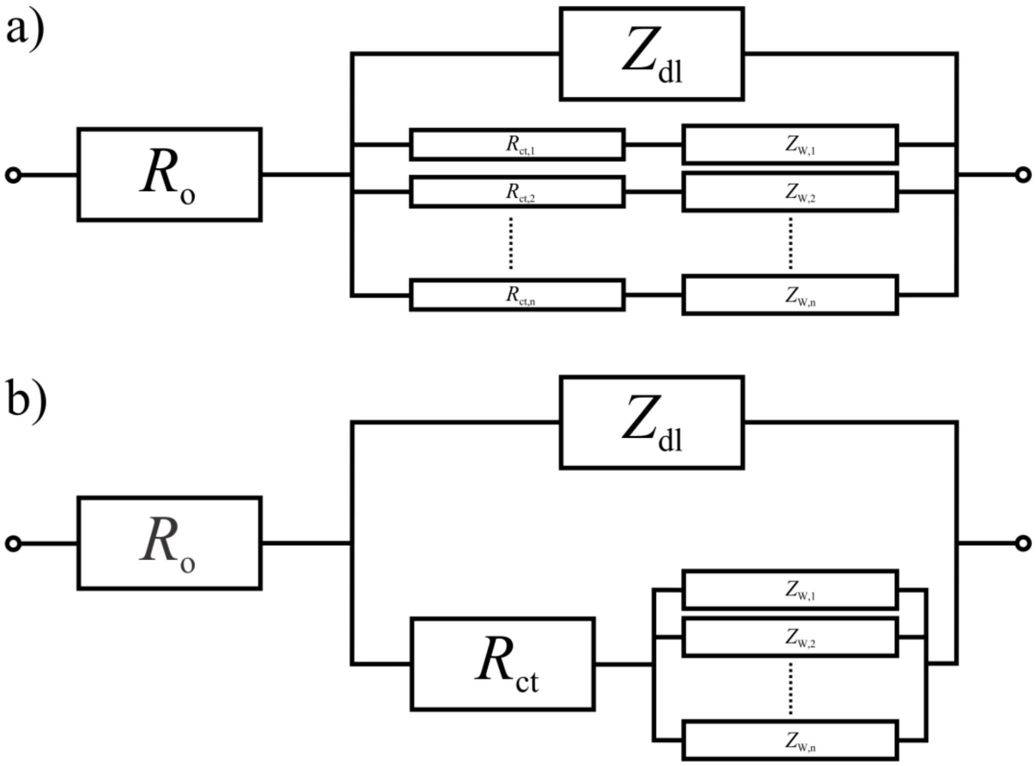

Fig.A1. a) The equivalent circuit corresponding to eq. A(5). R_{o} is the uncompensated ohmic resistance, Z_{dl} is the impedance of the double-layer region at the metal/polymer interface. $R_{\mathrm{ct,i}}$ is the charge transfer resistance and $Z_{\mathrm{W,i}}$ is the finite-length transport impedance which are associated with the polymer layer segment of thickness L_{i}. **b)** The equivalent circuit corresponding to eq. A(6). R_{o} is the uncompensated ohmic resistance, Z_{dl} is the impedance of the double-layer region at the metal/polymer interface, R_{ct} is the charge transfer resistance at the metal/polymer interface, and $Z_{\mathrm{W,i}}$ is the finite-length transport impedance associated with the polymer layer segment of thickness L_{i}.

It is worth noting here that based on the above considerations an alternative impedance model can be envisaged in which the charge transfer resistance is completely separated from the transport impedance. In this case, the approximate total impedance takes the following form:

$$
\begin{aligned}
Z(\omega) = R_{\mathrm{o}} + \frac{1}{Y_{\mathrm{dl}}(\omega) + \sum_{\mathrm{i}=1}^{\mathrm{n}} Y_{\mathrm{p,i}}(\omega)} = \\
= R_{\mathrm{o}} + \cfrac{1}{Y_{\mathrm{dl}}(\omega) + \cfrac{1}{R_{\mathrm{ct}} + \cfrac{1}{\sum_{\mathrm{i}=1}^{\mathrm{n}} x_{\mathrm{i}} Y_{\mathrm{W,i}}(\omega)}}} \qquad \text{A(6)}
\end{aligned}
$$

The equivalent circuit corresponding to equation A(6) is shown in **Fig.A1 b)**. The equivalent circuits in **Fig.A1 a)** and **b)** reveal that the differences between the two approximations lie essentially in the possible current routes. Nevertheless, in this section the discussion is limited to the model given by equation A(5).

A.1.3. Spline interpolation

The successive “impedance diagrams” recorded after overoxidation of the poly(BPA) / PEDOT change continuously with time, it is evident that the system is in a transient state. In such cases a post-experimental analytical procedure is necessary for the reconstruction of “instantaneous impedances”. The calculation of the “instantaneous impedances” was carried out using the real and imaginary parts of the impedances measured at identical frequencies („isofrequential components”).

For the interpolation procedure a smoothing cubic spline algorithm was used [15,202,251], implemented in LabVIEW. Mathematically, this corresponds to the 4-dimensional analysis proposed by Stoynov [160,163,164]. As a result a set of instantaneous impedances related to a selected instant of time has been obtained (see **Figure 13.**). The selected time instants correspond to the starting times of the frequency scans.

A.1.4. CNLS fitting

Complex non-linear least squares (CNLS) parameter estimations were carried out using the fitting program based on the Levenberg–Marquardt algorithm [202–204]. Poisson-weighting was applied in all cases. For checking the goodness-of-fit of the models the four-step procedure [192,193,252,253] has been adopted:

(1) Checking the information about the “mathematical” goodness of the fit, i.e., the statistical analysis of the results of the fitting procedure (sum of squares, variance, correlation matrix, confidence intervals, etc.).

(2) Comparison of impedances calculated by using the estimated (best fit) parameters and the experimental values. A “visual” inspection on both the complex plane plots (Argand diagrams) and the transformed curves (Bode diagrams, complex plane admittance plots,

etc.). A model and the estimated parameters can be considered acceptable only if the fit is good in all cases, i.e., for all types of graphical representation of the immittance data.

(3) Analysis of the error structure, i.e., the distribution of the deviations between the measured and calculated (fitted) curves.

(4) The analysis/proofing of the physical significance of the estimated parameters (e.g., dependence of the parameters on different physico-chemical variables, comparison of the estimated values with independent experimental and/or theoretical data, etc.). This step is evidently the most important one in the procedure.

A.1.5 Adaptation of equation A(5) to the specific conditions

Based on what we already know about these electrodes we tried to find a suitable impedance model for data analysis. Starting with the results of the morphological investigations (section VI.2.1) and based on the considerations concerning the impedance of modified electrodes if the thickness of the polymer layer is not uniform, we can assume that the surface of the electrode can be divided into 4 non-overlapping, but not necessarily contiguous regions or segments of uniform thicknesses, and the layer thicknesses in the different regions are different. In this special case the overall impedance function of the system (see equation A(5)) can be expressed as

$$Z(\omega) = R_\mathrm{o} + \frac{1}{Y_\mathrm{dl}(\omega) + \sum_{\mathrm{i}=1}^{\mathrm{n}} Y_\mathrm{p,i}(\omega)} =$$

$$= R_\mathrm{o} + \frac{1}{Y_\mathrm{dl}(\omega) + \sum_{\mathrm{i}=1}^{4} x_\mathrm{i} \frac{1}{R_\mathrm{ct,i} + Z_\mathrm{W,i}(\omega)}} \qquad \text{A(7)}$$

($x_1 + x_2 + x_3 + x_4 = 1$).

It should be noted here that we can measure the film thickness in the dry state, and an estimation can be made for the thickness distribution. However, due to the swelling of the polymer film the thicknesses determined in the dry state give only qualitative information about the real thickness of the film in contact with an electrolyte solution, especially in the charged state. Nevertheless, it is a plausible assumption that the characteristics of the thickness distributions are very similar in the two cases, and overoxidation does not change this either.

If we also assume that P_1 and D^* in equation A(3) and the charge transfer resistances ($R_{\mathrm{ct,i}}$) in equation A(7) are independent of the local thickness of the polymer film. Equation A(7) can be rewritten as

$$Z(\omega) = R_\mathrm{o} + \cfrac{1}{Y_\mathrm{dl}(\omega) + \sum_{\mathrm{i}=1}^{4} x_\mathrm{i} \cfrac{1}{R_\mathrm{ct} + \cfrac{P_1}{s}\coth\left[\cfrac{L_\mathrm{i} s}{\sqrt{D^*}}\right]}} \qquad \text{A(8)}$$

If the capacitance of the double layer region at the gold / polymer interface (C_dl) does not depend on the frequency, then equation A(8) takes the form:

$$Z(\omega) = R_\mathrm{o} + \cfrac{1}{\mathrm{i}\omega C_\mathrm{dl} + \sum_{\mathrm{i}=1}^{4} x_\mathrm{i} \cfrac{1}{R_\mathrm{ct} + \cfrac{P_1}{s}\coth\left[\cfrac{L_\mathrm{i} s}{\sqrt{D^*}}\right]}} \qquad \text{A(9)}$$

According to equation A(9), a constant, frequency-independent capacitance (C_L) should be observed at low frequencies. However, in contrast to this, the low-frequency parts of the impedance spectra recorded for the Au | PEDOT | 0.1 mol·dm^{-3} H_2SO_4 (aq.) and Au | PEDOT / poly(BPA) | 0.1 mol·dm^{-3} H_2SO_4 (aq.) electrodes are very similar to the impedance responses characteristic for constant phase elements with exponents slightly less than unity (see Eq. 26). On the other hand, well-defined but slightly depressed arcs can be identified in the complex plane plots at higher frequencies. Therefore, in order to obtain an impedance expression which fits the experimental data better [240,252], the theoretical expression has been modified heuristically by introducing a constant phase element (CPE) to describe the immittance of the substrate/polymer interfacial region (see also Eq. 8 and Eq. 26):

$$Z_\mathrm{dl}(\omega) = (\mathrm{i}\omega B)^{-b} \qquad \text{A(10)}$$

In this case instead of equation A(9), the following equation can be used in the parameter estimation procedure:

$$Z(\omega) = R_\mathrm{o} + \frac{1}{(\mathrm{i}\omega B)^b + \sum_{\mathrm{i}=1}^{4} x_\mathrm{i} \frac{1}{R_\mathrm{ct} + \frac{P_1}{s}\coth\left[\frac{L_\mathrm{i} s}{\sqrt{D^*}}\right]}} \qquad \text{A(11)}$$

The introduction of the new parameter b is only acceptable when the optimized value of b is not much smaller than 1 (see Eq. 26). In addition, it is well known that the effect of inductance is especially significant for circuits with low impedances. It can be clearly seen in **Figure 47. a)** (insert) that this is precisely the case here. The inductive impedance is most probably caused by the connector cables (wiring), since even a straight piece of wire has a small but measurable self inductance (L). This means that the expression has to be completed by adding the term of Eq. 9. in series to represent the inductive impedance behavior. This means that

$$Z(\omega) = \mathrm{i}\omega L + R_\mathrm{o} + \frac{1}{(\mathrm{i}\omega B)^b + \sum_{\mathrm{i}=1}^{4} x_\mathrm{i} \frac{1}{R_\mathrm{ct} + \frac{P_1}{s}\coth\left[\frac{L_\mathrm{i} s}{\sqrt{D^*}}\right]}} \qquad \text{A(12)}$$

where L, R_o, R_ct, B, b, x_1, x_2, x_3, P_1, D^*, L_1, L_2, L_3, and L_4 are frequency independent and real. Unfortunately, the fitting in the case of such a high number of parameters is always a very difficult task. In addition, due to the mathematical structure of equation A(12), the parameters are expected to be strongly correlated. For example, by inspecting equation A(12) we can immediately see that L_1, L_2, L_3, L_4 and D^* cannot be determined separately by CNLS fitting, only the

$$F_\mathrm{i} = \frac{L_\mathrm{i}}{\sqrt{D^*}} \qquad \text{A(13)}$$

values can be obtained by fitting equation A(12) to the experimental data. By introducing the variables F_1, F_2, F_3 and F_4 into equation A(12) the expression of the overall impedance takes the following form:

$$Z(\omega) = \mathrm{i}\omega L + R_\mathrm{o} + \frac{1}{(\mathrm{i}\omega B)^b + \sum_{\mathrm{i}=1}^{4} x_\mathrm{i} \frac{1}{R_\mathrm{ct} + \frac{P_1}{s}\coth[F_\mathrm{i} s]}} \qquad \text{A(14)}$$

Indeed, in respect of the statistical information one cannot expect too much from a fitting procedure with 13 free parameters. Nevertheless, we tried to use equation A(14) (as a model/objective function) for parameter estimation.

Appendix B

Table B1. Timestamps and the parameter estimates (estimated mean values, standard deviations, and confidence intervals at the 95% confidence level) for the electrochemical impedance measurements, which were performed right after the overoxidation in 0.1 mol/dm^3 H_2SO_4 (aq.) solution in the frequency range of 50 kHz – 96.1 mHz (sample S1, amplitude of the perturbing signal: 5 mV rms, electrode potential *E* = 0.4 V *vs.* SSCE). 16 subsequent sets of impedance data were recorded continuously to monitor changes in the polymer film.

a)

Number of the recording	Timestamp / s
#1	0
#2	341.569
#3	683.452
#4	1025.516
#5	1371.936
#6	1718.288
#7	2064.538
#8	2411.373
#9	2754.216
#10	3101.185
#11	3448.118
#12	3795.114
#13	4142.181
#14	4488.584
#15	4839.730
#16	5190.759

b)

Results of CNLS fitting (directly measured impedance data sets)

#1

starting time / s	0
degrees of freedom	41
weighted sum of squares (Q/Ω^2)	1.65466E+01
weighted standard error	4.03575E-01
critical *t*-value at 95% confidence level	2.02023E+00

Parameter	Estimated Value	St. Error	Lower Limit	Upper Limit
R_u / Ω	1.929190E+01	8.819456E-01	1.751017E+01	2.107364E+01
R_{ct} / Ω	9.609138E+02	1.323973E+01	9.341665E+02	9.876611E+02
B / F·$\Omega^{1-1/b}$	2.659689E-06	1.117687E-07	2.433891E-06	2.885488E-06
b	9.554718E-01	6.410788E-03	9.425206E-01	9.684231E-01
P_1 / Ω·$s^{-1/2}$	1.368481E+03	5.223521E+01	1.262954E+03	1.474008E+03
F_1 / $s^{1/2}$	4.316468E+00	3.922735E+00	-3.608352E+00	1.224129E+01
F_2 / $s^{1/2}$	1.664887E+00	1.625176E-01	1.336565E+00	1.993210E+00
F_3 / $s^{1/2}$	3.479370E-01	3.880553E-02	2.695410E-01	4.263331E-01
F_4 / $s^{1/2}$	8.919239E-01	7.638271E-02	7.376135E-01	1.046234E+00

#2

starting time / s	341.569
degrees of freedom	41
weighted sum of squares (Q/Ω^2)	1.07276E+01
weighted standard error	2.61648E-01
critical *t*-value at 95% confidence level	2.02023E+00

Parameter	Estimated Value	St. Error	Lower Limit	Upper Limit
R_u / Ω	1.911260E+01	7.363005E-01	1.762511E+01	2.060010E+01
R_{ct} / Ω	8.820254E+02	1.060103E+01	8.606089E+02	9.034419E+02
B / F·$\Omega^{1-1/b}$	2.411359E-06	8.572856E-08	2.238167E-06	2.584550E-06
b	9.637163E-01	5.584242E-03	9.524349E-01	9.749978E-01
P_1 / Ω·$s^{-1/2}$	1.271289E+03	4.991907E+01	1.170441E+03	1.372137E+03
F_1 / $s^{1/2}$	2.629159E+00	2.445995E-01	2.135012E+00	3.123306E+00
F_2 / $s^{1/2}$	1.236300E+00	6.254936E-02	1.109936E+00	1.362664E+00
F_3 / $s^{1/2}$	2.861187E-01	3.146216E-02	2.225580E-01	3.496795E-01
F_4 / $s^{1/2}$	7.564603E-01	6.368511E-02	6.278018E-01	8.851187E-01

#3

starting time / s	683.452
degrees of freedom	41
weighted sum of squares (Q/Ω^2)	8.47906E+00
weighted standard error	2.06806E-01
critical t-value at 95% confidence level	2.02023E+00

Parameter	Estimated Value	St. Error	Lower Limit	Upper Limit
R_u / Ω	1.893207E+01	6.797197E-01	1.755888E+01	2.030526E+01
R_ct / Ω	7.294572E+02	9.219217E+00	7.108323E+02	7.480821E+02
B / F·$\Omega^{1-1/b}$	2.266729E-06	8.101181E-08	2.103067E-06	2.430391E-06
b	9.625625E-01	5.770157E-03	9.509055E-01	9.742196E-01
P_1 / Ω·$\mathrm{s}^{-1/2}$	1.186668E+03	5.121455E+01	1.083203E+03	1.290133E+03
F_1 / $\mathrm{s}^{1/2}$	2.592456E+00	1.911331E-01	2.206324E+00	2.978589E+00
F_2 / $\mathrm{s}^{1/2}$	1.127590E+00	6.148592E-02	1.003375E+00	1.251806E+00
F_3 / $\mathrm{s}^{1/2}$	2.348744E-01	2.766693E-02	1.789809E-01	2.907679E-01
F_4 / $\mathrm{s}^{1/2}$	6.337234E-01	5.796702E-02	5.166168E-01	7.508300E-01

#4

starting time / s	1025.516
degrees of freedom	41
weighted sum of squares (Q/Ω^2)	5.63378E+00
weighted standard error	1.37409E-01
critical t-value at 95% confidence level	2.02023E+00

Parameter	Estimated Value	St. Error	Lower Limit	Upper Limit
R_u / Ω	1.872703E+01	5.721229E-01	1.757121E+01	1.988285E+01
R_ct / Ω	6.210382E+02	7.503385E+00	6.058797E+02	6.361968E+02
B / F·$\Omega^{1-1/b}$	2.140628E-06	6.917706E-08	2.000875E-06	2.280382E-06
b	9.593822E-01	5.322914E-03	9.486287E-01	9.701357E-01
P_1 / Ω·$\mathrm{s}^{-1/2}$	1.122313E+03	4.962191E+01	1.022065E+03	1.222560E+03
F_1 / $\mathrm{s}^{1/2}$	2.467586E+00	1.425545E-01	2.179593E+00	2.755578E+00
F_2 / $\mathrm{s}^{1/2}$	1.019885E+00	5.751929E-02	9.036829E-01	1.136087E+00
F_3 / $\mathrm{s}^{1/2}$	1.896728E-01	2.257335E-02	1.440695E-01	2.352761E-01
F_4 / $\mathrm{s}^{1/2}$	5.466958E-01	5.326945E-02	4.390793E-01	6.543122E-01

#5

starting time / s	1371.936
degrees of freedom	41
weighted sum of squares (Q/Ω^2)	4.07300E+00
weighted standard error	9.93414E-02
critical *t*-value at 95% confidence level	2.02023E+00

Parameter	Estimated Value	St. Error	Lower Limit	Upper Limit
R_u / Ω	1.820047E+01	4.841048E-01	1.722246E+01	1.917847E+01
R_ct / Ω	5.591024E+02	4.265077E+00	5.504859E+02	5.677188E+02
B / F·$\Omega^{1-1/b}$	1.954096E-06	5.013228E-08	1.852817E-06	2.055374E-06
b	9.472448E-01	3.959473E-03	9.392458E-01	9.552439E-01
P_1 / Ω·$\mathrm{s}^{-1/2}$	8.281575E+02	4.101685E+01	7.452942E+02	9.110209E+02
F_1 / $\mathrm{s}^{1/2}$	1.896670E+00	9.230176E-02	1.710199E+00	2.083140E+00
F_2 / $\mathrm{s}^{1/2}$	6.426228E-01	4.846779E-02	5.447069E-01	7.405388E-01
F_3 / $\mathrm{s}^{1/2}$	8.435154E-02	9.112251E-03	6.594272E-02	1.027604E-01
F_4 / $\mathrm{s}^{1/2}$	2.860470E-01	2.767506E-02	2.301371E-01	3.419570E-01

#6

starting time / s	1718.288
degrees of freedom	41
weighted sum of squares (Q/Ω^2)	3.49049E+00
weighted standard error	8.51340E-02
critical *t*-value at 95% confidence level	2.02023E+00

Parameter	Estimated Value	St. Error	Lower Limit	Upper Limit
R_u / Ω	1.842165E+01	4.629938E-01	1.748630E+01	1.935701E+01
R_ct / Ω	4.771468E+02	4.437124E+00	4.681828E+02	4.861108E+02
B / F·$\Omega^{1-1/b}$	1.968068E-06	5.316956E-08	1.860654E-06	2.075483E-06
b	9.534621E-01	4.422617E-03	9.445274E-01	9.623968E-01
P_1 / Ω·$\mathrm{s}^{-1/2}$	9.844639E+02	3.835513E+01	9.069779E+02	1.061950E+03
F_1 / $\mathrm{s}^{1/2}$	2.205707E+00	9.248630E-02	2.018864E+00	2.392550E+00
F_2 / $\mathrm{s}^{1/2}$	8.057827E-01	4.581272E-02	7.132306E-01	8.983349E-01
F_3 / $\mathrm{s}^{1/2}$	1.236992E-01	1.212190E-02	9.921017E-02	1.481882E-01
F_4 / $\mathrm{s}^{1/2}$	3.750491E-01	3.263271E-02	3.091235E-01	4.409746E-01

#7

starting time / s	2064.538
degrees of freedom	41
weighted sum of squares (Q/Ω^2)	2.75906E+00
weighted standard error	6.72942E-02
critical *t*-value at 95% confidence level	2.02023E+00

Parameter	Estimated Value	St. Error	Lower Limit	Upper Limit
R_{u} / Ω	1.878380E+01	4.252778E-01	1.792464E+01	1.964295E+01
R_{ct} / Ω	4.130086E+02	3.887161E+00	4.051556E+02	4.208615E+02
$B / \mathrm{F}\cdot\Omega^{1-1/b}$	2.022377E-06	5.470810E-08	1.911854E-06	2.132900E-06
b	9.630725E-01	4.660813E-03	9.536565E-01	9.724884E-01
$P_1 / \Omega\cdot\mathrm{s}^{-1/2}$	1.105970E+03	2.945361E+01	1.046467E+03	1.165473E+03
$F_1 / \mathrm{s}^{1/2}$	2.412067E+00	7.927048E-02	2.251922E+00	2.572211E+00
$F_2 / \mathrm{s}^{1/2}$	9.286110E-01	3.494575E-02	8.580126E-01	9.992093E-01
$F_3 / \mathrm{s}^{1/2}$	1.639221E-01	1.221345E-02	1.392481E-01	1.885960E-01
$F_4 / \mathrm{s}^{1/2}$	4.444520E-01	2.793457E-02	3.880178E-01	5.008862E-01

#8

starting time / s	2411.373
degrees of freedom	41
weighted sum of squares (Q/Ω^2)	3.43978E+00
weighted standard error	8.38970E-02
critical *t*-value at 95% confidence level	2.02023E+00

Parameter	Estimated Value	St. Error	Lower Limit	Upper Limit
R_{u} / Ω	1.877685E+01	4.808443E-01	1.780543E+01	1.974826E+01
R_{ct} / Ω	3.729357E+02	3.858053E+00	3.651416E+02	3.807298E+02
$B / \mathrm{F}\cdot\Omega^{1-1/b}$	1.991798E-06	6.199500E-08	1.866554E-06	2.117042E-06
b	9.637530E-01	5.390672E-03	9.528626E-01	9.746433E-01
$P_1 / \Omega\cdot\mathrm{s}^{-1/2}$	1.105396E+03	2.975420E+01	1.045286E+03	1.165507E+03
$F_1 / \mathrm{s}^{1/2}$	2.397803E+00	8.179909E-02	2.232550E+00	2.563056E+00
$F_2 / \mathrm{s}^{1/2}$	8.905202E-01	3.496466E-02	8.198836E-01	9.611568E-01
$F_3 / \mathrm{s}^{1/2}$	1.591962E-01	1.221830E-02	1.345124E-01	1.838799E-01
$F_4 / \mathrm{s}^{1/2}$	4.228833E-01	2.676312E-02	3.688157E-01	4.769509E-01

#9

starting time / s	2754.216
degrees of freedom	41
weighted sum of squares (Q/Ω^2)	2.75208E+00
weighted standard error	6.71239E-02
critical *t*-value at 95% confidence level	2.02023E+00

Parameter	Estimated Value	St. Error	Lower Limit	Upper Limit
R_u / Ω	1.902652E+01	4.359770E-01	1.814575E+01	1.990729E+01
R_ct / Ω	3.365048E+02	3.168995E+00	3.301027E+02	3.429069E+02
B / F·$\Omega^{1-1/b}$	2.027433E-06	5.875431E-08	1.908736E-06	2.146130E-06
b	9.709385E-01	5.138470E-03	9.605576E-01	9.813194E-01
P_1 / Ω·$s^{-1/2}$	1.165852E+03	2.354263E+01	1.118290E+03	1.213413E+03
F_1 / $s^{1/2}$	2.460426E+00	6.903624E-02	2.320957E+00	2.599895E+00
F_2 / $s^{1/2}$	9.194801E-01	2.711140E-02	8.647089E-01	9.742513E-01
F_3 / $s^{1/2}$	1.725372E-01	1.044624E-02	1.514334E-01	1.936410E-01
F_4 / $s^{1/2}$	4.381352E-01	2.129767E-02	3.951090E-01	4.811613E-01

#10

starting time / s	3101.185
degrees of freedom	41
weighted sum of squares (Q/Ω^2)	2.76682E+00
weighted standard error	6.74833E-02
critical *t*-value at 95% confidence level	2.02023E+00

Parameter	Estimated Value	St. Error	Lower Limit	Upper Limit
R_u / Ω	1.903830E+01	4.422711E-01	1.814481E+01	1.993179E+01
R_ct / Ω	3.112063E+02	2.976234E+00	3.051936E+02	3.172189E+02
B / F·$\Omega^{1-1/b}$	2.007482E-06	6.009823E-08	1.886070E-06	2.128894E-06
b	9.720876E-01	5.349145E-03	9.612811E-01	9.828941E-01
P_1 / Ω·$s^{-1/2}$	1.175802E+03	2.266179E+01	1.130020E+03	1.221584E+03
F_1 / $s^{1/2}$	2.406121E+00	6.140702E-02	2.282064E+00	2.530177E+00
F_2 / $s^{1/2}$	8.823569E-01	2.532054E-02	8.312036E-01	9.335101E-01
F_3 / $s^{1/2}$	1.654225E-01	9.627210E-03	1.459733E-01	1.848716E-01
F_4 / $s^{1/2}$	4.138458E-01	1.935711E-02	3.747400E-01	4.529516E-01

#11

starting time / s	3448.118
degrees of freedom	41
weighted sum of squares (Q / Ω^2)	3.22999E+00
weighted standard error	7.87802E-02
critical *t*-value at 95% confidence level	2.02023E+00

Parameter	Estimated Value	St. Error	Lower Limit	Upper Limit
R_u / Ω	1.917126E+01	4.832609E-01	1.819497E+01	2.014756E+01
R_{ct} / Ω	2.877811E+02	3.047233E+00	2.816250E+02	2.939372E+02
B / F·$\Omega^{1-1/b}$	2.022245E-06	6.752688E-08	1.885825E-06	2.158665E-06
b	9.765358E-01	6.063453E-03	9.642862E-01	9.887853E-01
P_1 / Ω·$s^{-1/2}$	1.209964E+03	2.309805E+01	1.163301E+03	1.256627E+03
F_1 / $s^{1/2}$	2.388866E+00	6.003715E-02	2.267577E+00	2.510155E+00
F_2 / $s^{1/2}$	8.775546E-01	2.505039E-02	8.269471E-01	9.281621E-01
F_3 / $s^{1/2}$	1.683815E-01	9.950772E-03	1.482787E-01	1.884843E-01
F_4 / $s^{1/2}$	4.102174E-01	1.927237E-02	3.712828E-01	4.491520E-01

#12

starting time / s	3795.114
degrees of freedom	41
weighted sum of squares (Q / Ω^2)	4.13859E+00
weighted standard error	1.00941E-01
critical *t*-value at 95% confidence level	2.02023E+00

Parameter	Estimated Value	St. Error	Lower Limit	Upper Limit
R_u / Ω	1.927957E+01	5.519194E-01	1.816457E+01	2.039457E+01
R_{ct} / Ω	2.674564E+02	3.231622E+00	2.609278E+02	2.739850E+02
B / F·$\Omega^{1-1/b}$	2.036173E-06	7.874144E-08	1.877097E-06	2.195249E-06
b	9.807880E-01	7.115648E-03	9.664127E-01	9.951632E-01
P_1 / Ω·$s^{-1/2}$	1.237393E+03	2.444036E+01	1.188018E+03	1.286768E+03
F_1 / $s^{1/2}$	2.374908E+00	6.215904E-02	2.249333E+00	2.500484E+00
F_2 / $s^{1/2}$	8.611684E-01	2.577800E-02	8.090910E-01	9.132459E-01
F_3 / $s^{1/2}$	1.689335E-01	1.056625E-02	1.475873E-01	1.902798E-01
F_4 / $s^{1/2}$	4.015895E-01	1.962750E-02	3.619375E-01	4.412415E-01

#13

starting time / s	4142.181
degrees of freedom	41
weighted sum of squares (Q / Ω^2)	3.84807E+00
weighted standard error	9.38554E-02
critical t-value at 95% confidence level	2.02023E+00

Parameter	Estimated Value	St. Error	Lower Limit	Upper Limit
R_u / Ω	1.931454E+01	5.368921E-01	1.822990E+01	2.039919E+01
R_ct / Ω	2.520544E+02	2.973675E+00	2.460469E+02	2.580619E+02
$B / \mathrm{F}\cdot\Omega^{1-1/b}$	2.035728E-06	7.762228E-08	1.878914E-06	2.192543E-06
b	9.831756E-01	7.079944E-03	9.688725E-01	9.974787E-01
$P_1 / \Omega\cdot\mathrm{s}^{-1/2}$	1.257589E+03	2.260440E+01	1.211923E+03	1.303255E+03
$F_1 / \mathrm{s}^{1/2}$	2.370029E+00	5.684408E-02	2.255191E+00	2.484867E+00
$F_2 / \mathrm{s}^{1/2}$	8.491242E-01	2.329483E-02	8.020633E-01	8.961850E-01
$F_3 / \mathrm{s}^{1/2}$	1.673314E-01	9.713475E-03	1.477079E-01	1.869548E-01
$F_4 / \mathrm{s}^{1/2}$	3.960934E-01	1.778518E-02	3.601632E-01	4.320235E-01

#14

starting time / s	4488.584
degrees of freedom	41
weighted sum of squares (Q / Ω^2)	4.07963E+00
weighted standard error	9.95032E-02
critical t-value at 95% confidence level	2.02023E+00

Parameter	Estimated Value	St. Error	Lower Limit	Upper Limit
R_u / Ω	1.934958E+01	5.573237E-01	1.822366E+01	2.047550E+01
R_ct / Ω	2.388090E+02	2.923642E+00	2.329025E+02	2.447154E+02
$B / \mathrm{F}\cdot\Omega^{1-1/b}$	2.030423E-06	8.124079E-08	1.866298E-06	2.194547E-06
b	9.850473E-01	7.481364E-03	9.699332E-01	1.000161E+00
$P_1 / \Omega\cdot\mathrm{s}^{-1/2}$	1.273186E+03	2.249711E+01	1.227737E+03	1.318636E+03
$F_1 / \mathrm{s}^{1/2}$	2.345071E+00	5.415533E-02	2.235665E+00	2.454477E+00
$F_2 / \mathrm{s}^{1/2}$	8.268766E-01	2.252284E-02	7.813753E-01	8.723779E-01
$F_3 / \mathrm{s}^{1/2}$	1.623061E-01	9.378435E-03	1.433595E-01	1.812527E-01
$F_4 / \mathrm{s}^{1/2}$	3.838792E-01	1.711612E-02	3.493007E-01	4.184577E-01

#15

starting time / s	4839.730
degrees of freedom	41
weighted sum of squares (Q/Ω^2)	5.20816E+00
weighted standard error	1.27028E-01
critical *t*-value at 95% confidence level	2.02023E+00

Parameter	Estimated Value	St. Error	Lower Limit	Upper Limit
R_u / Ω	1.945557E+01	6.354057E-01	1.817190E+01	2.073923E+01
R_ct / Ω	2.248355E+02	3.215313E+00	2.183399E+02	2.313312E+02
B / $\mathrm{F{\cdot}\Omega^{1-1/b}}$	2.052217E-06	9.527785E-08	1.859734E-06	2.244700E-06
b	9.897410E-01	8.822921E-03	9.719167E-01	1.007565E+00
P_1 / $\Omega{\cdot}\mathrm{s}^{-1/2}$	1.300342E+03	2.464159E+01	1.250560E+03	1.350123E+03
F_1 / $\mathrm{s}^{1/2}$	2.327029E+00	5.690054E-02	2.212077E+00	2.441982E+00
F_2 / $\mathrm{s}^{1/2}$	8.258205E-01	2.418518E-02	7.769609E-01	8.746800E-01
F_3 / $\mathrm{s}^{1/2}$	1.654126E-01	1.041600E-02	1.443699E-01	1.864553E-01
F_4 / $\mathrm{s}^{1/2}$	3.806047E-01	1.845403E-02	3.433233E-01	4.178860E-01

#16

starting time / s	5190.759
degrees of freedom	41
weighted sum of squares (Q/Ω^2)	5.77746E+00
weighted standard error	1.40914E-01
critical *t*-value at 95% confidence level	2.02023E+00

Parameter	Estimated Value	St. Error	Lower Limit	Upper Limit
R_u / Ω	1.950071E+01	6.749429E-01	1.813717E+01	2.086424E+01
R_ct / Ω	2.138982E+02	3.299439E+00	2.072326E+02	2.205638E+02
B / $\mathrm{F{\cdot}\Omega^{1-1/b}}$	2.054139E-06	1.027371E-07	1.846586E-06	2.261691E-06
b	9.922005E-01	9.598899E-03	9.728085E-01	1.011592E+00
P_1 / $\Omega{\cdot}\mathrm{s}^{-1/2}$	1.316296E+03	2.550532E+01	1.264770E+03	1.367823E+03
F_1 / $\mathrm{s}^{1/2}$	2.294505E+00	5.546787E-02	2.182447E+00	2.406563E+00
F_2 / $\mathrm{s}^{1/2}$	8.134465E-01	2.438342E-02	7.641865E-01	8.627066E-01
F_3 / $\mathrm{s}^{1/2}$	1.635489E-01	1.067367E-02	1.419856E-01	1.851121E-01
F_4 / $\mathrm{s}^{1/2}$	3.751332E-01	1.876240E-02	3.372288E-01	4.130375E-01

c)

Results of CNLS fitting (Corrected data sets, calculated “instantaneous” impedance spectra)

#1

time stamp / s	0
degrees of freedom	41
weighted sum of squares (Q / Ω^2)	1.42406E+01
weighted standard error	3.47331E-01
critical *t*-value at 95% confidence level	2.02023E+00

Parameter	Estimated Value	St. Error	Lower Limit	Upper Limit
R_u / Ω	1.950051E+01	8.184286E-01	1.784710E+01	2.115392E+01
R_{ct} / Ω	9.335262E+02	1.067437E+01	9.119616E+02	9.550909E+02
B / F·$\Omega^{1-1/b}$	2.682100E-06	9.894018E-08	2.482218E-06	2.881982E-06
b	9.723246E-01	5.768011E-03	9.606719E-01	9.839773E-01
P_1 / Ω·s^{-1}	1.329546E+03	4.268820E+01	1.243306E+03	1.415786E+03
F_1 / $s^{1/2}$	4.452452E+00	4.215468E+00	-4.063753E+00	1.296866E+01
F_2 / $s^{1/2}$	1.754109E+00	1.624221E-01	1.425979E+00	2.082238E+00
F_3 / $s^{1/2}$	3.483164E-01	3.263069E-02	2.823950E-01	4.142379E-01
F_4 / $s^{1/2}$	8.711615E-01	6.505528E-02	7.397350E-01	1.002588E+00

#2

time stamp / s	341.569
degrees of freedom	41
weighted sum of squares (Q / Ω^2)	6.22734E+00
weighted standard error	1.51886E-01
critical *t*-value at 95% confidence level	2.02023E+00

Parameter	Estimated Value	St. Error	Lower Limit	Upper Limit
R_u / Ω	1.934231E+01	5.538458E-01	1.822342E+01	2.046121E+01
R_{ct} / Ω	8.869932E+02	6.819560E+00	8.732161E+02	9.007702E+02
B / F·$\Omega^{1-1/b}$	2.448373E-06	6.243299E-08	2.322244E-06	2.574502E-06
b	9.666086E-01	3.954860E-03	9.586188E-01	9.745983E-01
P_1 / Ω·s^{-1}	1.385029E+03	2.719510E+01	1.330088E+03	1.439969E+03
F_1 / $s^{1/2}$	4.207552E+00	2.047490E+00	7.115579E-02	8.343949E+00
F_2 / $s^{1/2}$	1.753516E+00	9.948320E-02	1.552537E+00	1.954494E+00
F_3 / $s^{1/2}$	3.526109E-01	2.048019E-02	3.112362E-01	3.939855E-01
F_4 / $s^{1/2}$	8.603968E-01	4.010415E-02	7.793773E-01	9.414163E-01

#3

time stamp / s	683.452
degrees of freedom	41
weighted sum of squares (Q / Ω^2)	5.34318E+00
weighted standard error	1.30322E-01
critical *t*-value at 95% confidence level	2.02023E+00

Parameter	Estimated Value	St. Error	Lower Limit	Upper Limit
R_u / Ω	1.920905E+01	5.317698E-01	1.813475E+01	2.028334E+01
R_ct / Ω	7.362170E+02	6.082944E+00	7.239281E+02	7.485059E+02
B / F·$\Omega^{1-1/b}$	2.305153E-06	6.107699E-08	2.181763E-06	2.428542E-06
b	9.664698E-01	4.223857E-03	9.579367E-01	9.750030E-01
P_1 / Ω·s^{-1}	1.306749E+03	2.851337E+01	1.249146E+03	1.364353E+03
F_1 / $\mathrm{s}^{1/2}$	3.764374E+00	9.539414E-01	1.837195E+00	5.691553E+00
F_2 / $\mathrm{s}^{1/2}$	1.485480E+00	6.181629E-02	1.360597E+00	1.610363E+00
F_3 / $\mathrm{s}^{1/2}$	2.942572E-01	1.856334E-02	2.567550E-01	3.317594E-01
F_4 / $\mathrm{s}^{1/2}$	7.294530E-01	3.696795E-02	6.547693E-01	8.041367E-01

#4

time stamp / s	1025.516
degrees of freedom	41
weighted sum of squares (Q / Ω^2)	4.80456E+00
weighted standard error	1.17184E-01
critical *t*-value at 95% confidence level	2.02023E+00

Parameter	Estimated Value	St. Error	Lower Limit	Upper Limit
R_u / Ω	1.909141E+01	5.206283E-01	1.803962E+01	2.014319E+01
R_ct / Ω	6.174537E+02	5.540405E+00	6.062608E+02	6.286466E+02
B / F·$\Omega^{1-1/b}$	2.211968E-06	6.185745E-08	2.087002E-06	2.336934E-06
b	9.660257E-01	4.570921E-03	9.567914E-01	9.752600E-01
P_1 / Ω·s^{-1}	1.251116E+03	2.969232E+01	1.191131E+03	1.311102E+03
F_1 / $\mathrm{s}^{1/2}$	3.454593E+00	5.280039E-01	2.387905E+00	4.521282E+00
F_2 / $\mathrm{s}^{1/2}$	1.325793E+00	4.955564E-02	1.225680E+00	1.425907E+00
F_3 / $\mathrm{s}^{1/2}$	2.546157E-01	1.750379E-02	2.192540E-01	2.899773E-01
F_4 / $\mathrm{s}^{1/2}$	6.534164E-01	3.625453E-02	5.801740E-01	7.266589E-01

#5

time stamp / s	1371.936
degrees of freedom	3.62636E+00
weighted sum of squares (Q / Ω^2)	41
weighted standard error	8.84478E-02
critical *t*-value at 95% confidence level	2.02023E+00

Parameter	Estimated Value	St. Error	Lower Limit	Upper Limit
R_{u} / Ω	1.812562E+01	4.556745E-01	1.720505E+01	1.904618E+01
R_{ct} / Ω	5.724649E+02	3.518670E+00	5.653564E+02	5.795734E+02
$B / \mathrm{F}\cdot\Omega^{1-1/\mathrm{b}}$	1.919466E-06	4.557398E-08	1.827397E-06	2.011536E-06
b	9.443798E-01	3.599866E-03	9.371073E-01	9.516524E-01
$P_1 / \Omega\cdot\mathrm{s}^{-1}$	7.930482E+02	3.162413E+01	7.291603E+02	8.569362E+02
$F_1 / \mathrm{s}^{1/2}$	2.033774E+00	9.286573E-02	1.846164E+00	2.221384E+00
$F_2 / \mathrm{s}^{1/2}$	6.315228E-01	4.075506E-02	5.491882E-01	7.138573E-01
$F_3 / \mathrm{s}^{1/2}$	7.517906E-02	6.232837E-03	6.258731E-02	8.777081E-02
$F_4 / \mathrm{s}^{1/2}$	2.504635E-01	1.945666E-02	2.111566E-01	2.897703E-01

#6

time stamp / s	1718.288
degrees of freedom	41
weighted sum of squares (Q / Ω^2)	3.53358E+00
weighted standard error	8.61848E-02
critical *t*-value at 95% confidence level	2.02023E+00

Parameter	Estimated Value	St. Error	Lower Limit	Upper Limit
R_{u} / Ω	1.819609E+01	4.605104E-01	1.726576E+01	1.912643E+01
R_{ct} / Ω	4.940358E+02	3.476462E+00	4.870126E+02	5.010591E+02
$B / \mathrm{F}\cdot\Omega^{1-1/\mathrm{b}}$	1.898352E-06	4.827142E-08	1.800833E-06	1.995871E-06
b	9.467149E-01	3.964847E-03	9.387051E-01	9.547248E-01
$P_1 / \Omega\cdot\mathrm{s}^{-1}$	8.737718E+02	3.108471E+01	8.109736E+02	9.365700E+02
$F_1 / \mathrm{s}^{1/2}$	2.163795E+00	8.987951E-02	1.982218E+00	2.345372E+00
$F_2 / \mathrm{s}^{1/2}$	7.078970E-01	4.023421E-02	6.266147E-01	7.891792E-01
$F_3 / \mathrm{s}^{1/2}$	9.056281E-02	7.222703E-03	7.597130E-02	1.051543E-01
$F_4 / \mathrm{s}^{1/2}$	2.860542E-01	2.225224E-02	2.410996E-01	3.310088E-01

#7

time stamp / s	2064.538
degrees of freedom	41
weighted sum of squares (Q / Ω^2)	2.95192E+00
weighted standard error	7.19980E-02
critical t-value at 95% confidence level	2.02023E+00

Parameter	Estimated Value	St. Error	Lower Limit	Upper Limit
R_{u} / Ω	1.877914E+01	4.398716E-01	1.789050E+01	1.966778E+01
R_{ct} / Ω	4.172362E+02	4.028648E+00	4.090974E+02	4.253749E+02
$B / \mathrm{F}\cdot\Omega^{1-1/b}$	2.010609E-06	5.613192E-08	1.897209E-06	2.124008E-06
b	9.621907E-01	4.795650E-03	9.525024E-01	9.718790E-01
$P_1 / \Omega\cdot\mathrm{s}^{-1/2}$	1.117344E+03	3.003898E+01	1.056659E+03	1.178030E+03
$F_1 / \mathrm{s}^{1/2}$	2.669172E+00	1.156264E-01	2.435580E+00	2.902764E+00
$F_2 / \mathrm{s}^{1/2}$	9.975878E-01	3.888421E-02	9.190328E-01	1.076143E+00
$F_3 / \mathrm{s}^{1/2}$	1.668614E-01	1.245785E-02	1.416937E-01	1.920291E-01
$F_4 / \mathrm{s}^{1/2}$	4.533428E-01	3.018799E-02	3.923561E-01	5.143294E-01

#8

time stamp / s	2411.373
degrees of freedom	41
weighted sum of squares (Q / Ω^2)	3.64459E+00
weighted standard error	8.88924E-02
critical t-value at 95% confidence level	2.02023E+00

Parameter	Estimated Value	St. Error	Lower Limit	Upper Limit
R_{u} / Ω	1.878730E+01	4.966291E-01	1.778399E+01	1.979060E+01
R_{ct} / Ω	3.756813E+02	4.104309E+00	3.673896E+02	3.839729E+02
$B / \mathrm{F}\cdot\Omega^{1-1/b}$	1.985817E-06	6.444362E-08	1.855627E-06	2.116008E-06
b	9.633688E-01	5.634370E-03	9.519861E-01	9.747516E-01
$P_1 / \Omega\cdot\mathrm{s}^{-1/2}$	1.118289E+03	3.109674E+01	1.055466E+03	1.181111E+03
$F_1 / \mathrm{s}^{1/2}$	2.586254E+00	1.082207E-01	2.367623E+00	2.804884E+00
$F_2 / \mathrm{s}^{1/2}$	9.591728E-01	3.926094E-02	8.798568E-01	1.038489E+00
$F_3 / \mathrm{s}^{1/2}$	1.639746E-01	1.282763E-02	1.380599E-01	1.898894E-01
$F_4 / \mathrm{s}^{1/2}$	4.317480E-01	2.985620E-02	3.714317E-01	4.920643E-01

#9

time stamp / s	2754.216
degrees of freedom	41
weighted sum of squares (Q/Ω^2)	2.70590E+00
weighted standard error	7.08756E-02
critical *t*-value at 95% confidence level	2.02023E+00

Parameter	Estimated Value	St. Error	Lower Limit	Upper Limit
R_u / Ω	1.884799E+01	4.500282E-01	1.793883E+01	1.975715E+01
R_{ct} / Ω	3.427834E+02	3.462599E+00	3.357882E+02	3.497786E+02
B / F·$\Omega^{1-1/b}$	1.974850E-06	5.969006E-08	1.854262E-06	2.095437E-06
b	9.656328E-01	5.320135E-03	9.548850E-01	9.763807E-01
P_1 / Ω·$s^{-1/2}$	1.132282E+03	2.695812E+01	1.077820E+03	1.186743E+03
F_1 / $s^{1/2}$	2.501125E+00	8.170915E-02	2.336054E+00	2.666196E+00
F_2 / $s^{1/2}$	9.324988E-01	3.259398E-02	8.666515E-01	9.983461E-01
F_3 / $s^{1/2}$	1.598719E-01	1.093480E-02	1.377811E-01	1.819627E-01
F_4 / $s^{1/2}$	4.197430E-01	2.527035E-02	3.686911E-01	4.707948E-01

#10

time stamp / s	3101.185
degrees of freedom	41
weighted sum of squares (Q/Ω^2)	2.81509E+00
weighted standard error	6.86607E-02
critical *t*-value at 95% confidence level	2.02023E+00

Parameter	Estimated Value	St. Error	Lower Limit	Upper Limit
R_u / Ω	1.897721E+01	4.482323E-01	1.807168E+01	1.988274E+01
R_{ct} / Ω	3.142338E+02	3.173627E+00	3.078223E+02	3.206452E+02
B / F·$\Omega^{1-1/b}$	1.986156E-06	6.107612E-08	1.862768E-06	2.109544E-06
b	9.699269E-01	5.497656E-03	9.588204E-01	9.810335E-01
P_1 / Ω·$s^{-1/2}$	1.167188E+03	2.454730E+01	1.117597E+03	1.216779E+03
F_1 / $s^{1/2}$	2.472794E+00	7.068003E-02	2.330005E+00	2.615584E+00
F_2 / $s^{1/2}$	9.223601E-01	2.864064E-02	8.644995E-01	9.802207E-01
F_3 / $s^{1/2}$	1.631593E-01	1.013064E-02	1.426931E-01	1.836255E-01
F_4 / $s^{1/2}$	4.148409E-01	2.227961E-02	3.698310E-01	4.598508E-01

#11

time stamp / s	3448.118
degrees of freedom	41
weighted sum of squares (Q/Ω^2)	2.83581E+00
weighted standard error	6.91660E-02
critical *t*-value at 95% confidence level	2.02023E+00

Parameter	Estimated Value	St. Error	Lower Limit	Upper Limit
R_u / Ω	1.899891E+01	4.546159E-01	1.808048E+01	1.991734E+01
R_{ct} / Ω	2.928210E+02	3.000392E+00	2.867596E+02	2.988825E+02
B / F·$\Omega^{1-1/b}$	1.970540E-06	6.242121E-08	1.844435E-06	2.096645E-06
b	9.711129E-01	5.702811E-03	9.595919E-01	9.826339E-01
P_1 / Ω·$s^{-1/2}$	1.177654E+03	2.376619E+01	1.129641E+03	1.225667E+03
F_1 / $s^{1/2}$	2.403706E+00	6.194300E-02	2.278568E+00	2.528845E+00
F_2 / $s^{1/2}$	8.843524E-01	2.669025E-02	8.304320E-01	9.382728E-01
F_3 / $s^{1/2}$	1.565954E-01	9.407213E-03	1.375907E-01	1.756001E-01
F_4 / $s^{1/2}$	3.945629E-01	2.045545E-02	3.532382E-01	4.358876E-01

#12

time stamp / s	3795.114
degrees of freedom	41
weighted sum of squares (Q/Ω^2)	3.38208E+00
weighted standard error	8.24897E-02
critical *t*-value at 95% confidence level	2.02023E+00

Parameter	Estimated Value	St. Error	Lower Limit	Upper Limit
R_u / Ω	1.912619E+01	5.015057E-01	1.811303E+01	2.013935E+01
R_{ct} / Ω	2.716250E+02	3.096874E+00	2.653686E+02	2.778814E+02
B / F·$\Omega^{1-1/b}$	1.989215E-06	7.077893E-08	1.846225E-06	2.132205E-06
b	9.758006E-01	6.507358E-03	9.626542E-01	9.889469E-01
P_1 / Ω·$s^{-1/2}$	1.209437E+03	2.437314E+01	1.160197E+03	1.258676E+03
F_1 / $s^{1/2}$	2.377013E+00	6.037770E-02	2.255036E+00	2.498990E+00
F_2 / $s^{1/2}$	8.751968E-01	2.651501E-02	8.216304E-01	9.287632E-01
F_3 / $s^{1/2}$	1.593041E-01	9.777762E-03	1.395508E-01	1.790574E-01
F_4 / $s^{1/2}$	3.896515E-01	2.035725E-02	3.485252E-01	4.307778E-01

#13

time stamp / s	4142.181
degrees of freedom	41
weighted sum of squares (Q / Ω^2)	3.55312E+00
weighted standard error	8.66614E-02
critical t-value at 95% confidence level	2.02023E+00

Parameter	Estimated Value	St. Error	Lower Limit	Upper Limit
R_{u} / Ω	1.921164E+01	5.178751E-01	1.816541E+01	2.025786E+01
R_{ct} / Ω	2.550068E+02	2.985106E+00	2.489762E+02	2.610374E+02
$B / \mathrm{F}\cdot\Omega^{1-1/\mathrm{b}}$	2.002290E-06	7.434043E-08	1.852106E-06	2.152475E-06
b	9.796034E-01	6.865227E-03	9.657340E-01	9.934727E-01
$P_1 / \Omega\cdot\mathrm{s}^{-1/2}$	1.239370E+03	2.330795E+01	1.192283E+03	1.286457E+03
$F_1 / \mathrm{s}^{1/2}$	2.362946E+00	5.664860E-02	2.248503E+00	2.477389E+00
$F_2 / \mathrm{s}^{1/2}$	8.600473E-01	2.446072E-02	8.106311E-01	9.094635E-01
$F_3 / \mathrm{s}^{1/2}$	1.614448E-01	9.544013E-03	1.421637E-01	1.807259E-01
$F_4 / \mathrm{s}^{1/2}$	3.889247E-01	1.885051E-02	3.508424E-01	4.270070E-01

#14

time stamp / s	4488.584
degrees of freedom	41
weighted sum of squares (Q / Ω^2)	3.44010E+00
weighted standard error	8.39048E-02
critical t-value at 95% confidence level	2.02023E+00

Parameter	Estimated Value	St. Error	Lower Limit	Upper Limit
R_{u} / Ω	1.923207E+01	5.138249E-01	1.819403E+01	2.027011E+01
R_{ct} / Ω	2.416391E+02	2.809903E+00	2.359625E+02	2.473157E+02
$B / \mathrm{F}\cdot\Omega^{1-1/\mathrm{b}}$	1.994715E-06	7.432525E-08	1.844561E-06	2.144869E-06
b	9.811035E-01	6.934172E-03	9.670949E-01	9.951121E-01
$P_1 / \Omega\cdot\mathrm{s}^{-1/2}$	1.251793E+03	2.231636E+01	1.206709E+03	1.296877E+03
$F_1 / \mathrm{s}^{1/2}$	2.339007E+00	5.213963E-02	2.233673E+00	2.444341E+00
$F_2 / \mathrm{s}^{1/2}$	8.393975E-01	2.279607E-02	7.933443E-01	8.854508E-01
$F_3 / \mathrm{s}^{1/2}$	1.560035E-01	8.853960E-03	1.381165E-01	1.738905E-01
$F_4 / \mathrm{s}^{1/2}$	3.782369E-01	1.757301E-02	3.427354E-01	4.137384E-01

#15

time stamp / s	4839.730
degrees of freedom	41
weighted sum of squares (Q / Ω^2)	3.89178E+00
weighted standard error	9.49214E-02
critical t-value at 95% confidence level	2.02023E+00

Parameter	Estimated Value	St. Error	Lower Limit	Upper Limit
R_u / Ω	1.931552E+01	5.506094E-01	1.820317E+01	2.042788E+01
R_{ct} / Ω	2.283418E+02	2.847132E+00	2.225899E+02	2.340936E+02
B / F·$\Omega^{1-1/b}$	2.005915E-06	8.097827E-08	1.842321E-06	2.169510E-06
b	9.846680E-01	7.593739E-03	9.693269E-01	1.000009E+00
P_1 / Ω·$s^{-1/2}$	1.275234E+03	2.247974E+01	1.229820E+03	1.320648E+03
F_1 / $s^{1/2}$	2.331945E+00	5.182367E-02	2.227249E+00	2.436640E+00
F_2 / $s^{1/2}$	8.274750E-01	2.246974E-02	7.820810E-01	8.728690E-01
F_3 / $s^{1/2}$	1.564578E-01	8.926510E-03	1.384243E-01	1.744914E-01
F_4 / $s^{1/2}$	3.709760E-01	1.716143E-02	3.363060E-01	4.056460E-01

#16

time stamp / s	5190.759
degrees of freedom	41
weighted sum of squares (Q / Ω^2)	4.77402E+00
weighted standard error	1.16439E-01
critical t-value at 95% confidence level	2.02023E+00

Parameter	Estimated Value	St. Error	Lower Limit	Upper Limit
R_u / Ω	1.939078E+01	6.151301E-01	1.814807E+01	2.063348E+01
R_{ct} / Ω	2.157730E+02	3.062320E+00	2.095864E+02	2.219596E+02
B / F·$\Omega^{1-1/b}$	2.021115E-06	9.259606E-08	1.834050E-06	2.208180E-06
b	9.885361E-01	8.735981E-03	9.708875E-01	1.006185E+00
P_1 / Ω·$s^{-1/2}$	1.296593E+03	2.420246E+01	1.247698E+03	1.345487E+03
F_1 / $s^{1/2}$	2.296286E+00	5.233721E-02	2.190553E+00	2.402020E+00
F_2 / $s^{1/2}$	8.171172E-01	2.356349E-02	7.695136E-01	8.647209E-01
F_3 / $s^{1/2}$	1.571226E-01	9.633965E-03	1.376598E-01	1.765854E-01
F_4 / $s^{1/2}$	3.653992E-01	1.805132E-02	3.289314E-01	4.018670E-01

References

[1] K.J. Szekeres, K. Hegedüs, M. Ujvári, G.G. Láng, Investigation of the electrochemical properties of poly(3,4-ethylenedioxypyrrole) films electrodeposited from aqueous solutions, Journal of Electroanalytical Chemistry. 826 (2018) 16–22. doi:10.1016/j.jelechem.2018.08.017.

[2] K.J. Szekeres, É. Fekete, M. Ujvári, S. Vesztergom, V. V. Kondratiev, G.G. Láng, Some observations on the electrochemical reactions of bisphenol A on polycrystalline gold in contact with 0.1 M aqueous $NaClO_4$ solution, Russian Journal of Electrochemistry. 55 (2019) 1127–1135. doi:10.1134/S1023193519110132.

[3] K.J. Szekeres, M. Ujvári, S. Vesztergom, G.G. Láng, Voltammetric and electrochemical impedance analysis of poly(bisphenol A) supported poly(3,4-ethylenedioxythiophene) layers deposited on gold – the effects of thickness distribution, overoxidation and non-stationarity, Electrochimica Acta. 391 (2021) 138975. doi:10.1016/j.electacta.2021.138975.

[4] K. Szekeres, P. Bollella, Y. Kim, S. Minko, A. Melman, E. Katz, Magneto-Controlled Enzyme Activity with Locally Produced pH Changes, Journal of Physical Chemistry Letters. 12 (2021) 2523–2527. doi:10.1021/acs.jpclett.1c00036.

[5] K.J. Szekeres, S. Vesztergom, M. Ujvári, G.G. Láng, Some methods for the determination of valid impedance spectra in non-stationary electrochemical systems – concepts and techniques of practical importance, ChemElectroChem. 8 (2021) 1233–1250. doi:10.1002/celc.202100093.

[6] G.G. Láng, K.J. Szekeres, Vas-oxidot/hidroxidot tartalmazó vezető polimer kompozitok és előállításuk ferrátsók alkalmazásával, P2100074 számú magyar szabadalmi bejelentés, 2021.

[7] K.J. Szekeres, G.G. Láng, M. Ujvári, Electrochemical and morphological investigations of poly(3,4-ethylenedioxythiophene) films in different electrolyte solutions, in: Book of Abstracts, 6th Regional Symposium on Electrochemistry of South-East Europe, Budapest, Magyarország, 2017: pp. 25–26.

[8] K.J. Szekeres, U. Mária, G.G. Láng, Electrochemical and morphological investigations of poly(3,4-ethylenedioxypirrol) films, in: Book of Abstracts, 7th Regional Symposium on Electrochemistry – South East Europe & 8th Kurt Schwabe Symposium, Split, Croatia, 2019: p. 179.

[9] K.J. Szekeres, É. Fekete, G.G. Láng, Investigation of the electrochemical behavior of bisphenol A on gold in contact with 0.1 M aqueous $NaClO_4$ solution, in: Book of Abstracts, 7th Regional Symposium on Electrochemistry – South East Europe & 8th Kurt Schwabe Symposium, Split, Croatia, 2019: p. 83.

[10] K.J. Szekeres, M. Ujvári, G.G. Láng, Electrochemical and morphological characterization of poly(3, 4-ethylenedioxypyrrole) films electrodeposited from aqueous solutions, in: 11th International Symposium on Electrochemical Impedance Spectroscopy Program & Book of Abstracts, Lège-Cap-Ferret, France, 2019: p. 106.

[11] G.G. Láng, K.J. Szekeres, M. Ujvári, S. Vesztergom, Electrochemical Impedance Spectroscopy for the Characterization of Conductive Polymer Films – The Non-stationary Case, in: The 71st Annual Meeting of the International Society of Electrochemistry, Belgrade, Serbia, 2020. http://ise-2020-symposium17.fkit.hr/?page_id=132.

[12] M. Ujvári, J. Gubicza, V. Kondratiev, K.J. Szekeres, G.G. Láng, Morphological changes in electrochemically deposited poly(3,4-ethylenedioxythiophene) films during overoxidation, Journal of Solid State Electrochemistry. 19 (2015) 1247–1252. doi:10.1007/s10008-015-2746-6.

[13] G.G. Láng, M. Ujvári, S. Vesztergom, V. Kondratiev, J. Gubicza, K.J. Szekeres, The

electrochemical degradation of poly(3,4-ethylenedioxythiophene) films electrodeposited from aqueous solutions, Zeitschrift Für Physikalische Chemie. 230 (2016) 1281–1302. doi:10.1515/zpch-2016-0752.

[14] M. Ujvári, G.G. Láng, S. Vesztergom, K.J. Szekeres, N. Kovács, J. Gubicza, Structural changes during the overoxidation of electrochemically deposited poly(3,4-ethylenedioxythiophene) films, Journal of Electrochemical Science and Engineering. 6 (2016) 77–89. doi:10.5599/jese.225.

[15] D. Zalka, N. Kovács, K. Szekeres, M. Ujvári, S. Vesztergom, S. Eliseeva, V. Kondratiev, G.G. Láng, Determination of the charge transfer resistance of poly(3,4-ethylenedioxythiophene)-modified electrodes immediately after overoxidation, Electrochimica Acta. 247 (2017) 321–332. doi:10.1016/j.electacta.2017.06.177.

[16] G.G. Láng, N. Kovács, S. Vesztergom, M. Ujvári, D. Zalka, K. Szekeres, Experimental methods for the determination of stress changes at electrified solid-liquid interfaces, Technisches Messen. 84 (2017) 644–658. doi:10.1515/teme-2016-0082.

[17] G.G. Láng, V. Kondratiev, M. Ujvári, S. Vesztergom, K. Szekeres, D. Zalka, Structural Changes During the Overoxidation of Poly(3,4-Ethylenedioxythiophene) Films Electrodeposited from Surfactant-Free Aqueous Solutions, in: K. Wandelt (Ed.), Encyclopedia of Interfacial Chemistry Surface Science and Electrochemistry, 1st Editio, Amsterdam; London; New York; Tokyo, 2018: pp. 258–270.

[18] T. Földesi, G. Sipos, R. Adamik, B. Nagy, B.L. Tóth, A. Bényei, K.J. Szekeres, G.G. Láng, A. Demeter, T.J. Peelen, Z. Novák, Design and application of diimine-based copper(i) complexes in photoredox catalysis, Organic and Biomolecular Chemistry. 17 (2019) 8343–8347. doi:10.1039/c9ob01331h.

[19] К.Й. Секереш, Э. Фекете, М. Уйвари, С. Вестергом, В.В. Кондратьев, Г.Г. Ланг, Некоторые наблюдения электрохимических реакций бисфенола А на поликристаллическом золоте в контакте с водным раствором 0.1 М $NaClO_4$, Электрохимия. 55 (2019) 1381–1390. doi:10.1134/S0424857019110148.

[20] A.D. McNaught, A. Wilkinson, IUPAC, Compendium of Chemical Terminology (The Gold Book), 2nd ed., Blackwell Science, 1997.

[21] S. Hideki, E.J. Louis, A.G. MacDiarmid, C.K. Chiang, A.J. Heeger, Synthesis of Electrically-Conducting organic Polymers: Halogen Derivatives of Polyacatylene, $(CH)_x$, J.C.S., Chemical Communications. (1977) 578–580. doi:10.1039/c39770000578.

[22] A. Heeger, A.G. MacDiarmid, H. Shirakawa, The Nobel Prize in chemistry, 2000: conductive polymers, Stockholm, Sweden: Royal Swedish Academy of Sciences. (2000) 1–16. doi:http://www.nobelprize.org/nobel_prizes/chemistry/laureates/2000/advanced-chemistryprize2000.pdf.

[23] H. Letheby, On the Production of a Blue Substance by the Electrolpsis of Sulyhate of Aniline, Journal of the Chemical Society. 15 (1862) 161–163.

[24] A.J. Bard, G. Inzelt, F. Scholz, Electrochemical Dictionary, 2nd ed., Springer, Berlin–Heidelberg, 2012.

[25] J. Janata, M. Josowicz, Conducting polymers in electronic chemical sensors, Nature Materials. 2 (2003) 19–24. doi:10.1038/nmat768.

[26] M. Gereadr, A. Choubey, B.. Malhotra, Application of conducting polymer to biosensors, Biosensors and Bioelectronics. 17 (2002) 345–359. doi:10.1016/S0956-5663(01)00312-8.

[27] A. Ramanavičius, A. Ramanavičiene, A. Malinauskas, Electrochemical sensors based on conducting polymer-polypyrrole, Electrochimica Acta. 51 (2006) 6025–6037. doi:10.1016/j.electacta.2005.11.052.

[28] T.C. Pearce, J.W. Gardner, S. Friel, P.N. Bartlett, N. Blair, Electronic Nose for Monitoring the Flavour of Beers, Analyst. 118 (1993) 371–377. doi:10.1039/AN9931800371.

[29] C.J. Drury, C.M.J. Mutsaers, C.M. Hart, M. Matters, D.M. de Leeuw, Low-cost all-polymer integrated circuits, Applied Physics Letters. 73 (1998) 108–110. doi:10.1063/1.121783.

[30] D.D.L. Chung, Materials for electromagnetic interference shielding, Materials Chemistry and Physics. 255 (2020) 123587. doi:10.1016/j.matchemphys.2020.123587.

[31] A.P. Kulkarni, C.J. Tonzola, A. Babel, S.A. Jenekhe, Electron Transport Materials for Organic Light-Emitting Diodes, Chemistry of Materials. 16 (2004) 4556–4573. doi:10.1021/cm049473l.

[32] C.G. Granqvist, A. Azens, A. Hjelm, L. Kullman, G.A. Niklasson, D. Rönnow, M. Strømme Mattsson, M. Veszelei, G. Vaivars, Recent advances in electrochromics for smart windows applications, Solar Energy. 63 (1998) 199–216. doi:10.1016/S0038-092X(98)00074-7.

[33] X. Cui, V.A. Lee, Y. Raphael, J.A. Wiler, J.F. Hetke, D.J. Anderson, D.C. Martin, Surface modification of neural recording electrodes with conducting polymer/biomolecule blends, Journal of Biomedical Materials Research. 56 (2001) 261–272. doi:10.1002/1097-4636(200108)56:2<261::AID-JBM1094>3.0.CO;2-I.

[34] X. Cui, J.F. Hetke, J.A. Wiler, D.J. Anderson, D.C. Martin, Electrochemical deposition and characterization of conducting polymer polypyrrole/PSS on multichannel neural probes, Sensors and Actuators, A: Physical. 93 (2001) 8–18. doi:10.1016/S0924-4247(01)00637-9.

[35] Y. Xiao, X. Cui, J.M. Hancock, M. Bouguettaya, J.R. Reynolds, D.C. Martin, Electrochemical polymerization of poly(hydroxymethylated-3,4- ethylenedioxythiophene) (PEDOT-MeOH) on multichannel neural probes, Sensors and Actuators, B: Chemical. 99 (2004) 437–443. doi:10.1016/j.snb.2003.12.067.

[36] Y. Xiao, D.C. Martin, X. Cui, M. Shenai, Surface Modification of Neural Probes with Conducting Polymer Poly(hydroxymethylated-3,4-ethylenedioxythiophene) and Its Biocompatibility, Applied Biochemistry and Biotechnology. 128 (2006) 117–129. doi:10.1385/ABAB:128:2:117.

[37] L. Nyholm, G. Nyström, A. Mihranyan, M. Strømme, Toward Flexible Polymer and Paper-Based Energy Storage Devices, Advanced Materials. 23 (2011) 3751–3769. doi:10.1002/adma.201004134.

[38] D.P. Dubal, S.H. Lee, J.G. Kim, W.B. Kim, C.D. Lokhande, Porous polypyrrole clusters prepared by electropolymerization for a high performance supercapacitor, Journal of Materials Chemistry. 22 (2012) 3044–3052. doi:10.1039/c2jm14470k.

[39] R. Ramya, R. Sivasubramanian, M. V. Sangaranarayanan, Conducting polymers-based electrochemical supercapacitors - Progress and prospects, Electrochimica Acta. 101 (2013) 109–129. doi:10.1016/j.electacta.2012.09.116.

[40] R. Holze, Y.P. Wu, Intrinsically conducting polymers in electrochemical energy technology: Trends and progress, Electrochimica Acta. 122 (2014) 93–107. doi:10.1016/j.electacta.2013.08.100.

[41] A.M. Bryan, L.M. Santino, Y. Lu, S. Acharya, J.M. D'Arcy, Conducting Polymers for Pseudocapacitive Energy Storage, Chemistry of Materials. 28 (2016) 5989–5998. doi:10.1021/acs.chemmater.6b01762.

[42] J. Kim, J.H. Kim, K. Ariga, Redox-Active Polymers for Energy Storage Nanoarchitectonics, Joule. 1 (2017) 739–768. doi:10.1016/j.joule.2017.08.018.

[43] X. Li, X. Chen, Z. Jin, P. Li, D. Xiao, Recent progress in conductive polymers for advanced fiber-shaped electrochemical energy storage devices, Materials Chemistry Frontiers. 5 (2021) 1140–1163. doi:10.1039/d0qm00745e.

[44] P. Novák, K. Müller, K.S.V. Santhanam, O. Haas, Electrochemically Active Polymers for Rechargeable Batteries, Chemical Reviews. 97 (1997) 207–281. doi:10.1021/cr941181o.

[45] Y. Shi, L. Peng, Y. Ding, Y. Zhao, G. Yu, Nanostructured conductive polymers for advanced energy storage, Chemical Society Reviews. 44 (2015) 6684–6696. doi:10.1039/C5CS00362H.

[46] F. Meng, Y. Ding, Sub-Micrometer-Thick All-Solid-State Supercapacitors with High Power and Energy Densities, Advanced Materials. 23 (2011) 4098–4102. doi:10.1002/adma.201101678.

[47] T.F. Otero, J.G. Martinez, J. Arias-Pardilla, Biomimetic electrochemistry from conducting polymers. A review: Artificial muscles, smart membranes, smart drug delivery and computer/neuron interfaces, Electrochimica Acta. 84 (2012) 112–128. doi:10.1016/j.electacta.2012.03.097.

[48] X. Luo, X.T. Cui, Sponge-like nanostructured conducting polymers for electrically controlled drug

release, Electrochemistry Communications. 11 (2009) 1956–1959. doi:10.1016/j.elecom.2009.08.027.

[49] G. Inzelt, Conducting Polymers (A New Era in Electrochemistry), 2nd ed., Springer, Berlin, Heidelberg, 2012.

[50] G. Inzelt, Recent advances in the field of conducting polymers, Journal of Solid State Electrochemistry. 21 (2017) 1965–1975. doi:10.1007/s10008-017-3611-6.

[51] G. Inzelt, Conducting polymers: past, present, future, Journal of Electrochemical Science and Engineering. 8 (2018) 3–37. doi:10.5599/jese.448.

[52] M. Ujvári, M. Takács, S. Vesztergom, F. Bazsó, F. Ujhelyi, G.G. Láng, Monitoring of the electrochemical degradation of PEDOT films on gold using the bending beam method, Journal of Solid State Electrochemistry. 15 (2011) 2341–2349. doi:10.1007/s10008-011-1472-y.

[53] G. Láng, G. Inzelt, Some Problems Connected With Impedance Analysis of Polymer Film Electrodes : Effect of the Film Thickness and the Thickness Distribution, Electrochimica Acta. 36 (1991) 847–854. doi:10.1016/0013-4686(91)85284-E.

[54] X. Li, Y. Jiao, S. Li, The syntheses, properties and application of new conducting polymers, European Polymer Journal. 27 (1991) 1345–1351. doi:10.1016/0014-3057(91)90233-E.

[55] M.S. Ba-Shammakh, Ba-Shammakh_Thesis2002.pdf, King Fahd University of Petroleum and Minerals, Dhahran, Saudi Arabia, 2002.

[56] S.U. Rahman, M.S. Ba-Shammakh, Thermal effects on the process of electropolymerization of pyrrole on mild steel, Synthetic Metals. 140 (2004) 207–223. doi:10.1016/S0379-6779(03)00369-2.

[57] N. Belhadj Tahar, A. Savall, Electropolymerization of phenol on a vitreous carbon electrode in alkaline aqueous solution at different temperatures, Electrochimica Acta. 55 (2009) 465–469. doi:10.1016/j.electacta.2009.08.040.

[58] W. Poppendieck, K.-P. Hoffmann, Coating of neural microelectrodes with intrinsically conducting polymers as a means to improve their electrochemical properties, in: 4th European Conference of the International Federation for Medical and Biological Engineering IFMBE Proceedings, 2009: pp. 2409–2412.

[59] I.Y. Sapurina, J. Stejskal, The effect of pH on the oxidative polymerization of aniline and the morphology and properties of products, Russian Chemical Reviews. 79 (2010) 1123–1143. doi:10.1070/rc2010v079n12abeh004140.

[60] S.-C. Luo, J. Sekine, B. Zhu, H. Zhao, A. Nakao, H. Yu, Polydioxythiophene Nanodots, Nonowires, Nano-Networks, and Tubular Structures: The Effect of Functional Groups and Temperature in Template-Free Electropolymerization, ACS Nano. 6 (2012) 3018–3026. doi:10.1021/nn300737e.

[61] S.K. Mondal, K.R. Prasad, N. Munichandraiah, Analysis of electrochemical impedance of polyaniline films prepared by galvanostatic, potentiostatic and potentiodynamic methods, Synthetic Metals. 148 (2005) 275–286. doi:10.1016/j.synthmet.2004.10.010.

[62] S. Patra, K. Barai, N. Munichandraiah, Scanning electron microscopy studies of PEDOT prepared by various electrochemical routes, Synthetic Metals. 158 (2008) 430–435. doi:10.1016/j.synthmet.2008.03.002.

[63] V. Castagnola, C. Bayon, E. Descamps, C. Bergaud, Morphology and conductivity of PEDOT layers produced by different electrochemical routes, Synthetic Metals. 189 (2014) 7–16. doi:10.1016/j.synthmet.2013.12.013.

[64] E. Kriván, C. Visy, J. Kankare, Deprotonation and Dehydration of Pristine PPy/DS Films during Open-Circuit Relaxation: an Ignored Factor in Determining the Properties of Conducting Polymers, Journal of Physical Chemistry B. 107 (2003) 1302–1308. doi:10.1021/jp0214615.

[65] S.K. Mondal, K. Barai, N. Munichandraiah, High capacitance properties of polyaniline by electrochemical deposition on a porous carbon substrate, Electrochimica Acta. 52 (2007) 3258–3264. doi:10.1016/j.electacta.2006.09.067.

[66] W.E. Van der Linden, J.W. Dieker, Glassy carbon as electrode material in electro- analytical chemistry, Analytica Chimica Acta. 119 (1980) 1–24. doi:10.1016/S0003-2670(00)00025-8.

[67] A. Sumisha, K. Haribabu, Modification of graphite felt using nano polypyrrole and polythiophene for microbial fuel cell applications-a comparative study, International Journal of Hydrogen Energy. 43 (2018) 3308–3316. doi:10.1016/j.ijhydene.2017.12.175.

[68] P. Xue, X.M. Tao, K.W.Y. Kwok, M.Y. Leung, T.X. Yu, Electromechanical Behavior of Fibers Coated with an Electrically Conductive Polymer, Textile Research Journal. 74 (2004) 929–936. doi:10.1177/004051750407401013.

[69] Y.L. Kang, S. Ibrahim, S. Pichiah, Synergetic effect of conductive polymer poly(3,4-ethylenedioxythiophene) with different structural configuration of anode for microbial fuel cell application, Bioresource Technology. 189 (2015) 364–369. doi:10.1016/j.biortech.2015.04.044.

[70] A. Elschner, S. Kirchmeyer, W. Lövenich, U. Merker, K. Reuter, PEDOT - Principles and Applications of an Intrinsically Conductive Polymer, CRC Press, Boca Raton, FL, 2011.

[71] A.D. Aguilar, E.S. Forzani, M. Leright, F. Tsow, A. Cagan, R.A. Iglesias, L.A. Nagahara, I. Amlani, R. Tsui, N.J. Tao, A hybrid nanosensor for TNT vapor detection, Nano Letters. 10 (2010) 380–384. doi:10.1021/nl902382s.

[72] J. Jang, M. Chang, H. Yoon, Chemical sensors based on highly conductive poly(3,4-ethylene-dioxythiophene) nanorods, Advanced Materials. 17 (2005) 1616–1620. doi:10.1002/adma.200401909.

[73] K. Dunst, J. Karczewski, P. Jasiński, Nitrogen dioxide sensing properties of PEDOT polymer films, Sensors and Actuators, B: Chemical. 247 (2017) 108–113. doi:10.1016/j.snb.2017.03.003.

[74] J. Yang, D.H. Kim, J.L. Hendricks, M. Leach, R. Northey, D.C. Martin, Ordered surfactant-templated poly(3,4-ethylenedioxythiophene) (PEDOT) conducting polymer on microfabricated neural probes, Acta Biomaterialia. 1 (2005) 125–136. doi:10.1016/j.actbio.2004.09.006.

[75] A. Özcan, S. Ilkbaş, Preparation of poly(3,4-ethylenedioxythiophene) nanofibers modified pencil graphite electrode and investigation of over-oxidation conditions for the selective and sensitive determination of uric acid in body fluids, Analytica Chimica Acta. 891 (2015) 312–320. doi:10.1016/j.aca.2015.08.015.

[76] J.M. Lin, Y.L. Su, W.T. Chang, W.Y. Su, S.H. Cheng, Strong adsorption characteristics of a novel overoxidized poly(3,4-ethylenedioxythiophene) film and application for dopamine sensing, Electrochimica Acta. 149 (2014) 65–75. doi:10.1016/j.electacta.2014.10.030.

[77] N. Rozlosnik, New directions in medical biosensors employing poly(3,4-ethylenedioxy thiophene) derivative-based electrodes, Analytical and Bioanalytical Chemistry. 395 (2009) 637–645. doi:10.1007/s00216-009-2981-8.

[78] D.C. Martin, Molecular design, synthesis, and characterization of conjugated polymers for interfacing electronic biomedical devices with living tissue, MRS Communications. 5 (2015) 131–153. doi:10.1557/mrc.2015.17.

[79] S. Nagane, P. Sitarik, Y. Wu, Q. Baugh, S. Chhatre, J. Lee, D.C. Martin, Functionalized Polythiophene Copolymers for Electronic Biomedical Devices, MRS Advances. 5 (2020) 943–956. doi:10.1557/adv.2020.3.

[80] A. Zykwinska, W. Domagala, B. Pilawa, M. Lapkowski, Electrochemical overoxidation of poly(3,4-ethylenedioxythiophene) - PEDOT studied by means of in situ ESR spectroelectrochemistry, Electrochimica Acta. 50 (2005) 1625–1633. doi:10.1016/j.electacta.2004.10.026.

[81] G.G. Láng, M. Ujvári, F. Bazsó, S. Vesztergom, F. Ujhelyi, In situ monitoring of the electrochemical degradation of polymer films on metals using the bending beam method and impedance spectroscopy, Electrochimica Acta. 73 (2012) 59–69. doi:10.1016/j.electacta.2012.01.068.

[82] M. Ujvári, D. Zalka, S. Vesztergom, S. Eliseeva, V. Kondratiev, G.G. Láng, Electrochemical impedance measurements in non-stationary systems - application of the 4-dimensional analysis method for the impedance analysis of overoxidized poly(3,4-ethylenedioxythiophene)-modified electrodes, Bulgarian Chemical Communications. 49 (2017) 106–113.

[83] D. Zalka, S. Vesztergom, M. Ujvári, G.G. Láng, Electrochemical behaviour of poly(3,4-ethylenedioxytiophene) modified glassy carbon electrodes after overoxidation — the influence of the substrate on the charge transfer resistance, Journal of Electrochemical Science and Engineering. 8 (2018) 151–162. doi:10.5599/jese.508.

[84] Q. Pei, O. Inganäs, Electrochemical applications of the bending beam method. 1. Mass transport and volume changes in polypyrrole during redox, Journal of Physical Chemistry. 96 (1992) 10507–10514. doi:10.1021/j100204a071.

[85] Q. Pei, O. Inganäs, Electrochemical applications of the bending beam method. 2. Electroshrinking and slow relaxation in polypyrrole, Journal of Physical Chemistry. 97 (1993) 6034–6041. doi:10.1021/j100124a041.

[86] M. Seo, Electro-Chemo-Mechanical Properties of Solid Electrode Surfaces, Springer, Singapore, 2020. doi:10.1007/978-981-15-7277-7.

[87] Y. Hui, C. Bian, J. Wang, J. Tong, S. Xia, Comparison of two types of overoxidized PEDOT films and their application in sensor fabrication, Sensors. 17 (2017) 628. doi:10.3390/s17030628.

[88] L. Pigani, A. Heras, Á. Colina, R. Seeber, J. López-Palacios, Electropolymerisation of 3 , 4-ethylenedioxythiophene in aqueous solutions, Electrochemistry Communications. 6 (2004) 1192–1198. doi:10.1016/j.elecom.2004.09.021.

[89] C.L. Gaupp, K. Zong, P. Schottland, B.C. Thompson, C.A. Thomas, J.R. Reynolds, Poly(3,4-ethylenedioxypyrrole): organic electrochemistry of a highly stable electrochromic polymer, Macromolecules. 33 (2000) 1132–1133. doi:10.1021/ma9916180.

[90] S. Caramori, S. Cazzanti, L. Marchini, R. Argazzi, C.A. Bignozzi, D. Martineau, P.C. Gros, M. Beley, Dye-sensitized solar cells based on PEDOP as a hole conductive medium, Inorganica Chimica Acta. 361 (2008) 627–634. doi:10.1016/j.ica.2007.04.016.

[91] A. Kharkwal, D. Melepurath, A.G. Joshi, A.K. Srivastava, Red to blue high electrochromic contrast and rapid switching poly(3,4-ethylenedioxypyrrole)-Au/Ag nanocomposite devices for smart windows, ChemPhysChem. 12 (2011) 1176–1188. doi:10.1002/cphc.201000973.

[92] Ö. Türkarslan, S.K. Kayahan, L. Toppare, A new amperometric cholesterol biosensor based on poly(3,4- ethylenedioxypyrrole), Sensors and Actuators, B: Chemical. 136 (2009) 484–488. doi:10.1016/j.snb.2008.10.016.

[93] Ö. Türkarslan, A.E. Böyükbayram, L. Toppare, Amperometric alcohol biosensors based on conducting polymers: Polypyrrole, poly(3,4-ethylenedioxythiophene) and poly(3,4-ethylenedioxypyrrole), Synthetic Metals. 160 (2010) 808–813. doi:10.1016/j.synthmet.2010.01.027.

[94] J.Y. Wong, R. Langer, D.E. Ingber, Electrically conducting polymers can noninvasively control the shape and growth of mammalian cells., Proceedings of the National Academy of Sciences. 91 (1994) 3201–3204. doi:10.1073/pnas.91.8.3201.

[95] P. Schottland, K. Zong, C.L. Gaupp, B.C. Thompson, C.A. Thomas, I. Giurgiu, R. Hickman, K.A. Abboud, J.R. Reynolds, Poly(3,4-alkylenedioxypyrrole)s: Highly Stable Electronically Conducting and Electrochromic Polymers, Macromolecules. 33 (2000) 7051–7061. doi:10.1021/ma000490f.

[96] G. Sonmez, P. Schottland, K. Zong, J.R. Reynolds, Highly transmissive and conductive poly[(3,4--alkylenedioxy)pyrrole--2,5-diyl] (PXDOP) films prepared by air or transition metal catalyzed chemical oxidation, Journal of Materials Chemistry. 11 (2001) 289–294. doi:10.1039/b007976f.

[97] A. Kraft, M. Rottmann, H.D. Gilsing, H. Faltz, Electrodeposition and electrochromic properties of N-ethyl substituted poly(3,4-ethylenedioxypyrrole), Electrochimica Acta. 52 (2007) 5856–5862. doi:10.1016/j.electacta.2007.03.012.

[98] E. Unur, J.H. Jung, R.J. Mortimer, J.R. Reynolds, Dual-polymer electrochromic film characterization using bipotentiostatic control, Chemistry of Materials. 20 (2008) 2328–2334. doi:10.1021/cm703354q.

[99] R.M. Walczak, J.R. Reynolds, Poly(3,4-alkylenedioxypyrroles): The PXDOPs as versatile yet underutilized electroactive and conducting polymers, Advanced Materials. 18 (2006) 1121–1131. doi:10.1002/adma.200502312.

[100] E. Peintler-Kriván, A polipirrol / dodecil-szulfát rendszer tanulmányozása, Szegedi

Tudományegyetem, 2002.

[101] A. Suzuki, A. Sugihara, K. Uchida, T. Sato, Y. Ohta, Developmental effects of perinatal exposure to bisphenol-A and diethylstilbestrol on reproductive organs in female mice, Reproductive Toxicology. 16 (2002) 107–116. doi:10.1016/S0890-6238(02)00005-9.

[102] H.S. Kim, S. Han, S.D. Yoo, B.M. Lee, K.L. Park, Potential estrogenic effects of bisphenol-A estimated by in vitro and in vivo combination assays, The Journal of Toxicological Sciences. 26 (2001) 111–118. doi:10.2131/jts.26.111.

[103] J.R. Rochester, A.L. Bolden, Bisphenol S and F: a systematic review and comparison of the hormonal activity of bisphenol A substitutes, Environmental Health Perspectives. 123 (2015) 643–650. doi:10.1289/ehp.1408989.

[104] M. Petrovic, E. Eljarrat, M.J.L. de Alda, D. Barceló, Endocrine disrupting compounds and other emerging contaminants in the environment: A survey on new monitoring strategies and occurrence data, Analytical and Bioanalytical Chemistry. 378 (2004) 549–562. doi:10.1007/s00216-003-2184-7.

[105] EFSA CEF Panel, Scientific Opinion on the risks to public health related to the presence of bisphenol A (BPA) in foodstuffs: Executive summary, EFSA Journal. 13 (2015) 1–621. doi:10.2903/j.efsa.2015.3978.

[106] M. Giulivo, M. Lopez, D. Alda, E. Capri, D. Barceló, Human exposure to endocrine disrupting compounds: Their role in reproductive systems, metabolic syndrome and breast cancer. A review, Environmental Research. 151 (2016) 251–264. doi:10.1016/j.envres.2016.07.011.

[107] ECHA (European Chemicals Agency), MSC unanimously agrees that Bisphenol A is an endocrine disruptor, (2017). https://echa.europa.eu/hu/-/msc-unanimously-agrees-that-bisphenol-a-is-an-endocrine-disruptor.

[108] BPA update: working group to start reviewing new studies, (2018). http://www.efsa.europa.eu/en/press/news/180904.

[109] ECHA (European Chemicals Agency) and EFSA (European Food Safety Authority) with the technical support of the Joint Research Centre (JRC), N. Andersson, M. Arena, D. Auteri, S. Barmaz, E. Grignard, A. Kienzler, P. Lepper, A.M. Lostia, S. Munn, J. Manuel, P. Morte, F. Pellizzato, J. Tarazona, A. Terron, S. Van Der Linden, Guidance for the identification of endocrine disruptors in the context of Regulations (EU) No 528/2012 and (EC) No 1107/2009, EFSA Journal. 16 (2018) 1–135. doi:10.2903/j.efsa.2018.5311.

[110] K. Rajeshwar, J.G. Ibáñez, Environmental Electrochemistry: Fundamentals and Applications in Pollution Abatement, Academic Press, New York, USA, 1997.

[111] E. Rudd, B.E. Conway, No Title, in: Proc. Electrochemical Society Symp. on Water Purification by Photocatalytic, Photoelectrochemical Procedures and Electrochemical Procedures, Electrochemical Society, Pennington, NJ, 1994: p. 94.

[112] A.B. Boscoletto, F. Gottardi, L. Milan, P. Pannocchia, V. Tartari, M. Tavan, R. Amadelli, A. De Battisti, A. Barbieri, D. Patracchini, G. Battaglin, Electrochemical treatment of bisphenol-A containing wastewaters, Journal of Applied Electrochemistry. 24 (1994) 1052–1058.

[113] K. Matsumoto, B.D.B. Tiu, A. Kawamura, R.C. Advincula, T. Miyata, QCM sensing of bisphenol A using molecularly imprinted hydrogel / conducting polymer matrix, Polymer Journal. 48 (2016) 525–532. doi:10.1038/pj.2016.23.

[114] G. Gatidou, N.S. Thomaidis, A.S. Stasinakis, T.D. Lekkas, Simultaneous determination of the endocrine disrupting compounds nonylphenol , nonylphenol ethoxylates , triclosan and bisphenol A in wastewater and sewage sludge by gas chromatography – mass spectrometry, Journal of Chromatography A. 1138 (2007) 32–41. doi:10.1016/j.chroma.2006.10.037.

[115] A. Ballesteros-Gómez, S. Rubio, D. Pérez-Bendito, Analytical methods for the determination of bisphenol A in food, Journal of Chromatography A. 1216 (2009) 449–469. doi:10.1016/j.chroma.2008.06.037.

[116] M. Panizza, G. Cerisola, Direct and mediated anodic oxidation of organic pollutants, Chemical

Reviews. 109 (2009) 6541–6569. doi:10.1021/cr9001319.

[117] X. Dong, X. Qi, N. Liu, Y. Yang, Y. Piao, Direct electrochemical detection of bisphenol A using a highly conductive graphite nanoparticle film electrode, Sensors. 17 (2017) 836–846. doi:10.3390/s17040836.

[118] X. Li, Y. Cui, Y. Feng, Z. Xie, J. Gu, Reaction pathways and mechanisms of the electrochemical degradation of phenol on different electrodes, Water Research. 39 (2005) 1972–1981. doi:10.1016/j.watres.2005.02.021.

[119] G. Mengoli, M.M. Musiani, Protective coatings on iron by anodic oxidation of phenols in oxalic acid medium, Electrochimica Acta. 31 (1986) 201–210. doi:10.1016/0013-4686(86)87109-2.

[120] H. Kuramitz, Y. Nakata, M. Kawasaki, S. Tanaka, Electrochemical oxidation of bisphenol A. Application to the removal of bisphenol A using a carbon fiber electrode, Chemosphere. 45 (2001) 37–43. doi:10.1016/S0045-6535(01)00032-7.

[121] Y. Cui, X. Li, G. Chen, Electrochemical degradation of bisphenol A on different anodes, Water Research. 43 (2009) 1968–1976. doi:10.1016/j.watres.2009.01.026.

[122] J. Obirai, F. Bedioui, T. Nyokong, Electro-oxidation of phenol and its derivatives on poly-Ni(OH)TPhPyPc modified vitreous carbon electrodes, Journal of Electroanalytical Chemistry. 576 (2005) 323–332. doi:10.1016/j.jelechem.2004.11.006.

[123] B.O. Agboola, K.I. Ozoemena, T. Nyokong, Electrochemical properties of benzylmercapto and dodecylmercapto tetra substituted nickel phthalocyanine complexes : Electrocatalytic oxidation of nitrite, Electrochimica Acta. 51 (2006) 6470–6478. doi:10.1016/j.electacta.2006.04.033.

[124] B. Agboola, T. Nyokong, Electrocatalytic oxidation of chlorophenols by electropolymerised nickel(II) tetrakis benzylmercapto and dodecylmercapto metallophthalocyanines complexes on gold electrodes, Electrochimica Acta. 52 (2007) 5039–5045. doi:10.1016/j.electacta.2007.02.017.

[125] V. Chauke, F. Matemadombo, T. Nyokong, Remarkable sensitivity for detection of bisphenol A on a gold electrode modified with nickel tetraamino phthalocyanine containing Ni–O–Ni bridges, Journal of Hazardous Materials. 178 (2010) 180–186. doi:10.1016/j.jhazmat.2010.01.061.

[126] Y. Zhu, C. Zhou, X. Yan, Y. Yan, Q. Wang, Aptamer-functionalized nanoporous gold film for high-performance direct electrochemical detection of bisphenol A in human serum, Analytica Chimica Acta. 883 (2015) 81–89. doi:10.1016/j.aca.2015.05.002.

[127] C. Hou, W. Tang, C. Zhang, Y. Wang, N. Zhu, A novel and sensitive electrochemical sensor for bisphenol A determination based on carbon black supporting ferroferric oxide nanoparticles, Electrochimica Acta. 144 (2014) 324–331. doi:10.1016/j.electacta.2014.08.053.

[128] Y. Piao, D.J. Han, T.S. Seo, Highly conductive graphite nanoparticle based enzyme biosensor for electrochemical glucose detection, Sensors and Actuators: B. Chemical. 194 (2014) 454–459. doi:10.1016/j.snb.2013.12.045.

[129] G.-P. Nikoleli, D.P. Nikolelis, N. Tzamtzis, N. Psaroudakis, A selective immunosensor for D-dimer based on antibody immobilized on a graphene electrode with incorporated lipid films, Electroanalysis. 26 (2014) 1522–1527. doi:10.1002/elan.201400161.

[130] K. Varmira, M. Saed-Mocheshi, A.R. Jalalvand, Electrochemical sensing and bio-sensing of bisphenol A and detection of its damage to DNA: A comprehensive review, Sensing and Bio-Sensing Research. 15 (2017) 17–33. doi:10.1016/j.sbsr.2017.07.002.

[131] J. Monzó, Y. Malewski, F.J. Vidal-Iglesias, J. Solla-Gullon, Electrochemical oxidation of small organic molecules on Au nanoparticles with preferential surface orientation, ChemElectroChem. 2 (2015) 958–962. doi:10.1002/celc.201500084.

[132] N. Elgrishi, K.J. Rountree, B.D. McCarthy, E.S. Rountree, T.T. Eisenhart, J.L. Dempsey, A Practical Beginner's Guide to Cyclic Voltammetry, Journal of Chemical Education. 95 (2018) 197–206. doi:10.1021/acs.jchemed.7b00361.

[133] V. Climent, J.M. Feliu, Cyclic Voltammetry, in: K. Wandelt (Ed.), Encyclopedia of Interfacial Chemistry, Elsevier, 2018: pp. 48–74. doi:10.1016/B978-0-12-409547-2.10764-4.

[134] A.J. Bard, L.R. Faulkner, Electrochemical Methods, 2nd ed., Wiley, New York, 2001. doi:10.1016/B978-0-12-381373-2.00056-9.

[135] O. Gharbi, M.T.T. Tran, B. Tribollet, M. Turmine, V. Vivier, Revisiting cyclic voltammetry and electrochemical impedance spectroscopy analysis for capacitance measurements, Electrochimica Acta. 343 (2020) 136109. doi:10.1016/j.electacta.2020.136109.

[136] M.E. Orazem, B. Tribollet, Electrochemical Impedance Spectroscopy, John Wiley & Sons, Inc., Hoboken, NJ, 2008.

[137] M.P. Bolton, L.C. Ward, A. Khan, I. Campbell, P. Nightingale, O. Dewit, M. Elia, Sources of error in bioimpedance spectroscopy, Physiological Measurement. 19 (1998) 235–245. doi:10.1088/0967-3334/19/2/011.

[138] K. Darowicki, Theoretical description of the measuring method of instantaneous impedance spectra, Journal of Electroanalytical Chemistry. 486 (2000) 101–105. doi:10.1016/S0022-0728(00)00110-8.

[139] K. Darowicki, J. Orlikowski, G. Lentka, Instantaneous impedance spectra of a non-stationary model electrical system, Journal of Electroanalytical Chemistry. 486 (2000) 106–110. doi:10.1016/S0022-0728(00)00111-X.

[140] K. Darowicki, P. Ślepski, Determination of electrode impedance by means of exponential chirp signal, Electrochemistry Communications. 6 (2004) 898–902. doi:10.1016/j.elecom.2004.06.013.

[141] K. Darowicki, P. Ślepski, M. Szociński, Application of the dynamic EIS to investigation of transport within organic coatings, Progress in Organic Coatings. 52 (2005) 306–310. doi:10.1016/j.porgcoat.2004.06.007.

[142] G. Blanc, C. Gabrielli, M. Keddam, Measurement of the Electrochemical Noise by a Cross Correlation Method, Electrochimica Acta. 20 (1975) 687–689. doi:10.1016/0013-4686(75)90069-9.

[143] S.C. Creason, J.W. Hayes, D.E. Smith, Fourier transform faradaic admittance measurements III. Comparison of measurement efficiency for various test signal waveforms, Journal of Electroanalytical Chemistry. 47 (1973) 9–46. doi:10.1016/S0022-0728(73)80343-2.

[144] J.E. Garland, C.M. Pettit, D. Roy, Analysis of experimental constraints and variables for time resolved detection of Fourier transform electrochemical impedance spectra, Electrochimica Acta. 49 (2004) 2623–2635. doi:10.1016/j.electacta.2003.12.051.

[145] E. Van Gheem, R. Pintelon, J. Vereecken, J. Schoukens, A. Hubin, P. Verboven, O. Blajiev, Electrochemical impedance spectroscopy in the presence of non-linear distortions and non-stationary behaviour Part I: Theory and validation, Electrochimica Acta. 49 (2004) 4753–4762. doi:10.1016/j.electacta.2004.05.039.

[146] E. Van Gheem, R. Pintelon, A. Hubin, J. Schoukens, P. Verboven, O. Blajiev, J. Vereecken, Electrochemical impedance spectroscopy in the presence of non-linear distortions and non-stationary behaviour: Part II. Application to crystallographic pitting corrosion of aluminium, Electrochimica Acta. 51 (2006) 1443–1452. doi:10.1016/j.electacta.2005.02.096.

[147] O.L. Blajiev, R. Pintelon, A. Hubin, Detection and evaluation of measurement noise and stochastic non-linear distortions in electrochemical impedance measurements by a model based on a broadband periodic excitation, Journal of Electroanalytical Chemistry. 576 (2005) 65–72. doi:10.1016/j.jelechem.2004.09.029.

[148] Y. Van Ingelgem, E. Tourwé, O. Blajiev, R. Pintelon, A. Hubin, Advantages of odd random phase multisine electrochemical impedance measurements, Electroanalysis. 21 (2009) 730–739. doi:10.1002/elan.200804471.

[149] T. Breugelmans, E. Tourwé, J.B. Jorcin, A. Alvarez-Pampliega, B. Geboes, H. Terryn, A. Hubin, Odd random phase multisine EIS for organic coating analysis, Progress in Organic Coatings. 69 (2010) 215–218. doi:10.1016/j.porgcoat.2010.04.008.

[150] T. Breugelmans, J. Lataire, T. Muselle, E. Tourwé, R. Pintelon, A. Hubin, Odd random phase multisine electrochemical impedance spectroscopy to quantify a non-stationary behaviour: Theory and validation by calculating an instantaneous impedance value, Electrochimica Acta. 76 (2012) 375–382. doi:10.1016/j.electacta.2012.05.051.

[151] A. Battistel, G. Du, F. La Mantia, On the Analysis of Non-stationary Impedance Spectra, Electroanalysis. 28 (2016) 2346–2353. doi:10.1002/elan.201600260.

[152] A. Battistel, F. La Mantia, On the physical definition of dynamic impedance: How to design an optimal strategy for data extraction, Electrochimica Acta. 304 (2019) 513–520. doi:10.1016/j.electacta.2019.03.033.

[153] E. Madej, S. Klink, W. Schuhmann, E. Ventosa, F. La Mantia, Effect of the specific surface area on thermodynamic and kinetic properties of nanoparticle anatase TiO2 in lithium-ion batteries, Journal of Power Sources. 297 (2015) 140–148. doi:10.1016/j.jpowsour.2015.07.079.

[154] G.A. Ragoisha, A.S. Bondarenko, N.P. Osipovich, E.A. Streltsov, Potentiodynamic electrochemical impedance spectroscopy: Lead underpotential deposition on tellurium, Journal of Electroanalytical Chemistry. 565 (2004) 227–234. doi:10.1016/j.jelechem.2003.10.014.

[155] R.L. Sacci, D.A. Harrington, Dynamic Electrochemical Impedance Spectroscopy, ECS Transactions. 19 (2009) 31–42. doi:10.1149/1.3247564.

[156] R.L. Sacci, D.A. Harrington, Dynamic impedance of formic acid electrooxidation on polycrystalline palladium, ECS Transactions. 19 (2009) 123–129. doi:10.1149/1.3247570.

[157] R.L. Sacci, F. Seland, D.A. Harrington, Dynamic electrochemical impedance spectroscopy, for electrocatalytic reactions, Electrochimica Acta. 131 (2014) 13–19. doi:10.1016/j.electacta.2014.02.120.

[158] Z. Stoynov, Rotating fourier transform-engine for non-stationary impedance spectroscopy, Bulgarian Chemical Communications. 50 (2018) 123–130.

[159] B. Savova-Stoynov, Z.B. Stoynov, Instantaneous impedance analysis, Mechanical and Corrosion Properties. Series A, Key Engineering Materials. 59–60 (1991) 273–282. doi:10.4028/www.scientific.net/kem.59-60.273.

[160] Z. Stoynov, Nonstationary impedance spectroscopy, Electrochimica Acta. 38 (1993) 1919–1922. doi:10.1016/0013-4686(93)80315-Q.

[161] G.S. Popkirov, Fast time-resolved electrochemical impedance spectroscopy for investigations under nonstationary conditions, Electrochimica Acta. 41 (1996) 1023–1027. doi:10.1016/0013-4686(95)00434-3.

[162] C.A. Schiller, F. Richter, E. Gülzow, N. Wagner, Validation and evaluation of electrochemical impedance spectra of systems with states that change with time, Physical Chemistry Chemical Physics. 3 (2001) 374–378. doi:10.1039/b007678n.

[163] Z.B. Stoynov, B.S. Savova-Stoynov, Impedance study of non-stationary systems: four-dimensional analysis, Journal of Electroanalytical Chemistry. 183 (1985) 133–144. doi:10.1016/0368-1874(85)85486-1.

[164] B. Savova-Stoynov, Z.B. Stoynov, Four-dimensional estimation of the instantaneous impedance, Electrochimica Acta. 37 (1992) 2353–2355. doi:10.1016/0013-4686(92)85131-4.

[165] N. Wagner, E. Gülzow, Change of electrochemical impedance spectra (EIS) with time during CO-poisoning of the Pt-anode in a membrane fuel cell, Journal of Power Sources. 127 (2004) 341–347. doi:10.1016/j.jpowsour.2003.09.031.

[166] V. Horvat-Radošević, K. Kvastek, K.M. Košiček, Application of Stoynov’s 4-D analysis for nonstationary impedance spectra corrections of thin poly(o-ethoxyaniline) modified Pt electrode, Bulgarian Chemical Communications. 49 (2017) 119–127.

[167] K.M. Košiček, V. Horvat-Radošević, K. Kvastek, Frequency Response Analysis of a Nonstationary System: Electrochemical Transition of Polyaniline, Croatica Chemica Acta. 91 (2018) 463–473. doi:10.5562/cca3454.

[168] C. Gabrielli, H. Takenouti, O. Haas, A. Tsukada, Impedance investigation of the charge transport in film-modified electrodes, Journal of Electroanalytical Chemistry. 302 (1991) 59–89. doi:10.1016/0022-0728(91)85032-K.

[169] M.F. Mathias, O. Haas, Effect of Counterion Type on Charge Transport at Redox Polymer-Modified Electrodes, Journal of Physical Chemistry. 97 (1993) 9217–9225. doi:10.1021/j100138a025.

[170] K.L. Brown, R. Danforth, E. Bleitz, Y.H.D. Rens, Cyclic Voltammetric and Spectroelectrochemical Studies of Tris(5-amino-1,10-phenantroline)Iron(II) Polymer Films, International Journal of Electrochemical Science. 15 (2020) 10707–10721. doi:10.20964/2020.11.66.

[171] I. Ivanko, J. Pánek, J. Svoboda, A. Zhigunov, E. Tomšík, Tuning the photoluminescence and anisotropic structure of PEDOT, Journal of Materials Chemistry C. 7 (2019) 7013–7019. doi:10.1039/c9tc00955h.

[172] T.A. Rokob, G.G. Láng, Remarks on the electrochemical application of optical methods for the determination of stress in electrodes, Electrochimica Acta. 51 (2005) 93–97. doi:10.1016/j.electacta.2005.04.006.

[173] G.G. Láng, N.S. Sas, S. Vesztergom, Experimental Determination of Surface Stress Changes in Electrochemical Systems – Possibilities and Pitfalls, Chemical and Biochemical Engineering Quarterly. 23 (2009) 1–9.

[174] G.G. Láng, Comment on “Refractive error correction for in situ curvature measurement using laser beam deflection method,” Journal of Applied Physics. 107 (2010) 116104. doi:10.1063/1.3415565.

[175] J. Mostany, B.R. Scharifker, Impedance spectroscopy of undoped, doped and overoxidized polypyrrole films, Synthetic Metals. 87 (1997) 179–185. doi:10.1016/S0379-6779(97)80105-1.

[176] K. Krukiewicz, T. Jarosz, A.P. Herman, R. Turczyn, S. Boncel, J.K. Zak, The effect of solvent on the synthesis and physicochemical properties of poly(3,4-ethylenedioxypyrrole), Synthetic Metals. 217 (2016) 231–236. doi:10.1016/j.synthmet.2016.04.005.

[177] K. Hegedüs, 3,4-dialkoxi-pirrolok és származékaik előállítása, Eötvös Loránd Tudományegyetem, 2015.

[178] T. Murashima, Y. Uchihara, N. Wakamori, H. Uno, T. Ogawa, N. Ono, The first preparation of crown ether-annulated porphyrin, Tetrahedron Letters. 37 (1996) 3133–3136. doi:10.1016/0040-4039(96)00509-6.

[179] G.A. Sotzing, J.R. Reynolds, P.J. Steel, Electrochromic conducting polymers via electrochemical polymerization of bis(2-(3,4-ethylenedioxy)thienyl) monomers, Chemistry of Materials. 8 (1996) 882–889. doi:10.1021/cm9504798.

[180] I.F. Perepichka, S. Roquet, P. Leriche, J.M. Raimimdo, P. Frère, J. Roncali, Electronic properties and reactivity of short-chain oligomers of 3,4-phenylenedioxythiophene (PheDOT), Chemistry - A European Journal. 12 (2006) 2960–2966. doi:10.1002/chem.200501284.

[181] K.M.N. De Silva, E. Hwang, W.K. Serem, F.R. Fronczek, J.C. Garno, E.E. Nesterov, Long-chain 3,4-ethylenedioxythiophene/thiophene oligomers and semiconducting thin films prepared by their electropolymerization, ACS Applied Materials and Interfaces. 4 (2012) 5430–5441. doi:10.1021/am301349g.

[182] G.E. Wnek, Charge carrier chemistry in electroactive polymers, in: D.E. Bergbreiter, R. Martin (Eds.), Functional Polymers, Plenum Press, New York, 1989: pp. 107–118.

[183] A.D. Jannakoudakis, P.D. Jannakoudakis, E. Theodoridou, Electrochemical oxidation of carbon fibres in aqueous solutions and analysis of the surface oxides, Journal of Applied Electrochemistry. 20 (1990) 619–624.

[184] P.L. Runnels, J.D. Joseph, M.J. Logman, R.M. Wightman, Effect of pH and Surface Functionalities on the Cyclic Voltammetric Responses of Carbon-Fiber Microelectrodes, Analytical Chemistry. 71 (1999) 2782–2789. doi:10.1021/ac981279t.

[185] K. Kato, K. Kano, T. Ikeda, Electrochemical Characterization of Carbon Felt Electrodes for Bulk Electrolysis and for Biocatalyst-Assisted Electrolysis, Journal of The Electrochemical Society. 147 (2000) 1449–1453. doi:10.1149/1.1393376.

[186] C. Li, L. Zhang, L. Ding, H. Ren, H. Cui, Effect of conductive polymers coated anode on the performance of microbial fuel cells (MFCs) and its biodiversity analysis, Biosensors and Bioelectronics. 26 (2011) 4169–4176. doi:10.1016/j.bios.2011.04.018.

[187] X. Liu, W. Wu, Z. Gu, Poly (3,4-ethylenedioxythiophene) promotes direct electron transfer at the interface between Shewanella loihica and the anode in a microbial fuel cell, Journal of Power

Sources. 277 (2015) 110–115. doi:10.1016/j.jpowsour.2014.11.129.

[188] H. Zhou, H. Zhang, P. Zhao, B. Yi, A comparative study of carbon felt and activated carbon based electrodes for sodium polysulfide/bromine redox flow battery, Electrochimica Acta. 51 (2006) 6304–6312. doi:10.1016/j.electacta.2006.03.106.

[189] Y.L. Kang, S. Ibrahim, P. Saravanan, Enhancement of microbial fuel cell anode through conductive polymer, Proceedings of the 6th European Fuel Cell - Piero Lunghi Conference, EFC 2015. (2015).

[190] Y.L. Kang, S. Pichiah, S. Ibrahim, Facile reconstruction of microbial fuel cell (MFC) anode with enhanced exoelectrogens selection for intensified electricity generation, International Journal of Hydrogen Energy. 42 (2017) 1661–1671. doi:10.1016/j.ijhydene.2016.09.059.

[191] D.T. Sawyer, A. Sobkowiak, J.J.L. Roberts, Electrochemistry for chemists, Second Ed., John Wiley & Sons, NY, 1995.

[192] G. Inzelt, G.G. Láng, Electrochemical Impedance Spectroscopy (EIS) for Polymer Characterization, in: S. Cosnier, A. Karyakin (Eds.), Electropolymerization (Concepts, Materials and Applications), WILEY-VCH Verlag GmbH & Co. KGaA, Weinheim, Germany, 2010.

[193] G. Inzelt, G. Láng, Impedance analysis of poly(tetracyanoquinodimethane) electrodes: effect of electrolyte concentration and temperature, Electrochimica Acta. 36 (1991) 1355–1361. doi:10.1016/0013-4686(91)80016-2.

[194] H. Kuramitz, M. Matsushita, S. Tanaka, Electrochemical removal of bisphenol A based on the anodic polymerization using a column type carbon fiber electrode, Water Research. 38 (2004) 2331–2338. doi:10.1016/j.watres.2004.02.023.

[195] B. Gözmen, M.A. Oturan, N. Oturan, O. Erbatur, Indirect electrochemical treatment of bisphenol A in water via electrochemically generated Fenton's reagent, Environmental Science & Technology. 37 (2003) 3716–3723. doi:10.1021/es034011e.

[196] H. Maeda, T. Okada, Y. Matsumoto, K. Katayama, Y. Yamauchi, H. Ohmori, Electrochemical coating with poly(phenylene oxide) films bearing oligoether groups as a tool for elimination of protein adsorption to electrode surfaces, Analytical Sciences. 15 (1999) 633–639. doi:10.2116/analsci.15.633.

[197] J. Zhang, Q. Li, M. Chen, H. Li, Z. Xu, Electrochemically monitoring the removal of bisphenol A based on its anodic deposition at an ITO electrode, Sensors and Actuators, B: Chemical. 160 (2011) 784–790. doi:10.1016/j.snb.2011.08.063.

[198] G.F. Pereira, R.C. Rocha-filho, N. Bocchi, S.R. Biaggio, Electrochemical degradation of bisphenol A using a flow reactor with a boron-doped diamond anode, Chemical Engineering Journal. 198–199 (2012) 282–288. doi:10.1016/j.cej.2012.05.057.

[199] Q. Li, H. Li, J. Zhang, Z. Xu, A novel pH potentiometric sensor based on electrochemically synthesized polybisphenol A films at an ITO electrode, Sensors and Actuators B: Chemical. 155 (2011) 730–736. doi:10.1016/j.snb.2011.01.038.

[200] E. Mazzotta, C. Malitesta, E. Margapoti, Direct electrochemical detection of bisphenol A at PEDOT-modified glassy carbon electrodes, Analytical and Bioanalytical Chemistry. 405 (2013) 3587–3592. doi:10.1007/s00216-013-6723-6.

[201] B.W. Silverman, Density Estimation for Statistics and Data Analysis, First CRC, Chapman & Hall/CRC, London, UK, 1998.

[202] P. Valkó, S. Vajda, Advanced scientific computing in BASIC with applications in chemistry, biology and pharmacology, Data handl, Elsevier, Amsterdam, 1989.

[203] K. Levenberg, A Method for the Solution of Certain Non-Linear Problems in Least Squares, Quarterly of Applied Mathematics. 2 (1944) 164–168.

[204] D.W. Marquardt, An algorithm for least-squares estimation of nonlinear parameters, SIAM Journal on Applied Mathematics. 11 (1963) 431–441.

[205] B. Cain, P.L. Schechter, M.W. Bautz, Measuring gravitational lensing flexion in A1689 using an analytic image model, Astrophysical Journal. 736 (2011) 43. doi:10.1088/0004-637X/736/1/43.

[206] G.G. Láng, M. Ujvári, G. Inzelt, Possible origin of the deviation from the expected impedance

response of polymer film electrodes, Electrochimica Acta. 46 (2001) 4159–4175. doi:10.1016/S0013-4686(01)00704-6.

[207] G.G. Láng, M. Ujvári, T.A. Rokob, G. Inzelt, The brush model of the polymer films — analysis of the impedance spectra of Au,Pt|poly (o-phenylenediamine) electrodes, Electrochimica Acta. 51 (2006) 1680–1694. doi:10.1016/j.electacta.2005.02.100.

[208] L. Bich, M. Mossio, K. Ruiz-Mirazo, A. Moreno, Biological regulation: controlling the system from within, Biology and Philosophy. 31 (2016) 237–265. doi:10.1007/s10539-015-9497-8.

[209] Y. Tu, W.J. Rappel, Adaptation in Living Systems, Annual Review of Condensed Matter Physics. 9 (2018) 183–205. doi:10.1146/annurev-conmatphys-033117-054046.

[210] H. Chang, A. Levchenko, Adaptive molecular networks controlling chemotactic migration: Dynamic inputs and selection of the network architecture, Philosophical Transactions of the Royal Society B: Biological Sciences. 368 (2013) No. 20130117. doi:10.1098/rstb.2013.0117.

[211] B.C. Buddingh', J.C.M. Van Hest, Artificial Cells: Synthetic Compartments with Life-like Functionality and Adaptivity, Accounts of Chemical Research. 50 (2017) 769–777. doi:10.1021/acs.accounts.6b00512.

[212] P.J. Steiner, R.J. Williams, J. Hasty, L.S. Tsimring, Criticality and Adaptivity in Enzymatic Networks, Biophysical Journal. 111 (2016) 1078–1087. doi:10.1016/j.bpj.2016.07.036.

[213] F. He, E. Murabito, H. V. Westerhoff, Synthetic biology and regulatory networks: Where metabolic systems biology meets control engineering, Journal of the Royal Society Interface. 13 (2016) No. 20151046. doi:10.1098/rsif.2015.1046.

[214] C. Claaßen, T. Gerlach, D. Rother, Stimulus-Responsive Regulation of Enzyme Activity for One-Step and Multi-Step Syntheses, Advanced Synthesis and Catalysis. 361 (2019) 2387–2401. doi:10.1002/adsc.201900169.

[215] T.W. Traut, Allosteric Regulatory Enzymes, Springer, Berlin, Germany, 2008.

[216] Z. Guo, W.A. Johnston, J. Whitfield, P. Walden, Z. Cui, E. Wijker, S. Edwardraja, I.R. Lantadilla, F. Ely, C. Vickers, J.P.J. Ungerer, K. Alexandrov, Generalizable Protein Biosensors Based on Synthetic Switch Modules, Journal of the American Chemical Society. 141 (2019) 8128–8135. doi:10.1021/jacs.8b12298.

[217] V. Stein, K. Alexandrov, Synthetic protein switches: Design principles and applications, Trends in Biotechnology. 33 (2015) 101–110. doi:10.1016/j.tibtech.2014.11.010.

[218] M. Ostermeier, Designing switchable enzymes, Current Opinion in Structural Biology. 19 (2009) 442–448. doi:10.1016/j.sbi.2009.04.007.

[219] A. Bautista-Barrufet, F. López-Gallego, V. Rojas-Cervellera, C. Rovira, M.A. Pericàs, J.M. Guisán, P. Gorostiza, Optical control of enzyme enantioselectivity in solid phase, ACS Catalysis. 4 (2014) 1004–1009. doi:10.1021/cs401115s.

[220] I. Willner, R. Blonder, E. Katz, A. Stocker, A.F. Bückmann, Reconstitution of Apo-Glucose Oxidase with a Nitrospiropyran-Modified FAD Cofactor Yields a Photoswitchable Biocatalyst for Amperometric Transduction of Recorded Optical Signals, Journal of the American Chemical Society. 118 (1996) 5310–5311. doi:10.1021/ja960228f.

[221] Y. Cao, Y. Wang, Temperature-Mediated Regulation of Enzymatic Activity, ChemCatChem. 8 (2016) 2740–2747. doi:10.1002/cctc.201600406.

[222] G. Cirillo, F.P. Nicoletta, M. Curcio, U.G. Spizzirri, N. Picci, F. Iemma, Enzyme immobilization on smart polymers: Catalysis on demand, Reactive and Functional Polymers. 83 (2014) 62–69. doi:10.1016/j.reactfunctpolym.2014.07.010.

[223] P. Wang, S. Liu, H. Liu, Multiple stimuli-switchable bioelectrocatalysis under physiological conditions based on copolymer films with entrapped enzyme, Journal of Physical Chemistry B. 118 (2014) 6653–6661. doi:10.1021/jp501624y.

[224] J. Lee, D. Lee, E. Oh, J. Kim, Y.P. Kim, S. Jin, H.S. Kim, Y. Hwang, H.K. Ja, J.G. Park, C.H. Shin, J. Kim, T. Hyeon, Preparation of a magnetically switchable bioelectrocatalytic system employing

cross-linked enzyme aggregates in magnetic mesocellular carbon foam, Angewandte Chemie - International Edition. 44 (2005) 7427–7432. doi:10.1002/anie.200502995.

[225] I. Willner, E. Katz, Magnetic Control of Electrocatalytic and Bioelectrocatalytic Processes, Angewandte Chemie - International Edition. 42 (2003) 4576–4588. doi:10.1002/anie.200201602.

[226] Y. Filipov, A. Zakharchenko, S. Minko, E. Katz, Magneto-Controlled Biocatalytic Cascades with Logically Processed Input Signals – Substrate Channeling versus Free Diffusion, ChemPhysChem. 19 (2018) 3035–3043. doi:10.1002/cphc.201800851.

[227] A. Zakharchenko, N. Guz, A.M. Laradji, E. Katz, S. Minko, Magnetic field remotely controlled selective biocatalysis, Nature Catalysis. 1 (2018) 73–81. doi:10.1038/s41929-017-0003-3.

[228] V. Leskovac, Comprehensive Enzyme Kinetics, Springer, Boston, MA, 2003.

[229] P. Bollella, A. Melman, E. Katz, Electrochemically Generated Interfacial pH Change: Application to Signal-Triggered Molecule Release, ChemElectroChem. 7 (2020) 3383–3383. doi:10.1002/celc.202000892.

[230] V.K. Kadambar, M. Bellare, P. Bollella, E. Katz, A. Melman, Electrochemical control of the catalytic activity of immobilized enzymes, Chemical Communications. 56 (2020) 13800–13803. doi:10.1039/d0cc06190e.

[231] E. Katz, ed., Implantable Bioelectronics - Devices, Materials and Applications, Wiley-VCH, Weinheim, Germany, 2014.

[232] O. Parlak, A. Salleo, A. Turner, eds., Wearable Bioelectronics, Elsevier, Amsterdam, The Netherlands, 2020.

[233] B. Krajewska, S. Ciurli, Jack bean (Canavalia ensiformis) urease. Probing acid-base groups of the active site by pH variation, Plant Physiology and Biochemistry. 43 (2005) 651–658. doi:10.1016/j.plaphy.2005.05.009.

[234] F. Bergmann, R. Segal, A. Shimoni, M. Wurzel, The pH-Dependence of Enzymic Ester Hydrolysis, The Biochemical Journal. 63 (1956) 684–690. doi:10.1042/bj0630684.

[235] V.F. Valuk, G. Duportail, V.G. Pivovarenko, A wide-range fluorescent pH-indicator based on 3-hydroxyflavone structure, Journal of Photochemistry and Photobiology A: Chemistry. 175 (2005) 226–231. doi:10.1016/j.jphotochem.2005.05.003.

[236] B. Fuladpanjeh-Hojaghan, M.M. Elsutohy, V. Kabanov, B. Heyne, M. Trifkovic, E.P.L. Roberts, In-Operando Mapping of pH Distribution in Electrochemical Processes, Angewandte Chemie. 131 (2019) 16971–16975. doi:10.1002/ange.201909238.

[237] B. Solomon, Y. Levin, Adsorption of Amyloglucosidase on Inorganic Carriers, Biotechnology and Bioengineering. 17 (1975) 1323–1333. doi:10.1002/bit.260170907.

[238] T.K. Tam, J. Zhou, M. Pita, M. Ornatska, S. Minko, E. Katz, Biochemically controlled bioelectrocatalytic interface, Journal of the American Chemical Society. 130 (2008) 10888–10889. doi:10.1021/ja8043882.

[239] V. Bocharova, T.K. Tam, J. Halámek, M. Pita, E. Katz, Reversible gating controlled by enzymes at nanostructured interface, Chemical Communications. 46 (2010) 2088–2090. doi:10.1039/b927156b.

[240] G.G. Láng, G. Inzelt, An advanced model of the impedance of polymer film electrodes, Electrochimica Acta. 44 (1999) 2037–2051. doi:10.1016/S0013-4686(98)00312-0.

[241] I. Rubinstein, J. Rishpon, S. Gottesfeld, An AC-Impedance Study of Electrochemical Processes at Nafion-Coated Electrodes, Journal of The Electrochemical Society. 133 (1986) 729–734. doi:10.1149/1.2108663.

[242] L. “Bert” Groenendaal, F. Jonas, D. Freitag, H. Pielartzik, J.R. Reynolds, Poly(3,4-ethylenedioxythiophene) and Its Derivatives: Past, Present, and Future, Advanced Materials. 12 (2000) 481–494. doi:10.1002/(SICI)1521-4095(200004)12:7<481::AID-ADMA481>3.0.CO;2-C.

[243] B. Winther-Jensen, K. West, Vapor-Phase Polymerization of 3,4-Ethylenedioxythiophene: A Route to Highly Conducting Polymer Surface Layers, Macromolecules. 37 (2004) 4538–4543. doi:10.1021/ma049864l.

[244] R.D. Armstrong, Impedance Plane Display for an Electrode with Diffusion Restricted to a Thin Layer, Journal of Electroanalytical Chemistry. 198 (1986) 177–180.

[245] M.F. Mathias, O. Haas, An Alternating Current Impedance Model Including Migration and Redox-Site Interactions at Polymer-Modified Electrodes, Journal of Physical Chemistry. 96 (1992) 3174–3182. doi:10.1021/j100186a073.

[246] O. Contamin, E. Levart, G. Magner, R. Parsons, M. Savy, Restricted diffusion impedance. Theory and application to the reaction of oxygen on a hydrogen phthalocyanine film, Journal of Electroanalytical Chemistry. 179 (1984) 41–52. doi:10.1016/S0022-0728(84)80273-9.

[247] C. Gabrielli, O. Haas, H. Takenouti, Impedance analysis of electrodes modified with a reversible redox polymer film, Journal of Applied Electrochemistry. 17 (1987) 82–90. doi:10.1007/BF01009134.

[248] J.R. Macdonald, D.R. Franceschetti, Precision of impedance spectroscopy estimates of bulk, reaction rate, and diffusion parameters, Journal of Electroanalytical Chemistry. 307 (1991) 1–11. doi:10.1016/0022-0728(91)85534-V.

[249] J. Bobacka, A. Lewenstam, A. Ivaska, A. Fin, Electrochemical impedance spectroscopy of oxidized poly(3,4-ethylenedioxythiophene) film electrodes in aqueous solutions, Journal of Electroanalytical Chemistry. 489 (2000) 17–27. doi:10.1016/S0022-0728(00)00206-0.

[250] M.R. Abidian, D.C. Martin, Experimental and theoretical characterization of implantable neural microelectrodes modified with conducting polymer nanotubes, Biomaterials. 29 (2008) 1273–1283. doi:10.1016/j.biomaterials.2007.11.022.

[251] C. de Boor, A Practical Guide to Splines, Applied Ma, Springer, New York, 2001.

[252] G. Inzelt, G. Láng, Model dependence and reliability of the electrochemical quantities derived from the measured impedance spectra of polymer modified electrodes, Journal of Electroanalytical Chemistry. 378 (1994) 39–49. doi:10.1016/0022-0728(94)87055-1.

[253] T. Komura, T. Yamaguti, K. Takahasi, Impedance Study of the Charge Transport at Poly-o-Phenylenediamine Film Electrodes, Electrochimica Acta. 41 (1996) 2865–2870. doi:10.1016/0013-4686(96)00114-4.